# ttH, H en WW avec analysis at ATLAS, LHC and very low energy electron studies of 2004 combined test beam

H. Zhang

H. Zhang. ttH, H en WW avec analysis at ATLAS, LHC and very low energy electron studies of 2004 combined test beam. Physics [physics]. Université de la Méditerranée - Aix-Marseille II, 2008. English. NNT : . tel-00366852

**HAL Id: tel-00366852**

**https://theses.hal.science/tel-00366852v1**

Submitted on 9 Mar 2009

CPPM-T-2008-03

UNIVERSITÉ DE LA MÉDITERRANÉE AIX-MARSEILLE II
FACULTÉ DES SCIENCES DE LUMINY
163 Avenue de Luminy 13288 MARSEILLE Cedex 09

**THÈSE DE DOCTORAT**

*Spécialité : Physique mathématique, physique des particules et modélisation*
*dans le cadre d'une co-tutelle de thèse entre:*
*Institute of High Energy Physics, Chinese Academy of Sciences, China*
*Centre de Physique des Particules de Marseille, France*

présentée par

**Huaqiao ZHANG**

en vue d'obtenir le grade de docteur de l'Université de la Méditerranée

# Analyse $ttH, H \rightarrow WW^{(*)}$ avec ATLAS au LHC et Étude des Électron à Très Basses Énergie dans le Test Faisceau Combiné 2004

## $ttH, H \rightarrow WW^{(*)}$ analysis at ATLAS, LHC and Very Low Energy electron studies of 2004 combined test beam

Soutenue le 10 Juin 2008 devant le jury composé de :

| | |
|---|---|
| M. GuoMing Chen | |
| M. YuanNing Gao | Président |
| M. Liang Han | |
| M. Yi Jiang | |
| M. Shan Jin | Directeur de thèse IHEP |
| M. YaJun Mao | |
| M. Emmanuel Monnier | Directeur de thèse CPPM |
| M. Qun OuYang | |

# Contents

# Chapter 1

# Preface

## Contents

## 1.1 Standard Model and Higgs

The Standard Model is the most accurate theory that describe the fundamental structure of mater and interactions. In this model, the fundamental constituents of mater are quarks and leptons, and the interaction are linked to carrier particles called bosons. Quarks and leptons are fermions of spin $\frac{1}{2}$ while interaction particles are of integer spin. Under the present knowledge, all of them are point like particles. No experimental evidence of finer structure was found. These leptons and quarks are divided into three generations, each generation has four members, each member of same generation has different charge and mass. For these leptons and quarks, there are corresponding anti-particles. These anti-particles have same masses, but opposite sign of all other quantum numbers compared to the corresponding particles [1, 2]. There are upper, charm and top quarks, whose charges are $(-\frac{2}{3})$. There are also down, strange and bottom quarks, whose charges are $(-\frac{1}{3})$. Leptons are of two kinds. One set of them like electron, muon and tau particles, with a charge $(-1)$, while the other set of them are neutral neutrinos, corresponding to each type of lepton. Figure 1.1 is the schematic plots of the fundamental particle classification.

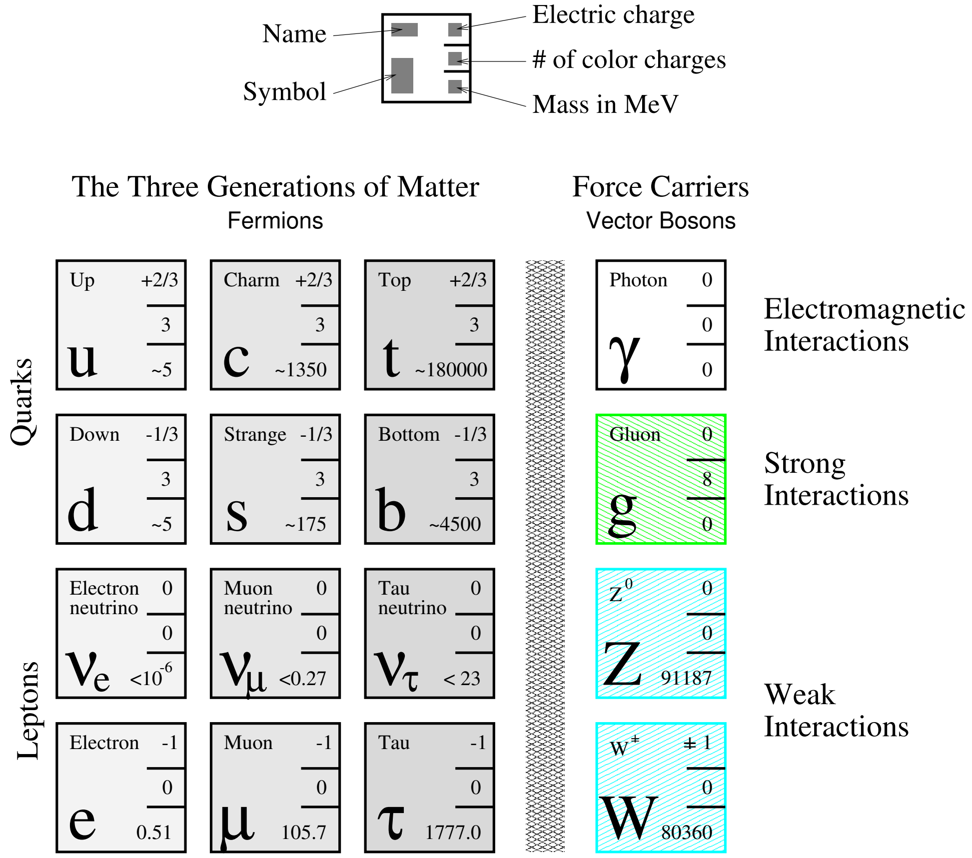

FIGURE 1.1: Categories of fundamental particles

There are four different interactions in nature: Strong force, Electromagnetism, Weak force and Gravity. The propagators of these interactions are the names of force carrier particles. They are Gluon for strong force, photon for electromagnetism, $W^{\pm}, Z^0$ for weak force and graviton for gravity. The first three kinds of force carriers all have spin one bosons and have been found experimentally, while the fourth has not been found until now and the theoretical prediction is spin two. The unique particle, Higgs, which give masses to these fundamental particles, does not belong to any category of particles described above. The properties of the four force carriers are listed in table 1.1.

| | electromagnetism | weak interaction | strong interaction | gravity |
|---|---|---|---|---|
| Sources | charge | weak charge | color | mass |
| Intensity | $\frac{e^2}{\hbar c} \simeq \frac{1}{137}$ | $(\frac{m_p c}{\hbar})^2 \frac{G}{\hbar c} \sim 10^{-5}$ | $\frac{g^2}{\hbar c} \simeq 10$ | $\frac{G m_p^2}{\hbar c} \sim 10^{-38}$ |
| Force range (m) | Long range<br>$\infty$ | short range<br>$\sim 10^{-18}$ | short range<br>$10^{-15}$ | long range<br>$\infty$ |
| propagator | photon<br>$\gamma$ | $W^{\pm}, Z^0$<br>$W^{\pm}$,$Z^0$ | Gluon<br>$g$ | Graviton(in theory)<br>$G$ |
| $J^P$ | $1^-$ | $1^?$ | $1^-$ | $2^+$ |
| Mass(GeV) | $M_\gamma = 0$ | $M_{W^\pm} = 80.4$<br>$M_{Z^0} = 91.2$ | $M_g = 0$ | $M_G = 0$ |
| Theories | Electro-Weak Dynamics (EW) | | Quantum Chromodynamics (QCD) | Geometric Dynamics (General relativity) |

Table 1.1: Properties of four interactions

Since the last 70 years, physicists are trying to unify these four interactions. Varies attempts have been tried in different directions. But the most successful ones belong to Gauge Theory. Electro-Weak theory is $SU(2)_L \times U(1)_Y$ Gauge Theory. Quantum Chromo Dynamics is $SU_c(3)$ Gauge Theory. These two theories constitute the Standard Model, which is a $SU_c(3) \times SU(2)_L \times U(1)_Y$ Gauge Theory. Higgs particle is a scalar which gives masses to gauge bosons through the Higgs mechanism and gives mass to fermions by Yukawa Coupling [3].

### 1.1.1 Symmetry in particle physics

The phenomena of symmetry have existed since time begins. Such as day after day, year after year. Also phenomena of symmetry are very common in our lives. Such as sun in the sky, Si He Yuan in Beijing, the rolling wheel. Symmetry picture is popular. Such as most people prefer symmetrical plots, symmetrical face. So, in our lives, people are likely using symmetry approach to describe things.

Although the symmetry is beautiful, the symmetry breaking makes people more profound understand the nature of things. Like the symmetry of sunrise, let people believe that the earth is the center of the universe, because it is in people's love of symmetry, but those strange tracks and movements of planets and stars destroy the symmetry of Earth as the center, so that people come to the awareness of sun as the center, and now the knowledge of galaxies and even the knowledge of the entire universe.

In particle physics, symmetry and symmetry breaking are also ubiquitous. Field theories are used to describe the dynamics of particle physics. According to Noether's theorem, any differentiable symmetry of the action of a physical system has a corresponding conservation law. The action of a physical system is an integral of a so-called Lagrangian function, from which the system's behavior can be determined by the principle of least action. Thus, the invariance of time-space transformation accounts for energy and linear momentum conservation of this system. The invariance of Lorentz transformation accounts for angular conservation. Gauge transformation invariance is one of the basic transformations of field.

**Gauge Transformation:** Under the rotation of internal space, if the field component of $\phi_\sigma(x)$ with the transformation of:

$$\phi_\sigma(x) \rightarrow \phi'_\sigma(x) = exp[-i\theta^\alpha T^\alpha_{\sigma\rho}]\phi_\rho(x) \quad . \tag{1.1}$$

of which $T^\alpha$ matrices are the generators of gauge group $G$. There is one conserved current for every generator. This group is non Abelian. Their commutation relations are:

$$[T^\alpha, T^\beta] = if^{\alpha\beta\gamma}T^\gamma \tag{1.2}$$

Where $f^{\alpha\beta\gamma}$ are the group structure constants of SU(3). The transformation satisfy the form described above is called gauge transformation. If the Group Parameters $\theta^\alpha$ is time-space independent constant, it is a global gauge transformation. If $\theta^\alpha$ is time-space dependent function of $\theta^\alpha(x)$, it is a local gauge transformation.

**Gauge Field:** Unfortunately, the transformations of normal Lagrangian can not pass the derivatives of gauge invariance if $\theta^\alpha(x)$ is time-space dependent. In order to get a local gauge invariant symmetry, the gauge transformation Lagrangian density can be written as:

$$\mathcal{L} = -\frac{1}{4}F^\alpha_{\mu,\nu}F^{\mu,\nu,\alpha} \quad . \tag{1.3}$$

Of witch $F^\alpha_{\mu,\nu}$ is the strength of gauge field, and it is defined as:

$$F^\alpha_{\mu,\nu} = \partial_\mu A^\alpha_\nu - \partial_\nu A^\alpha_\mu + gf^{\alpha\beta\gamma}A^\beta_\mu A^\gamma_\nu \quad , \tag{1.4}$$

This Lagrangian describes particles of spin 1, such as photon, intermediate bosons, gluons. And g is the coupling constant - a quantity defining the strength of an interaction. However, If mass term of $\frac{1}{2}M_A^2 A_\mu A^\mu$ added in this Lagrangian, it is not invariant with the gauge transformation of equation 1.1. Since there is no way to add the square term of field $A^\alpha_\mu(x)$, it means that all the gauge bosons that described by this Lagrangian are massless. While in fact, $W^\pm, Z^0$ intermediate bosons have masses $\sim 80 - 90GeV$. So, the Higgs mechanism described in the following section was introduced to solve this problem.

## 1.1.2 Higgs mechanism

Due to the constraint of gauge invariance, the Lagrangian of gauge field can not contain square term of the field. It results that gauge particles are massless in this theory. Therefor this Gauge Theory is not the exact description of intermediate bosons since they have masses. To solve this problem, the Higgs mechanism has been introduced.

### 1.1.2.1 Spontaneous symmetry breaking and Goldstone particles

Consider a simple real scaler field $\phi(x)$ with a usual Lagrangian:

$$\mathcal{L} = \frac{1}{2}\partial\mu\phi\partial^\mu\phi - V(\phi), \quad V(\phi) = \frac{1}{2}\mu^2\phi^2 + \frac{1}{4}\lambda\phi^4 \quad , \tag{1.5}$$

It is invariant under the internal space reflection transformation of $\phi(x) \rightarrow -\phi(x)$ since there is no odd power item of this Lagrangian. If the coefficient of mass term $\mu^2 < 0$, it is the the Higgs field. Due to the potential bound condition, the self coupling coefficient $\lambda$ must be greater than zero. So, the potential $V(\phi)$ is symmetrical of its internal space. But the minimum $V(\phi)$ is not any more at $\phi(x)$=0(see figure 1.2).

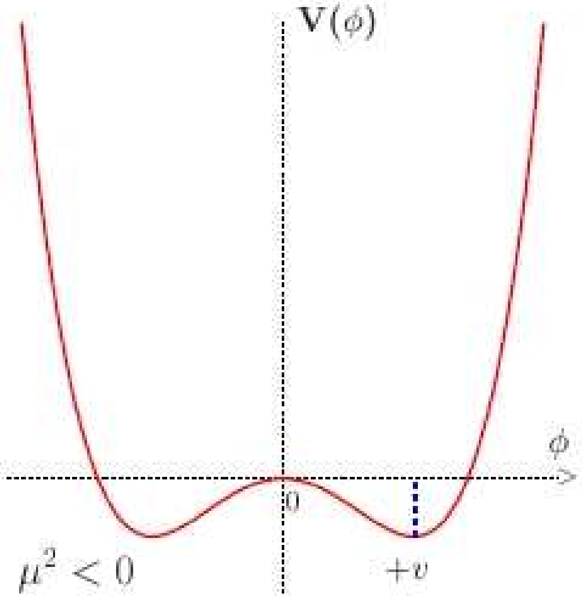

Figure 1.2: The potential V of the Higgs field $\phi$

The vacuum expectation value (vev) of $\phi^2$ is defined as $< 0|\phi^2|0 > \equiv \phi_0^2 = -\frac{\mu^2}{\lambda} \equiv v^2$. In order to interpret correctly the theory, we expand the Lagrangian around one of the minimal $v$ by a translation transformation of $\phi(x)$:

$$\phi(x) = \phi'(x) + v \quad , \tag{1.6}$$

Then, the Lagrangian of Higgs field becomes:

$$\mathcal{L}_{\phi'} = \frac{1}{2}\partial\mu\phi'\partial^{\mu}\phi' + \mu^2\phi'^2 - \lambda v\phi'^3 - \frac{1}{4}\phi'^4 \quad , \tag{1.7}$$

This is a scalar field with a real mass of $\sqrt{-2\mu^2}$ instead of virtual mass $i\sqrt{-\mu^2}$ before transformation. And it has cubic and fourth order self coupling terms. So, this Lagrangian is not invariant under the reflection transformation of its internal space. Goldstone theorem indicates that: for each generator of the symmetry that is broken, there is one massless(light if the symmetry was not exact) scalar particle - called a Goldstone boson. For $O(N)$ rotation group, there are $\frac{1}{2}n(n-1)$ generators, of which $\frac{1}{2}(n-1)(n-2)$ generators are vacuum invariant transformations, and $(n-1)$ generators of the symmetry that is broken. So, there exist $(n-1)$ massless Goldstone particles. In gauge theory, the Goldstone bosons are "eaten" by the gauge bosons. The latter become massive and their new, longitudinal polarization is provided by the Goldstone boson.

#### 1.1.2.2 Higgs mechanism

In Electro-Weak theory, the Lagrangian of free boson can be written as:

$$\mathcal{L}_{boson} = -\frac{1}{4}W^{\alpha}_{\mu\nu}W^{\mu\nu}_{\alpha} - \frac{1}{4}B_{\mu\nu}B^{\mu\nu} \quad , \tag{1.8}$$

of which:

$$W^{\alpha}_{\mu,\nu} = \partial_\mu W^{\alpha}_{\nu} - \partial_\nu W^{\alpha}_{\mu} + gf^{\alpha\beta\gamma}W^{\beta}_{\mu}W^{\gamma}_{\nu} \quad , \tag{1.9}$$

$$B_{\mu,\nu} = \partial_\mu B_\nu - \partial_\nu B_\mu \quad , \tag{1.10}$$

$W^{\alpha}_{\mu,\nu}$,$\alpha = 1, 2, 3$ are the field strength of $SU(2)_L$ vector bosons. $B_{\mu,\nu}$ is the field strength of $U(1)_Y$ vector boson. Together with the Lagrangian of Higgs scalar:

$$\mathcal{L}_S = (D^\mu\phi)^\dagger(D_\mu\phi) - \mu^2\phi^\dagger\phi - \lambda(\phi^\dagger\phi)^2 \quad , \tag{1.11}$$

of which

$$D_\mu = \partial_\mu - ig_2\frac{\tau_\alpha}{2}W^{\alpha}_{\mu} - ig_1\frac{1}{2}B_\mu \quad , \tag{1.12}$$

It already includes the interaction term between Higgs field and $SU(2)_L$,$U(1)_Y$ vector field. Expand Higgs field according to its four compartments, after the vev calculation and local gauge transformation, we define:

$$W^{\pm} = \frac{1}{\sqrt{2}}(W^1 \mp iW^2) \tag{1.13}$$

$$Z_\mu = \frac{g_2W^3_\mu - g_1B_\mu}{\sqrt{g_1^2 + g_2^2}} \tag{1.14}$$

$$A_\mu = \frac{g_2W^3_\mu + g_1B_\mu}{\sqrt{g_1^2 + g_2^2}} \tag{1.15}$$

After these calculation of $\mathcal{L}_{boson} + \mathcal{L}_S$, and from the square terms of $W^{\pm}, Z, A$ fields, one can obtain the mass term for each particle as:

$$M^{\pm}_{W} = \frac{1}{2}vg_2, \quad M_Z = \frac{1}{2}v\sqrt{g_1^2 + g_2^2}, \quad M_A = 0 \quad , \tag{1.16}$$

Now, in $SU(2)_L + U(1)_Y \rightarrow U(1)_Q$ spontaneous symmetry breaking gauge theory, the Goldstone bosons are "eaten" by the gauge bosons $W^{\pm}$ and $Z$. The gauge bosons longitudinal polarization is provided by the Goldstone bosons, corresponding to the broken generators, which gives the gauge bosons masses and the associated necessary third polarization degree of freedom. Since $U(1)_Q$ does not break its symmetry, photon remains massless and has only transverse components.

### 1.1.3 Yukawa Coupling of top quark and Higgs

Under the framework of Standard Model, fermions obtain masses from Yukawa Coupling with Higgs. The Lagrangian of fermions can be written as:

$$L_{Fermion} = -\sum_{F,\sigma} \frac{g_{F,\sigma}}{\sqrt{2}} \left( \overline{\psi^L_F}\phi\psi^R_{F,\sigma} + \overline{\psi^R_{F,\sigma}}\bar{\phi}\psi^L_f \right) \tag{1.17}$$

of which $g$ is the Yukawa Coupling constant. L and R denote left hand and right hand Dirac wave function respectively. $F$ denotes the generations of fermions and $\sigma$ denotes the spin. After similar transformations and simplifications as section 1.1.2.2, one gets:

$$L_{Yukawa} = -(1 + \frac{h}{v}) \sum_{F} \left( m_F \overline{\psi_F}\psi_F \right) \tag{1.18}$$

So, the mass term of fermions are:

$$m_F = \frac{v g_F}{\sqrt{2}} \tag{1.19}$$

of which, $g_F$ is the corresponding fermion to Higgs Yukawa Coupling constant. $v$ is the Higgs field vacuum expectation value, which is about 246 GeV. Equation 1.19 shows that $g_F$ is independent of Higgs mass, and proportional to the mass of its corresponding fermion. In Standard Model. The heaviest quark is top, with a mass about 172 GeV. Which means that top Yukawa Coupling constant is the largest one, about one, and therefor will be most probably the first Yukawa Coupling constant that could be measured experimentally.

### 1.1.4 Quantum Chromo Dynamics(QCD)

Quantum Chromo Dynamics is a non-abelian gauge field theory of the strong interaction compartment of $SU(3) \times SU(2) \times U(1)$ Standard Model. It describes the dynamics of colored quarks and gluons. A quark of special flavor has three different color states, while gluons have 8 possible color states. Hadrons are colorless combination of quarks, anti-quarks and gluons. The dynamics of the quarks and gluons are controlled by the quantum chromo dynamics Lagrangian. The gauge invariant QCD Lagrangian can be written up to the gauge fixing terms as:

$$\mathcal{L}_{QCD} = -\frac{1}{4} F^{(a)}_{\mu\nu} F_{(a)\mu\nu} + i \sum_q \bar{\psi}^i_q \gamma^\mu (D_\mu)_{ij} \psi^j_q - \sum_q m_q \bar{\psi}^i_q \psi_{qi} \quad , \tag{1.20}$$

$$F^{(a)}_{\mu\nu} = \partial_\mu A^a_\nu - \partial_\nu A^a_\mu - g_s f_{abc} A^b_\mu A^c_\nu \quad , \tag{1.21}$$

$$(D_\mu)_{ij} = \delta_{ij}\partial_\mu + i g_s \sum_a \frac{\lambda^a_{i,j}}{2} A^a_\mu \quad , \tag{1.22}$$

where $g_s$ is the QCD coupling constant, $f_{abc}$ are the structure constants of SU(3), The $\psi_q^i(x)$ are the 4-component Dirac spinors of each quarks of color i and flavor q. And $A_\mu^a(x)$ are the Yang-Mills gluon fields. QCD has two peculiar properties:

- **Asymptotic freedom:** which means that in very high-energy reactions, quarks and gluons interact very weakly. This prediction of QCD was first discovered in the early 1970s by David Politzer and by Frank Wilczek and David Gross. For this work they were awarded the 2004 Nobel Prize in Physics.
- **Confinement:** which means that the force between quarks does not diminish as they are separated. Because of this, it would take an infinite amount of energy to separate two quarks; they are forever bound into hadrons such as the proton and the neutron. Although analytically unproven, confinement is widely believed to be true because it explains the consistent failure of free quark searches, and it is easy to demonstrate in lattice QCD.

There are several methods in QCD calculations, one of them is Perturbative QCD, which is based on the Asymptotic freedom and could be accurate at very high energies. This can be tested with a certain accuracy at TeV energy scale.

### 1.1.5 Challenge of the Standard Model

The Standard Model is based on quark model and gauge theory. It successes in describing strong interactions, weak interactions and electromagnetism, which provides an internally consistent theory describing interactions between all experimentally observed particles, only the predicted Higgs particle has not yet been found experimentally. SM is one of the greatest achievements of physics in 20th century, and proved to be correct in the recent 30 years of precision experimental tests:

- In 1973, neutral current was predicted and confirmed shortly thereafter, in a neutrino experiment in the Gargamelle bubble chamber at CERN.
- In 1974, the fourth quark -Charm quark- was discovered by Ting and Richter. Which was highlighted by the rapid changes in high-energy physics at that time.
- In 1975, tau lepton was discovered by Perl, which extend leptons to be three generations.
- In 1979, three-jet events were observed at the electron-positron collider at DESY by X.L. Wu and Ting. Which gives the evidence of gluons.
- In 1983, $W^\pm$ and $Z^0$ were discovered by Rubbia at SPS, which are the intermediate bosons that carrying weak forces.
- In 1995, Top quark was discovered at Fermi lab. It is the heaviest quark ever found.

- During 1990 to 2000, LEP experiments performed precision tests on Standard Model, including the running $\alpha_s$ coupling constant, which proves the asymptotic freedom predicted by the Standard Model.

Although the Standard Model gives answers to many questions raised in particle physics, and predicts many particles confirmed by experiment. It is still not a complete theory of fundamental interactions and still raised unanswered questions.

- The Standard Model can not be a complete theory, primarily because of its lack of inclusion of the gravity, the fourth known fundamental interaction, but also because of the eighteen numerical parameters (such as masses and coupling constants) that must be put "by experimental measurement" into the theory rather than being derived from first principles. Of these 18 parameters, a small fraction of them comes from gauge theory, relevant to the symmetry of physics. It needs deeper understanding of these possible symmetries. Other free parameters come from the Higgs field and breaking of symmetry, also need more studies. Higgs particles has not yet been found experimentally, Higgs searching is one of the direct tests of Standard Model.
- Similar as the periodic table of the chemical elements, leptons and quarks have some properties in common. They may have more fundamental bases and structures. High energy physics are approaching a finer structure of mater: the structure of quarks and leptons. Also, the possible structure of force carriers are important research area.
- How to understand the properties of leptons, quarks, force carriers of photon, intermediate bosons, gluons, graviton, Higgs and the interactions between them, How to develop a fundamental theory, which can unifies the experimental results and take the Standard Model as proximation. These questions still need a long way to be answered.
- Three generations of leptons and quarks have different properties, but they also have same quantum numbers such as hyper charge and isospin. How to understand the "generations", why there are 2 generations of unstable particles. Is there new generations other than these three? All these need further experimental evidence and studies.
- the asymmetry of mater and anti-mater in universe. Scientists predicts that about 14 billion years ago, when universe was born, the mater and anti-mater were generated equally. But now, the observed universe are mostly composed of mater, the missing anti-mater need more studies.

There are great efforts of both theoretical and experimental researches exploring whether the Standard Model could be extended into a complete theory of everything, at grand energy range. This area of research is often described by the term "Beyond the Standard Model". Maybe one day, there will be a "super standard model" that could solve all these problems of Standard Model, from first principles.

## 1.2 Physics at TeV proton-proton collision

The Large Hadron Collider (LHC) is a particle accelerator located at CERN. It is a proton proton collider at the designed center of mass energy of 14 TeV. The designed luminosity is $10^{34}cm^{-2}s^{-1}$. The total reaction cross section at LHC is about $100mb$, and the inelastic reaction is about $10^9$ per second [4]. Under such extreme hard environment, the Higgs signal that we are most interested in only has about $10^{-10}$ of the total production cross section. At this new experimental energy scale, there are many interesting physics that can be studied.

### 1.2.1 $QCD$ processes

$QCD$ processes have the largest production cross section at LHC. There are two main goals of $QCD$ processes studies. One is precision measurement and tests of $QCD$ predictions. Additional constraints to be established by these tests. Such as parton density function in the proton, or the running strong coupling constant $\alpha_s$ tested at various energy scales. The other main goal is that since $QCD$ processes represent a major part of the backgrounds to all other Standard Model processes or new physics, they need to be known precisely to verify the deviations from $QCD$ expectations.

### 1.2.2 Physics of electroweak gauge bosons

There will be abundant gauge bosons and gauge-boson pairs produced at LHC. Thanks to the high statistics and center of mass energy, we can perform several precision measurements at LHC, which will significantly improve the precision achieved at present machines. Such as the $W^{\pm}$ bosons masses, and the measurement of Triple Gauge Couplings (TGCs). Meanwhile, the measurement of these gauge boson production will be important to understand the underlying physics and the background prediction in new physics analysis. In addition, these gauge bosons processes also be used to calibrate detector, such as using $Z \rightarrow ee$ for the in situ calibration of the detector mass scale.

### 1.2.3 B physics

Under the energy scale of LHC, B quark pairs have a production cross section about 1% of the total reaction. B physics are focused on Standard Model precision testing by measuring B-hadron decays, CKM matrix elements measurement(CP violation in B-meson decays) and giving indirect evidence for new physics. There are many studies that can be made of B-hadron production, such as b-jet differential cross-sections, differential cross-sections of single particles in b-jets, production asymmetries, production polarisation, b-b correlations, bbg final states, doubly-heavy-flavoured hadrons, double b-quark-pair production, and prompt $J/Psi$ production.

### 1.2.4 Heavy quarks and leptons

The production cross section of top at LHC is about 833 $pb$ [5]. Study of the top quark may provide an excellent probe of the sector of electroweak symmetry breaking (EWSB), and new physics hunting in either its production or decay. A large variety of top physics studies will be possible once large statistics of top samples is accumulated: top mass precision measurement, which will provide constraint on Higgs mass; top-antitop resonance; $t\bar{t}$ spin correlations; the $W \rightarrow jj$ decay in top quark events provides an important in situ calibration source for calorimetry at the LHC, and the b quark in top pair events provides a possible b-jets ID and calibration source. Since top quark events will be the dominant background in many searches for new physics at the TeV scale, precision understanding its production rates and properties will be essential in new physics searching.

Searches for fourth generation of heavy quarks and leptons are also important at LHC. The fourth generation of up and down quarks may appear in bound states produced and decay similarly to top quarks.

### 1.2.5 Higgs Physics

One of the primary goals of LHC is Higgs particle hunting. And its properties measurement once the Higgs was found. At LHC proton-proton collision, There are four production mechanisms of Higgs:

- Associate production with W/Z: $q\bar{q} \rightarrow V + H$
- Vector boson fusion: $qq \rightarrow V^*V^* \rightarrow qq + H$
- Gluon-gluon fusion: $gg \rightarrow H$
- Associated production with heavy quarks: $gg, q\bar{q} \rightarrow Q\bar{Q} + H$

Figure 1.2.5 shows the Feymann diagrams of the four Higgs production mechanisms.

The theoretical decay models of Higgs are $H \rightarrow \gamma\gamma, H \rightarrow b\bar{b}, H \rightarrow WW, H \rightarrow 4leptons, H \rightarrow t\bar{t}$. These channels could be discovery channels at different Higgs mass range. From 100 GeV to 1 TeV, at early integral luminosity. Once Higgs is found, LHC will perform Higgs properties measurements, such as the mass, width, Yukawa Couplings. $t\bar{t}H, H \rightarrow WW^{(*)}$ is one of the possible best channels that can measure top quark Yukawa Coupling during the intermediate Higgs mass range between 120 and 200 GeV.

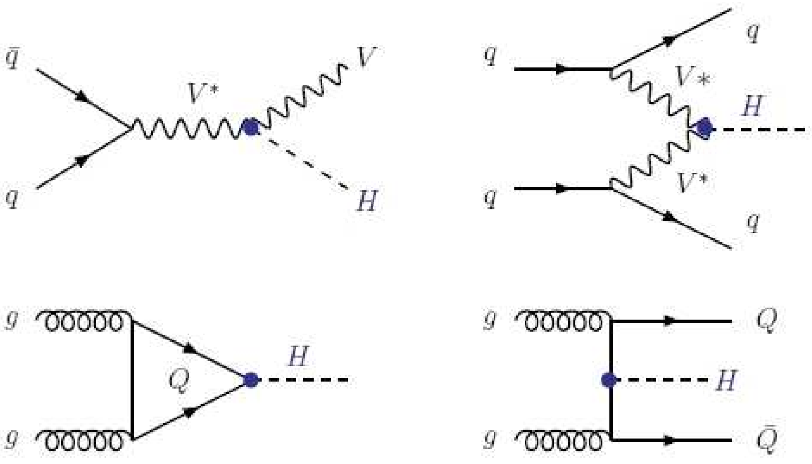

Figure 1.3: Higgs production Feyman diagrams at hadron collider

### 1.2.6 SUSY and Physics beyond Standard Model

Supersymmetry(SUSY) is one of the best extensions of the Standard Model, and SUSY particles hunting is one of the primary physics goals of LHC. SUSY is a theory that introduce the symmetry between bosons and fermions, it predicts that for every particle, there is a particle of same properties except the spin is 1/2 different, which is called its super partner(Nevertheless, SUSY cannot be an exact symmetry since there are no fundamental scalar particles having the same mass as the known fermions). That means for each bosons, there exist a corresponding fermion, and vice-versa. SUSY solves several puzzles compared to Standard Model, such as the calculation of radiative corrections to the SM Higgs boson mass encounters divergences, which are quadratic in the cut-off scale $\Lambda$ at which the theory stops to be valid and New Physics should appear. It is the so-called hierarchy problem. The Minimal Supersymmetric Standard Model(MSSM) predicts two doublets of Higgs fields, which leads to five Higgs particles. Two CP-even h,H bosons, a pseudoscalar A boson and two charged $H^{\pm}$ bosons. Of which the lightest Higgs mass is less than $M_Z$ [6].

Other theories predictions beyond standard model, such as Technicolor theory, can be discovered at LHC. It predicts that the high mass of top quark, partly due to kinematics reason, which could be checked by direct measurement of the Yukawa Coupling between top quark and Higgs in channel $t\bar{t}H, H \to WW^{(*)}$ [7].

## 1.3 Motivations of thesis

### 1.3.1 Research background

Standard Model has been tested and proved to be correct in the recent decades. While the most important particle -Higgs- that predicted in SM has not yet been found experimentally. Higgs searching and Higgs properties measurements are the physics goals of recent experiments. LEP experiments performed the precision tests of SM electroweak parameters(Figure 1.4), and gave the constrains on Higgs mass(Figure 1.5 shows the constraints on Higgs mass of effective weak mixing angle $\sin^2\theta_{eff}^{lep}$ and $M_W$). All these constraints come to a upper limit of Higgs mass less than 207 GeV. Meanwhile, the direct searching at LEP gives the Higgs mass lower limit is 114.4 GeV [8]. Further more, due to triviality bound and the vacuum stability bound, Higgs mass constraints dependent on the new physics energy scale $\Lambda_c$. If $\Lambda_c \sim$TeV, then, Higgs mass should be in the range of $50GeV \leq M_H \leq 800GeV$. If $\Lambda_c \sim \Lambda_{GUT}$, Higgs mass is constrained to $130GeV \leq M_H \leq 180GeV$(figure 1.7). So, a Higgs of intermediate mass is favored.

No Higgs signal has been found in all the experiments until now. The primary goal of LHC is Higgs searching and precision tests of electro-weak theory. It allows Higgs searching from the energy range of ~100 GeV to 1 TeV(Figure 1.8). LHC will take data in summer of 2008. Once Higgs is discovered at LHC, the properties measurement will became an important goal of experiment. As one of the fundamental properties of Higgs, Yukawa Coupling can give the information of fermions mass origin. In the framework of Standard Model, from equation 1.19, one can get that $g_t \approx 1$, It is the biggest one of fermion Higgs Yukawa Coupling constants. And it is likely to be the first Yukawa Coupling that could be measured experimentally. Further more, $g_t$ is an important parameters that can distinguish SM Higgs and Multi-Higgs bosons of other model. The TechniColor theory predicts that high top quark mass is partly due to dynamics. Direct measurement of Higgs to Top quark Yukawa Coupling will give important information to distinguish this.

### 1.3.2 Historical status of the study

As early as 2000, in a Higgs Working Group Summary Report, D. Zeppenfeld et al studied the feasibilities of measuring Higgs Yukawa Couplings at LHC. They proposed the method of combining the results of different Higgs decay channels to measure Higgs to top quark Yukawa Coupling [10, 11, 12, 13, 14]. After that, studies of parton level and fast simulation were performed, focusing on the feasibility of measuring $g_t$ through the channel of $t\bar{t}H$ [15, 16]. In the work of J. Leveque et al in 2002, based on ATLAS detector fast simulation(Atlfast), $t\bar{t}H, H \rightarrow WW$ channel is studied in the Higgs mass between 120 and 200 GeV, and an accuracy of $g_t$ that can reach a maximum of 13% for $m_H = 160GeV$. However, the fast simulation base on random sampling quantifies is a very crude simulation of the ATLAS detector that can not be used for refined analysis. It did not include trigger and pileup effects, and isolation effects are not accurately accounted which results in the underestimation of $t\bar{t}$ background. Moreover, all these studies did not include systematics.

The ATLAS full simulation software has recently provide with an accurate description of the real detector behavior. A study of $g_t$ measurement based on full simulation was needed before data taking in 2008 with $t\bar{t}H, H \rightarrow WW$ channel. This thesis work based on Computing System Commissioning(CSC) full simulation Monte Calor data, fulfill this need. It includes full trigger, pileup and systematics uncertainties studies. However, these studies especially the systematics are relevant to the performance of real detector. The study presented in chapter 5 of 2004 ATLAS detector Combined Test Beam data pro-

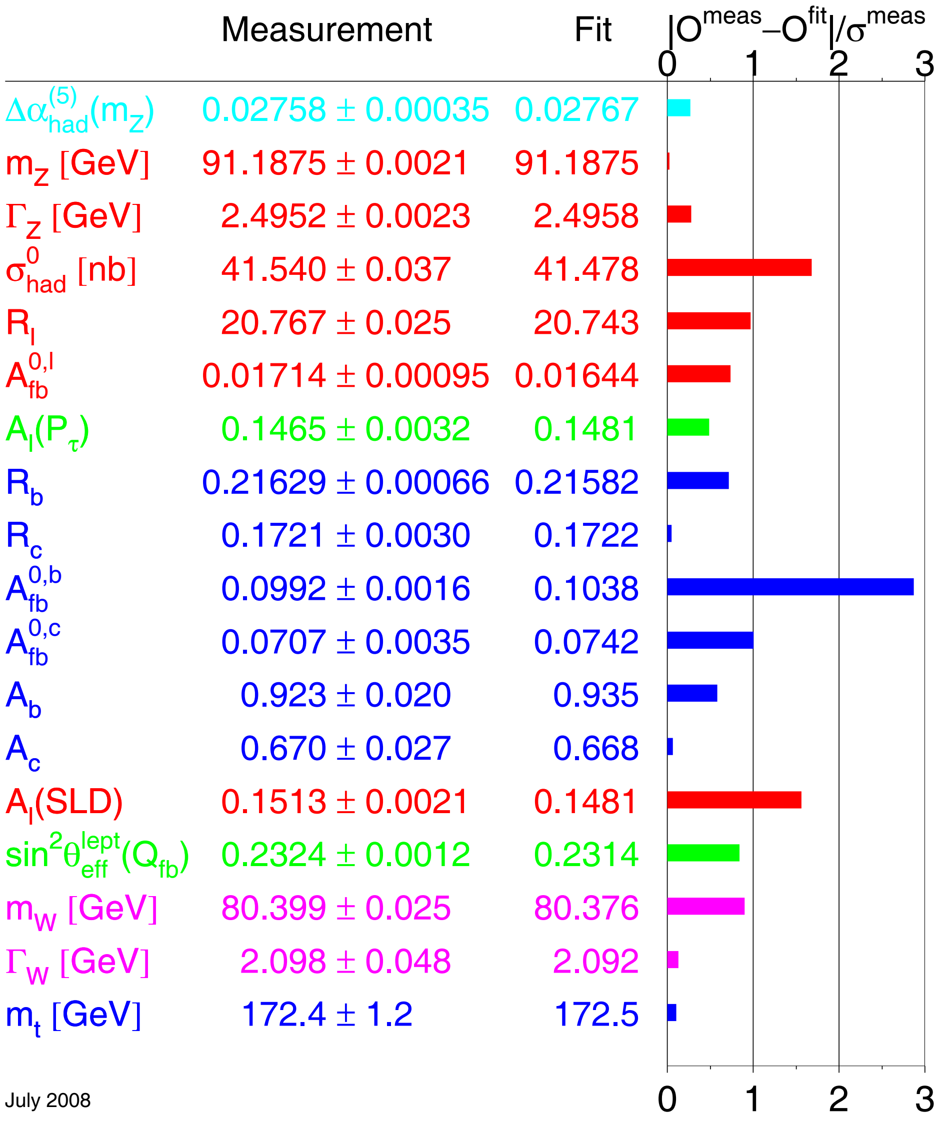

| | Measurement | Fit |
|---|---|---|
| $\Delta\alpha_{had}^{(5)}(m_Z)$ | 0.02758 ± 0.00035 | 0.02767 |
| $m_Z$ [GeV] | 91.1875 ± 0.0021 | 91.1875 |
| $\Gamma_Z$ [GeV] | 2.4952 ± 0.0023 | 2.4958 |
| $\sigma_{had}^0$ [nb] | 41.540 ± 0.037 | 41.478 |
| $R_l$ | 20.767 ± 0.025 | 20.743 |
| $A_{fb}^{0,l}$ | 0.01714 ± 0.00095 | 0.01644 |
| $A_l(P_\tau)$ | 0.1465 ± 0.0032 | 0.1481 |
| $R_b$ | 0.21629 ± 0.00066 | 0.21582 |
| $R_c$ | 0.1721 ± 0.0030 | 0.1722 |
| $A_{fb}^{0,b}$ | 0.0992 ± 0.0016 | 0.1038 |
| $A_{fb}^{0,c}$ | 0.0707 ± 0.0035 | 0.0742 |
| $A_b$ | 0.923 ± 0.020 | 0.935 |
| $A_c$ | 0.670 ± 0.027 | 0.668 |
| $A_l$(SLD) | 0.1513 ± 0.0021 | 0.1481 |
| $\sin^2\theta_{eff}^{lept}(Q_{fb})$ | 0.2324 ± 0.0012 | 0.2314 |
| $m_W$ [GeV] | 80.399 ± 0.025 | 80.376 |
| $\Gamma_W$ [GeV] | 2.098 ± 0.048 | 2.092 |
| $m_t$ [GeV] | 172.4 ± 1.2 | 172.5 |

FIGURE 1.4: Summary of electroweak precision measurements at LEP1, LEP2, SLC and the Tevatron; The SM fit results, which have been derived including all radiative corrections, and the standard deviations are also shown [9]

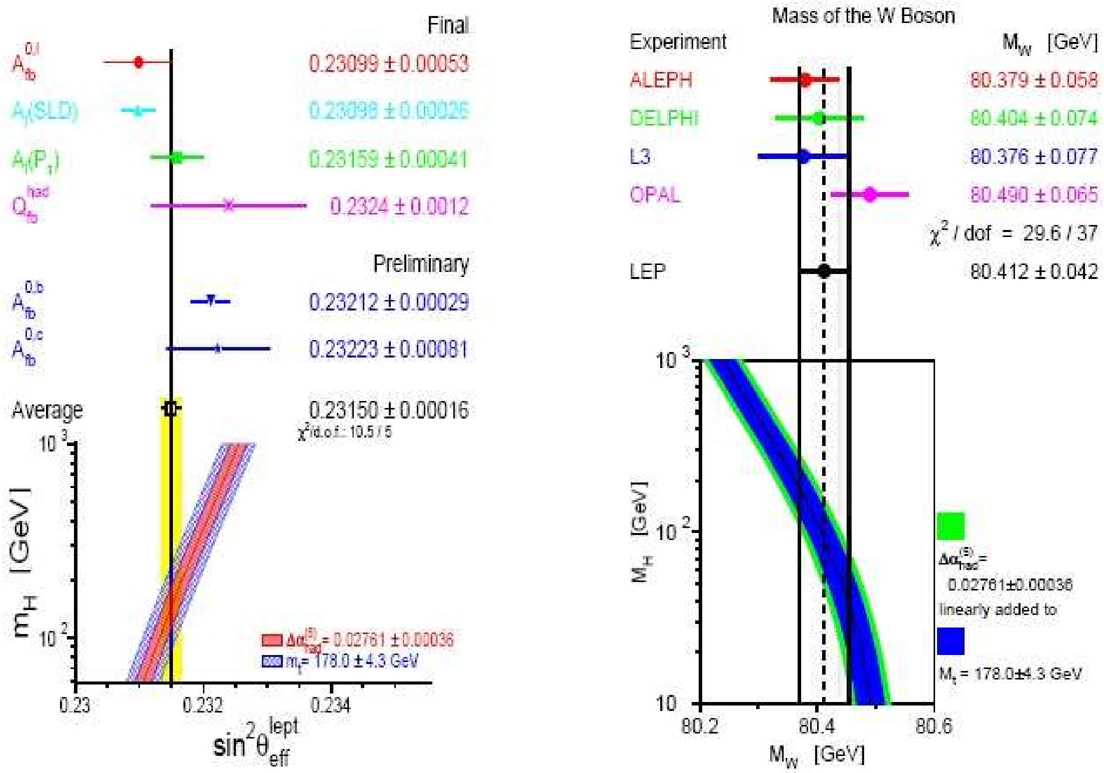

FIGURE 1.5: The measurement [vertical band] and the theoretical prediction [the hatched bands] for $\sin^2\theta_{eff}^{lep}$ and $M_W$ as a function of the Higgs boson mass [9]

vides a unique window to understand the real detector performance with a real detector configuration.

### 1.3.3 Motivation of the study

Once Higgs is found, the properties measurements of Higgs will become important. $g_t$ is one of Higgs most important properties, which can tell whether it is a SM like Higgs or not. $t\bar{t}H$ is the best physics channel of $g_t$ measurement. According to SM. At the intermediate Higgs mass range of 120 and 200 GeV, Higgs mainly decays to $WW, ZZ, \tau\tau, \gamma\gamma, b\bar{b}$. And the branching ratio of Higgs decays is dominated by $H \to WW$ [17]. So, $ttH, H \to WW$ is the most promising channel for $g_t$ measurement. In the Higgs mass range of 130 to 200 GeV, $ttH, H \to WW$ will gives an accuracy of ~25% for $g_t$ measurement(see Chapter 3). For Higgs mass less than 130 GeV, $ttH, H \to WW$ combined with $ttH, H \to b\bar{b}$ studies, give an accurate $g_t$ measurement. Furthermore, $ttH, H \to WW$ results can be combined with other channels like $H \to \gamma\gamma$. It can give the ratios of different Higgs decay model partial width, which are important input for Higgs properties study and new physics searching.

Systematics uncertainties are the dominant error in $g_t$ measurement at $t\bar{t}H, H \to WW$. These systematics uncertainties concerning to calorimeter, such as jet energy scale,

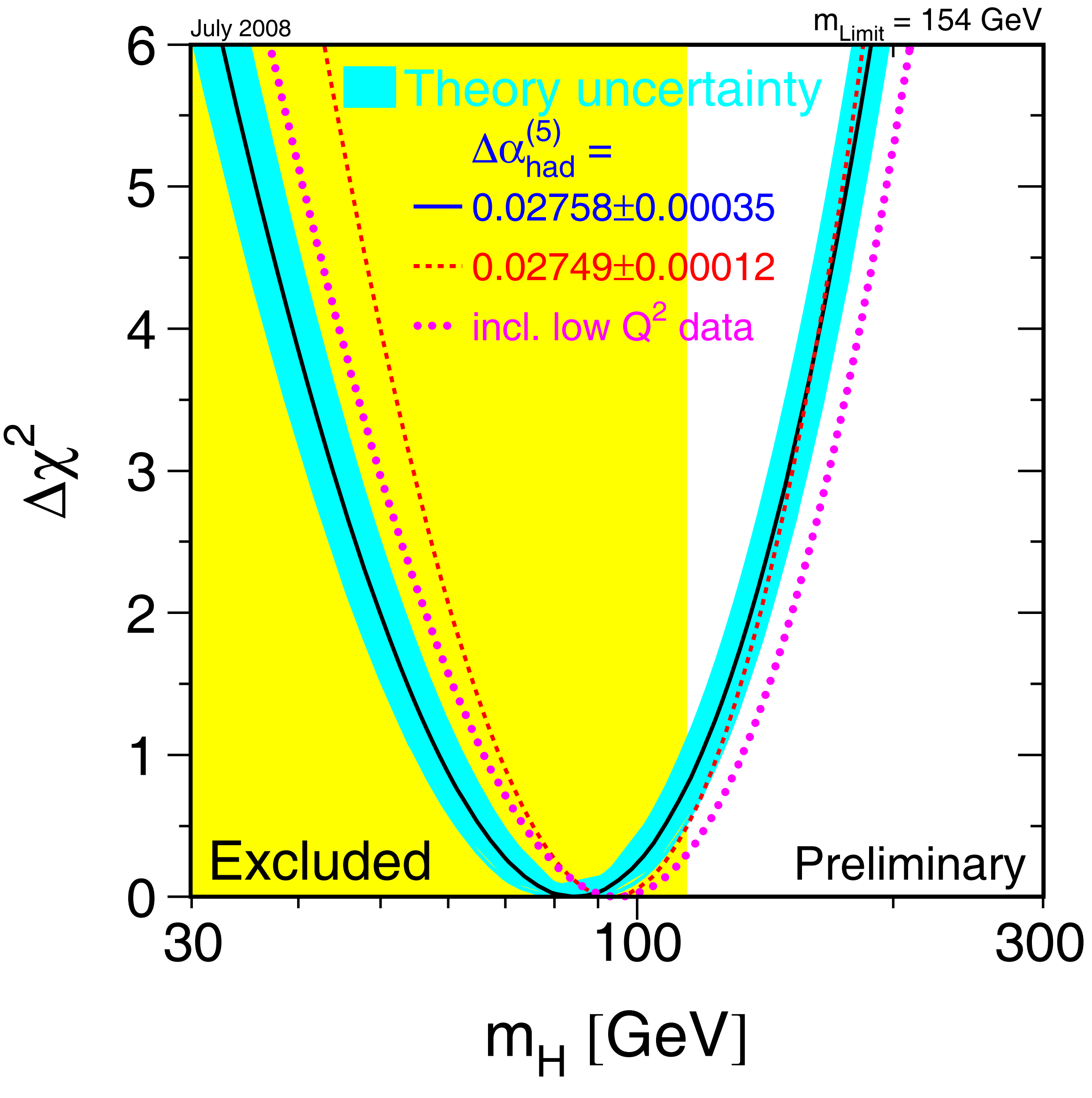

FIGURE 1.6: The $\Delta\chi^2$ of the fit to the electroweak precision data as a function of $M_H$. The solid line results when all data are included and the blue/shaded band is the estimated theoretical error from unknown higher order corrections. The effect of including the low $Q^2$ data and the use of a different value for $\Delta\alpha_{had}$ are also shown [9]

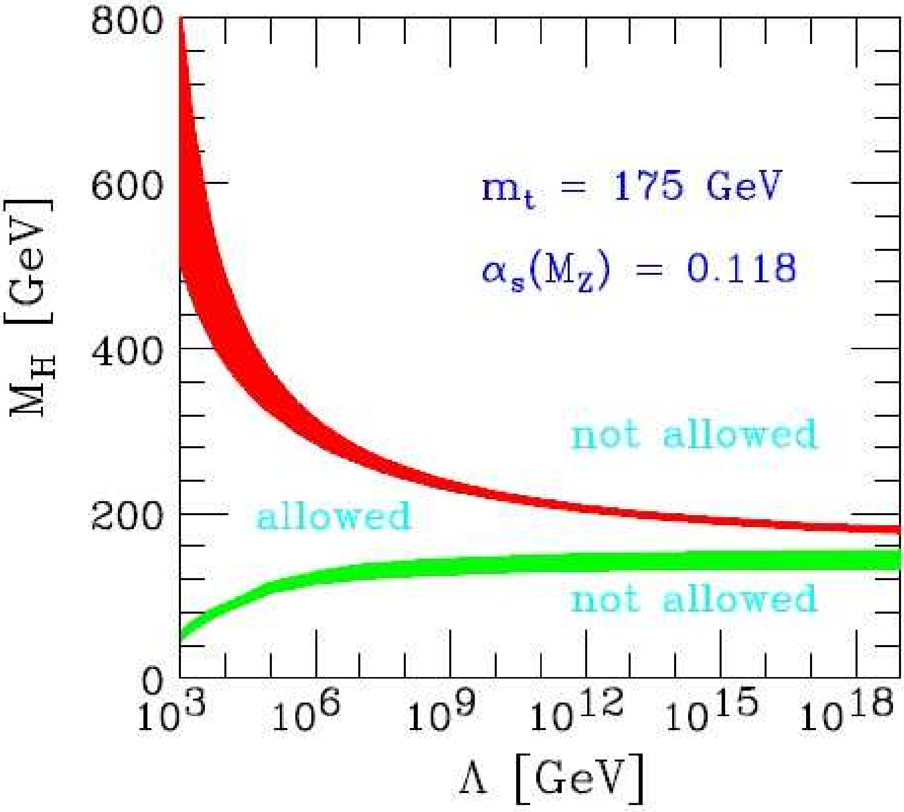

FIGURE 1.7: The triviality (upper) bound and the vacuum stability (lower) bound on the Higgs boson mass as a function of the New Physics or cut off scale $\Lambda_c$ for a top quark mass $m_t$ = 175±6 GeV and $\alpha_s(M_Z)$ = 0.118±0.002; the allowed region lies between the bands and the colored/shaded bands illustrate the impact of various uncertainties [3]

electron identification efficiency, are important systematics uncertainties sources. The knowledge about the performance of calorimeter, especially the electromagnetic calorimeter, are essential in this analysis. In the second half of this thesis, analysis of Combined test beam very low energy electron is presented, to understand the energy reconstruction and linearity of electron.

This thesis is the first study using ATLAS full simulation MC data, of the $t\bar{t}H, H \rightarrow WW^{(*)}$ with two leptons and three leptons final states. A special Cone isolation is proposed and developed to suppress background. This analysis on $t\bar{t}H, H \rightarrow WW^{(*)}$ also includes a detailed studies on systematics uncertainties.

Toward a better understanding of the detector performance and to compare them to full simulation, 2004 ATLAS detector Combined Test Beam data have been analyzed. The chapter 5 present the full analysis of the linearity of VLE electrons using Beam Chamber information and the default calculation. Then, a $5 \times 5$ multiple seeding clustering method is studied, and given the calibration constants obtained to simulated data. It show that this calibration method may improve the energy linearity in the reconstruction of electrons.

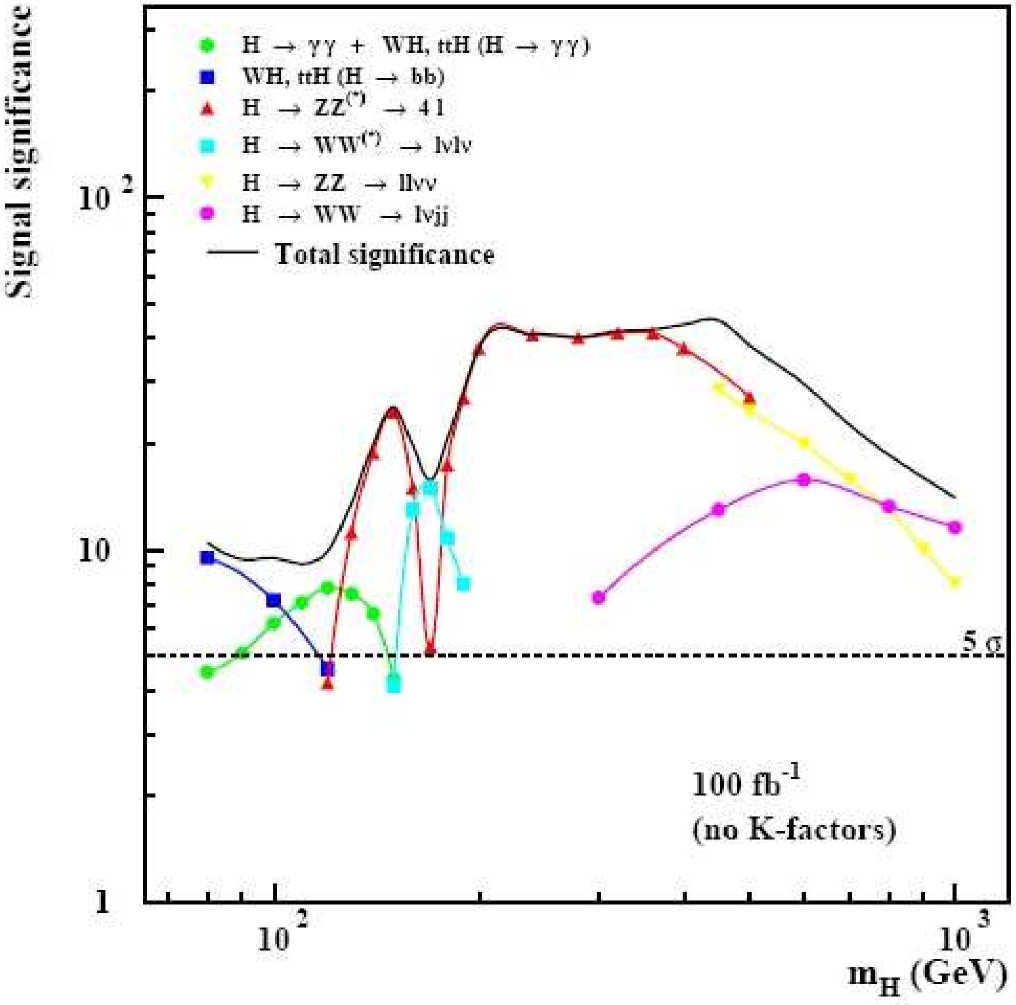

FIGURE 1.8: ATLAS discovery potential for a Higgs mass range in [100, 1000]GeV [7]

### 1.3.4 Structure of this thesis

This thesis include the work of my doctoral studies of 2005 to 2008. The contents of each chapter is:

- Chapter one: Introduction of the Higgs searching and $g_t$ measurements in particle physics. Including theoretical motivations and historical status.
- Chapter two: Introduction of Large Hadron Collider and ATLAS detector equipments.
- Chapter three: The studies of $ttH, H \to WW$.
- Chapter four: Introduction of ATLAS Combined Test Beam.

- Chapter five: Very Low Energy(VLE) electron linearity studies by using beam chamber at single electron level and one possible improvement of the calibration procedure.
- Chapter six: Summary and prospects.

# Chapter 2

# Introduction of LHC and ATLAS

## Contents

## 2.1 The Large Hardron Collider(LHC)

The Large Hadron Collider(LHC) is an accelerator located at CERN, at the boundaries of France and Switzerland, 20 kilometers from the center of Geneva. The concept of this machine was started in the meddle of the 80s. Before LEP start taking data, scientists already thought of a machine at a high center of mass energy and luminosity that no machine had ever explored, to uncover the structure of mater to a deeper understanding. This project was approved by CERN Council in December 1994 and started its construction from then. Now, this miracle has almost become true and will start running this summer.

The LHC is a proton-proton collider. Its center of mass energy is 14 TeV, hosted in circle tunnel of about 27 km, 100 meters underground(Figure 2.1). In order to keep the 7 TeV proton beam in track, there are about 1232 superconducting dipole magnets in the tunnel. Each of them is 14.2 meters long, and the magnetic field at its maximum is 8.4 tesla [4].

The luminosity of collider can be calculated from:

$$\mathcal{L} = \frac{1}{4\pi} \frac{N_1 \cdot N_2 \cdot f}{\sigma_x \cdot \sigma_y \cdot t} \tag{2.1}$$

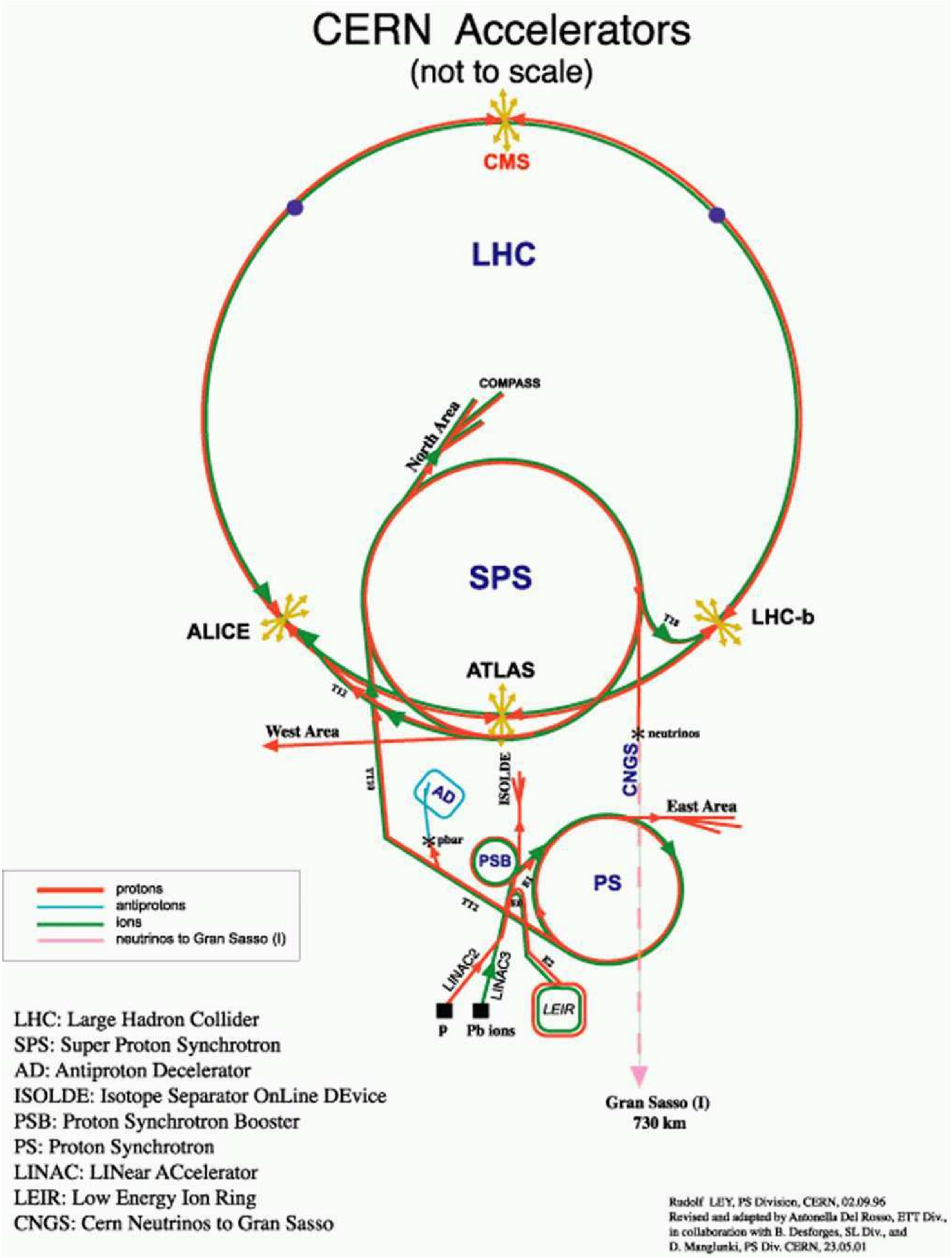

LHC: Large Hadron Collider
SPS: Super Proton Synchrotron
AD: Antiproton Decelerator
ISOLDE: Isotope Separator OnLine DEvice
PSB: Proton Synchrotron Booster
PS: Proton Synchrotron
LINAC: LINear ACcelerator
LEIR: Low Energy Ion Ring
CNGS: Cern Neutrinos to Gran Sasso

Rudolf LEY, PS Division, CERN, 02.09.96
Revised and adapted by Antonella Del Rosso, ETT Div.,
in collaboration with B. Desforges, SL Div., and
D. Manglunki, PS Div. CERN, 23.05.01

FIGURE 2.1: over view of the CERN accelerator facilities [18]

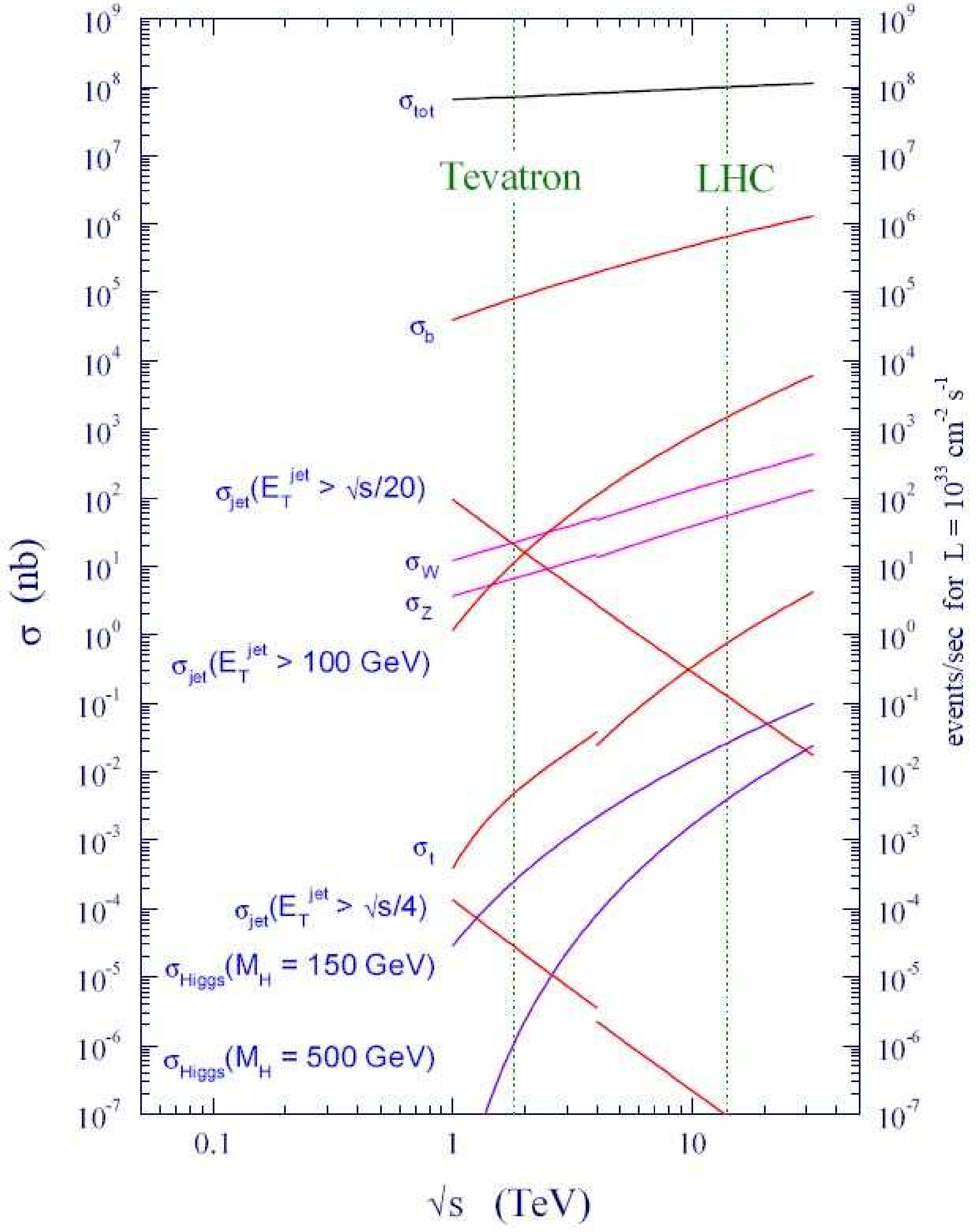

FIGURE 2.2: Channels cross section as a function of center mass [19]

Where $N_1, N_2$ are the protons numbers in the two crossing bunches. $\sigma_x, \sigma_y$ are the transverse sizes of the bunches, $f$ is the fraction of effective bunches, $t$ is the time between two neighboring collisions. The design luminosity of LHC is $10^{34}\ cm^{-2}s^{-1}$. There are abundant physics at the energy scale of LHC. Each cross of two bunches will have an average of 23 inelastic interactions of proton to proton. All these reactions in one bunch crossing is defined as one event. Figure 2.2 shows the production cross section of possible physics channels as a function of the center of mass energy at proton-proton collision. Under the center of mass energy of LHC, the total production cross section is about 100mb. Table 2.1 lists the main design parameters of LHC.

| **LHC parameters** | **value** | **LHC parameters** | **value** |
|---|---|---|---|
| Center mass energy | 14 TeV | Dipole field | 8.4 T |
| Luminosity | $10^{34}cm^{-2}s^{-1}$ | Beam-Beam parameter | 0.0034 |
| Injection energy | 450 GeV | circulating current | 0.53 A |
| number of bunchs | 2835 | Particles per bunch | $1.0510^{11}$ |
| stored energy | 334MJ | bunch space | 25ns |
| Beam Lifetime | 22h | Luminorsity Lifetime | 10h |

Table 2.1: part of LHC important design parameters

The main physics goals of LHC are Higgs searching and precision tests of electroweak theory. There are four detectors at LHC: ATLAS, CMS, ALICE and LHC-b, of which ATLAS and CMS are general purpose detectors. ALICE is a special purpose detector for heavy ion collision physics. LHC-b is a B physics dedicated detector.

## 2.2 The ATLAS detector

### 2.2.1 ATLAS detector requirements to fulfill the physics goals

The ATLAS(A Toroidal ApparatuS) detector is a general purpose detector at LHC. The primary physics goals of this experiment are Higgs searching and electro-weak precision tests, and possible new physics searching. Due to the high luminosity, extreme center of mass energy, and high background over signal ratio at LHC, ATLAS must satisfy the constrains as following:

- Due to the extreme experimental conditions at LHC, ATLAS detector must uses very fast and radiation-hard electronics and sensors. In order to reduce the overlap at high particle fluxes, all sub detectors need fine granularity.

- Large acceptance of pseudorapidity and azimuthal angle coverage are required, to tag and reconstruct physics events of particular interest.

- Good charge particle identification and momentum resolution are required. Meanwhile, in order to reconstruct and identify $\tau$ lepton and $b-jets$, good vertexing ability is needed for vertex detector near the interaction point, to precisely measure the secondary vertexes.

- Good energy measurement and resolution are needed in the electromagnetic calorimeter, in order to identify photon, electron. And almost full azimuthal coverage of hadron calorimeters is needed, in order to give the precise measurement of missing transverse energy.

- High muon identification efficiency and good muon momentum resolution, of a wide range for both coverage and energy are essential in physics with final states that include muons. Good charge determination even for very high energy muons is also needed.

- Heavy gauge bosons $W'$ and $Z'$ may be produced at LHC. Considering their leptonic decays, ATLAS needs good identification, energy resolution and charge separation power at the level of several TeV.

- In order to reduce the events rates to an acceptable level, and keep as much as possible interesting physics events, a high efficiency trigger system is needed to handle the 40 MHz input to an output of about 200Hz.

### 2.2.2 ATLAS designed performance

To fulfill the above requirements, the designed ATLAS performance are list in table 2.2:

| Detector Component | Required Resolution | $\eta$ Coverage | |
|---|---|---|---|
| | | Measurement | Trigger |
| Tracking | $\sigma_{p_T}/p_T = 0.05\% p_T \oplus 1\%$ | ±2.5 | |
| EM calorimetry | $\sigma_E/E = 10\%/\sqrt{E} \oplus 0.7\%$ | ±3.2 | ±2.5 |
| Hadronic calorimetry | | | |
| barrel and end-cap | $\sigma_E/E = 50\%/\sqrt{E} \oplus 3\%$ | ±3.2 | ±3.2 |
| forward | $\sigma_E/E = 100\%/\sqrt{E} \oplus 10\%$ | $3.1 < \lvert\eta\rvert < 4.9$ | $3.1 < \lvert\eta\rvert < 4.9$ |
| Muon spectrometer | $\sigma_{p_T}/p_T = 10\%$ at $p_T$=1TeV | ±2.7 | ±2.4 |

TABLE 2.2: General performance goals of the ATLAS detector. Note that, for $high - p_T$ muons, the muon-spectrometer performance is independent of the inner-detector system. The units for E and pT are in *GeV* [20].

### 2.2.3 ATLAS overview

The ATLAS detector is composed of an Inner Detector(ID), a calorimeter system, a muons spectrometer, a trigger and Data Acquisition(DAQ) system. Its dimension are 44 meters long and 25 meters high, for a total of about 7000 tons. The ATLAS detector is located at the IP1(impact point 1) of the tunnel of LHC, about 100 meters underground. Figure 2.4 and 2.3 show the overview of the ATLAS detector and the schematic of its components. The function of the Inner Detector is for vertexing, charge particles tracking and identification. And the Calorimeter system is used for photon, electron, jets identification and energy measurements, the Muon spectrometer is used to track and measure the energy of muons. Magnet system that provides the bending power on charged particles. The coordinate system of ATLAS is defined as following: the beam direction defines the z-axis and the $x - y$ plane is transverse to the beam direction. The positive $x - axis$ is defined as pointing from the interaction point to the center of the LHC ring and the positive y-axis is defined as pointing upwards. The $side - A$ of the detector is corresponding to positive z and $side - C$ to negative z. The azimuthal angle $\phi$ is measured around the beam axis, and the polar angle $\theta$ is the angle from the beam axis. The pseudorapidity is defined as $\eta \equiv -\ln(\tan(\theta/2))$. The transverse momentum $p_T$ , the transverse energy ET , and the missing transverse energy ET are defined in the x-y plane unless stated otherwise. The distance $\Delta R$ in the pseudorapidity-azimuthal angle space is defined as $\Delta R \equiv \sqrt{\Delta\eta^2 + \Delta\phi^2}$ [20]. The following sections will introduce each component of the ATLAS detector.

#### 2.2.3.1 Inner Detector

The design goals of ATLAS ID are: Large coverage in azimuthal and pseudorapidity. robust pattern recognizability. Good momentum resolution and secondary vertexing for charged particles in the acceptance of $|\eta| < 2.5$ and above a $p_T$ threshold(the threshold is usually 0.5 GeV, while it is possible to have 0.1 GeV at early stages for some minimal deviation events measurements). Meanwhile, it can provide electron identification of $|\eta| < 2.0$ and energy between 0.5 GeV and 150 GeV, even at high luminosity runs of LHC [21] [22]. Its construction reaches the utmost of the modern technics.

ID hosts inside one cylinder of dimension ±3512 mm long, semidiameter of 1150 mm. It is in a solenoid of magnet 2 tesla field (Figure 2.5). The parameters are shown in table 2.3, and the plan view are shown in figure 2.6. Figure 2.7 and figure 2.8 demonstrate a 10 GeV track travels through the barrel and end cap ID sensors separately.

The ID consists of three independent but complementary sub-detectors. At small radii region, there are silicon pixel layers and solid stereo pairs silicon microstrip layers to achieve a robust pattern recognition. At larger radii region, there are Transition Radiation Tracker(TRT), which is composed of multi-layers, up to 73 layers of straws interleaved with fibres (barrel) and 160 straw planes interleaved with foils (end-cap). All charged tracks with $p_T > 0.5$ GeV and $|\eta| < 2.0$ will traverse at least 36 straws of the most regions, which provide a continuous track and therefore enhance the pattern recognition as well as improve the electron identification performance. Table 2.4 lists the track parameters resolution of each ID sub-detector.

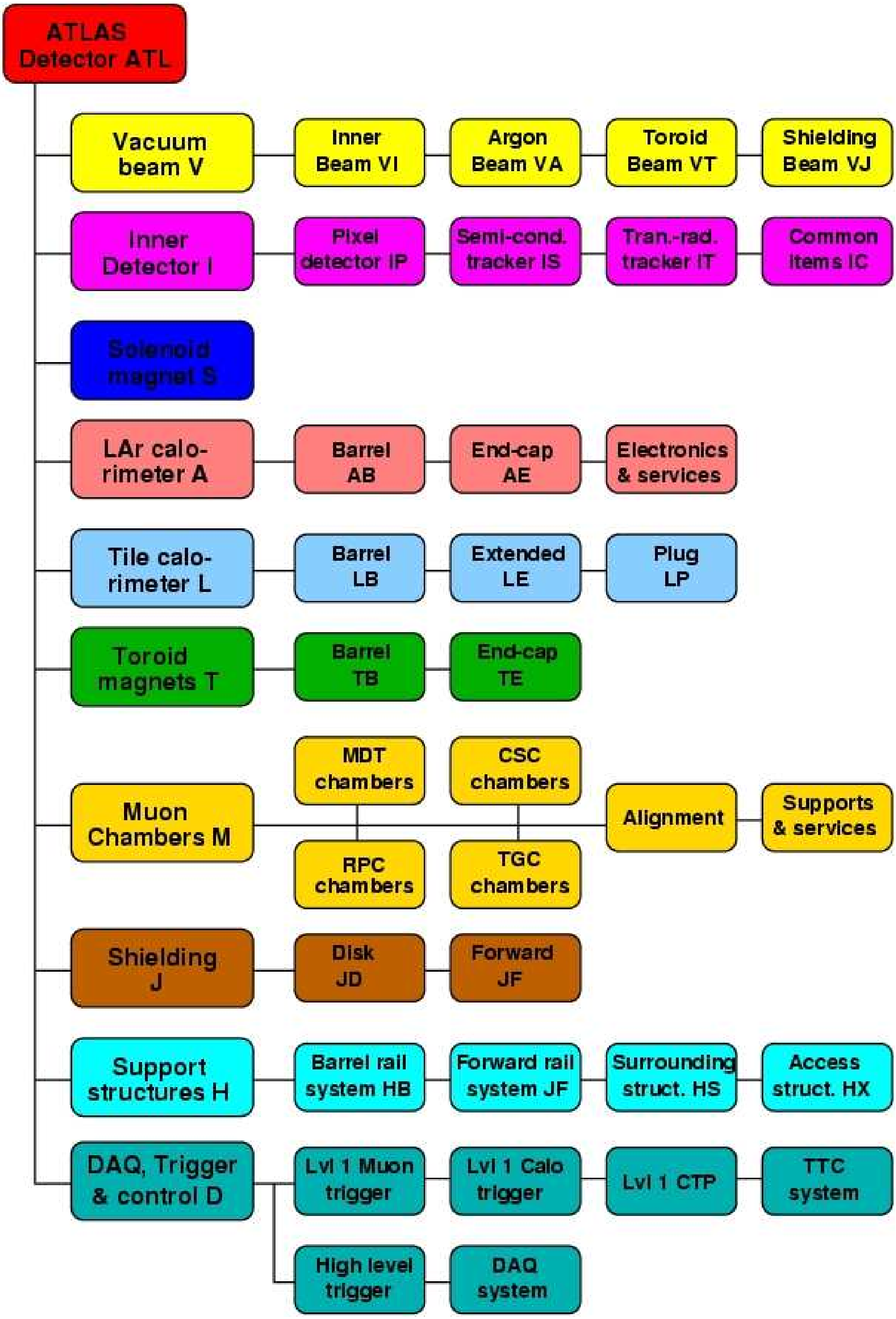

FIGURE 2.3: ATLAS detector components

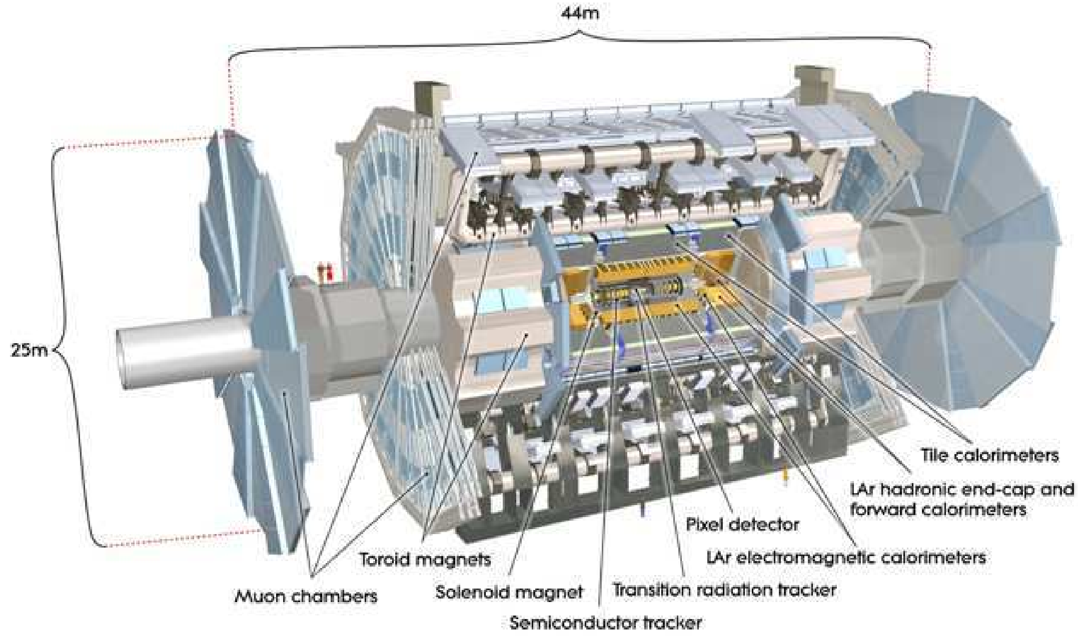

FIGURE 2.4: Overview of ATLAS detector

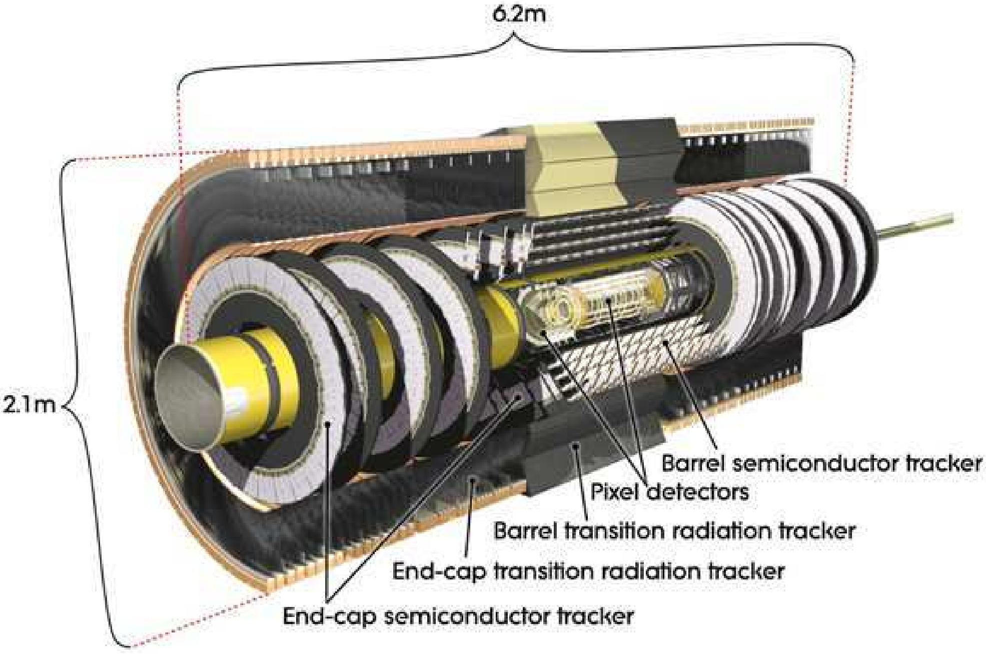

FIGURE 2.5: Overview of ATLAS inner detector

| **Item** | | **Radial extension(mm)** | **Length(mm)** |
|---|---|---|---|
| Overall ID envelope | | $0 < R < 1150$ | $0 < \|z\| < 3512$ |
| Beam-pipe | | $29 < R < 36$ | |
| **Pixel** | Overall envelope | $45.5 < R < 242$ | $0 < \|z\| < 3092$ |
| 3 cylindrical layers | Sensitive barrel | $50.5 < R < 122.5$ | $0 < \|z\| < 400.5$ |
| 2 x 3 disks | Sensitive end-cap | $88.8 < R < 149.6$ | $495 < \|z\| < 650$ |
| **SCT** | Overall envelope | $255 < R < 549(barrel)$ | $0 < \|z\| < 805$ |
| | | $251 < R < 610(endcap)$ | $810 < \|z\| < 2797$ |
| 4 cylindrical layers | Sensitive barrel | $299 < R < 514$ | $0 < \|z\| < 749$ |
| 2 x 9 disks | Sensitive end-cap | $275 < R < 560$ | $839 < \|z\| < 2735$ |
| **TRT** | Overall envelope | $554 < R < 1082(barrel)$ | $0 < \|z\| < 780$ |
| | | $617 < R < 1106(endcap)$ | $827 < \|z\| < 2744$ |
| 73 straw planes | Sensitive barrel | $563 < R < 1066$ | $0 < \|z\| < 712$ |
| 160 straw planes | Sensitive end-cap | $644 < R < 1004$ | $848 < \|z\| < 2710$ |

TABLE 2.3: Main parameters of inner detector

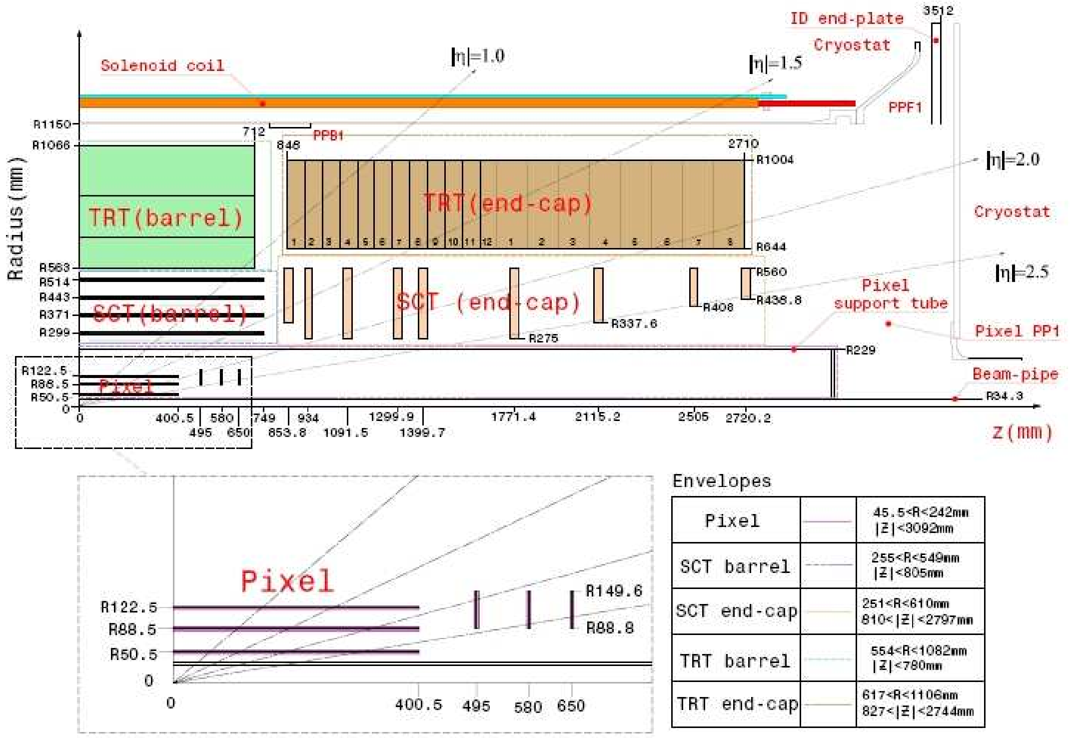

| Envelopes | | |
|---|---|---|
| Pixel | | 45.5<R<242mm<br>\|Z\|<3092mm |
| SCT barrel | | 255<R<549mm<br>\|Z\|<805mm |
| SCT end-cap | | 251<R<610mm<br>810<\|Z\|<2797mm |
| TRT barrel | | 554<R<1082mm<br>\|Z\|<780mm |
| TRT end-cap | | 617<R<1106mm<br>827<\|Z\|<2744mm |

FIGURE 2.6: Plan view of a quarter-section of the ATLAS inner detector showing each of the major detector elements with its active dimensions and envelopes. The labels PP1, PPB1 and PPF1 indicate the patch-panels for the ID services.

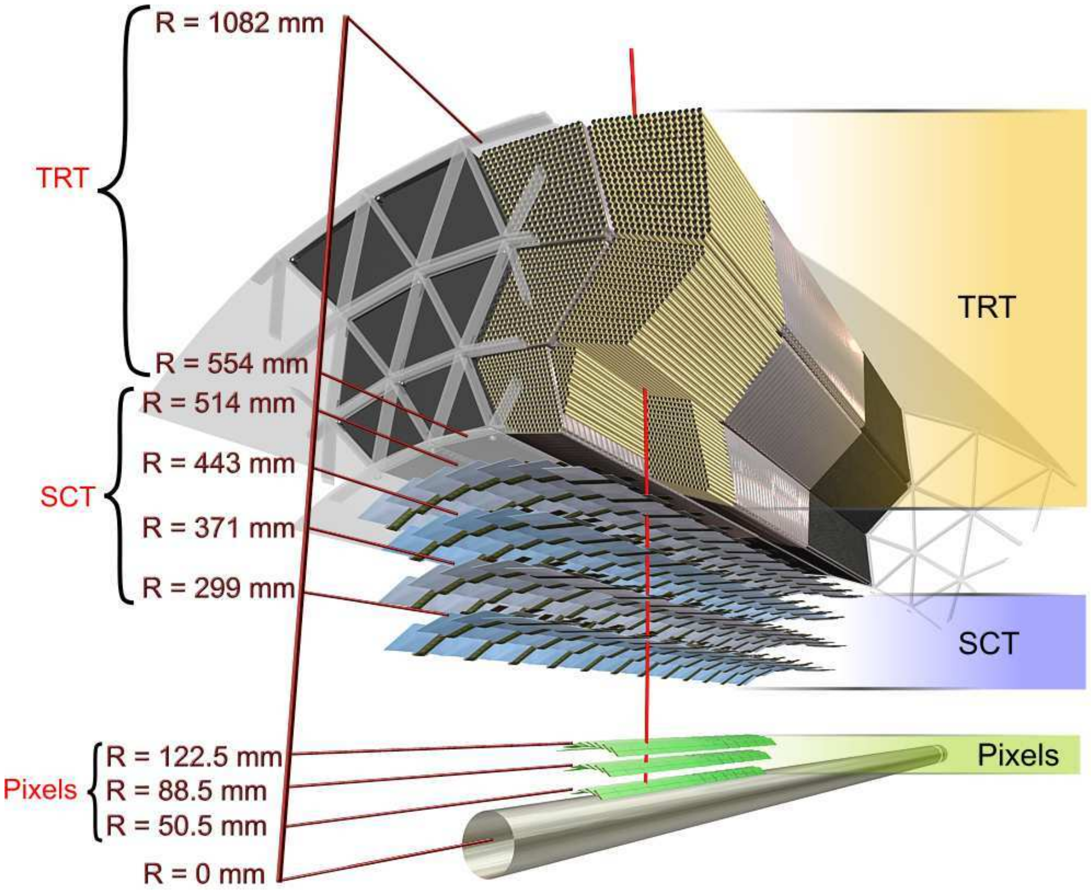

Figure 2.7: Drawing showing the sensors and structural elements traversed by a charged track of 10 GeV $p_T$ in the barrel inner detector ($\eta = 0.3$). The track traverses successively the beryllium beam-pipe, the three cylindrical silicon pixel layers with individual sensor elements of $50 \times 400 \mu m^2$, the four cylindrical double layers (one axial and one with a stereo angle of 40 mrad) of barrel silicon microstrip sensors (SCT) of pitch 80 $\mu$m and approximately 36 axial straws of 4 mm diameter contained in the barrel transition radiation tracker modules within their support structure.

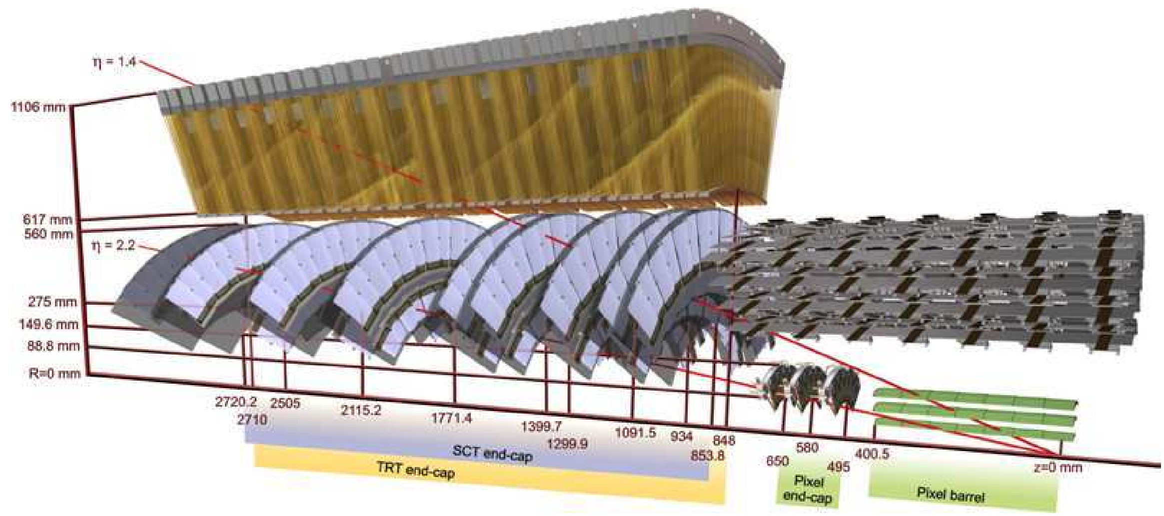

Figure 2.8: Drawing showing the sensors and structural elements traversed by two charged tracks of 10 GeV $p_T$ in the end-cap inner detector ($\eta = 1.4$ and 2.2). The end-cap track at $\eta = 1.4$ traverses successively the beryllium beam-pipe, the three cylindrical silicon pixel layers with individual sensor elements of $50 \times 400 \mu m^2$, four of the disks with double layers (one radial and one with a stereo angle of 40 mrad) of end-cap silicon microstrip sensors (SCT) of pitch $\sim 80 \mu m$ and approximately 40 straws of 4 mm diameter contained in the end-cap transition radiation tracker wheels. In contrast, the end-cap track at $\eta = 2.2$ traverses successively the beryllium beam-pipe, only the first of the cylindrical silicon pixel layers, two end-cap pixel disks and the last four disks of the end-cap SCT. The coverage of the end-cap TRT does not extend beyond $|\eta| = 2$

| **Track Parameter** | $0.25 < \|\eta\| < 0.5$ | | $1.50 < \|\eta\| < 1.75$ | |
|---|---|---|---|---|
| | $\sigma_x(\infty)$ | $p_X$ (GeV) | $\sigma_x(\infty)$ | $p_X$ (GeV) |
| Inverse transverse momentum$(1/p_T)$ | 0.34 $TeV^{-1}$ | 44 | 0.41 $TeV^{-1}$ | 80 |
| Azimuthal angle $(\phi)$ | 70 $\mu\ rad$ | 39 | 92 $\mu\ rad$ | 49 |
| Polar angle$(\cot\theta)$ | 0.7 $\times 10^{-3}$ | 5.0 | 1.2 $\times 10^{-3}$ | 10 |
| Transverse impact parameter$(d_0)$ | 10 $\mu\ m$ | 14 | 12 $\mu\ m$ | 20 |
| Longitudinal impact parameter$(z_0 \times \sin\theta)$ | 91 $\mu\ m$ | 2.3 | 71 $\mu\ m$ | 3.7 |

Table 2.4: Expected track-parameter resolutions (RMS) at infinite transverse momentum, $\sigma_x(\infty)$, and transverse momentum, $p_X$, at which the multiple-scattering contribution equals that from the detector resolution. The momentum and angular resolutions are shown for muons, whereas the impact-parameter resolutions are shown for pions. The values are shown for two $\eta$-regions, one is in the barrel inner detector where the amount of material is close to its minimum and one is in the end-cap where the amount of material is close to its maximum.

The high radiation environment is a challenge for inner detector sensors, the electronics, and the mechanical structure. Over the life time of 10 years of the designed detector, pixel inner vertexing layer must be replaced after approximately three years of operation at design luminosity. The other pixel layers and the pixel disks must withstand up to $\sim 8 \times 10^{14}\text{cm}^{-2}$ 1MeV neutron equivalent fluency($\text{F}_{\text{neq}}$, the equivalent radiation of 1 MeV neutron). While the innermost parts of the SCT must withstand $\sim 2 \times 10^{14}\text{cm}^{-2}$ $\text{F}_{\text{neq}}$. In order to maintain an adequate noise performance after radiation damage, the silicon sensors must be kept at low temperature of $-5°\text{C} \sim -10°\text{C}$ by a cooling material of $-25°\text{C}$. In contrast, the TRT is designed to operate at room temperature.

The above operating specifications imply requirements on the alignment precision which are summarized in table 2.5 and which serve as stringent upper limits on the silicon-module build precision, the TRT straw-tube position, and the measured module placement accuracy and stability.

- **Pixel**

  The pixel modules are 2715 arranged in three barrel layers and two end-caps each with three disk layers. A total of 112 barrel staves and 48 end-cap sectors (8 sectors per disk) form the barrel and disk layers. The minimum pixel module(innermost) size is $50 \times 400\ mm^2$, dictated by the readout pitch of the front-end electronics. There are 47232 pixels on each sensor, but for reasons of space there are four ganged pixels in each column of the front-end chip, thus leading to a total of 46080 readout channels. Each pixel of a sensor is bump-bonded through a hole in the passivation layer to an element of the front-end readout integrated circuit as part of the module.

- **SCT**

  SCT consists of 4088 modules tiling four coaxial cylindrical layers in the barrel region and two end-caps each containing nine disk layers. The modules cover a surface of $63m^2$ of silicon and provide almost hermetic coverage with at least four precision space-point measurements over the fiducial coverage of the inner detector.

  The 2112 barrel SCT modules use 80 $\mu$m pitch micro-strip sensors, The sensors are connected to binary signal readout chips. The main parameter of SCT are listed in table 2.6.

- **TRT**

  The TRT contains up to 73 layers of straws interleaved with fibres (barrel) and 160 straw planes interleaved with foils (end-cap), which provide transition radiation for electron identification. All charged tracks with $p_T > 0.5\text{GeV}$, $|\eta| < 2.0$ will traverse at least 36 straws, except in the barrel-end-cap transition region($0.8 < \eta < 1.0$). where this number decreases to a minimum of 22 crossed straws. Typically, seven

| **Item** | **Intrinsic accuracy** ($\mu\ m$) | **Alignment tolerances** ($\mu\ m$) | | |
|---|---|---|---|---|
| | | **Radial(R)** | Axial(z) | AZIMUTH(R-$\phi$) |
| **Pixel** | | | | |
| Layer-0 | 10(R-$\phi$) 115(Z) | 10 | 20 | 7 |
| Layer-1 and -2 | 10(R-$\phi$) 115(Z) | 20 | 20 | 7 |
| Disks | 10(R-$\phi$) 115(R) | 20 | 100 | 7 |
| **SCT** | | | | |
| Barrel | 17(R-$\phi$) 580(Z)$^1$ | 100 | 50 | 12 |
| Disks | 17(R-$\phi$) 580(R)$^1$ | 50 | 200 | 12 |
| **TRT** | 130 | | | 30$^2$ |

1. Arises from the 40 mrad stereo angle between back-to-back sensors on the SCT modules

with axial (barrel) or radial (end cap) alignment of one side of the structure

The z-resolution results from two axial-stereo points with opposite stereo directions

The result is pitch-dependent for end cap SCT modules

2. The quoted alignment accuracy is related to the TRT drift-time accuracy

Table 2.5: Intrinsic measurement accuracies and mechanical alignment tolerances for the inner-detector sub-systems, as defined by the performance requirements of the ATLAS experiment.

to ten high-threshold hits from transition radiation are expected for electrons with energies above 2 GeV.

The barrel TRT is divided into three rings of 32 modules each, supported at each end by a space frame, which is the main component of the barrel support structure. Each module consists of a carbon-fibre laminate shell and an internal array of straws embedded in a matrix of 19 $\mu m$-diameter polypropylene fibres serving as the transition radiation material. The straws, form a uniform axial array with a mean spacing of ~7 mm. The module shells are non projective to reduce the dead region for high $p_T$ tracks

The dimensional specifications are set by the intrinsic straw $R - \phi$ resolution of 130 $\mu$m. implying that each wire position is constrained to within $\pm 50\mu$m. The module shell, made of 400 $\mu$m thick carbon fibre with high thermal conductivity and flat to within 250 $\mu$m, is measured to satisfy maximum distortions of $< 40\mu$m under full load.

| **Parameter** | **Description** |
|---|---|
| Strips | 2 × 768 active strips, ± 20 mrad stereo rotation |
| Nominal resolution | 17 $\mu\ m$ in-plane lateral(R-$\phi$)<br>580 $\mu\ m$ in-plane longitudinal(z or R) |
| Mudule dimensions | |
| -barrel | Active length 126.09 mm + 2.09 mm dead space between sensors |
| -outer end-cap | Active length 119.14 mm + 2.09 mm dead space, radius 438.77 - 560.00 mm |
| -middle end-cap | Active length 115.61 mm + 2.09 mm dead space, radius 337.60 - 455.30 mm |
| -short-middle end-cap | Active length 52.48 mm, radius 402.82 - 455.30 mm |
| -inner end-cap | Active length 59.1 mm, radius 275.00 - 334.10 mm |
| Specified build tolerance | Barrel back-to-back in plane: $< 8\ \mu\ m(lateral) < 20\ \mu\ m(longitudinal)$<br>End-cap back-to-back in plane: $< 5\ \mu\ m(lateral) < 10\ \mu\ m(longitudinal)$<br>Barrel out-of-plane(module thickness and sensor bowing): $< 70\ \mu\ m$<br>Barrel envelope: $< 200\ \mu\ m$<br>End-cap envelope: $< 115\ \mu\ m$<br>Barrel module fixation points with respect to module center: $< 40\ \mu\ m$<br>End-cap module fixation points with respect to module center: $< 20\ \mu\ m$ |
| Build accuracy of accepted modules(RMS) | Barrel back-to-back in plane: $\pm\ 2.1\ \mu\ m(lateral) \pm\ 2.7\ \mu\ m(longitudinal)$<br>End-cap back-to-back in plane: $\pm\ 1.6\ \mu\ m(lateral) \pm\ 1.3\ \mu\ m(longitudinal)$<br>Barrel module thickness: $\pm\ 33\ \mu\ m$<br>Barrel out-of-plane(sensor bowing): $\pm\ 9\ \mu\ m$<br>End-cap module thickness: $\pm\ 15\ \mu\ m$<br>End-cap out-of-plane(sensor bowing): $\pm\ 20\ \mu\ m$<br>Barrel module fixation points with respect to module center $\pm\ 10\ \mu\ m$<br>End-cap module fixation points with respect to module center $\pm\ 6\ \mu\ m$ |
| Hybrid power consumption | 5.5 - 7.5 W |
| Sensor power consumption | Up to 460 V bias, < 1W at -7°C |

Table 2.6: SCT barrel and end-cap module specifications and the RMS build accuracy for accepted modules. The barrel out-of-plane bowing specifications and the measured results are with respect to an average module shape.

#### 2.2.3.2 Calorimeter system

The ATLAS calorimeters consist of a number of sampling detectors with full $\phi$-symmetry and coverage around the beam axis. The calorimeters closest to the beam-line are housed in three cryostats, one barrel and two end-caps. The barrel cryostat contains the electromagnetic barrel calorimeter, whereas the two end-cap cryostats each contains an electromagnetic end-cap calorimeter (EMEC), a hadronic end-cap calorimeter (HEC), located behind the EMEC, and a forward calorimeter (FCal) to cover the region closest to the beam. All these calorimeters use liquid argon as the active detector medium; liquid argon has been chosen for its intrinsic linear behavior, its stability of response over time and its intrinsic radiation-hardness [23] [24].

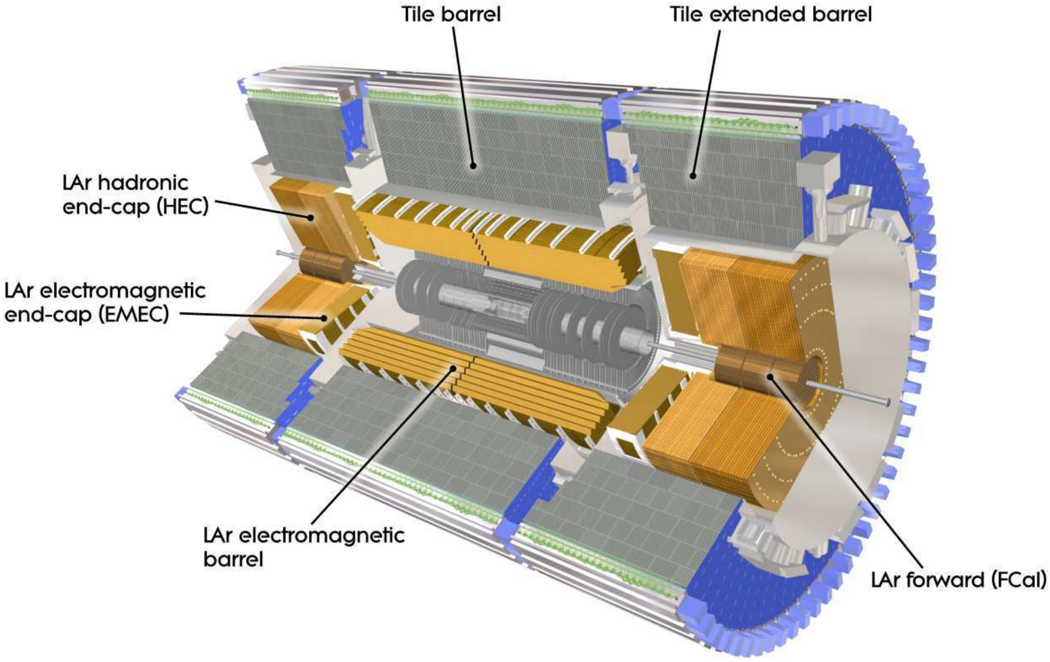

Figure 2.9: The Cut-away view of ATLAS calorimeter

The precision electromagnetic calorimeters are lead-liquid argon detectors with accordion shape absorbers and electrodes. This geometry allows to have several active layers in depth, three in the precision-measurement region$(0 < |\eta| < 2.5)$ and two in the $2.5 < |\eta| < 3.2$ region and in the overlap region between the barrel and the EMEC. In the precision-measurement region, an accurate position measurement is obtained by finely segmenting the first compartment in $\eta$. The $\eta$-direction of photons is determined by the position of the photon cluster in the first and the second compartments. in the region $(0 < |\eta| < 1.8)$ the electromagnetic calorimeters are complemented by presamplers, an instrumented argon layer, which provides a measurement of the energy lost in front of the electromagnetic calorimeters.

For the outer hadronic calorimeter, the sampling medium consists of scintillator tiles and the absorber medium is steel. The tile calorimeter is composed of three parts,

| | Barrel | | End-cap | |
|---|---|---|---|---|
| **EM calorimeter** | | | | |
| Number of layers and $\lvert\eta\rvert$ coverage | | | | |
| presampler | 1 | $\lvert\eta\rvert < 1.52$ | 1 | $1.5 < \lvert\eta\rvert < 1.8$ |
| Calorimeter | 3 | $\lvert\eta\rvert < 1.35$ | 2 | $1.375 < \lvert\eta\rvert < 1.5$ |
| | 2 | $1.35 < \lvert\eta\rvert < 1.475$ | 3 | $1.5 < \lvert\eta\rvert < 2.5$ |
| | | | 2 | $2.5 < \lvert\eta\rvert < 3.2$ |
| **Granularity $\Delta\eta \times \Delta\phi versus \lvert\eta\rvert$** | | | | |
| presampler | $0.025 \times 0.1$ | $\lvert\eta\rvert < 1.52$ | $0.025 \times 0.1$ | $1.5 < \lvert\eta\rvert < 1.8$ |
| Calorimeter 1st layer | $0.025/8 \times 0.1$ | $\lvert\eta\rvert < 1.40$ | $0.050 \times 0.1$ | $1.375 < \lvert\eta\rvert < 1.425$ |
| | $0.025 \times 0.025$ | $1.40 < \lvert\eta\rvert < 1.475$ | $0.025 \times 0.1$ | $1.425 < \lvert\eta\rvert < 1.5$ |
| | | | $0.025/8 \times 0.1$ | $1.5 < \lvert\eta\rvert < 1.8$ |
| | | | $0.025/6 \times 0.1$ | $1.8 < \lvert\eta\rvert < 2.0$ |
| | | | $0.025/4 \times 0.1$ | $2.0 < \lvert\eta\rvert < 2.4$ |
| | | | $0.025 \times 0.1$ | $2.4 < \lvert\eta\rvert < 2.5$ |
| | | | $0.1 \times 0.1$ | $2.5 < \lvert\eta\rvert < 3.2$ |
| Calorimeter 2nd layer | $0.025 \times 0.025$ | $\lvert\eta\rvert < 1.40$ | $0.05 \times 0.025$ | $1.375 < \lvert\eta\rvert < 1.425$ |
| | $0.075 \times 0.025$ | $1.40 < \lvert\eta\rvert < 1.475$ | $0.025 \times 0.025$ | $1.425 < \lvert\eta\rvert < 2.5$ |
| | | | $0.1 \times 0.1$ | $2.5 < \lvert\eta\rvert < 3.2$ |
| Calorimeter 3rd layer | $0.05 \times 0.025$ | $\lvert\eta\rvert < 1.35$ | $0.05 \times 0.025$ | $1.5 < \lvert\eta\rvert < 2.5$ |
| Number of readout channels | | | | |
| Presampler | 7808 | | 1536(both sides) | |
| Calorimeter | 101760 | | 62208(both sides) | |
| **LAr hadronic end-cap** | | | | |
| $\lvert\eta\rvert coverage$ | | | $1.5 < \lvert\eta\rvert < 3.2$ | |
| Number of layers | | | 4 | |
| Granularity $\Delta\eta \times \Delta\phi$ | | | $0.1 \times 0.1$ | $1.5 < \lvert\eta\rvert < 2.5$ |
| | | | $0.2 \times 0.2$ | $2.5 < \lvert\eta\rvert < 3.2$ |
| Readout channels | | | 5632(both sides) | |
| **LAr forward calorimeter** | | | | |
| $\lvert\eta\rvert coverage$ | | | $3.1 < \lvert\eta\rvert < 4.9$ | |
| Number of layers | | | 3 | |
| Granularity $\Delta x \times \Delta y(cm)$ | | | $FCal1 : 3.0 \times 2.6$ | $3.15 < \lvert\eta\rvert < 4.30$ |
| | | | $FCal1 :\sim 4x finer$ | $3.10 < \lvert\eta\rvert < 3.15$ |
| | | | | $4.30 < \lvert\eta\rvert < 4.83$ |
| | | | $FCal2 : 3.3 \times 4.2$ | $3.24 < \lvert\eta\rvert < 4.50$ |
| | | | $FCal2 :\sim 4x finer$ | $3.20 < \lvert\eta\rvert < 3.24$ |
| | | | | $4.50 < \lvert\eta\rvert < 4.81$ |
| | | | $FCal3 : 3.3 \times 4.2$ | $3.32 < \lvert\eta\rvert < 4.60$ |
| | | | $FCal3 :\sim 4x finer$ | $3.29 < \lvert\eta\rvert < 3.32$ |
| | | | | $4.60 < \lvert\eta\rvert < 4.75$ |
| Readout channels | | | 3524(both sides) | |
| **Scintillator tile calorimeter** | | | | |
| | Barrel | | Extended barrel | |
| $\lvert\eta\rvert coverage$ | $\lvert\eta\rvert < 1.0$ | | $0.8 < \lvert\eta\rvert < 1.7$ | |
| Number of layers | 3 | | 3 | |
| Granularity $\Delta\eta \times \Delta\phi$ | $0.1 \times 0.1$ | | $0.1 \times 0.1$ | |
| last layer | $0.2 \times 0.1$ | | $0.2 \times 0.1$ | |
| Readout channels | 5760 | | 4092(both sides) | |

TABLE 2.7: Main parameters of ATLAS Calorimeter

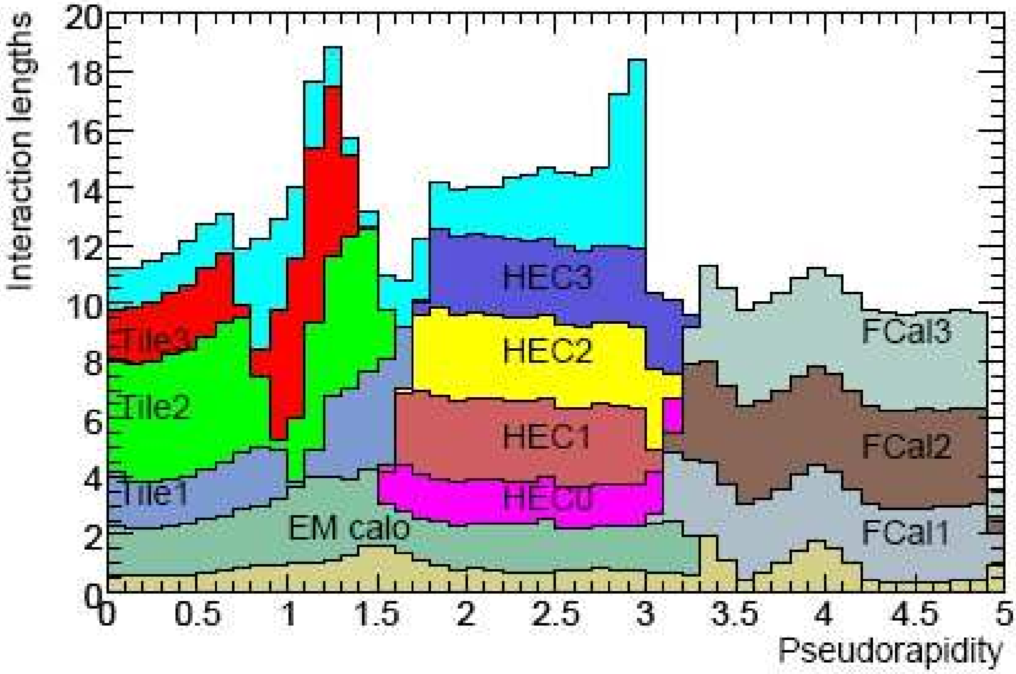

Figure 2.10: Cumulative amount of material, in units of interaction length, as a function of $|\eta|$, in front of the electromagnetic calorimeters, in the electromagnetic calorimeters themselves, in each hadronic compartment, and the total amount at the end of the active calorimetry. Also shown for completeness is the total amount of material in front of the first active layer of the muon spectrometer (up to $|\eta| < 3.0$).

one central barrel and two extended barrels. The choice of this technology provides maximum radial depth for the least cost for ATLAS. The tile calorimeter covers the range of $0 < |\eta| < 1.7$. The hadronic calorimetry is extended to larger pseudorapidity by the HEC, a copper/liquid-argon detector, and the FCal, a copper-tungsten/liquid-argon detector. The hadronic calorimetry thus reaches one of its main design goals, namely coverage 3850 over $|\eta| < 4.9$. Figure 2.9 shows the schematic drawing of the calorimeter system. Table 2.7 show the main design parameters of the calorimeter. Figure 2.10 show the mater distribution before and in the calorimeter. The structure of the calorimeter will be introduced in the following section.

- **Electromagnetic Calorimeter:**

  An accordion geometry has been chosen for the absorbers and the electrodes of the barrel and end cap electromagnetic calorimeters. Such a geometry provides naturally a full coverage in $\phi$ without any cracks, and a fast extraction of the signal at the rear or at the front of the electrodes. In the barrel, the accordion waves are axial and run in $\phi$, and the folding angles of the waves vary with radius to keep the liquid-argon gap constant. In the end-caps, the waves are parallel to the radial direction and run axially. Since the liquid-argon gap increases with radius in the end-caps, the wave amplitude and the folding angle of the absorbers and electrodes vary with radius. All these features of the accordion geometry lead to a very uniform performance in terms of linearity and resolution as a function of $\phi$.

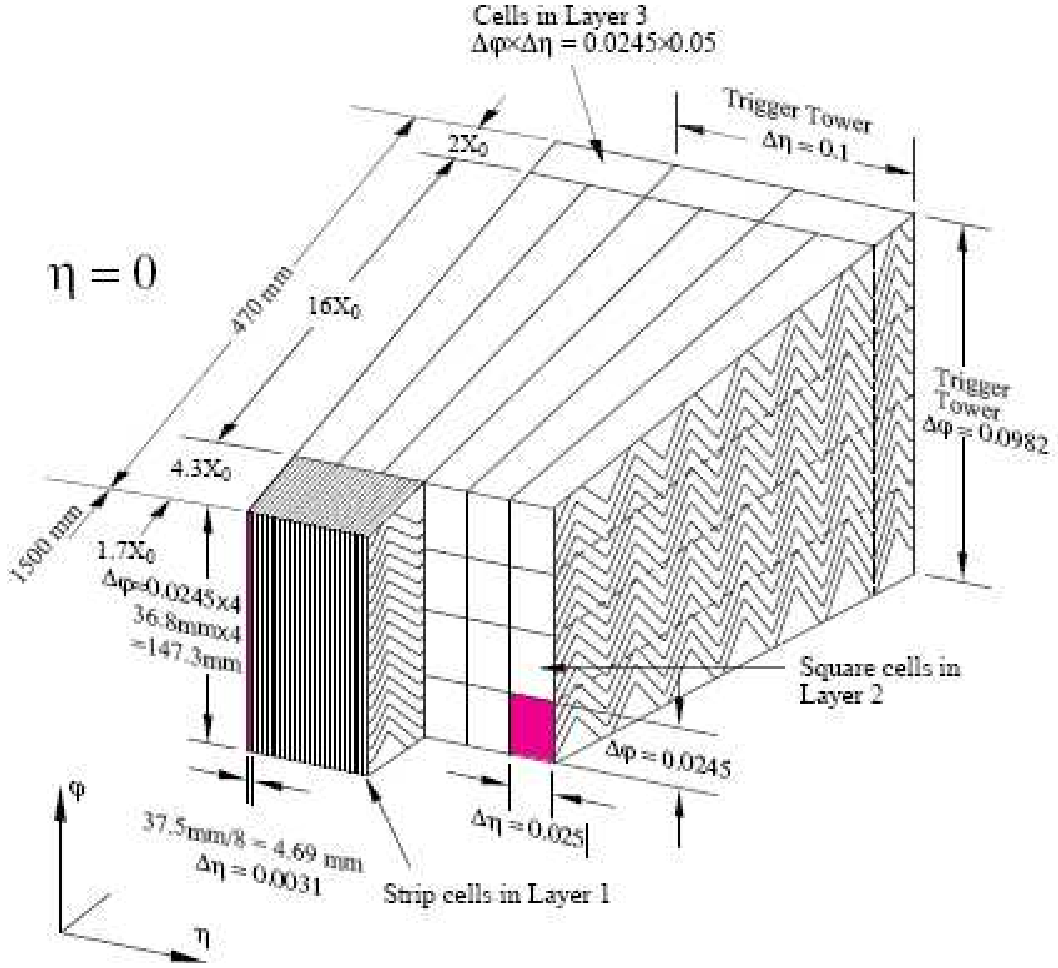

FIGURE 2.11: Sketch of a barrel module where the different layers are clearly visible with the ganging of electrodes in $\phi$ . The granularity in $\eta$ and $\phi$ of the cells of each of the three layers and of the trigger towers is also shown.

The barrel electromagnetic calorimeter is made of two half-barrels [25], centered around the z-axis. One half-barrel covers the region with $z > 0(0 < \eta < 1.475)$ and the other one the region with $z < 0(-1.475 < \eta < 0)$. The length of each half-barrel is 3.2 m, their inner and outer diameters are 2.8 m and 4 m respectively, and each half-barrel weighs 57 tonnes. One of the module is shown as figure 2.11.

The EMEC calorimeters consist of two wheels, on each side of the electromagnetic barrel. Each wheel is 63 cm thick and weighs 27 tonnes, with external and internal radii at ambient temperature of 2098 mm and 330 mm, respectively. It covers the region of $1.375 < |\eta| < 3.2$.

- **Hadron Calorimeter:**

  ATLAS Hadron Calorimeter system is composed of the tile calorimeter, the liquid-argon hadronic end-cap calorimeter (HEC) and the liquid-argon forward calorimeter (FCal). Of which Tile calorimeter is a sampling calorimeter using steel as the absorber and scintillator as the active medium. It is subdivided into a central barrel, 5.8 m in length, and two extended barrels, 2.6 m in length and each having an inner radius of 2.28 m and an outer radius of 4.25 m. One of its modules is shown in figure 2.12.

  The hadronic end-cap calorimeter (HEC) [26] is a copper/liquid-argon sampling calorimeter with a flat plate design, which covers the range $1.5 < \eta < 3.2$. The HEC shares each of the two liquid argon end-cap cryostats with the electromagnetic end-cap (EMEC) and forward (FCal) calorimeters. The HEC consists of two wheels in each end-cap cryostat: a front wheel (HEC1) and a rear wheel (HEC2), each wheel containing two longitudinal sections. The wheels are cylindrical with an outer radius of 2030 mm. Each of the four HEC wheels is constructed of 32 identical wedge-shaped modules. The forward calorimeters (FCal) provide coverage over $3.1 < \eta < 4.9$. The FCal modules are located at high $\eta$, at a distance of approximately 4.7 m from the interaction point, they are exposed to high particle fluxes. It is composed with 3 layers, one is electromagnet calorimeters and the other two are hadron calorimeters.

#### 2.2.3.3 Muon Spectrometer

The Muon Spectrometer forms the outer part of the ATLAS detector and it is designed to detect charged particles exiting the barrel and end-cap calorimeters and to measure their momentum in the pseudorapidity range $|\eta| < 2.7$. It is also designed to trigger these particles in the region $|\eta| < 2.4$. The driven performance goal is a stand-alone transverse momentum resolution of approximately 10% for 1 TeV tracks. The schematic picture of Muon Spectrometer are shown in figure 2.13 and the main parameters of Muon Spectrometer are listed in table 2.8.

The identification and measurements of muon particles are dependent on the tracks deflexions by the magnetic system. It is very import to have a precisely known magnetic field to ensure the precise measurement of muon.

Region of $|\eta| < 1.4$ are surrounded by a toroidal magnetic field generated by a eight-lateral symmetry of the superconducting magnets; In the $1.6 < |\eta| < 2.7$, the magnetic field is provided by two superconducting magnets of flat coils from eight radial symmetrical position. In the $1.4 < |\eta| < 1.6$ region (known as the transition zone), the magnetic field is provided by both end cap and barrel magnets. This magnetic field is designed so that most of magnetic force lines are vertical to the $\mu$'s track and lead to the establishment of a

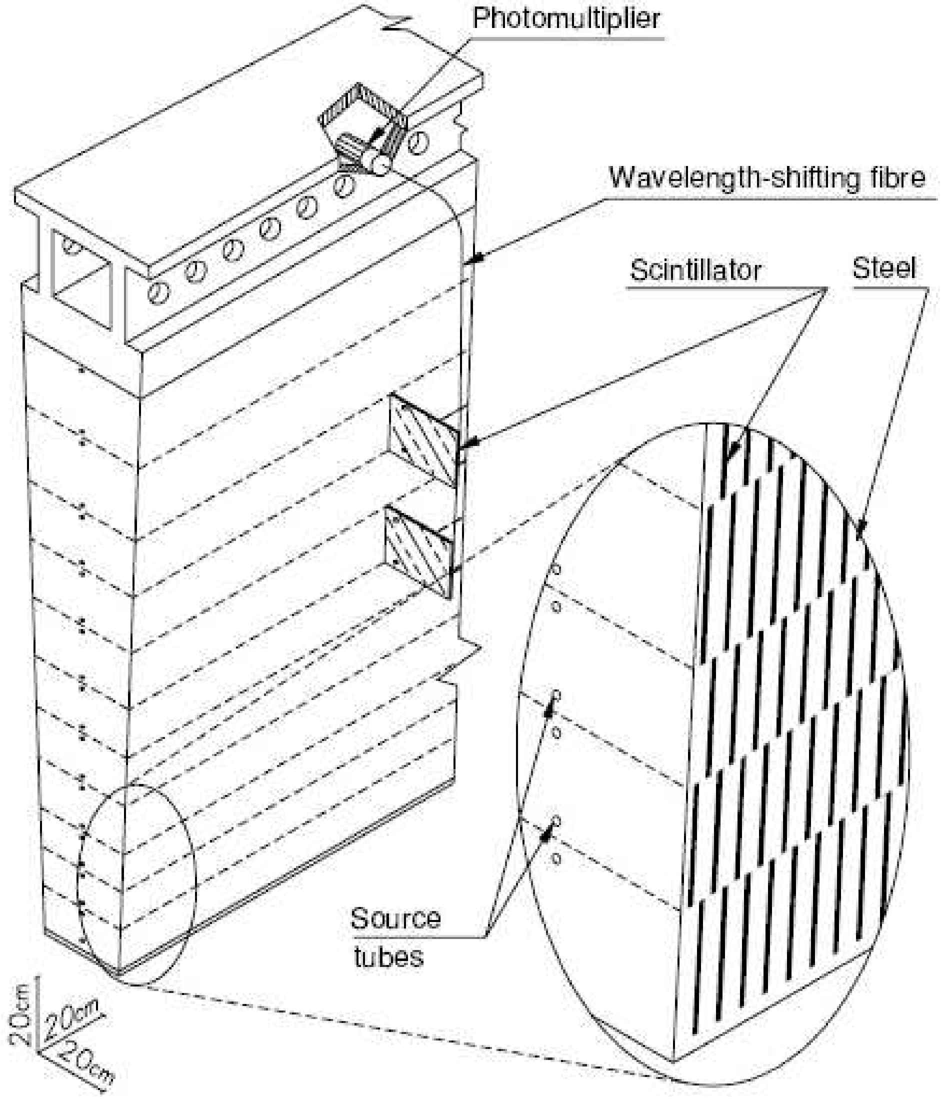

FIGURE 2.12: Schematic showing how the mechanical assembly and the optical readout of the tile calorimeter are integrated together. The various components of the optical readout, namely the tiles, the fibres and the photomultipliers, are shown.

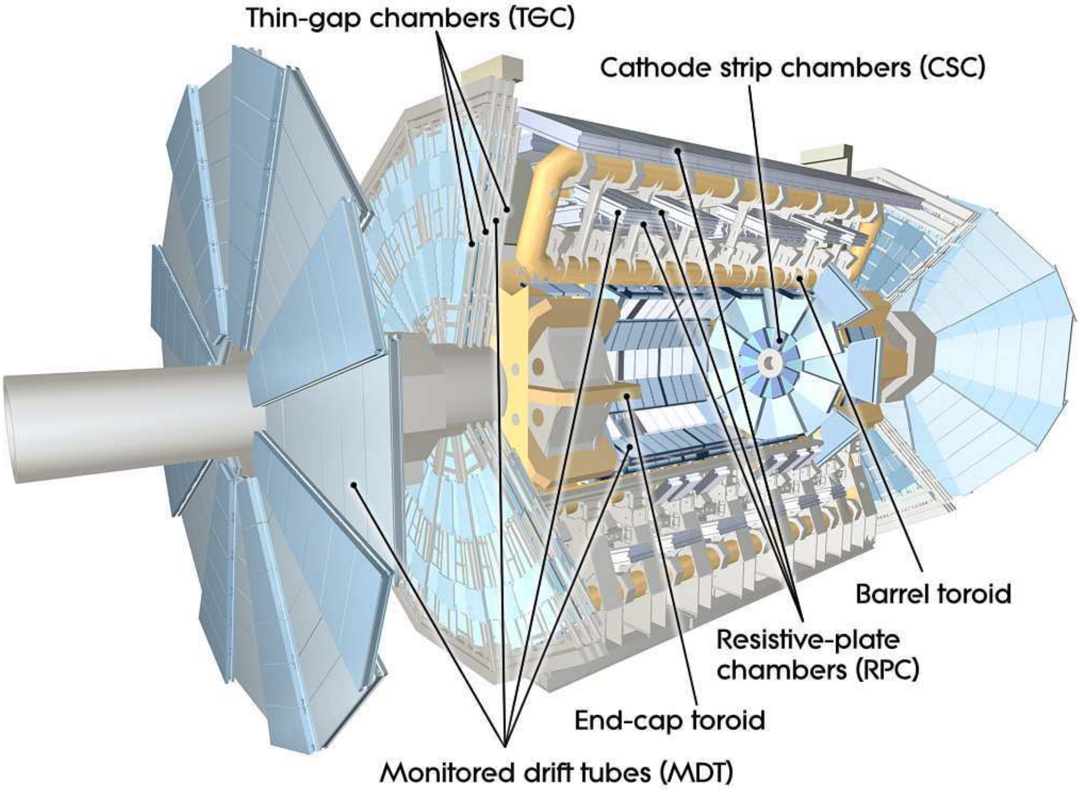

FIGURE 2.13: The cut-away plots of ATLAS Muon Spectrometer

| | |
|---|---|
| **Monitored drift tubes** | **MDT** |
| - Coverage | $|\eta| < 2.7(innermostlayer : |\eta| < 2.0)$ |
| - Number of chambers | 1088(1150) |
| - Number of channels | 339 000(354 000) |
| - Function | Precision tracking |
| **Cathode strip chambers** | **CSC** |
| - Coverage | $2.0 < |\eta| < 2.7$ |
| - Number of chambers | 32 |
| - Number of channels | 31 000 |
| - Function | Precision tracking |
| **Resistive plate chambers** | **RPC** |
| - Coverage | $|\eta| < 1.05$ |
| - Number of chambers | 544(606) |
| - Number of channels | 359 000(373 000) |
| - Function | Triggering, second coordinate |
| **Thin gap chambers** | **TGC** |
| - Coverage | $1.05 < |\eta| < 2.7$(2.4 for triggering) |
| - Number of chambers | 3588 |
| - Number of channels | 318 000 |
| - Function | Triggering, second coordinate |

TABLE 2.8: Main parameters of muon spectrometer. Numbers in brackets for the MDT's and the RPC's refer to the final configuration of the detector in 2009

high precision and high coverage, stable and independent $\mu$ spectrometer, with minimum impact to the calorimeter and inner detector measurements.

Muon spectrometer magnets are air-core superconducting magnets, which can reduce the degradation of resolution caused by multiple scattering. The barrel magnet is 25.3 meters long, with inner diameter of 9.4 meters, outer diameter of 20.1 meters. The end cap magnets are located at the end of the barrel, with inner diameter of 1.65 meters, and outer diameter of 10.7 meters. The typical magnetic field strength of the barrel is 0.5 Tesla, and the end cap is one Tesla. Because of the limited magnet coils, the magnetic field does not have a perfect cylindrical shape, especially in the transitional zone, of which the magnetic field has more radial component.

The barrel MDT (Monitored Drift Tube) are based on three cylinders, coaxial to the beam lines, of a radius of 5 m, 7.5m, 10m, in the middle of the magnetic field and two marginal. They are used to measure the momentum of muons. In the end cap(Pseudorapidity of $|\eta| > 1.6$), the low-temperature superconducting magnet system prevents detectors to be fully in the magnetic field, the distances of the three MDT discs from the impact point are 7 m, 14m, 21m. Point-to-angle measurement method is used in order to get the best $\mu$ momentum resolution. As the region of $2 < |\eta| < 2.7$, there is high radiation intensity, CSC (Cathode Strip Chamber) are used to measure muon properties instead of the MDT. Trigger detectors cover the range of $|\eta| < 2.4$. RPC are used as barrels trigger detectors, while TGC are used as end cap trigger detectors. These two detectors will provide the information of the secondary coordinate position which is perpendicular to the $\mu$ deflection plane(and almost parallel to the magnetic field). During the running time of ATLAS experiment, alignment system is used to monitor the small position changes of the sub detectors. The performance of various detectors of muon spectrometer are given in the following parts.

- **MDT:**

  The MDT module is composed of 30 mm diameter Aluminum tubes and a 50 $\mu m$ coaxial Tungsten-Rhenium wire [27]. Both ends of the tube are gagged by stoppers [28]. The stoppers are responsible for fixing the position of anode wire, keeping and exchanging the gas and electronics readout. The working gas of MDT is Argon and Carbon dioxide mixtures at 3 bar. One end of the anode wire in the drift chamber is connected to a low-impedance current amplifier, a differential amplifier, a shaper and a discriminator. Then, the signal is sent to a 24 bit TDC, which measures the drifting time with an accuracy of 300 ps. MDT has a good space - time relation. In addition to extremely close to the anode wire particles, the typical MDT spatial resolution is 80 $\mu$m [29, 30, 31]. In order to improve the spatial resolution, MDT drift tubes are assembled into three or four-layers structure. ATLAS detector has three sections of MDT, the innermost is $2 \times 4$ MDT tubes structure, while the middle and outer are $2 \times 3$ MDT tubes structure. This combination of multi-MDT can further improve th spatial resolution.

- **CSC:**

  The distance between neighboring CSC anode wire is 2.54 mm, the width of the cathode is 1.13 mm with a gap of 1.72 mm between the two cathodes. Their mutual interval is 0.25 mm. By measuring the faradic charge of the adjacent cathode, and calculate the charge center by using charge interpolation method, CSC can determine the exact particle tracks positions up to an accuracy of 30 $\mu m$ [32].

- **RPC:**

  RPC is a gas detector with a typical spatial resolution of 1 cm and time resolution of 1 ns [33]. The module of RPC is composed with two parallel high resistance artificial gum board of 2mm. Its internal electric field is uniformly distributed, with a typical field of 4.9 kV/mm. Early ionizing electrons lead to the electron avalanche [34]. The typical induction charge of outer copper strips is 0.5 pC [35]. Their working gas is the mixture of $C_2H_2F_4$ and butane.

- **TGC:**

TGC detector is a special multi-wire chamber, similar to multi-wire proportional chamber. It have very small(1.4 mm) gap between its cathode plane and anode plane, therefore name of so Thin Gap Chamber (TGC).

Table 2.9 lists the main performance of MDT, CSC, RPC and TGC sub detectors.

| | | **Chamber resolution(RMS) in** | | | **Measurements/track** | |
|---|---|---|---|---|---|---|
| **Type** | **Function** | z/R | $\phi$ | time | barrel | end-cap |
| MDT | tracking | 35$\mu m(z)$ | - | - | 20 | 20 |
| CSC | tracking | 40$\mu m(R)$ | 5mm | 7ns | - | 4 |
| RPC | trigger | 10$mm(z)$ | 10mm | 1.5ns | 6 | - |
| TGC | trigger | 2-6$mm(R)$ | 3-7mm | 4ns | - | 9 |

Table 2.9: Parameters of the four sub-systems of the muon detector. The quoted spatial resolution (columns 3, 4) does not include chamber-alignment uncertainties. Column 5 lists the intrinsic time resolution of each chamber type, to which contributions from signal-propagation and electronics contributions need to be added. Numbers in brackets refer to the complete detector configuration as planned for 2009.

#### 2.2.3.4 Magnet system

ATLAS magnet system has one solenoid and three toroids. They are all superconducting magnets. The solenoid magnet field is two tesla, providing bending power for the Inner Detector. A barrel toroid of 0.5 tesla, provides bending power for the muon spectrometer barrel. Two end cap toroids of 1 tesla each, provide bending power for the muon spectrometer end cap. Figure 2.14 shows the real picture of ATLAS magnets system, and table 2.10 shows the main parameters for these magnets.

Since these magnet system are essential for measuring the momentum of charged particles and charge identification. It is important to have a detail knowledge of the magnetic field mapping. The modeling of ATLAS magnets and detecting system can provide a precise magnet fields mapping, which guaranties the high precision measurements.

#### 2.2.3.5 Trigger and DAQ

There are 40M collisions of proton-proton bunches crossing per second at LHC. Each collision has an average of about 23 inelastic reactions. Technically it is impossible to record all these information. But it is not necessary to record all of them since the events we are interested in are only a very small fraction of them. So, a trigger system is needed, to select the events of specific interest. The ATLAS trigger system has three levels of triggers. The first level(L1) is a hardware based trigger system while the second(L2) and third trigger(EF) are software based high level trigger. Each trigger is use the output of the upper trigger, with more accurate reconstructed information to trigger events. The following will introduce the triggers of each level.

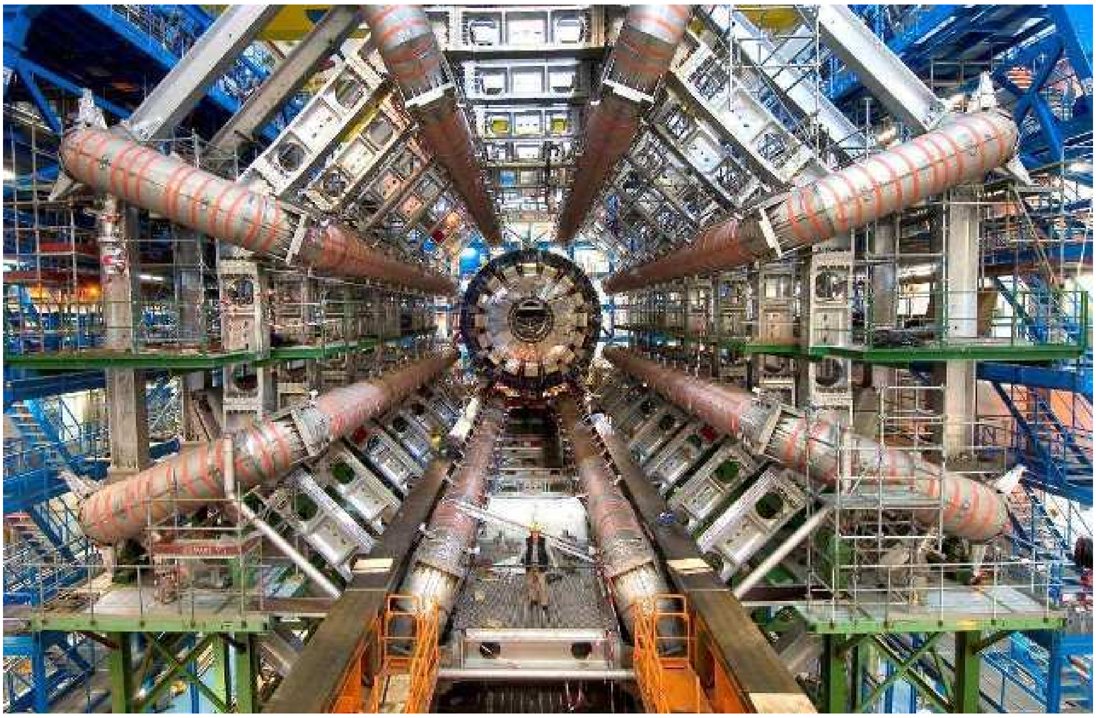

FIGURE 2.14: Picture of ATLAS Magnets system

- **Level one trigger(L1):**

  The L1 trigger is used for triggering high $p_T$ muons, electromagnetic calorimeter energetic clusters, jets and hadronic decay $\tau$ leptons, as well as high total transverse energy events and high missing transverse energy($E_T^{miss}$) events. It uses reduced-granularity information from a subset of detectors: the Resistive Plate Chambers (RPC) and Thin-Gap Chambers (TGC) for highpT muons, and all the calorimeter sub-systems for electromagnetic clusters, jets, $\tau$-leptons, $E_T^{miss}$ , and large total transverse energy. The maximum L1 accept rate which the detector readout systems can handle is 75 kHz (upgrade able to 100 kHz), and the L1 decision must reach the front-end electronics within 2.5 $\mu s$ after the bunch-crossing with which it is associated.

- **Level two(L2):**

  The L2 trigger is seeded by Regions-of-Interest (RoI′s). These are regions of the detector where the L1 trigger has identified possible trigger objects within the event. The L2 trigger uses RoI information on coordinates, energy, and type of signatures to limit the amount of data which must be transferred from the detector readout. The L2 trigger reduces the event rate to below 3.5 kHz, with an average event processing time of approximately 40 ms.

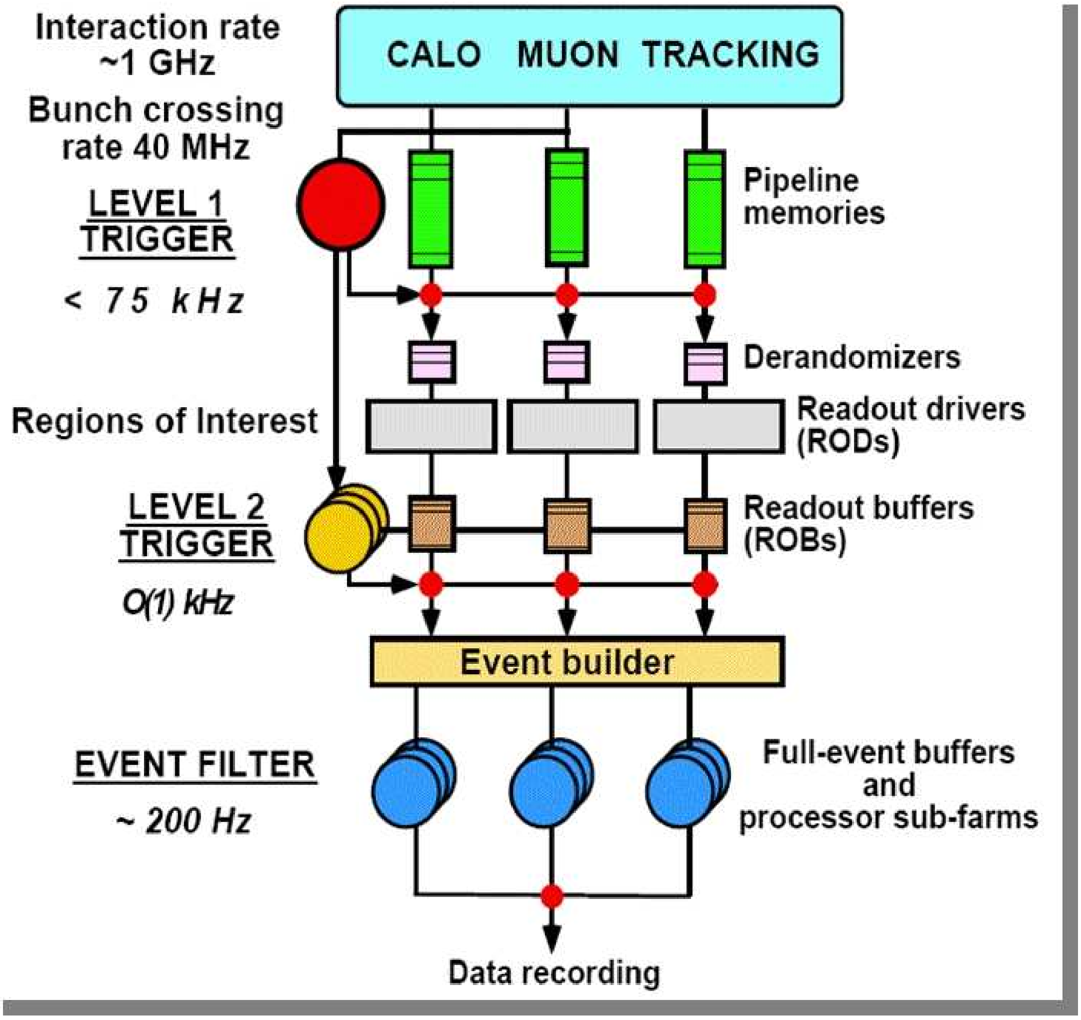

FIGURE 2.15: Schematic view of ATLAS trigger system

| **Property** | **Feature** | **Unit** | **Solenoid** | **Barrel toroid** | **Endcap toroid** |
|---|---|---|---|---|---|
| **Size** | Inner diameter | m | 2.46 | 9.4 | 1.65 |
| | Outer diameter | m | 2.56 | 20.1 | 10.7 |
| | Axial length | m | 5.8 | 25.3 | 5.0 |
| | Number of coils | | 1 | 8 | $2 \times 8$ |
| **Mass** | Conductor | t | 3.8 | 118 | $2 \times 20.5$ |
| | Cold mass | t | 5.4 | 370 | $2 \times 140$ |
| | Total assembly | t | 5.7 | 830 | $2 \times 239$ |
| **Coils** | Turns per coil | | 1154 | 120 | 116 |
| | Nominal current | kA | 7.73 | 20.5 | 20.5 |
| | Magnet stored energy | GJ | 0.04 | 1.08 | $2 \times 0.25$ |
| | Peak field in the windings | T | 2.6 | 3.9 | 4.1 |
| | Field range in the bore | T | 0.9-2.0 | 0.2-2.5 | 0.2-3.5 |
| **Conductor** | Overall size | $mm^2$ | 30 x 4.25 | 57 x 12 | 41 x 12 |
| | Ratio Al:Cu:NbTi | | 15.6:0.9:1 | 28:1.3:1 | 19:1.3:1 |
| | Number of strands(NbTi) | | 12 | 38-40 | 40 |
| | Strand diameter(NbTi) | mm | 1.22 | 1.3 | 1.3 |
| | Critical current(at 5T and 4.2k) | kA | 20.4 | 58 | 60 |
| | Operatingcritical-current ratio at 4.5K | % | 20 | 30 | 30 |
| | Residual resistivity ratio(RRR) for Al | | $> 500$ | $> 800$ | $> 800$ |
| | Temperature margin | K | 2.7 | 1.9 | 1.9 |
| | Number of units × length | m | 4 x 2290 | 8x4x1730 | 2x8x2x800 |
| | Total length(produced) | km | 10 | 56 | 2 x 13 |
| **Heat load** | At 4.5 K | W | 130 | 990 | 330 |
| | At 60-80 K | kW | 0.5 | 7.4 | 1.7 |
| | Liquid helium mass flow | g/s | 7 | 410 | 280 |

Table 2.10: The main parameters of ATLAS magnets

- **Event Filter(EF):**

  The event filter uses offline analysis procedures on fully-built events to further select events down to a rate which can be recorded for subsequent offline analysis. It reduces the event rate to approximately 200 Hz, with an average event processing time of the order of four seconds.

The L2 and EF trigger are called High Level Triggers (HLT). The HLT algorithms use the full granularity and precision of calorimeter and muon chamber data, as well as the data from the inner detector, to refine the trigger selections. Better information on energy deposition improves the threshold cuts, while track reconstruction in the inner detector significantly enhances the particle identification (for example distinguishing between electrons and photons). The event selection at both L1 and L2 primarily uses inclusive criteria, for example high-$E_T$ objects above defined thresholds.

The data acquisition system (DAQ) receives and buffers the event data from the detector specific readout electronics at the L1 trigger rate. The data transmission is performed over point to point Readout Links (ROL′s). It transmits any data to the L2 trigger requested by the trigger (typically the data corresponding to RoI′s) and, for those events fulfilling the L2 selection criteria, event-building is performed. The assembled events are then moved by the data acquisition system to the event filter, and the events selected there are moved to permanent event storage. These events that passed the trigger

| **Stream** | e | $\mu$ | Jet | $\gamma$ | $E_T^{miss}\&\tau$ | B-physics |
|---|---|---|---|---|---|---|
| e | $31 \pm 7.9$ | $0.0056 \pm 0.00058$ | $0.00053 \pm 6.2 * 10^{-5}$ | $1.2 \pm 0.4$ | $1.4 \pm 0.035$ | $(1.3 \pm 1.3) * 10^{-5}$ |
| $\mu$ | - | $34 \pm 8.7$ | $0.021 \pm 0.015$ | $0.0028 \pm 0.002$ | $0.22 \pm 0.022$ | $0.076 \pm 0.0043$ |
| Jet | - | - | $38 \pm 5.9$ | $0.48 \pm 0.4$ | $0.71 \pm 0.4$ | $0 \pm 0$ |
| $\gamma$ | - | - | - | $22 \pm 5.7$ | $0.22 \pm 0.073$ | $0 \pm 0$ |
| $E_T^{miss}\&\tau$ | - | - | - | - | $32 \pm 7.9$ | $15 \pm 6.4 * 10^{-6}$ |
| B-physics | - | - | - | - | - | $9.5 \pm 5.5$ |

TABLE 2.11: Overlap(Hz) between the data streams at a luminosity of $10^{33} cm^{-2} s^{-1}$

will be recorded according to the stream classification made by the event-filter processing task. The ATLAS-defined data streams are: electrons, muons, jets, photons, $E_T^{miss}$, $\tau$-leptons, and B-physics. The peak event rate of up to 400 Hz. Table 2.11 shows the event rates of each stream (diagonal elements) and their overlaps.

In addition to the data streams mentioned above, a subset of the events is also written to calibration streams and an express stream. The express stream is a subset of the events selected by the event filter and fulfil additional criteria which select the events as being useful for monitoring the quality of the data and the detector. The calibration stream provides the minimum amount of information needed for detector calibration, possibly at a rate higher than the data streams provide. These events will only contain a subset of the event data.

## 2.3 Data transportation, storage and analysis of ATLAS

The important data formats of ATLAS are listed and described as following [36]:

- **RAW data:**

  RAW data is the output of event filter(the last level of trigger). It is used for events reconstruction, and of size of about 1.6 MB per event. The output rates is about 200 Hz, with the format of byte-stream of detector direct output.

- **ESD data:**

  ESD(Event Summary Data) is the output of reconstruction. It records most of the information that we are interested in physics analysis except the calibration and reconstruction. The format of ESD storage is POOL ROOT of object-oriented representation, and about 500 kB per event.

- **AOD data:**

  AOD(Analysis Object Data) is a reduced event presentation from ESD. It include the physics objects and others physics information common in physics analysis, record in the object-oriented POOL ROOT files. The event size of AOD is about 100 kB per event.

- **TAG data:**

  TAG data are the metadata at event level. It records very few information which could be identify and select events of interesting at a very high efficiency. TAG data are stored in relation database, which makes it is very easy to access. It allow to navigate back to AOD, ESD or even RAW data. The average size of TAG is about 1 kB per event.

- **DPD data:**

  DPD(Derived Physics Data) is a representation of events based on ntuple. It is used for end-user analysis and histogramming.

- **SIM data:**

  SIM(Simulated Event Data) are the data from Menta Carlo generation(e.g. Pythia) to the simulation of interactions with detector and detector response(Digitization). It is even include pile-up, cavern background. All the events at different stages could be stored to the format of POOL ROOT. The events after digitization could be save a byte-stream, and include trigger information. All these SIM events have "truth" information stored, which make them bigger that real data. it is about 2 MB per event.

The storage and analysis of ATLAS data is very much Grid based. It could be separated into several layers by their functions:

- **Tier-0:**

  The computation equipments at Tire-0 of CERN are used to store and transform RAW data of event filter outputs. It provides calibration stream and express stream reconstruction. Then, reconstruct and distribute the output of first round reconstruction outputs of ESD, AOD, TAG to Tier-1s facilities described below. More automated calibration tasks will also be run by the Tier-0.

- **Tier-1:**

There are about 10 Tier-1s all over the world servers for ATLAS. They will keep part of the RAW data for long term access. Meanwhile, they also proved the capacity of reprocessing the RAW data. Tile-1s mainly provide world wide access of ESD, AOD and TAG.

- **Tier-2:**

  Tier-2 will provide the computation resources for calibration constants, MC simulation and physics analysis. They usually keep one third of the AOD and whole set of TAG samples, as well as subsets of DPD. Meanwhile, they perform almost all ATLAS simulation tasks, and transport the output back to Tier-1. They also may store some RAW and ESD data for code development.

- **Tier-3:**

  Tire-3s are used to store user ntuples and analysis work allowed to work off grid. These Tire-3s may be of only numbers of desktop or cluster, with the function of access grid, submit grid jobs and retrieve the output of grid jobs.

The resources needed for physics analysis will be distributed on ATLAS servers world wide. The priorities giving by the fair share, and determine whether this jobs will be executed and when. In principle, users could access all the computation and storage resources of ATLAS sites if they follow certain security and priority rules. Due to the limitation of the resources that one user working at, they need a distributed analysis tool to do the distribution analysis, which will submit jobs to the sites which have the required resources and execute there. The MC sample used in this analysis are using distributed analysis tool, generated on grid. Figure 2.16 shows the network from ATLAS data taking to user analysis.

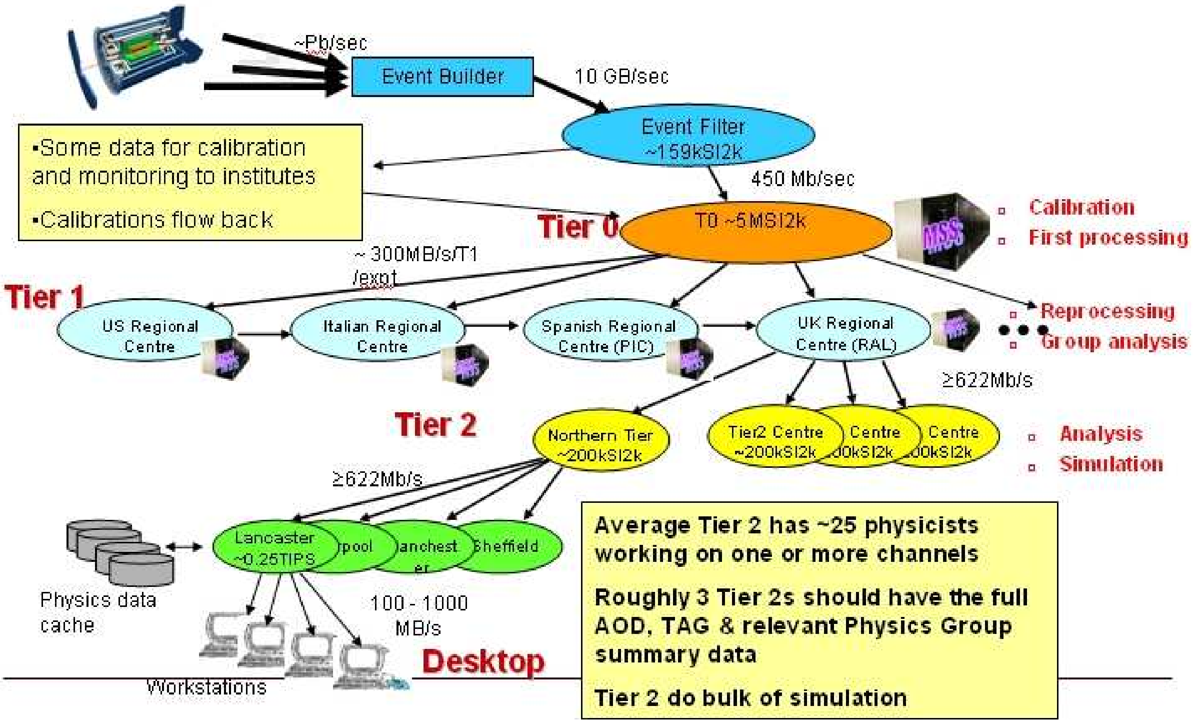

FIGURE 2.16: From RAW data to Analysis

# Chapter 3

# Analysis of $t\bar{t}H(H \rightarrow WW^{(*)})$ production channel

## Contents

## 3.1 Introduction

The Yukawa coupling is an important property of Higgs. Its measure will give information on fermion mass origin. Yukawa coupling measurement will become important once the Higgs is discovered at LHC. $t\bar{t}H, H \to WW^{(*)}$ is a good channel to measure the top quark Yukawa coupling at the intermediate Higgs mass range given in table 1.3. Its main production feynman diagrams are shown in fig 3.1. The $t\bar{t}$ production cross section decreases as the Higgs mass increases while the branching ratio of $H \to WW^{(*)}$ increases then decrease as shown in table 3.1. However, this channel suffers a lot from several type of backgrounds. Compared to $t\bar{t}$ and $QCD$ processes, $t\bar{t}H(H \to WW^{(*)})$ Next to Leading Order($NLO$) calculation have a cross section of 291 $fb$ at the most favorable mass point of 160 GeV(table 3.2), which is only $10^{-3}$ of the $t\bar{t}$, or $10^{-4}$ to $10^{-5}$ of $QCD$ jets(shown in table 3.2 and table 3.1). Besides that, initial states radiations(ISR) and final states radiations(FSR) will generate extra jets in such a TeV scale high energy, almost identical to these from quarks. It is difficult to suppress $t\bar{t}$ by only looking at the different jet multiplicity. So, the lepton multiplicity becomes the dominate rejection criteria for $t\bar{t}$. At high transverse energy, jets especially jets from b-quark decays, have a certain probability contain leptons. If these leptons have been reconstructed, $t\bar{t}$ will containment $t\bar{t}H(H \to WW^{(*)})$ signal because of the large cross sections. So, the discrimination of leptons from jets(un-isolated leptons) and leptons from $W/Z$ decays(isolated leptons) is the key point to suppress $t\bar{t}$ background in $t\bar{t}H(H \to WW^{(*)})$ analysis. Moreover, $QCD$ jets process can be suppressed to an appropriate level by requiring well isolated leptons.

TABLE 3.1: $t\bar{t}H$ production cross sections(LO and NLO) and $H \to WW^{(*)}$ branching ratios at different Higgs masses [17].

| $m_H$ [GeV] | 120 | 130 | 140 | 150 | 160 | 170 | 180 | 190 | 200 |
|---|---|---|---|---|---|---|---|---|---|
| $\sigma_{t\bar{t}H}$ LO [fb] | 537 | 428 | 345 | 282 | 232 | 193 | 162 | 137 | 117 |
| $\sigma_{t\bar{t}H}$ NLO [fb] | 669 | 534 | 431 | 352 | 291 | 243 | 204 | 174 | 149 |
| $BR_{H\to WW^{(*)}}$ | .1331 | .2888 | .4854 | .6831 | .9015 | .9654 | .9346 | .7761 | .7347 |

The $t \to Wb$ branching ratio is almost 100%, and $W$ decays leptonically or hadronically. The topology of $t\bar{t}H, H \to WW^{(*)}$ are shown in figure 3.3. In this thesis, we

Table 3.2: main background production cross sections

| process | Z+jets | $t\bar{t}$ | $t\bar{t}W + jets$ | $t\bar{t}Z$ |
|---|---|---|---|---|
| $\sigma$[fb] | 52,700,000 | 833,000 | 582 | 1188 |

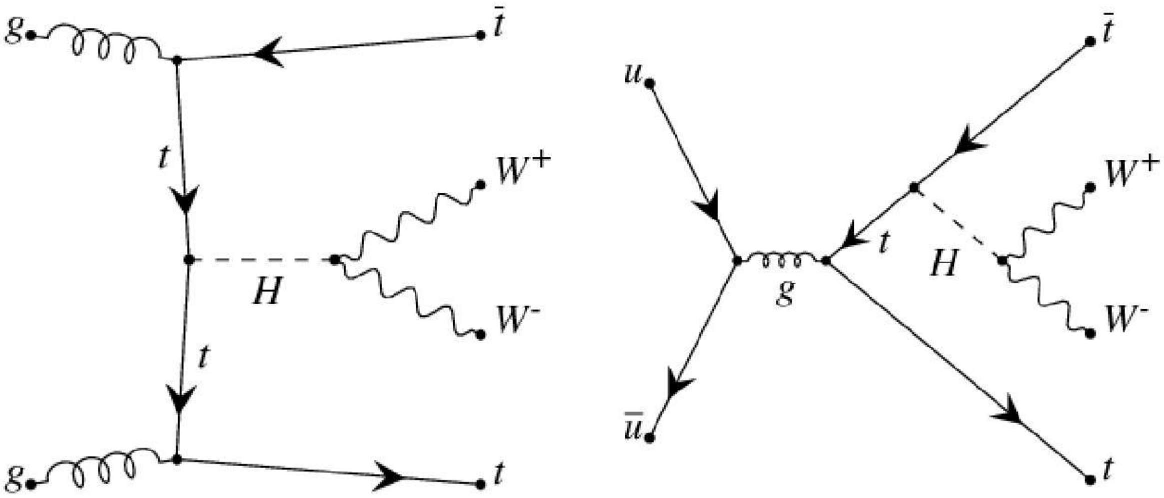

Figure 3.1: Feynman diagrams for the main LO contributions to $ttH, H \to WW^{(*)}$ production.

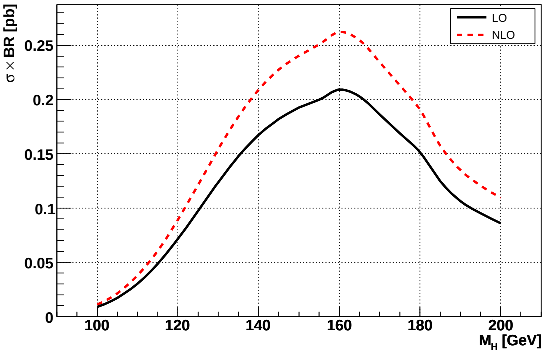

Figure 3.2: Dependence of $\sigma \times BR$ for the channel $t\bar{t}H, H \to WW$ on the Higgs boson mass.

denote $t\bar{t}H(H \rightarrow WW^{(*)})$ by the different leptons number in the final states, ttHWW1L to ttHWW4L for the final states containing one to four leptonic decay W(s). Here, lepton refers to electron and muon, and do not include $\tau$ since $\tau$ lepton decays hadronically or leptonically, and reconstruction performance is different from electron and muon.

Since ttHWW1L is suffering from a huge $t\bar{t}$ background and ttHWW4L is only $\sim 3\%$ of total ttHWW cross section, which is too low to be considered at the first few years of low luminosity data, we only study ttHWW2L and ttHWW3L here. Table 3.1 lists the cross section of ttH and branching ratio of $H \rightarrow WW^{(*)}$ as a function of Higgs mass. Figure 3.2 shows ttH*Br($H \rightarrow WW$) Leading Order(LO) and Next to Leading Order(NLO) cross section as a function of Higgs mass. It reaches a maximum around 160GeV for the $t\bar{t}H, H \rightarrow WW$ combined cross section.

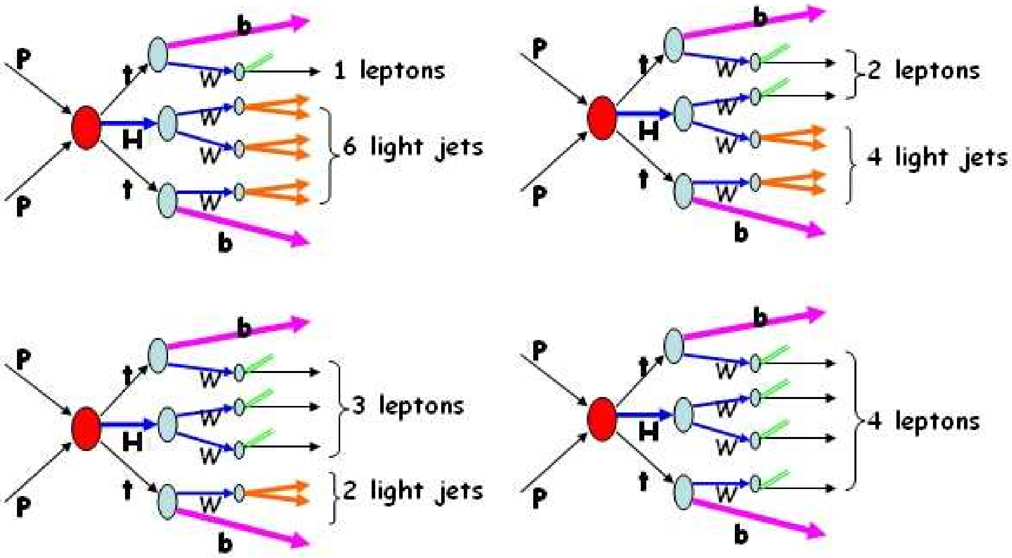

FIGURE 3.3: $t\bar{t}H, H \rightarrow WW$ topology of different final states, here p refers to proton, t refers to top quark, H refers to Higgs, W refers to W boson, b refers to b jets, the double line with no label refers to neutrino

The studies of $t\bar{t}H, H \rightarrow WW^{(*)}$ are based on Computing System Commissioning(CSC) MC full simulation data. The main goal of CSC is to test the computing and software infrastructure, develop Event Data Model(EDM), and get them ready for data taking. CSC data are widely used in many physics studies. These studies will be assembled in a TDR-like CSC book. $t\bar{t}H, H \rightarrow WW^{(*)}$ study is one of these studies, performed within the ATLAS Higgs Working Group.

The contents of this chapter are: First, an introdution of the Monte Carlo sample from the settings of the generators to the simulation for all signals and backgrounds. Then a study of the trigger effects is given with emphasis on the ATLAS physics objects spectra. Following that are the events selection and objects identification, with some dedicated lepton isolation studies. These steps are common and essential in both two leptons and three leptons final states of $t\bar{t}H, H \rightarrow WW^{(*)}$ analysis. Then, the complete analysis of ttHWW2L and ttHWW3L are presented. Detailed pileup impact and systematic uncertainties are presented in sequence after that. Finally, the results of the top quark Yukawa coupling measurement and conclusions are given.

## 3.2 Generation of Monte Carlo Sample

### 3.2.1 Signal Generation

Signal Monte Carlo samples were produced with the $W$-boson decays forced to generate the desired lepton signatures. Samples for $t\bar{t}H \rightarrow 2b4j2l2\nu$ and $t\bar{t}H \rightarrow 2b2j3l3\nu$ were generated for different Higgs boson masses between 120 and 200 GeV in Leading Order, using the pythia 6.4 [37] [38] generator. The different signature of same charge were forced by turning on $W^+ \rightarrow l^+\nu, W^- \rightarrow q\bar{q}$ or $W^- \rightarrow l^-\nu, W^+ \rightarrow q\bar{q}$, and three leptons final state samples were generated by an event decay model selector. In three leptons final state, there are two kinds of topologies that can lead to the same signature: in the first case one of the $W$-bosons from the Higgs boson decays hadronically, and the other three $W$-bosons decay leptonically, while in the second case the hadronically decaying $W$-boson originates from one of the two top quarks. Both topologies were generated and considered together. Results obtained with these samples were scaled to the NLO cross sections and branching ratios that are given in [39]. The characteristics of the samples were generated for Higgs boson masses between 120 and 200 GeV are summarized in Table 3.3.

Table 3.3: Signal samples generated for the $t\bar{t}H, H \rightarrow WW$ analysis. The ID refers to the ATLAS MC generation management global ID

| process | generator | $\sigma * BR$ | $N_{events}$ | $\epsilon_{filter}$ | $\int \mathcal{L}dt_{[fb^{-1}]}$ | ID |
|---|---|---|---|---|---|---|
| $t\bar{t}H \rightarrow 2b4j2l2\nu, m_H$=120 GeV | pythia 6.4 | 3.9 fb | 19k | 0.929 | 5581 | 6549, 6550 |
| $t\bar{t}H \rightarrow 2b4j2l2\nu, m_H$=130 GeV | pythia 6.4 | 6.7 fb | 15k | 0.937 | 2483 | 9039, 9040 |
| $t\bar{t}H \rightarrow 2b4j2l2\nu, m_H$=140 GeV | pythia 6.4 | 9.1 fb | 7k | 0.940 | 880 | 9041, 9042 |
| $t\bar{t}H \rightarrow 2b4j2l2\nu, m_H$=150 GeV | pythia 6.4 | 10.3 fb | 17k | 0.940 | 1851 | 9043, 9044 |
| $t\bar{t}H \rightarrow 2b4j2l2\nu, m_H$=160 GeV | pythia 6.4 | 11.1 fb | 18k | 0.945 | 1715 | 6385, 6386 |
| $t\bar{t}H \rightarrow 2b4j2l2\nu, m_H$=170 GeV | pythia 6.4 | 9.9 fb | 10k | 0.940 | 1049 | 9045, 9046 |
| $t\bar{t}H \rightarrow 2b4j2l2\nu, m_H$=180 GeV | pythia 6.4 | 8.0 fb | 10k | 0.948 | 1397 | 9047, 9048 |
| $t\bar{t}H \rightarrow 2b4j2l2\nu, m_H$=190 GeV | pythia 6.4 | 5.8 fb | 5k | 0.948 | 845 | 9049, 9050 |
| $t\bar{t}H \rightarrow 2b4j2l2\nu, m_H$=200 GeV | pythia 6.4 | 4.7 fb | 19k | 0.949 | 4473 | 6555, 6556 |
| $t\bar{t}H \rightarrow 2b2j3l3\nu, m_H$=120 GeV | pythia 6.4 | 2.5 fb | 36k | 1 | 15465 | 6551 - 6554 |
| $t\bar{t}H \rightarrow 2b2j3l3\nu, m_H$=130 GeV | pythia 6.4 | 4.3 fb | 33k | 1 | 8148 | 9015 - 9018 |
| $t\bar{t}H \rightarrow 2b2j3l3\nu, m_H$=140 GeV | pythia 6.4 | 5.8 fb | 20k | 1 | 3681 | 9019 - 9022 |
| $t\bar{t}H \rightarrow 2b2j3l3\nu, m_H$=150 GeV | pythia 6.4 | 6.6 fb | 26k | 1 | 4095 | 9023 - 9026 |
| $t\bar{t}H \rightarrow 2b2j3l3\nu, m_H$=160 GeV | pythia 6.4 | 7.1 fb | 17k | 1 | 2462 | 5344 - 5347 |
| $t\bar{t}H \rightarrow 2b2j3l3\nu, m_H$=170 GeV | pythia 6.4 | 6.3 fb | 28k | 1 | 4586 | 9027 - 9030 |
| $t\bar{t}H \rightarrow 2b2j3l3\nu, m_H$=180 GeV | pythia 6.4 | 5.2 fb | 30k | 1 | 5937 | 9031 - 9034 |
| $t\bar{t}H \rightarrow 2b2j3l3\nu, m_H$=190 GeV | pythia 6.4 | 3.8 fb | 21k | 1 | 5983 | 9035 - 9038 |
| $t\bar{t}H \rightarrow 2b2j3l3\nu, m_H$=200 GeV | pythia 6.4 | 3.1 fb | 30k | 1 | 10393 | 6557 - 6560 |

### 3.2.2 Generation of Background Samples

The main backgrounds for the studied $t\bar{t}H$ final states are $t\bar{t}$, $t\bar{t}W$, $t\bar{t}Z$, $t\bar{t}t\bar{t}$ and $t\bar{t}b\bar{b}$. Single top backgrounds are negligible. Also QCD jets and WZ+X processes could be sources of backgrounds. However, lepton identification and isolation requirements and high jets multiplicity requirements are expected to reject a large fraction of these. The QCD background is considered to be under control and will not be further discussed here.

Two different MC@NLO [40] $t\bar{t}$ samples were used for this analysis. The generated cross sections of both samples are normalized to the value of $\sigma_{t\bar{t}}^{NLO+NLL} = 833$ pb [5]. The standard MC@NLO sample forced with at least one leptonic $W$-decay (electron or muon or tau),does not contain sufficient events for a reliable estimation of the $t\bar{t}$ background contribution accepted by the complete event selection. Therefore, the second MC@NLO sample is filtered at generator level with a pair of same-sign leptons (electrons or muons), which satisfy $p_T > 13$ GeV and $|\eta| < 2.6$(and a historical crack of when there are three or more generated leptons, events with oppositely charged leptons from $W$ bosons falling into a special domain ( $p_T \geq 30GeV$ and $||\eta| - 1.5| \leq 0.2$ for electron, $p_T \geq 15GeV$ and $||\eta| - 1.25| \leq 0.2$ for muon ) were rejected.), which results in a filter efficiency of 0.0384. This filter provides a huge increase in statistics, at the cost of introducing a bias, as effects like lepton fakes or charge flips cannot be correctly described by this sample and there is an additional internal kinematic cut on the leptons in the filter code. For the $t\bar{t}H$ (2L) analysis, another $(15 \pm 10)\%$ were added to compensate this loss. This number was obtained by comparing the filtered and standard sample at the level of the requirement of exactly two well isolated same-sign leptons in the cut flow described in section 3.6. For the $t\bar{t}H$ (3L) analysis the loss was estimated to be 135%, with a large statistical uncertainty due to the small number of filtered Monte Carlo events surviving the event selection. Hence it is considered too large and not known precisely enough, to ensure a reliable estimation of the $t\bar{t}$ expectation from this sample. The standard sample was therefore used for the analysis of this final state.

Since $t\bar{t}W + 2jets$ is expected to be the dominant irreducible background(have two isolated same-sign lepton and 6 jets), dedicated $t\bar{t}W$ samples were produced with ALPGEN [41]. Samples of $t\bar{t}W$ + 0 parton, $t\bar{t}W$ + 1 parton, and $t\bar{t}W$ + 2 or more partons were produced separately. The minimum $p_T$ for the additional jets was set to 15 GeV, while the maximum $|\eta|$ was set to 6.0. In addition, the generated jets were required to be separated by at least 0.4 cone radius. MLM matching [41] was performed to avoid double counting of additional jets, and a multi-lepton filter was applied. In order to be consistent with the results obtained for the signal, the LO cross section for this process was scaled to NLO. Since no NLO calculations are available, a K-factor of 1.2 was assumed to ensure a conservative estimation of the background contribution.

The leading order generator ACERMC [42] was used to produce samples for $t\bar{t}Z$, $t\bar{t}t\bar{t}$, $t\bar{t}b\bar{b}$ and $t\bar{t}b\bar{b}$(EW), which contains the electroweak contribution to $t\bar{t}b\bar{b}$. Again, the LO cross sections were scaled by K-factors of 1.2, except for the $t\bar{t}b\bar{b}$ sample from EW production. In order to avoid double counting, $t\bar{t}t\bar{t}$ events found in the MC@NLO $t\bar{t}$ data sets were excluded from the analysis. The $t\bar{t}b\bar{b}$ samples were analyzed as a cross check and were not taken into account for the calculation of total background expectations.

Table 3.4 summarizes the characteristics of all background samples relevant for the $t\bar{t}H$ analyzes.

TABLE 3.4: List of the samples used to estimate the background contribution to the $t\bar{t}H, H \rightarrow WW$ analyzes. Numbers marked with a * denote numbers after MC@NLO re-weighting ($N_-/N_+ = 1/6.5$ for the no all-hadronic and $N_-/N_+ = 1/6.7$ for the pre-filtered $t\bar{t}$ samples). Note that $\sigma \times BR$ in the fourth row refers to the branching ratio of the decays that were forced by the generator or filtered on generator level. The ID refers to the ATLAS MC generation management global ID.

| Process | Generator | $\sigma_{tot}$ [fb] | $\sigma \times BR$ | $N_{events}$ | $\epsilon_{filter}$ | $K_{factor}$ |
|---|---|---|---|---|---|---|
| $t\bar{t}$ no all-hadronic | MC@NLO | 833000 | 450000 fb | 440k* | 1 | - |
| $t\bar{t}$ pre-filtered | MC@NLO | 833000 | 833000 fb | 350k* | 0.0384 | - |
| $t\bar{t}b\bar{b}$(EW)→ $l\nu jj4b$,($l = e, \mu$) | ACERMC 3.3 | 900 | 259 fb | 25k | 0.943 | 1.0 |
| $t\bar{t}b\bar{b} \rightarrow l\nu jj4b$,($l = e, \mu$) | ACERMC 3.3 | 8200 | 2360 fb | 50k | 0.951 | 1.2 |
| $t\bar{t}W$ + 0 partons | ALPGEN | 189 | 61.1 fb | 20k | 0.414 | 1.2 |
| $t\bar{t}W$ + 1 partons | ALPGEN | 156 | 50.5 fb | 20k | 0.410 | 1.2 |
| $t\bar{t}W$ + $\geq$ 2 partons | ALPGEN | 237 | 76.9 fb | 20k | 0.442 | 1.2 |
| $t\bar{t}Z, Z \rightarrow ll$, ($l = e, \mu, \tau$) | ACERMC 3.4 | 1188 | 120 fb | 20k | 0.790 | 1.2 |
| $gg \rightarrow t\bar{t}t\bar{t}$ | ACERMC 3.4 | 2.2 | 2.2 fb | 25k | 0.655 | 1.2 |
| $qq \rightarrow t\bar{t}t\bar{t}$ | ACERMC 3.4 | 0.48 | 0.48 fb | 10k | 0.651 | 1.2 |

### 3.2.3 Monte Carlo simulation and reconstruction

After generation of a particular channel, events are passed to ATLAS detector Geant 4(G4) simulation, with a real detector geometry of misalignment and distortion, including the simulation of trigger and pileup. The output files of simulation are called sim files. Then, these sim files are sent to digitalization and reconstruction. Finally, Analysis Objects Data(AOD) are obtained, ready for individual analysis. The pile up events are included at digitalization level by superposing minimum bias events, and simulated cavern background [36].

The current status of *CSC* simulation has good description and simulation of the three levels of trigger, and provides us a set of trigger menus, such as the hardware first level trigger L1_EMXX, L1_MUXX, L1_XETXX, the corresponding second level trigger L2_XXXX and the software third level trigger $EF\_XXX$. The last two digits are the $p_T$ threshold the trigger(the internal $p_T$ threshold to insure the trigger $p_T$ threshold is lower than trigger $p_T$ threshold, depends on the accuracy of $p_T$ reconstruction at different trigger levels). The $p_T$ definitions at different trigger levels are different. Level one $p_T$ is hardware sum, with very fast speed, but less accurate. Level two and level three trigger $p_T$ is reconstructed with fast reconstruction algorithm, of different optimizations, and gives more accurate information on the objects ID as well as isolation information. The reconstruction speed is decreased for these three trigger levels, while the accuracy of the information used in trigger menus is increased.

Full simulation and reconstruction need huge CPU time and storage, typically, 8 minutes for one event per CPU, and 1.0M storage needed for one event of reconstructed

AOD, with an even larger size of pileup event are included. So, in order to generate and store these MC events, all generation samples are validated, then, sent to CERN center production system managers, and submitted to LHC Computing Grid. Tens of thousands CPUs and storage resources are available on Grid. These resources deal with the MC simulation and store the outputs. The center production system guaranties the quality of these simulation. The outputs are so called "official" MC sample.

## 3.3 Trigger study

At *LHC*, with a collision frequency of 40MHz and hardware, software and technical limitations, it is impossible to record every events. Most of these events are proton-proton elastic or inelastic scattering, The trigger is then aim to select these interesting events.

In $ttH, H \to WW$ analysis, all final states contain well isolated leptons and hence can be triggered by demanding either one isolated high-$p_T$ lepton or two isolated leptons of lower $p_T$. Currently, the two lepton trigger menu is not fully implemented in the trigger simulation, therefore this study concentrates on the single high-$p_T$ lepton triggers.

The single-electron triggers studied for the $t\bar{t}H, H \to WW$ final states are the Level 1 trigger L1_EM25I, the Level 2 trigger L2_e25i and EF_e25i at the Event Filter level [43], which require one isolated electron candidate above a threshold of $p_T = 25$ GeV. In case of the muons L1_MU20, L1_MU40, L2_mu20i and EF_mu20i [44] are considered, which trigger isolated muon candidates with transverse momenta above 20 GeV. Table 3.5 summarized all the trigger menu and its criteria used in this analysis.

Figure 3.4 shows the linearity and uniformity of trigger efficiency for electron and muon, at three different trigger levels. Tables 3.6 and 3.7 list the resulting event level trigger efficiencies for the $t\bar{t}H$ (2L) and $t\bar{t}H$ (3L) signals and for the most relevant backgrounds before and after the event selection criteria being applied. The **absolute efficiency** $\epsilon_{abs}$ is given by the fraction of all events passing the electron or muon trigger, while the **off-line efficiency** $\epsilon_{off}$ is defined by the ratio of events at a given cut that in addition pass the lepton trigger requirements over the total number of events at the same cut level.

As shown, the requirement of the high-$p_T$ lepton trigger causes only a small loss in the event rates accepted by the off-line selection for both final states. and the impact on the lepton $p_T, \eta, \phi$ spectra is smooth.

TABLE 3.5: Trigger menu and its criteria

| Trigger menu | criteria |
|---|---|
| L1_EM25 | $p_T > 25GeV$, electron or gamma candidates |
| L2_e25i | $p_T > 25GeV$, isolated, electron candidates |
| EF_e25i | $p_T > 25GeV$, isolated, electron candidates |
| L1_MU20+L1_MU40 | $p_T > 20GeV$, muon candidates |
| L2_mu20i | $p_T > 20GeV$, isolated, muon candidates |
| EF_mu20i | $p_T > 20GeV$, isolated, muon candidates |

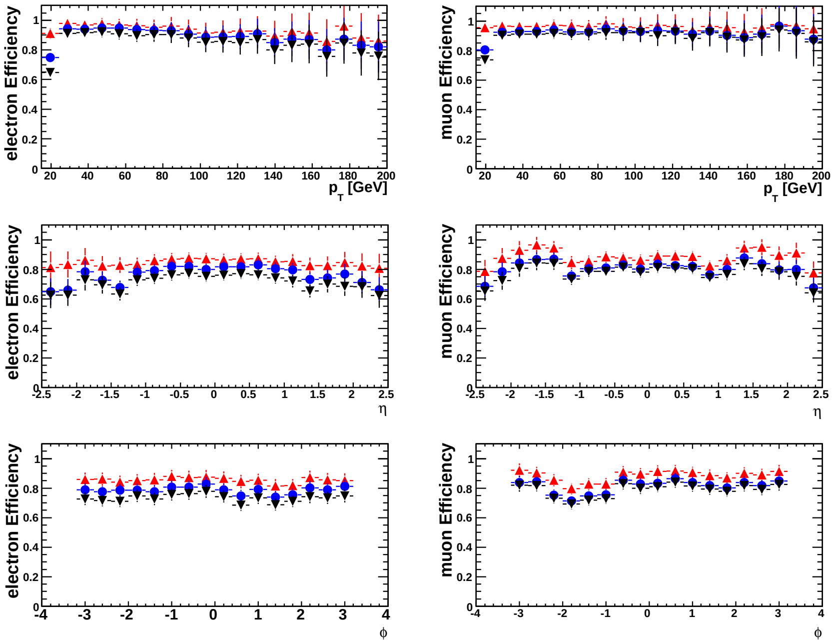

FIGURE 3.4: Electron and muon trigger efficiencies at the three trigger levels as functions of $p_T$, $\eta$ and $\phi$. The plots on the left show the trigger efficiency for electrons above $p_T^{thres.} = 25GeV$, on the right, the corresponding efficiencies for muons above $p_T^{thres.} = 20GeV$ are shown. The upward triangles denote the L1 trigger efficiency, while the circles mark the efficiencies at the L2- and black triangles at the EF stage.

TABLE 3.6: Absolute trigger efficiencies $\epsilon_{abs}$ at the event level for the studied $t\bar{t}H$ final states and the most relevant backgrounds.

| | $t\bar{t}H$ (2L) | $t\bar{t}H$ (3L) | $t\bar{t}$ | $t\bar{t}W$+2j | $t\bar{t}Z$ |
|---|---|---|---|---|---|
| L1 | (93.2±0.3)% | (97.7±0.2)% | (66.2±0.1)% | (91.4±0.3)% | (92.8±0.3)% |
| L2 | (86.2±0.4)% | (94.2±0.3)% | (51.6±0.1)% | (81.5±0.4)% | (85.4±0.4)% |
| EF | (81.7±0.4)% | (91.3±0.3)% | (46.6±0.1)% | (76.4±0.4)% | (81.1±0.4)% |

TABLE 3.7: Event level EF trigger efficiencies $\epsilon_{off}$ after the offline event selection described as following. The efficiency for $t\bar{t}$ is given at the level of the first subset of cuts ("basic selection") because of lack of statistics.

| | $t\bar{t}H$ (2L) | $t\bar{t}H$ (3L) | $t\bar{t}$ | $t\bar{t}W$+2j | $t\bar{t}Z$ |
|---|---|---|---|---|---|
| 2L selection[%] | (95.6±0.5) | $(98.0^{+0.6}_{-1.0})$ | (81.4±0.6) | (96.4±1.0) | $(94.8^{+0.1.4}_{-2.4})$ |
| 3L selection[%] | $(100^{+0}_{-33})$ | (99.1±0.3) | (88.3±0.7) | $(98.5^{+0.7}_{-1.9})$ | $(99.5^{+0.3}_{-1.2})$ |

## 3.4 Electron, Muon, Jet Definition and Identification

In this section, The electron, muon and jets identification algorithm are described in first part and the selection criteria used in this analysis are described in second part.

### 3.4.1 Common Electron, Muon, Jet identification at ATLAS

A brief description of ATLAS electron, muon, jet identification algorithm are as following:

#### 3.4.1.1 Electron ID

At present, two algorithms have been implemented in the ATLAS off-line reconstruction software, both integrated into one single package and a common event data model.

- The standard one, calorimetry based, starts from the cluster reconstructed in the calorimeters and then builds the identification variables based on information from the inner detector and calorimeter.

  Electrons with high transverse momentum are likely to deposit the majority of their energy in the electromagnetic (EM) calorimeter; and given the busy tracking environment expected in physics events, the reconstruction and identification of hard electrons are seeded by calorimeter based measurements.

  In the standard reconstruction of electrons and photons, a seed is taken from the electromagnetic calorimeter and a matching track is searched for among all reconstructed tracks. Additionally, the candidate is flagged if it matches to an early conversion reconstructed in the Inner Detector. Electron and photon candidates are then separated by requiring electrons to have an associated track and not having been identified as a conversion. The cluster and the track are required to lie within a broad $\Delta\eta \times \Delta\phi$ window of $0.025 \times 0.05$ (tracks are extrapolated to the calorimeter) and the ratio of the energy of the cluster to the momentum of the track to be lower than 10. These requirements define an electron candidate. Approximately 93% of true electrons are selected as electron candidates. The loss comes from a poor reconstruction of the track. This should be improved in the near future, thanks to back-tracking techniques. Clusters that do not fit these requirements are defined as photon candidates.

  After separating electron from photon clusters, several criterias can be defined based on shower shapes, track and TRT information as well as combined variables in order to discriminate jets and background electrons from signal. A variable so called isEM is defined for each electron candidates based on those criteria for electron candidates.

- A track seeded algorithm, optimized for electron with low transverse energy range between 8-30 GeV, starts by selecting good quality tracks which provide a seed.

| | | |
|---|---|---|
| Loose cuts | | |
| `ClusterEtaRange` | | Acceptance of the detector : $\|\eta\| < 2.47$ |
| `ClusterHadronicLeakage` | | The ratio of $E_T$ in the first sampling of the hadronic calorimeter to the $E_T$ of the EM cluster |
| `ClusterMiddleEnergy` | Second sampling | The energy deposit |
| `ClusterMiddleEratio37` | | Ratio of cell energies of $3 \times 7$ to $7 \times 7$ |
| `ClusterMiddleWidth` | | The lateral width of the shower |
| Medium cuts (includes loose cuts) | | |
| `ClusterStripsDeltaEmax2` | First sampling | The second maximal deposit |
| `ClusterStripsDeltaE` | | The difference between the second maximal and the minimal deposit |
| `ClusterStripsWtot` | | The total shower width |
| `ClusterStripsFracm` | | The energy outside core of the shower |
| `ClusterStripsWeta1c` | | The width in $\eta$ |
| `TrackPixel` | Track quality | The number of hits in the pixel layer (>0) |
| `TrackSi` | | The number of hits in the pixel and SCT (>8) |
| `TrackA0` | | The transverse impact parameter (<0.1 cm) |
| Tight cuts (includes medium cuts) | | |
| `ClusterIsolation` | Isolation | The ratio of transverse energy in a cone to the total transverse energy of the cluster |
| `TrackBlayer` | B-layer | The number of hits in the B-layer (>0) |
| `TrackMatchEta` | Track matching | $\Delta\eta$ between the cluster and the track ($< 0.005$) |
| `TrackMatchPhi` | | $\Delta\phi$ between the cluster and the track ($< 0.02$) |
| `TrackMatchEoverP` | | The ratio of the energy of the cluster to the momentum of the matched track () |
| `TrackTRThits` | TRT | The number of hits in the TRT |
| `TrackTRTratio` | | The ratio of the number of high threshold hits to the number of hits in the TRT |
| Tight No Isolation cuts (includes tight cuts without `ClusterIsolation`) | | |
| `TrackTRTratio90` | TRT | Replaces the previous cut with tighter values |

TABLE 3.8: Summary of identification cuts. Cut values are given only when they are independant of $\eta$ and $p_T$ . The names of the first colum are common name used in the ATLAS software

#### 3.4.1.2 Muon ID

ATLAS employs a variety of strategies for identifying and reconstructing muons. The direct approach is to reconstruct standalone muons by finding tracks in the muon spectrometer and then extrapolating these to the beam line. Combined muons are found by matching standalone muons to nearby inner detector tracks and then combining the measurements from the two systems. Spectrometer tagging algorithms start from inner detector tracks and extrapolate those to the spectrometer detectors and search for nearby hits. Calorimeter tagging algorithms are also being developed to tag inner detector tracks using the presence of a minimum ionizing signal in calorimeter cells.

Multiple independent algorithms have been developed to implement each of these strategies and the current ATLAS baseline reconstruction includes two algorithms for each strategy. Here we briefly describe the algorithms that are included in this reconstruction.

The algorithms are grouped into families such that each family includes one algorithm for each strategy. The event data intended for use in physics analysis includes two collections of muons, one for each family. The containers (and families) are named after the corresponding combined algorithms: Staco and Muid. The former has been declared the default for physics analysis but future analyses may make use of the other container or make use of muons from both.

Both of the muon combination algorithms, Staco and Muid, pair muon-spectrometer tracks with inner detector tracks to identify combined muons. The match chi-square, defined as the difference between outer and inner track vectors weighted by their combined error matrix:

$$c^2_{match} = (T_{MS} - T_{ID})(C_{ID} + C_{MS})^{-1}(T_{MS} - T_{ID}) \tag{3.1}$$

provides an important measure of the quality of this match and is used to decide which pairs are retained. Here T denotes a track vector and C its error matrix. Staco does a statistical combination of the of the inner and outer track vectors to obtain the combined track vector:

$$T = (C_{ID}^{-1} + C_{MS}^{-1})^{-1}(C_{ID}^{-1}T_{ID} + C_{MS}^{-1}T_{MS}) \tag{3.2}$$

Muid fits the combined track, at present starting from the inner track fit and adding the points from the muon-spectrometer track.

#### 3.4.1.3 Jets ID

A jet algorithm or jet finding procedure or jet clustering procedure consists basically in grouping some 4-momentums from a given set (the jets constituents) into different subsets (the jets, the jet 4momentum being the sum of 4momentum in the subset). For these procedures to have a physical sense, they must represent a correct QCD calculation. But from the algorithmic point of view, jet finding is simply "grouping 4-momentum into subsets". There are two types of jets by default:

- **Cone:**

  A geometrical algorithm. A jet is the subset of constituents lying in a cone with a given radius in the $(\eta, \phi)$ plan. The requirement is that the cone axis is aligned with the jets 4-momentum. The default cone algorithm (release 13 and below) is a seeded algorithm (it searches cones around highest pt constituent only). Some implementation of seedless algorithm (theoretically better) are available and a fast version is under consideration for a replacement of the default. All cone algorithm require and use a split-merge procedure to define non overlapping exclusive jets. The default cone has a seed pt of 1 GeV (2 GeV). Split-merge algorithm is run with overlap fraction=50% to decide split or merge. Radius=0.4 or 0.7, corresponding to so-called cone4 and cone7 jets.

- **Kt:**

  A recursively aggregative algorithm. Kt algorithms group constituents (or protojets) having minimal 'Jet distance' in the $(\eta, \phi)$ plan. The jet distance and rules to stop the aggregation process differ in the different variants of the algorithms. The current default is the Atlas fast-kt version with "standard" inclusive Kt variant. and D parameter =0.4 or 0.6 corresponding to two different sets of jets.

### 3.4.2 Electron, Muon, Jets ID in this analysis

All analysis are based on physics objects as provided by the ATLAS software ATHENA, at the period of Computing System Commissioning. The electron, muon, jets definition and identification are as following:

- **Electrons**:

  Electron candidates are required to be reconstructed and identified with the high-$p_T$ electron reconstruction algorithm egammaRec [45]. Only electron candidates that match the "medium" electron definition requirements are taken into account for the analysis. This choice was made as the optimal trade-off between sufficient rejection of jets and a reasonable efficiency for the selection of electrons. It means that the electron candidate has passed a set of cuts on the electromagnetic shower shape, and that a track has been reconstructed and matched to the cluster, which satisfies several track quality criteria. Figure 3.5 shows the reconstructed electron spectra for $t\bar{t}H$ signal and the identification efficiency as a function of $p_T$ and $\eta$. The ID efficiency is almost flat at high energy region and decrease slightly under 40 GeV, the ID efficiency decrease at gaps($\eta = 0, |\eta| \approx 1.3$) and high $|\eta|$ region due to inefficiency of of tracking.

- **Muons**:

  The selected muon candidates are reconstructed and identified in the muon spectrometer with the Staco algorithm [46]. In addition, a match to an inner detector track segment is required to reduce the contribution of fakes and ensure the best possible $p_T$-resolution. Among all track segments that could match the muon spectrometer tracks, the best matching one is chosen. Figure 3.6 shows the muon spectra and muon identification efficiency as functions of $p_T$ and $\eta$. the ID efficiency is high

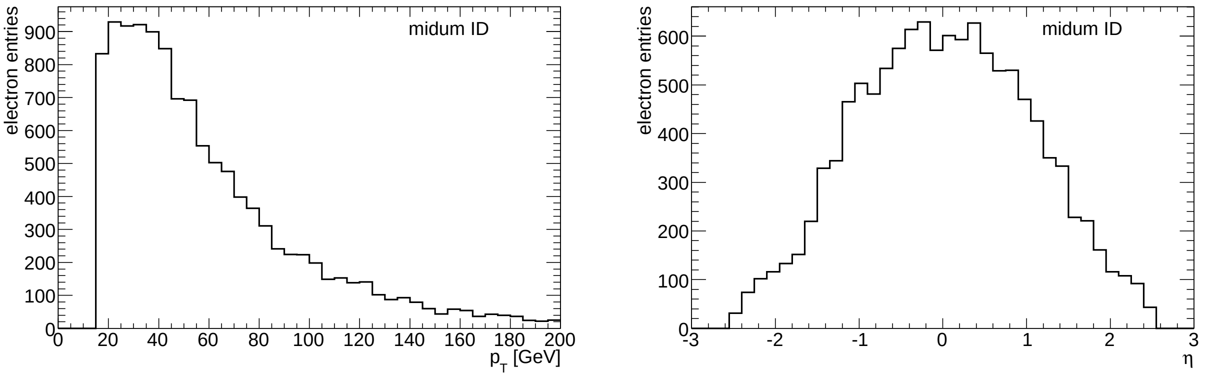

(a) electron $p_T(ttH)$ distribution for medium ID cuts (b) electron $\eta(ttH)$ distribution for medium ID cuts

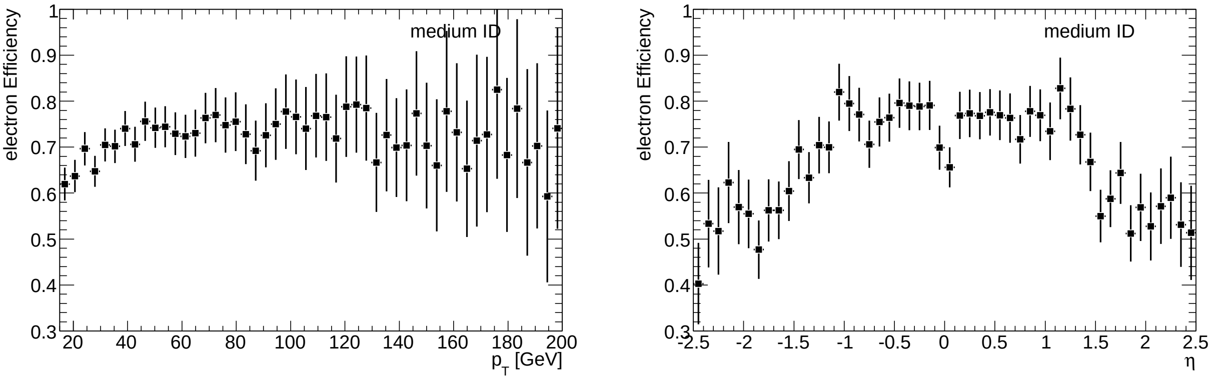

(c) electron ID efficiency vs $p_T(ttH)$

(d) electron ID efficiency vs $\eta(ttH)$

FIGURE 3.5: electron and electron identification efficiency as a function of $p_T$ and $\eta$ at medium ID cuts

and almost flat as function of $p_T$, and there are 3 gap as $\eta$, corresponding to the three gaps of barrel-barrel ar $\eta$=0 and barrel-endcap at $\eta \approx \pm 1.3$.

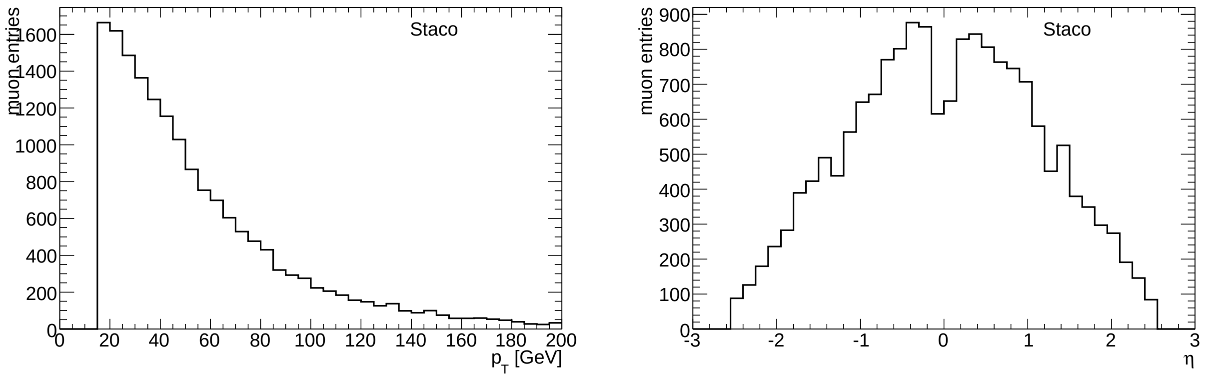

(a) muon $p_T(ttH)$ distribution

(b) muon eta$(ttH)$ distribution

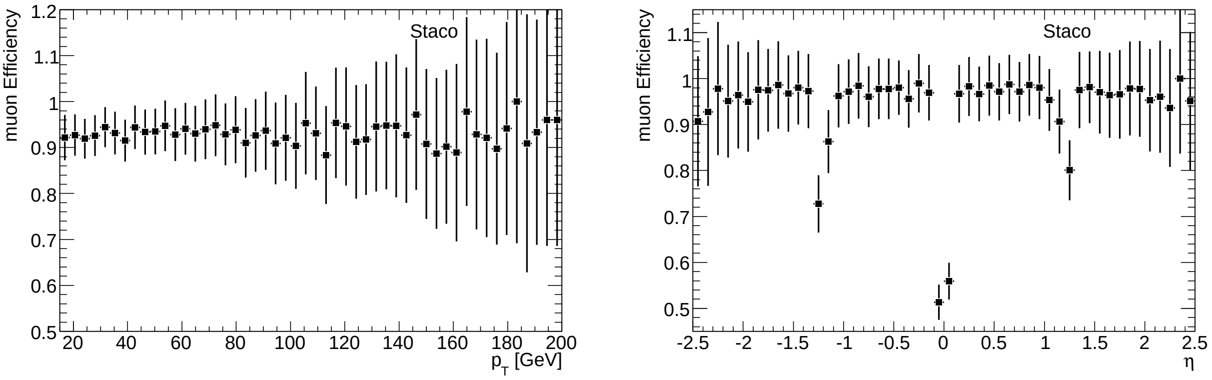

(c) muon ID efficiency vs $p_T(ttH)$

(d) muon ID efficiency vs $\eta ttH)$

FIGURE 3.6: muon and muon identification efficiency as a function of $p_T$ and $\eta$

- **Jets**:

  The $t\bar{t}H$ analysis require jets which are reconstructed with the cone tower clustering algorithm [47] using a cone size of $\Delta R = 0.4$ ("cone-0.4") to ensure the reconstruction of individual jets despite the huge activity in the final states considered(if 6 cone-7 jets in one event, these jets will have many cells shared, which may decrease the performance of of jets). Jet fakes from electrons are removed by retaining only those jets which fulfil $\Delta R(jet, ele) > 0.1$ or $E_{ele}/E_{jet} < 0.65$ with respect to an electron tagged as isolated by the calorimeter- and tracker isolation requirements described below. Figure 3.7 shows the jets $p_T$ and $\eta$ spectra.

The identification efficiencies for isolated leptons and the corresponding purities (defined as the lepton candidates matched these form W/Z decay over all lepton candidates

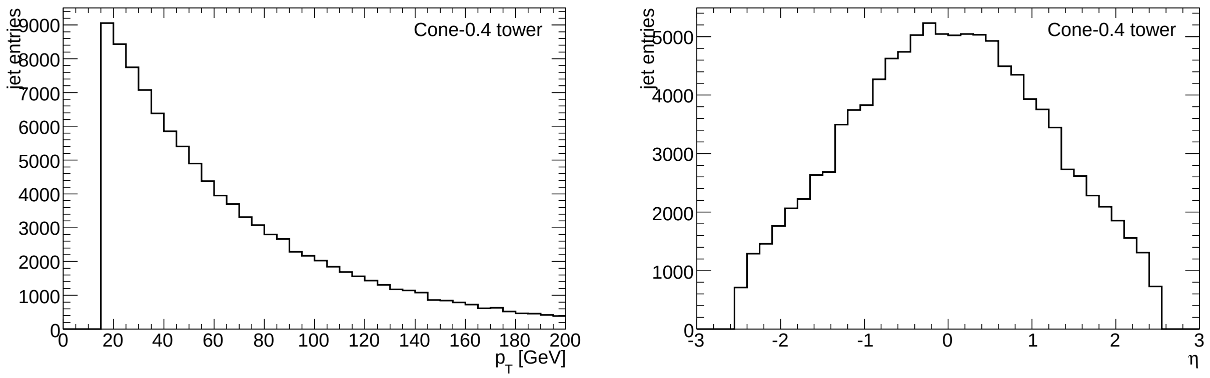

(a) jet $p_T(ttH)$ distribution (b) jet $\eta(ttH)$ distribution

FIGURE 3.7: jet $p_T$ and $\eta$ spectra

that pass the identification criteria ) in the $t\bar{t}H$ data sets are listed in Table 3.9. All physics objects used in the $t\bar{t}H$ analysis have to fulfil the kinematic requirements of $p_T > 15$ GeV and $|\eta| < 2.5$, to be inside the acceptance regions of the trigger and the inner detector.

TABLE 3.9: Selection efficiencies for leptons from $W$-decays and corresponding purities with respect to non-isolated lepton background in the $t\bar{t}H$ signal samples.

| | $t\bar{t}H$ (2L) | | $t\bar{t}H$ (3L) | |
|---|---|---|---|---|
| | efficiency | purity | efficiency | purity |
| muon ID | 92.7% | 86.6% | 92.4% | 91.0% |
| electron ID | 70.5% | 95.3% | 71.2% | 96.5% |

## 3.5 Lepton Isolation

Lepton isolation is crucial for the effective suppression of the main reducible background $t\bar{t}$, with a cross section of 3 order of magnitude higher than that for signals. Though the lepton identification described above provide good efficiency and isolated lepton purity, It is not enough to suppress $t\bar{t}$ to a accepted level. So, the calorimeter- and track-based isolation requirements ("calorimeter isolation" and "tracker isolation") are exploited, as well as the angular separation of leptons and its closest jets, which is further referred to as "cone isolation".

- **Calorimeter Isolation**:

  The transverse energy deposit in the calorimeter in a cone of $\Delta R = 0.2$ around the lepton[1], including electromagnetic and hadronic calorimeter cells, is required to be

---

[1] The lepton $E_T$-contribution is removed by subtracting the energy deposited in $5 \times 14$ calorimeter cells in $\eta \times \phi$-direction for electrons and all cells within a 0.05-cone for muons.

less than 10 GeV for both electrons and muons.

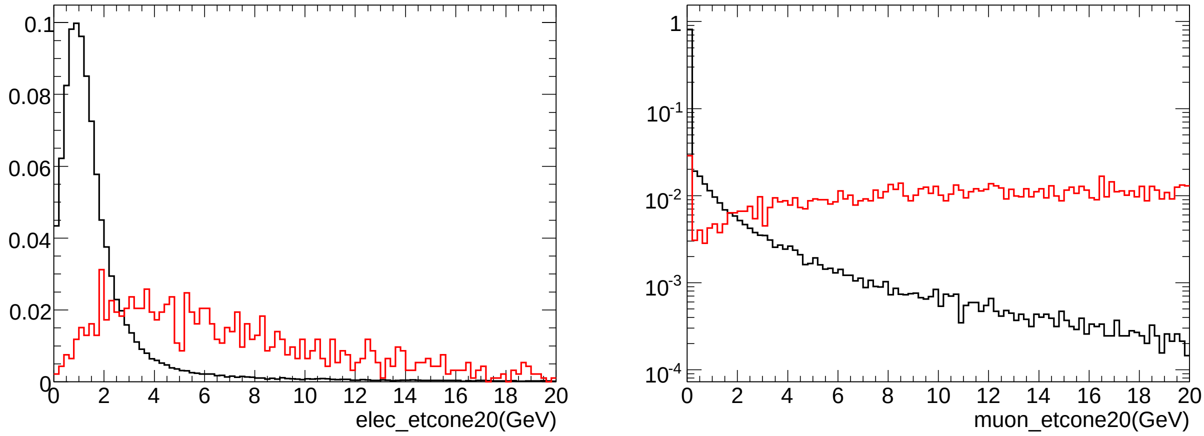

(a) electron etcone20($t\bar{t}$) (b) muon etcone20($t\bar{t}$)

FIGURE 3.8: Energy deposited in calorimeter of a cone $\Delta R = 0.2$ for isolated and non-isolated lepton(left:electron, right:muon)

- **Tracker Isolation**:

  Additional tracks in the vicinity of a lepton can also be exploited for the selection of isolated leptons, by cutting on quantities like the number of additional tracks in a certain cone around the lepton, the sum of their transverse momenta or the $p_T$ of the hardest track. A cut on the latter was chosen for the $t\bar{t}H$ analysis, which requires $p_T^{max} < 2$ GeV within a 0.2 $\Delta R$-cone. In order to suppress contributions from pile-up tracks, only tracks are considered that fulfil additional requirements on the track quality and maximum transverse and longitudinal impact parameters.

- **Cone Isolation**:

  Leptons from semi-leptonic heavy quark decays are expected to be found close to the direction of a jet. This characteristic can be used to reject them, by demanding a minimum distance $\Delta R_{min}$ between the lepton and the closest jet. Figure 3.10(a) shows the $\Delta R_{min}$-distribution for muons from $W$-decays as well as for non-$W$ muons. Obviously, the latter show an enhancement at small $\Delta R_{min}$. For the $t\bar{t}H$ analysis, the muons are required to be separated from their neighboring jet by at least $\Delta R_{min} > 0.25$. Due to the ambiguity in the reconstruction of electron clusters and jets, electron candidates usually are found in close vicinity of a jet candidate. Although electrons from $W$-decays tend to be closer to this fake jet candidate than those from semi-leptonic heavy quark decays are to their corresponding jet, this is not sufficient to reliably remove the overlap with jets and reject electrons from

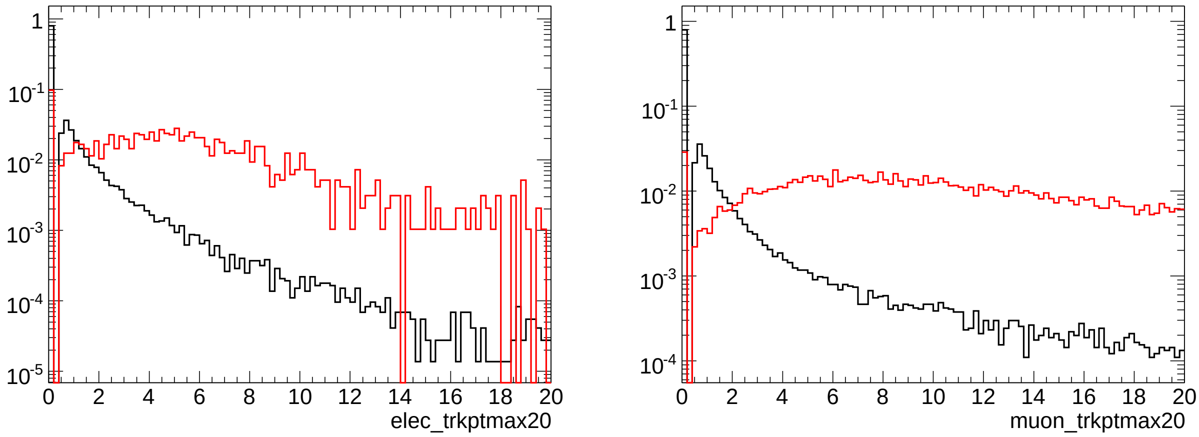

(a) electron track $p_T$ max($t\bar{t}$)

(b) muon track $p_T$ max($t\bar{t}$)

FIGURE 3.9: maxim pt of tracks in inner detector around isolated and non isolated lepton(left:electron, right:muon) within $\Delta R = 0.2$

> heavy quark decays. Therefore, in addition to cuts on $\Delta R_{min}$, a cut on the energy ratio $E_{ele}/E_{jet}$ is applied. The distributions of the two variables are shown in figures 3.10(b) and 3.10(c). Identified electron objects are considered as isolated electrons, as long as they satisfy $\Delta R_{min} > 0.2$ or $\Delta R_{min} < 0.1$ and $E_{ele}/E_{jet} > 0.65$.

Cone isolation is the strongest means to reject background from semi-leptonic heavy quark decays. Although all three isolation variables are strongly correlated, each of them adds further separation power if they are used in combination, because the tracker is more robust to the presence of pile-up, while the calorimeter is more sensitive to neutral particles. Since the determination of the $t\bar{t}$ background contribution, which is expected to be the dominant background to $t\bar{t}H$ and also one of the largest backgrounds for $WH$, from data will be very challenging, it is essential to suppress it as far as possible.

## 3.6 $t\bar{t}H, H \to WW^{(*)}$ two lepton final states analysis

The decay chain of $t\bar{t}H, H \to WW^{(*)}$ is $t\bar{t}H \to WbWbWW^{(*)} \to 2b4j2l2\nu(l = e\mu)$, the final state observed in detector is: two b-jets, four light jets, two same sign charge isolated leptons and missing Et for two neutrinos. Of the two same charged leptons, one is from top decayed W, while the other one from Higgs boson decayed W. The possible backgrounds are $t\bar{t}$,$t\bar{t}W + jets$, $t\bar{t}Z$, $t\bar{t}t\bar{t}$,$t\bar{t}b\bar{b}$, $t\bar{t}WW$. These backgrounds can be classified into two categories, one is that has the same final states as signal, such as $t\bar{t}W + jets$, which have small production cross sections, and need to be suppressed using the differences of physics shapes; the other one has different final states compared to signal, but have big production cross sections, such as $t\bar{t}$. They pass the selection due to un-isolated leptons from heavy quark decays or lepton fakes, and ISR/FSR generate extra jets. They are suppressed by

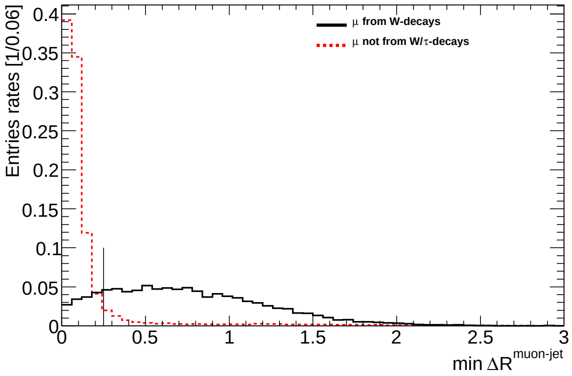

(a) $\Delta R_{min}$ muon-jet in $t\bar{t}H$

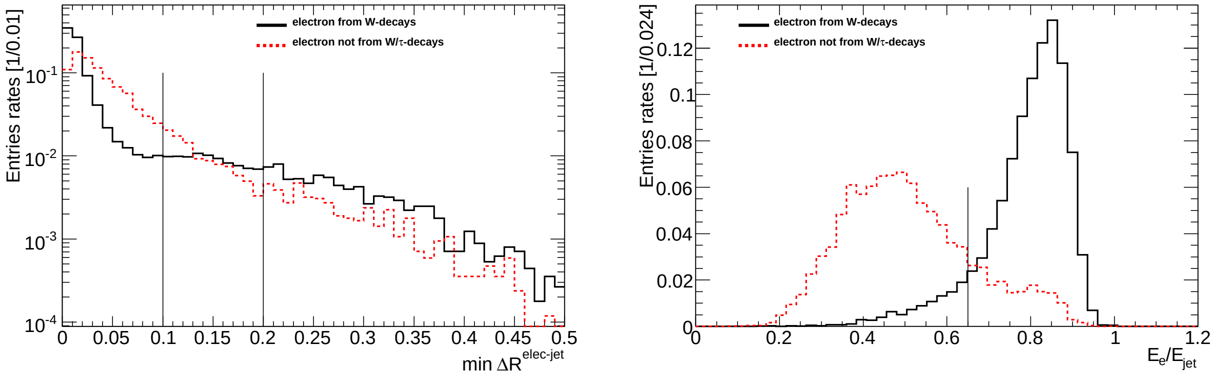

(b) $\Delta R_{min}$ electron-jet in $t\bar{t}H$

(c) Electron-jet energy ratio in $t\bar{t}H$

FIGURE 3.10: Distributions of the variables used for the cone isolation of muons (a) and electrons (b, c) in the $t\bar{t}H$ analysis, all variables are calculated with respect to cone-0.4 jets. All distributions are normalized to integral 1.

using isolation criteria. The selection criteria and the performance of each samples are presented here.

### 3.6.1 Event selection and background suppression

$t\bar{t}H, H \rightarrow WW^{(*)}$ two leptons final state event selection criteria are as following:

- At least two good reconstructed leptons and six jets full fill the identification criteria described as 3.4, which is called as basic selection. A typical selection efficiency of signal at Higgs mass 160 GeV is 38%. while the main background $t\bar{t}$ lost more than 98% statistics.

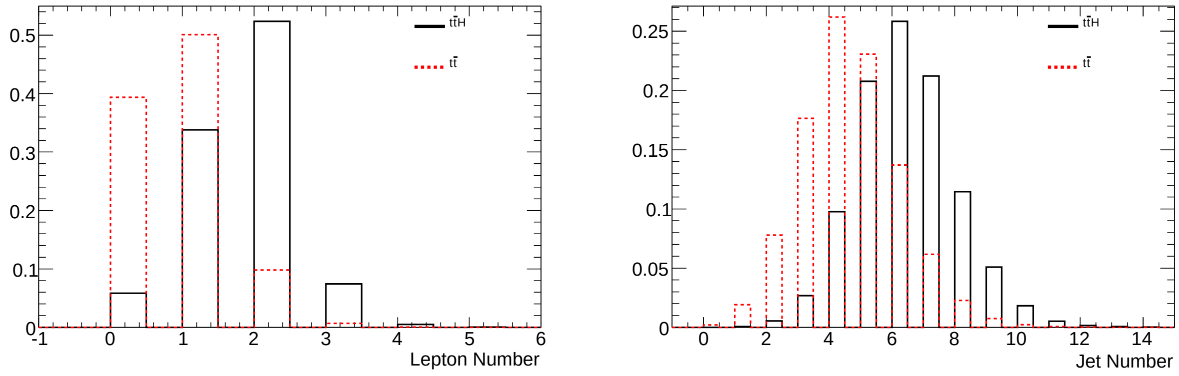

(a) Lepton Multiplicity (b) Jet Multiplicity

FIGURE 3.11: Lepton Multiplicity and Jet Multiplicity

- Since this background rejection rate is not sufficient, the selected leptons are in addition required to pass the cuts on calorimeter-, tracker- and cone-isolation described in section 3.5. Then at least two leptons are required. Signal loss is about 50% while more than 75% for $t\bar{t}$, with mainly are $t\bar{t}$ full leptonic events.

- A lepton veto of lepton number exactly equal to two is required, this mainly reject ttZ since ttZ could have three isolated lepton from W or Z.

- A same sign charge is required for these two leptons, this will kill $t\bar{t}$ full leptonic decays drastically. Only 3% $t\bar{t}$ pass this criteria and almost all the signal passed(if no same sign charge required at generation level, two thirds of signal lost).

- Since $ttZ$ may have three isolated leptons from W/Z decays, but due to kinematical reason(ex. out of detector acceptance), reconstruction efficiency or isolation efficiency, one of them did not pass lepton selection, then, this event probably pass our selection criteria of two leptons and six jets. In order to get rid of these kind of $ttZ$ events, a Z veto is applied, which requires:
  - Release $p_T$ criteria of leptons to 6 GeV, and requires to pass the lepton selection criteria described in section 3.4, except for the $p_T$-requirement.
  - pairing these leptons with same flavor, opposite sign charge as Z candidates.
  - If these Z candidates have invariant mass between 75 and 100 GeV, then, this event will be rejected since it is considered as a event with Z meson.

  The reconstructed Z candidates mass spectra for signal and $ttZ$ are shown in figure 3.12(a), a clear Z peak found in $ttZ$ events and flat for signal. This criteria get rid of one quarter of $ttZ$ while keeps about 98% or other samples.

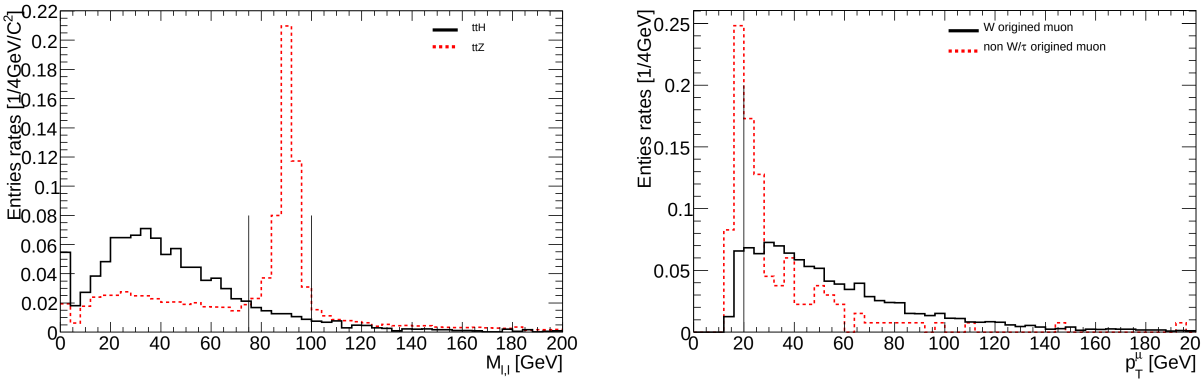

(a) Di-lepton invariant mass distributions

(b) $p_T$-distributions of isolated muons

FIGURE 3.12: (a) Di-lepton invariant mass distributions in $t\bar{t}H$ (2L) and $t\bar{t}Z$ and (b) $p_T$-distributions of muons passing the isolation criteria listed in Section 3.4. The solid distribution shows electrons from $W$-decays in the $160GeV$ signal sample, the dotted distribution shows muons in $t\bar{t}$, which could not be matched to a truth muon from a $W$- of $\tau$-decay. All distributions are normalized to integral 1.

- Tighten muon $p_T$: at this stage of the selection, 73% of all remaining $t\bar{t}$ events contain a muon from a semi-leptonic heavy quark decay, while the fraction of events with electrons of this origin is only 20%. This discrepancy in rejection can partly be explained by the electron identification criteria, which suppress a sizable fraction of the background electrons, as demonstrated by the lepton selection purities given in Section 3.4. In addition, the cone isolation works differently for the two lepton flavors and performs more efficiently in the electron case, where in fact two variables are combined. Further rejection of these muon events is achieved by a cut on the minimum muon $p_T$ at 20 GeV, since leptons from heavy quark decays tend to be softer than leptons from weak boson decays, as shown in Figure 3.12(b). This equalizes the contributions from electrons and muons to 41% and 46%, respectively.

TABLE 3.10: Origin of the second selected like-sign lepton in the pre-filtered $t\bar{t}$ data set before and after the requirement of $p_T^{muon}$ >20GeV (2L analysis). The category "others" sums up the contributions by fake leptons, charge mismeasurement, pion- and tau lepton decays etc.

| | $p_T(\mu) > 15GeV$ | $p_T(\mu) > 20GeV$ |
|---|---|---|
| $\mu$ from heavy quark decays | (73 ± 4)% | (46 ± 6)% |
| $e$ from heavy quark decays | (20 ± 3)% | (41 ± 6)% |
| others | (7 ± 2)% | (14 ± 4)% |

An overview on the cut flow in the $t\bar{t}H, H \to WW$ (2L) analysis and the corresponding accepted signal cross sections is given in table 3.11, from 120 GeV to 200 GeV. And the background cut flow is given in table 3.12. After the selection, for a 160 GeV Higgs mass, the signal selection efficiency is 17.6%. For the three years of low luminosity run and an integrated luminosity of 30 fb$^{-1}$, it correspond to 56 events, and the backgrounds are greatly suppressed, for a S/B of 1/6.

TABLE 3.11: Cut flow and expected cross sections (fb) for the $t\bar{t}H$ (2L) analysis signals at Higgs mass point from 120 GeV to 200 GeV.

| Sample | Tot. | Basic sel. | Calo iso. | Track iso. | Cone iso | Like-sign | $Z$-veto | $p_T^{\mu}$ |
|---|---|---|---|---|---|---|---|---|
| $t\bar{t}H_{2L,120\text{ GeV}}$ | 3.9 | 1.05±0.01 | 0.80±0.01 | 0.65±0.01 | 0.52±0.01 | 0.52±0.01 | 0.51±0.01 | 0.45±0.01 |
| $t\bar{t}H_{2L,130\text{ GeV}}$ | 6.7 | 1.98±0.03 | 1.50±0.03 | 1.25±0.02 | 0.97±0.02 | 0.95±0.02 | 0.95±0.02 | 0.84±0.02 |
| $t\bar{t}H_{2L,140\text{ GeV}}$ | 9.1 | 2.96±0.06 | 2.28±0.05 | 1.93±0.05 | 1.57±0.04 | 1.57±0.04 | 1.54±0.04 | 1.38±0.04 |
| $t\bar{t}H_{2L,150\text{ GeV}}$ | 10.3 | 3.55±0.04 | 2.69±0.04 | 2.26±0.04 | 1.83±0.03 | 1.82±0.03 | 1.78±0.03 | 1.63±0.03 |
| $t\bar{t}H_{2L,160\text{ GeV}}$ | 11.1 | 4.01±0.05 | 3.02±0.04 | 2.57±0.04 | 2.09±0.03 | 2.09±0.03 | 2.04±0.03 | 1.87±0.03 |
| $t\bar{t}H_{2L,170\text{ GeV}}$ | 9.9 | 3.67±0.06 | 2.76±0.05 | 2.38±0.05 | 1.92±0.04 | 1.91±0.04 | 1.86±0.04 | 1.70±0.04 |
| $t\bar{t}H_{2L,180\text{ GeV}}$ | 8.0 | 3.06±0.05 | 2.31±0.04 | 1.98±0.04 | 1.61±0.03 | 1.61±0.03 | 1.58±0.03 | 1.28±0.04 |
| $t\bar{t}H_{2L,190\text{ GeV}}$ | 5.8 | 2.20±0.05 | 1.69±0.05 | 1.45±0.04 | 1.21±0.04 | 1.20±0.04 | 1.18±0.04 | 1.10±0.04 |
| $t\bar{t}H_{2L,200\text{ GeV}}$ | 4.7 | 1.83±0.02 | 1.43±0.02 | 1.24±0.02 | 1.05±0.02 | 1.04±0.02 | 1.02±0.01 | 0.95±0.01 |

### 3.6.2 Optimization of isolation

At the selection level described above, an optimization procedure was performed to find the best lepton isolation criteria to improve the statistics significance of the $t\bar{t}H$ signal by using $\frac{S}{\sqrt{S+B}}$, where B includes all the listed backgrounds: $t\bar{t}$, $t\bar{t}b\bar{b}$, $t\bar{t}t\bar{t}$, $t\bar{t}W + jets$, $t\bar{t}Z$.

- **Variables optimized:**

TABLE 3.12: Cut flow and expected cross sections (fb) for the $t\bar{t}H$ (2L) analysis backgrounds.

| sample | total | basic sel. | calo iso. | track iso. | cone iso. | like-sign | $Z$-veto | $p_T^\mu$ |
|---|---|---|---|---|---|---|---|---|
| $t\bar{t}$ | 833k | 6170±80 | 1970±50 | 870±30 | 500±20 | 16±1 | 16 ±1 | 7.41±1.11 |
| $t\bar{t}b\bar{b}$(EW) | 259 | 15.8±0.8 | 4.1±0.4 | 0.9±0.2 | 0.3±0.1 | 0.2±0.1 | 0.2±0.1 | 0.11±0.07 |
| $t\bar{t}b\bar{b}$ | 2693 | 213±4 | 38±2 | 7.6±0.7 | 2.2±0.4 | 1.0±0.3 | 1.0±0.3 | 0.55±0.18 |
| $gg \to t\bar{t}t\bar{t}$ | 2.64 | 0.65±0.01 | 0.33±0.01 | 0.26±0.00 | 0.20±0.00 | 0.07±0.00 | 0.07±0.00 | 0.06±0.00 |
| $qq \to t\bar{t}t\bar{t}$ | 0.58 | 0.13±0.00 | 0.07±0.00 | 0.05±0.00 | 0.04±0.00 | 0.01±0.00 | 0.01±0.00 | 0.01±0.00 |
| $t\bar{t}W$+0j | 73.3 | 1.40±0.05 | 0.55±0.03 | 0.36±0.02 | 0.23±0.02 | 0.12±0.01 | 0.12±0.01 | 0.11±0.01 |
| $t\bar{t}W$+1j | 60.6 | 2.51±0.06 | 1.11±0.04 | 0.79±0.03 | 0.58±0.03 | 0.28±0.02 | 0.28±0.02 | 0.25±0.02 |
| $t\bar{t}W$+2j | 92.3 | 10.3±0.2 | 5.9±0.1 | 4.9±0.1 | 3.9±0.1 | 1.89±0.07 | 1.85±0.07 | 1.68±0.06 |
| $t\bar{t}Z$ | 1440 | 33.6±0.4 | 26.8±0.4 | 23.7±0.4 | 17.9±0.3 | 2.1±0.1 | 1.57±0.10 | 1.49±0.09 |
| **total background** | | | | | | | | 11.0 ± 1.1 |

All the variables that are used to do the lepton isolation are optimized, such as electron and muon *etcone*; the maximum $p_T$ of the tracks around leptons in a cone size of 0.2 in the inner detector; the electron upper and lower boundary of $\Delta R_{min}^{ele,jet}$ and $E_{ele}/E_{jet}$, and $\Delta R_{min}^{muon,jet}$ for cone isolation. There are unknown correlations between these variables.

- **Steps of optimization**
  - Give a set of initial values to these isolation criteria
  - Scan the first variable, find the value to maximum $\frac{S}{\sqrt{S+B}}$.
  - Adjust this variable to the value found of last step.
  - Scan second variable, find and adjust it to maximum $\frac{S}{\sqrt{S+B}}$.
  - Scan and adjust the variables one by one, start scan the first variable once the last variable is scanned and adjusted.
  - Stop scan once $\frac{S}{\sqrt{S+B}}$ can not be improved by scanning every variables. The variable value of the last scan is the best criteria value for this multi-dimensional scans.

Figure 3.13 shows that under the best isolation criteria, $\frac{S}{\sqrt{S+B}}$ shifts according to the changing of each variable. It is found that the most sensitive variables are cone isolation variables $E_{elec}/E_{jet}$ and $min\Delta R_{muon,jet}$. and other variables have small impact on the significance.

## 3.7 $t\bar{t}H, H \to WW^{(*)}$ three leptons final state analysis

The decay chain of $t\bar{t}H, H \to WW^{(*)}$ three final state is $t\bar{t}H \to Wb\ Wb\ WW^{(*)} \to 2b\ 2j\ 3l\ 3\nu(l = e\mu)$, the final state observed in detector is: two b-jets, two light jets, three isolated leptons and missing energy(three neutrinos). The possible backgrounds are $t\bar{t}$,$t\bar{t}W + jets$, $t\bar{t}Z$.

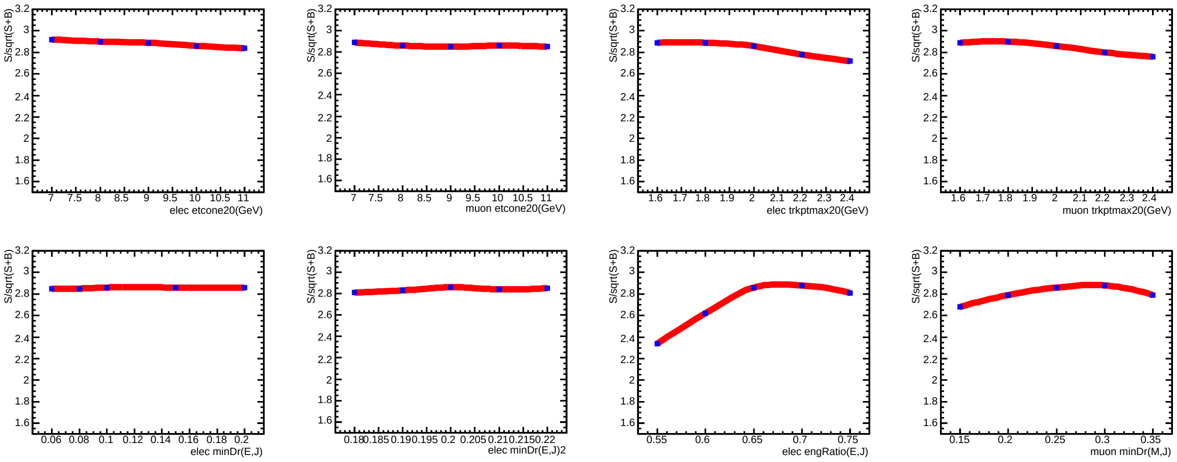

FIGURE 3.13: Optimization scan of each isolation variable

### 3.7.1 Event selection and background suppression

$t\bar{t}H, H \to WW^{(*)}$ three leptons final state event selection criteria are as following:

- At least three leptons and four jets fully satisfied the identification criteria described in section 3.4. So-called the basic selection. A typical selection efficiency of signal at Higgs mass of 160 GeV, is 35%. while the backgrounds efficiencies are: $t\bar{t}W + 2j$ : 8.2%; $t\bar{t}Z$ : 17.2%; $t\bar{t}$ : 0.4%.

- Then, the selected leptons are in addition required to pass the cuts on calorimeter-, tracker- and cone-isolation described in section 3.5. and ask exactly three leptons. Signal have 45% passed while $t\bar{t}$ have only about 1/200 passed.

- The same Z-veto as ttHWW2L analysis is used in order to suppress $t\bar{t}Z$. 83% signal passed while 80% $t\bar{t}Z$ are suppressed.

- To further suppress $t\bar{t}$ background, as in ttHWW2L analysis, muon $p_T$ request to be greater than 20 GeV.

An overview on the cut flow in the $t\bar{t}H, H \to WW$ (3L) analysis and the corresponding accepted signal cross sections is given in table 3.13, from 120 GeV to 200 GeV. And the background cut flow is given in table 3.14. After the selection, for a 160 GeV Higgs mass, the signal selection efficiency is 11.5%. For the three years of low luminosity run and integrated luminosity of 30 fb$^{-1}$, it correspond to 25 events, and greatly suppressed backgrounds, for a S/B of 1/4.5.

Table 3.13: Cut flow and expected cross sections (fb) for the $t\bar{t}H$ (3L) analysis signal at Higgs mass point from 120 GeV to 200 GeV.

| Sample | Total | Basic sel. | Calo iso. | Track iso. | Cone iso. | $Z$-veto | $p_T^\mu$ |
|---|---|---|---|---|---|---|---|
| $t\bar{t}H$ (3L, 120 GeV) | 2.5 | 0.66±0.01 | 0.46±0.01 | 0.38±0.00 | 0.29±0.00 | 0.24±0.00 | 0.20±0.00 |
| $t\bar{t}H$ (3L, 130 GeV) | 4.3 | 1.27±0.01 | 0.89±0.01 | 0.73±0.01 | 0.56±0.01 | 0.48±0.01 | 0.40±0.01 |
| $t\bar{t}H$ (3L, 140 GeV) | 5.8 | 1.90±0.02 | 1.34±0.02 | 1.11±0.02 | 0.86±0.02 | 0.72±0.01 | 0.63±0.01 |
| $t\bar{t}H$ (3L, 150 GeV) | 6.6 | 2.22±0.02 | 1.56±0.02 | 1.28±0.02 | 0.99±0.02 | 0.81±0.01 | 0.70±0.01 |
| $t\bar{t}H$ (3L, 160 GeV) | 7.1 | 2.53±0.03 | 1.78±0.03 | 1.47±0.02 | 1.14±0.02 | 0.95±0.02 | 0.82±0.02 |
| $t\bar{t}H$ (3L, 170 GeV) | 6.3 | 2.34±0.02 | 1.64±0.02 | 1.37±0.02 | 1.08±0.02 | 0.88±0.01 | 0.77±0.01 |
| $t\bar{t}H$ (3L, 180 GeV) | 5.2 | 1.93±0.02 | 1.38±0.02 | 1.16±0.01 | 0.92±0.01 | 0.73±0.01 | 0.65±0.01 |
| $t\bar{t}H$ (3L, 190 GeV) | 3.8 | 1.42±0.02 | 1.02±0.01 | 0.86±0.01 | 0.70±0.01 | 0.54±0.01 | 0.49±0.01 |
| $t\bar{t}H$ (3L, 200 GeV) | 3.1 | 1.16±0.01 | 0.82±0.01 | 0.70±0.01 | 0.55±0.01 | 0.43±0.01 | 0.39±0.01 |

Table 3.14: Cut flow and expected cross sections (fb) for the $t\bar{t}H$ (3L) analysis backgrounds.

| sample | total | basic sel. | calo iso. | track iso. | cone iso. | $Z$-veto | $p_T^\mu$ |
|---|---|---|---|---|---|---|---|
| $t\bar{t}$ | 833k | 1600±40 | 230± 20 | 50± 7 | 9.3±3.1 | 7.2±2.7 | 2.06±2.06 |
| $t\bar{t}W$+0j | 73.3 | 0.94±0.04 | 0.20± 0.02 | 0.09±0.01 | 0.05±0.01 | 0.04±0.01 | 0.03±0.01 |
| $t\bar{t}W$+1j | 60.6 | 1.28±0.04 | 0.33± 0.02 | 0.17±0.01 | 0.10±0.01 | 0.09±0.01 | 0.07±0.01 |
| $t\bar{t}W$+2j | 92.3 | 3.32±0.09 | 1.02± 0.05 | 0.72±0.04 | 0.60±0.04 | 0.50±0.03 | 0.45±0.03 |
| $t\bar{t}Z$ | 1440 | 19.6±0.3 | 11.2±0.3 | 8.9±0.2 | 7.0±0.2 | 1.37±0.09 | 1.12±0.08 |
| **total background** | | | | | | | 3.7 ± 2.1 |

## 3.8 Pileup study

At LHC, under the designed low luminosity of $1{\cdot}10^{33}$ cm$^2$/s, there will be average of 2.3 inelastic proton-proton scattering per bunch crossing. Moreover, a cloud of slow neutrons from earlier collisions is expected to constitute the so-called “cavern background” in the muon spectrometer. These effects results in extra action in the detector and degrade the reconstruction and identification of physics objects. In order to simulate these effects, A set of low transverse momentum proton-proton inelastic scattering events are simulated(minimum bias events), and added to the events at the digitization step, proportional to the luminosity.

Though pileup did not bring in high $p_T$ objects, it smear energy all over the detector. This will affect lepton identification and isolation. Pileup have un-neglectable impact on jets since it will increase low energy jets candidates, impact calibration of calorimeters and makes the jet energy scale systematically overestimated.

### 3.8.1 Pileup impact on lepton ID efficiency

Figure 3.14 compared lepton reconstruction efficiency before and after pileup as a function of $p_T$ and $\eta$. 1% decrease due to pileup for both electrons and muons.

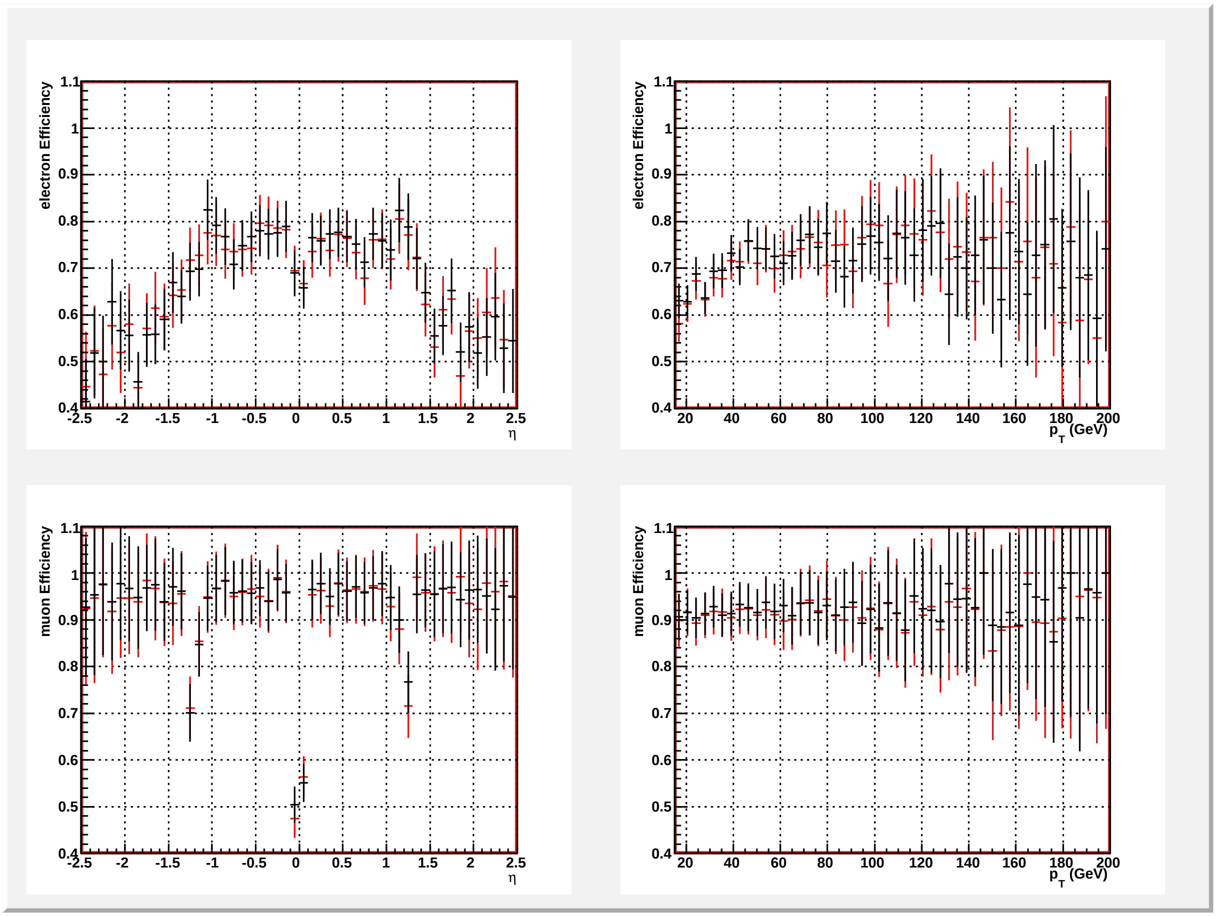

FIGURE 3.14: lepton ID efficiency: before (black) and after pileup (gray/red)

## 3.8.2 Pileup impact on jets

Since pileup brings extra energy activities in the calorimeters, and results in extra jets reconstructed in low $p_T$ region. The average multiplicity of jets with $p_T > 15$ GeV in signal events increases by 2.9%, while for the $t\bar{t}$ and $t\bar{t}W$ backgrounds it increases by 5.2% and 4.6%, respectively. Figure 3.15 shows the the jet multiplicity and $p_t$ distribution before and after pileup.

## 3.8.3 Pileup impact on lepton isolation

Comparing the distributions of lepton isolation variables before and after pileup (Figure 3.16), calorimeter isolation variables are cut on the tails of safe region; tracker isolation variables are very similar since there is a criteria on impact parameter in track selections, which suppress pileup tracks; and more jets candidates at low energy decrease discrimination power of $E_{ele}/E_{jet}$. All these effects are at 1% level for isolated electrons.

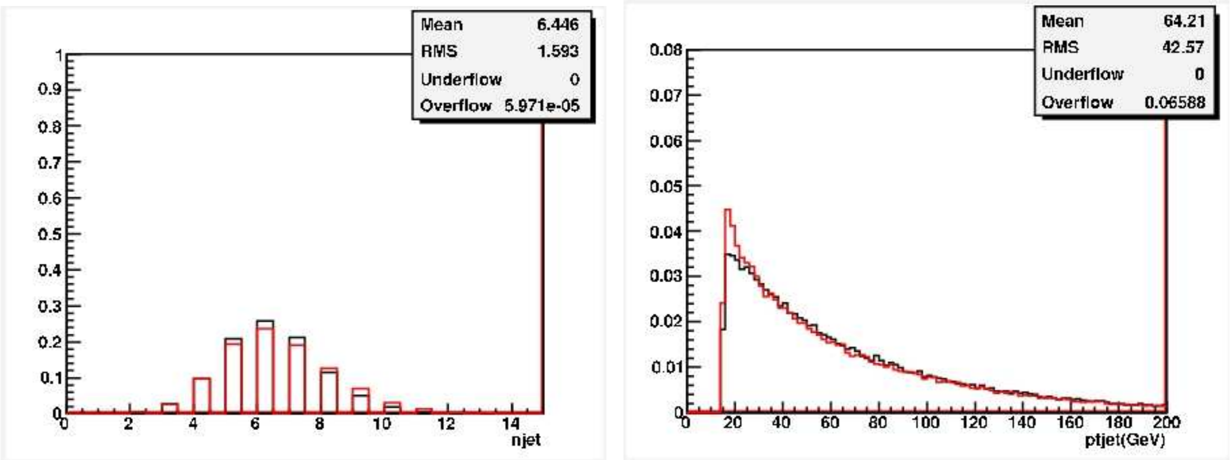

(a) jet multiplicity before and after pileup (b) jet pt before and after pileup

Figure 3.15: jet multiplicity and pt distributions: before (black) and after pileup (gray/red)

### 3.8.4 Pileup impact on signal and background

The effectiveness of the lepton isolation variables is expected to degrade as a result of pile-up. Calorimeter-based isolation variables suffer more from the presence of pile-up than track-based variables. The restriction to tracks close to the primary vertex helps to keep the pile-up effects small. In this analysis, the cone isolation is hardly exploited, so the effect of pile-up on the lepton isolation efficiency is negligible.

Over all, for the signal as well as for all backgrounds, one has to expect a decrease in the lepton selection efficiency due to additional jets. At the same time, backgrounds with relatively low jet multiplicities in the final state are selected more efficiently by requiring six jets in the final state. This results in an overall reduction of the signal significance. In order to estimate the size of this decrease, the available data sets were fed through the baseline selection procedure. Taking into account the weights of the MC@NLO $t\bar{t}$ data set, no event from the $t\bar{t}$+pile-up sample survives the selection because of the limited statistics. In order to estimate the expected contribution from this background, the standard cut flow was therefore re-ordered such that the like-sign and the cone isolation requirement on the lepton candidates are tested at the beginning. The like-sign cut ensures the comparability of the two $t\bar{t}$ data sets. The cone isolation criterion is much more critical in terms of pile-up than the calorimeter and tracker isolation and veto cuts, which were applied afterwards. The selection efficiency at this stage, together with the selection efficiency for the remaining cuts as obtained from the pre-filtered $t\bar{t}$ data set without pile-up was used to estimate the expected number of $t\bar{t}$ events in the presence of pile-up. Still, there is a large systematic error on the $t\bar{t}$ expectation in the pile-up case. The results are summarized in Table 3.15. As can be seen, for the signal and the $t\bar{t}W$ sample, the selection efficiency for the second half of the re-ordered cut flow, including two out of three lepton isolation cuts, does not change in the presence of pile-up. Therefore, the assumption of equal efficiency for this part of the selection is justified also for $t\bar{t}$.

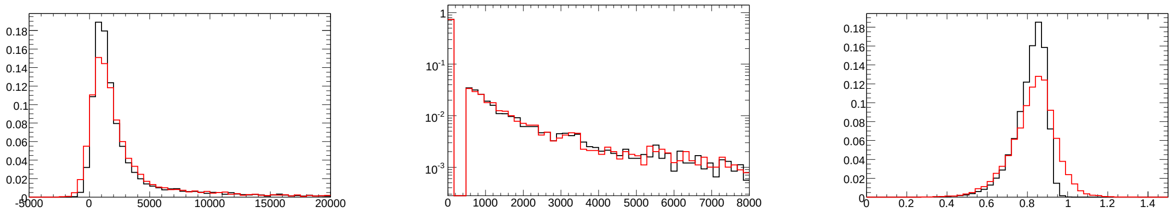

(a) electron etcone20 before and after pileup (b) electron track pt max before and after pileup (c) electron jet energy ratio before and after pileup

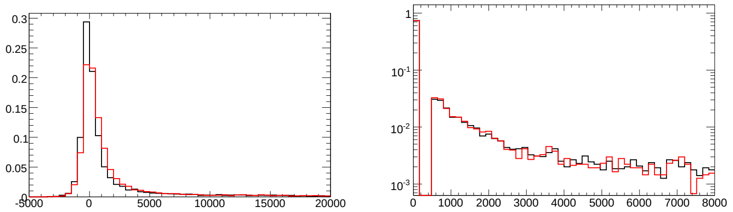

(d) muon etcone20 before and after pileup (e) muon track pt max before and after pileup

FIGURE 3.16: lepton isolation: before (black) and after pileup (gray/red)

For the remaining backgrounds, especially for $t\bar{t}Z$, no pile-up samples are available. In order to estimate the overall signal significance under the effect of pile-up, the expectations in these channels in absence of pile-up were scaled to the 28% increase observed for the $t\bar{t}W$-contribution. As expected, the signal significance $S/\sqrt{B}$ decreases by roughly 20% down to 2.4 from a starting value of 3.0 in the non-pile-up case. This number is, however, only a rough estimate, due to large statistical errors and the additional uncertainties introduced by the methods to estimate the accepted cross sections in the presence of pile-up.

## 3.9 Systematic uncertainties

Predictions of signal expectations are affected not only by the available Monte Carlo statistics, but also by systematic uncertainties introduced e.g. by limited description of physics processes and the detector performance. Even more important, the signal significance that can be achieved to claim an observation of the Higgs boson in the $t\bar{t}H, H \rightarrow WW$ channel, as well as the accuracy of a subsequent $\sigma_{t\bar{t}H} \times BR(H \rightarrow WW)$ measurement depend strongly on the accuracy of the background estimation. Since the reconstruction of the Higgs boson is difficult in the complex final states of the signal, background estimation from data, will be very challenging. No strategy has yet been studied to determine the background contribution in the data with sufficient precision. In the following, an estimation of the uncertainty on the Monte Carlo predictions on the number of expected signal and background events is presented. The three main sources of systematic uncertainties that are considered are the limited accuracy of the luminosity measurement as well as uncertainties from the theory and the description of the detector performance.

Table 3.15: Selection efficiencies and accepted cross sections for the standard scenario and under the influence of pile-up. The background numbers for the no-pileup case vary somewhat from those given in Table 3.12, since slightly different sub-sets of the available data sets have been analysed.

| **no pile-up** | | | | | |
|---|---|---|---|---|---|
| | signal | $t\bar{t}$ (pre-filtered) | $t\bar{t}W$ | $t\bar{t}Z$ | $t\bar{t}t\bar{t}$ |
| $\epsilon_g$ (generator level filter) | 0.95 | 0.038 | 0.42 | 0.79 | 0.65 |
| $\epsilon_1$ (6jets+S.S+coneIso.) | 0.23 | $2.8 \cdot 10^{-3}$ | 0.032 | 0.050 | 0.07 |
| $\epsilon_2$ (remaining cuts) | 0.77 | 0.071 | 0.65 | 0.26 | 0.48 |
| $\epsilon_{tot} = \epsilon_g \cdot \epsilon_1 \cdot \epsilon_2$ | 0.17 | $8 \cdot 10^{-6}$ | 0.009 | 0.010 | 0.022 |
| accepted $\sigma$ [fb] | 1.85±0.03 | 7.21±0.9 | 2.00±0.07 | 1.50±0.09 | 0.067±0.003 |

| **pile-up + cavern background** | | | | | |
|---|---|---|---|---|---|
| | signal | $t\bar{t}$ | $t\bar{t}W$ | $t\bar{t}Z$ | $t\bar{t}t\bar{t}$ |
| $\epsilon_g$ (generator level filter) | 0.95 | 0.54 | 0.42 | **no pile-up samples**<br>expectations<br>extrapolated<br>from $t\bar{t}W$ | |
| $\epsilon_1$ (6jets+S.S+coneIso.) | 0.23 | $0.34 \cdot 10^{-3}$ | 0.040 | | |
| $\epsilon_2$ (remaining cuts) | 0.76 | 0.071 | 0.67 | | |
| $\epsilon_{tot} = \epsilon_g \cdot \epsilon_1 \cdot \epsilon_2$ | 0.16 | $13 \cdot 10^{-6}$ | 0.011 | | |
| accepted $\sigma$ [fb] | 1.81±0.04 | 10.73±3.27 | 2.55±0.12 | 1.91±0.16 | 0.087±0.007 |

### 3.9.1 Luminosity

The measurement of the luminosity that will be delivered by the LHC is expected to introduce an uncertainty of ±3% on the determination of reaction cross sections and on Monte Carlo-based event yield predictions.

### 3.9.2 Theoretical uncertainties

Monte Carlo predictions suffer from systematic uncertainties inherent in the theoretical description of the physics processes involved.

- **Cross sections and higher order calculations**

  The total cross section of the main background $t\bar{t}$ has been calculated at next-to-leading order to an accuracy of ±12%. The resulting uncertainty on the total background expectation can be obtained by weighting this value with the fractions of 66% $t\bar{t}$-contribution in the 2L and 56% in the 3L background.

  It has to be admitted, however, that this number certainly underestimates the impact of the background cross section uncertainty for two reasons: First, the uncertainty on the cross sections of the non-$t\bar{t}$ contributions is neglected completely. Since for these so far only LO calculations exist and therefore K-factors had to be guessed, the uncertainty on their cross sections is presumably larger than that for the inclusive $t\bar{t}$ cross-section. Second, the inclusive $t\bar{t}$ cross section introduces only a small fraction of the overall error, which is caused by the fact that the $t\bar{t}H$ final states require several additional hard jets. Therefore the relevant cross sections would be those for $t\bar{t}$+$n$ jets with $n \geq 2$, which cannot be accessed by NLO calculations and thus have to be assumed to carry much larger uncertainty, as long as they are not measured experimentally.

- **Generator settings uncertainties on the signal expectation**

  To estimate the influence of the uncertainties of the generation input parameters on the prediction of the signal cross section and the event selection efficiency, the impact of variations to the "standard" PYTHIA settings used to generate the $t\bar{t}H$ signal samples described in Section 3.2 was studied. The input parameters that were considered are the $Q^2$-scale, the choice of the parton distribution functions (PDFs), the description of initial- and final state radiation (ISR and FSR) as well as heavy- and light quark fragmentation. The changes to these inputs were applied independently one after the other. While the 2L and 3L final state "standard" samples contain 100k and 80k events, respectively, 40k events were generated for both final states for a Higgs boson mass of 160 GeV with each of the changes to the generator settings.

  The CTEQ6L1 PDFs were replaced by the MRST2001-LO parametrization, in order to estimate the influence of the choice of the PDFs. To test the dependence on the $Q^2$-scale, $Q^2$ was changed from the average squared transverse mass of the outgoing objects to the squared center-of-mass energy. To quantify the sensitivity to changes in the ISR and FSR modeling, two samples were generated where the $\Lambda_{QCD}$ and $k_T$ cut-off parameters were varied by consistently inserting half or twice the default values in the $p_T$-ordered ISR/FSR description in PYTHIA 6.4. To determine the impact of the fragmentation description, the values of the quark fragmentation parameters were varied according to the range allowed for by the results of the fits by the OPAL collaboration [48, 49], which are $\epsilon_b = -0.0041 \pm 0.0004$ and $\epsilon_c = -0.031 \pm 0.011$ for the $b$- and $c$-quarks and $b = 0.52 \pm 0.04$ and $\sigma_q = 0.40 \pm 0.03$ for the fragmentation of light quarks. As expected, only the change of the PDFs caused a sizable change of +7.8% in the total production cross section.

  The resulting effects on the event selection efficiency were estimated from samples reconstructed with the ATLAS fast detector simulation ATLFAST [50]. The basic event selection criteria for the $t\bar{t}H$ 2L and 3L analyses were implemented by the requirement of isolated leptons that pass $p_T^e$ >15 GeV and $p_T^\mu$ >20 GeV and jets that satisfy $p_T$ >15 GeV. For the 2L final state, events that fulfil $N_{lep} \geq 2$ and $N_{jets} \geq 6$ were selected, whereas $N_{lep} \geq 3$ and $N_{jets} \geq 4$ were the corresponding requirements for the 3L analysis.

  The relative differences of the selection efficiencies on the "varied" and "standard" signal data sets were used to quantify the effects of the changes. The modifications to the ISR/FSR description were found to cause the dominant uncertainty of +4.8% and -1.5% for the 2L and -1.7% and -3.4% for the 3L analysis, The uncertainties on the fragmentation parameters were found to be ±1.0% for the 2L and ±2.8% for the

3L analysis, All results were combined to a total systematic theory error which includes the uncertainty on the cross section as well as on the event selection efficiency.

- **Description of background processes**

  The effects studied for the signal also cause uncertainties on the selection of background events. Especially for $t\bar{t}$, the uncertainty on the multiplicity and $p_T$-spectra of jets caused by the choice of the generator is expected to introduce sizable uncertainties in the backgrounds.

  However, estimating the size of these uncertainties from testing samples with varied input parameters or other event generators in a similar way as was done for the signal is not feasible with the fast detector simulation. Since the rejection of non-isolated leptons and contributions of jets faking leptons strongly influence the selection efficiency of background events, it is doubtful that reasonable results can be obtained from fast simulation studies. Changes introduced in the description of the ISR/FSR require adjusting the jet energy scales properly. The softer the jet spectrum of a process is expected to be, the more important this is, which causes especially the $t\bar{t}$ background to be very sensitive and hence cannot be neglected as has been done for the signal. This recalibration procedure needs to be well understood before corresponding studies can provide reliable results for the background.

Table 3.16 gives an overview on the standard and varied generator settings that were used to determine the systematic uncertainties on the signal description.

### 3.9.3 Detector performance uncertainties

Various effects due to limited knowledge of the detector performance give rise to further uncertainties. To determine the impact of energy scale and resolution uncertainties, as well as reconstruction and identification efficiency uncertainties, the corresponding quantities of leptons and jets were modified according to the expected uncertainties [47, 45, 46]. The changes were applied one after the other and the result of the event selection on the modified objects was compared to the standard selection efficiency to determine the uncertainties on the accepted cross sections given in Table 3.19.

- **Energy scale**

  Systematic errors on the energy scale of electrons and jets are caused by calorimeter calibration uncertainties, while the muon energy scale suffers from the limited knowledge of the magnetic field in the muon spectrometer. To account for these effects, the $E_T$ of the reconstructed electrons was varied by $\pm 0.5\%$, while the muon-$p_T$ was shifted by $\pm 1\%$ of the original value. In the case of the jets, the complete four-vector was scaled by $\pm 7\%$, to account for the uncertainty on the measurement of $E$. Positive and negative corrections were considered separately in all cases.

Table 3.16: Variation of the pythia input parameters used for the estimation of the generator uncertainties to the signal cross sections and selection efficiencies. Note that the statistical uncertainty on the results is of the order of 1% and small changes were therefore neglected in the combination.

| | Standard configuration | Varied settings | $\Delta\epsilon$(signal selection) | |
|---|---|---|---|---|
| | | | 2L | 3L |
| PDF | CTEQ6L1 | MRST2001-LO | +1.0% | +0.02% |
| | | | +7.8% ($\sigma_{tot}$) | |
| $Q^2$ | `MSTP(32) = 8` | `MSTP(32)` = 4 | +0.3% | −0.2% |
| FSR $\Lambda_{QCD}$ | `PARJ(81)` = 0.14 GeV | `PARJ(81)` = 0.28 GeV | | |
| ISR $\Lambda_{QCD}$ | `PARP(61)` = 0.192 GeV | `PARP(61)` = 0.096 GeV | −1.5% | −3.4% |
| ISR $k_T$ | `PARP(62)` = 1.0 GeV | `PARP(62)` = 2.0 GeV | | |
| | | `PARJ(81)` = 0.07 GeV | | |
| | | `PARP(61)` = 0.384 GeV | +4.8% | −1.7% |
| | | `PARP(62)` = 0.5 GeV | | |
| $\epsilon_b$ | `PARJ(55)` = −0.006 | `PARJ(55)` = −0.0037 | +0.4% | −0.4% |
| | | `PARJ(55)` = −0.0045 | +0.9% | −1.3% |
| $\epsilon_c$ | `PARJ(54)` = −0.07 | `PARJ(54)` = −0.020 | −1.0% | −1.1% |
| | | `PARJ(54)` = −0.042 | +0.1% | −1.4% |
| $b$ | `PARJ(42)` = 0.58 | `PARJ(42)` = 0.48 | +0.1% | −1.1% |
| | | `PARJ(42)` = 0.56 | +0.2% | −0.4% |
| $\sigma_q$ | `PARJ(21)` = 0.36 | `PARJ(21)` = 0.37 | +0.1% | −1.2% |
| | | `PARJ(21)` = 0.43 | −0.1% | −2.0% |
| Fragmentation combined | | | ±1.0% | ±2.8% |
| Total | | | −1.8%<br>+9.2% | −4.4%<br>+7.8% |

- **Energy resolution**

  Due to incomplete modeling of the material distribution inside the detector, additional smearing of the energy measurement caused by multiple scattering has to be expected. To evaluate the impact of this contribution, the transverse energy resolution of the electrons was enhanced by an additional Gaussian smearing with $\sigma(E_T) = 0.0073 \cdot E_T$. For jets, further smearing with $\sigma(E) = 0.45 \cdot \sqrt{E}$ was applied to all components of the four-momentum. In the case of muons, additional uncertainties are expected due to misalignment uncertainties. To take both effects into account, the width of the $1/p_T$-distribution of the muons was enhanced by an additional Gaussian of width $\sigma(1/p_T) = 0.011/p_T$.

- **Reconstruction efficiency**

  To estimate the impact of the uncertainties on the lepton reconstruction and identification, a certain fraction of all leptons were removed randomly before the event selection. A 1% fraction was discarded in case of the muons, while 0.2% of the electrons were removed.

- **Isolation efficiency**

  For many analysis, the uncertainty on the lepton isolation efficiency will be determined from data in clean $Z \to e^+e^-$ or $Z \to \mu^+\mu^-$ control samples. However, leptons in events with high jet multiplicity and pile-up are less isolated than leptons in final states with little jet activity. Semi-leptonic $t\bar{t}$ events will be produced abundantly at the LHC with a cross section of 360 pb and their final state contains at least four jets, of which two are $b$-jets. This event topology is much closer to the jet signature of the signal events than $Z \to \ell^+\ell^-$, and can therefore be used for a more realistic estimation of the lepton isolation uncertainty from data.

  **Selection of a control sample:**

  To determine the lepton isolation efficiency, a control sample of $t\bar{t}$ events with one isolated lepton in the final state needs to be selected. The selection of a sample which contains about 600k events will be possible with an integrated luminosity of about 1 fb$^{-1}$. A sufficiently high purity of the selected $t\bar{t}$ sample can be achieved by requiring that two top quarks be reconstructed: Based on a selection of leptons and jets and the electron/jet overlap removal as described in Section 3.4, at least one lepton, two $b$-jets, two light jets and missing $E_T$ greater than 20 GeV are required, which leads to a selection efficiency of 10%. All possible combinations of two light jets and a $b$-jet are built and the combination which yields an invariant light-jet pair mass closest to the nominal $W$-boson mass and overall invariant mass closest to the nominal top quark mass is assigned to the hadronic top. The $W$-mass constraint on the lepton-neutrino pair and the measured $\not{E}_T$ can be exploited to reconstruct the four-momentum of the neutrino. Out of two possible solutions, the neutrino four-momentum which provides the invariant mass closest to the top quark mass, when combined with the selected lepton and the remaining $b$-jet, is chosen. Mass window cuts of ±20 GeV around $M_W$ and of ±35 GeV around $M_t$ ensure a high probability that the selected event really is a $t\bar{t}$ event, and that the correct combination is chosen. 14% of all events satisfying the number of jet and lepton-cuts pass these additional requirements. Finally, the lepton control sample can be defined from leptons assigned to the leptonic top-decay, which are further required to be well separated from the $b$-tagged jet by $\Delta R$(lepton,$b$-jet)$> 0.4$.

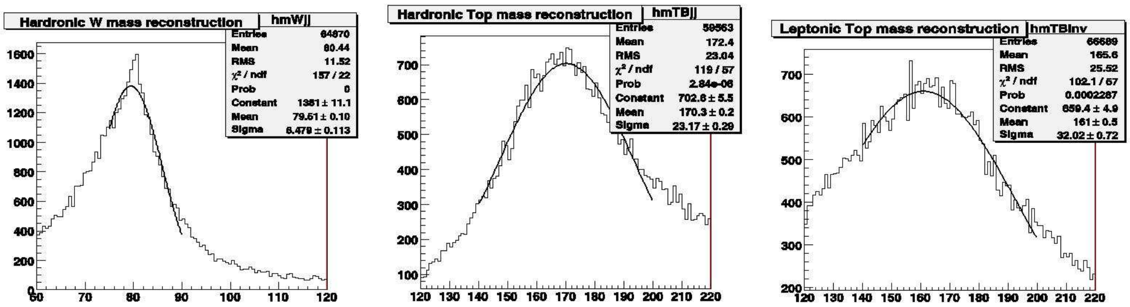

(a) hadronic W mass in $t\bar{t}$ control sample (b) jet pt before and after pileup (c) jet pt before and after pileup

FIGURE 3.17: hadronic W, hadronic and lepton top reconstructed mass distribution of control sample

### Contamination of the lepton sample:

Sources of contamination of the leptons tagged as $W$-decay products according to the procedure described above are leptons from $\tau$- or semi-leptonic heavy quark decays and fake leptons. Their contributions are below 10%, as shown in Table 3.17.

TABLE 3.17: Contamination of the lepton (in %) control sample.

| Lepton source | $W$ | $\tau$ | $b$ | Other |
|---|---|---|---|---|
| Electron | 90.9 | 6.7 | $< 0.1$ | 2.3 |
| Muon | 91.2 | 7.0 | 0.8 | 1.0 |

Table 3.18 shows the isolation efficiencies for the leptons in the lepton control sample after applying corrections for this contamination and for the differences in the $t\bar{t}$ and $t\bar{t}H, H \rightarrow WW$ final states. The latter correction factor accounts for the deviations of the $p_T$- and $\eta$-distributions in the $t\bar{t}$ control sample from those in the $t\bar{t}H$ Monte Carlo prediction by $\eta$- and $\phi$-dependent weights, which are obtained from a comparison of the $t\bar{t}$ and $t\bar{t}H$ Monte Carlo distributions. The statistical uncertainty on the isolation efficiencies reduces to $< 0.3\%$ for 30 fb$^{-1}$ of data. Taking the uncertainties on the correction factors to be 5% each, the overall uncertainty on the calorimeter-, tracker- and cone-isolation efficiency can be controlled at the level of 1% for both electrons and muons. This value scales up to a resulting event-level uncertainty of 1% for the 2L and 1.5% for the 3L final state, assuming an average of one (1.5) electron(s) or muon(s) per 2L (3L) event.

Table 3.18: Isolation efficiencies in the semi-leptonic $t\bar{t}$ control sample. Only statistical errors are given.

| | Control sample (after correction) | | | $t\bar{t}H$ (2L) | | |
|---|---|---|---|---|---|---|
| | Calo iso. | Track iso. | Cone iso. | Calo iso. | Track iso. | Cone iso. |
| Electron | (93.3±1.4)% | (89.8±1.4)% | (81.4±1.4)% | (93.1±1.0)% | (90.3±1.0)% | (82.7±1.4)% |
| Muon | (88.9±1.2)% | (87.2±1.2)% | (82.1±1.2)% | (89.4±0.9)% | (87.7±0.9)% | (85.2±0.9)% |

### 3.9.4 Systematic uncertainty on Monte Carlo based predictions

Table 3.19 lists all considered systematic uncertainties and the impact on the number of expected signal and background events at 30 fb$^{-1}$ for a Higgs mass of 160 GeV. For the 2L analysis, these contributions sum to a total uncertainty of roughly 10% for the signal and 11% for the background, if they are added in quadrature (i.e. neglecting possible correlations). In case of the 3L analysis, the total uncertainty for the signal is 9% and 14% for the background.

Table 3.19: Overview of the systematic uncertainties on the signal and background predictions.

| | $t\bar{t}H$ (2L) | | $t\bar{t}H$ (3L) | |
|---|---|---|---|---|
| | $N_{sig}$ | $N_{bkg}$ | $N_{sig}$ | $N_{bkg}$ |
| Standard($m_H = 160$ GeV) | 56.1 | 330 | 24.6 | 112 |
| Luminosity ±3% | ±3% | ±3% | ±3% | ±3% |
| Electron ID efficiency ±0.2% | ±0.2% | ±0.2% | ±0.3% | ±0.3% |
| Muon ID efficiency ±1% | ±1.0% | ±1.0% | ±1.5% | ±1.5% |
| Electron $E_T$ scale ±0.5% | ±0.1% | $< 0.1\%$ | ±0.2% | ±0.3% |
| Muon $E_T$ scale ±1% | ±0.5% | ±0.2% | ±0.7% | ±1.0% |
| Electron $p_T$ resolution | $< 0.1\%$ | $< 0.1\%$ | $-0.1\%$ | $+0.2\%$ |
| Muon $E_T$ resolution | $-0.6\%$ | $+2.2\%$ | $+0.3\%$ | $+0.9\%$ |
| Jet $E$ scale ±7% | $-1.2\%$ | $-4.9\%$ | ±2.7% | ±10.1% |
| Jet $E$ resolution | $-1.0\%$ | $-1.4\%$ | $-1.9\%$ | $-5.7\%$ |
| Electron isolation efficiency | ±1% | ±1% | ±1.5% | ±1.5% |
| Muon isolation efficiency | ±1% | ±1% | ±1.5% | ±1.5% |
| Total experimental uncertainty | ±3.9% | (±6.5%) | ±5.2% | (±12%) |
| $\sigma_{t\bar{t}} \pm 12\%$ | - | (±8.0%) | - | (±6.7%) |
| Theoretical | $^{+9.2\%}_{-1.8\%}$ | | $^{+7.8\%}_{-4.4\%}$ | |
| Total uncertainty | ±10% | (±11%) | ±9% | (±14%) |

The list of sources that were considered here is not complete, as the size of major contributions like e.g. the uncertainty on $t\bar{t}$+$n$ jets discussed above, or the non-isolated lepton rejection can hardly be estimated with our present knowledge. Even so, this study reveals that a reliable Monte Carlo based background subtraction will hardly be feasible, as the Monte Carlo prediction already suffers from sizable uncertainties on the order of the expected signal yield already at the level of the considered uncertainties. To control the background to this channel, it will therefore be mandatory to find a means to measure the background from the data in future analysis. Moreover, the cross section uncertainties-big contribution to systematics-will be reduced once have the real data and do the corresponding measurement. So, in the following, predictions of signal significance and coupling measurement accuracies will be given for the case of a maximum 10% uncertainty, which hopefully can be achieved with real data.

## 3.10 Top quark and Higgs boson Yukawa Coupling measurement

For an intermediate Higgs mass, above the $WW$ threshold but still too low for the “golden” $ZZ \rightarrow 4l$ signatures, $t\bar{t}H$ and $WH$ associated production with Higgs boson decaying to $WW$ are key channels for observing the Higgs boson. Both production channels are of particular interest since they provide access to important Higgs boson couplings and therefore give valuable contributions to tests of the Standard Model.

### 3.10.1 Significance of signal

Table 3.20 and Figure 3.18 summarize the signal significance that can be achieved by the analysis as a function of Higgs mass for the statistical only and a assumption of 10% uncertainties both on signal and backgrounds(which is hopefully achieved with real data studies). It indicate that for Higgs masses close to the $W$-pair mass, the observation of an excess of more than $2\sigma$ will be feasible in $t\bar{t}H, H \rightarrow WW$ channels with the first 30 fb$^{-1}$.

### 3.10.2 Precision of $\sigma_{t\bar{t}H} * Br_{H\rightarrow WW}$ measurement at 30 fb$^{-1}$

$\sigma_{t\bar{t}H} * Br_{H\rightarrow WW}$ is an observable from real data, and have less relevant on modeling. Once Higgs boson found at given mass at LHC, we can give the results of this observable.

If $S^{n\mathrm{L}} = N^{n\mathrm{L}}_{observed} - B^{n\mathrm{L}}$ signal events are observed in the $n$L ($n = 2, 3$) final state of $t\bar{t}H, H \rightarrow WW$ or $WH, H \rightarrow WW$, where $B^{n\mathrm{L}}$ is the estimated Standard Model background for the channel, the $\sigma_{t\bar{t}H} \times BR$ can be calculated as

$$\sigma_{t\bar{t}H} \times BR_{H\rightarrow WW} = \frac{S^{n\mathrm{L}}}{\mathcal{L} \cdot \epsilon_{n\mathrm{L}} \cdot C_{n\mathrm{L}}} \quad . \tag{3.3}$$

The integrated luminosity $\mathcal{L}$ needs to be measured and the signal event selection efficiency $\epsilon_{n\mathrm{L}}$ must be determined from Monte Carlo studies. The factor $C_{n\mathrm{L}}$ accounts for the combinatorics and $W$-decay branching ratios leading to the observed final state. The branching ratios are known to good precision [53] and therefore their errors can be neglected. Since the uncertainties on $\mathcal{L}$ and $\epsilon_{n\mathrm{L}}$ are considered to be negligible as well, the relative accuracy of the $\sigma \times BR$ measurements is given by the statistical uncertainty of $N_{observed}$ and the relative systematic uncertainty $a$ of the measurement of the background contribution according to:

TABLE 3.20: Overview on the signal significances that can be reached by the considered $t\bar{t}H$, $H \to WW$ channels at 30 $fb^{-1}$, taking into account once only the statistical errors and once in addition a systematic uncertainty on the background subtraction. The calculation of the significances for $t\bar{t}H$ was performed with frequentist approaches as implemented in the `LEPStats4LHCs` (no systematic errors) and `ProfileCombination` (including systematic errors) tools [51, 52].

| | stat. error only | | | ±10% systematic unc. | | |
|---|---|---|---|---|---|---|
| | 2L | 3L | combined | 2L | 3L | combined |
| $t\bar{t}H$ ($M_H = 120GeV$) | 0.7 | 0.5 | 0.9 | 0.4 | 0.4 | 0.6 |
| $t\bar{t}H$ ($M_H = 130GeV$) | 1.4 | 1.0 | 1.8 | 0.7 | 0.7 | 1.1 |
| $t\bar{t}H$ ($M_H = 140GeV$) | 2.2 | 1.6 | 2.8 | 1.2 | 1.1 | 1.6 |
| $t\bar{t}H$ ($M_H = 150GeV$) | 2.6 | 1.8 | 3.3 | 1.4 | 1.3 | 1.9 |
| $t\bar{t}H$ ($M_H = 160GeV$) | 3.0 | 2.1 | 3.8 | 1.5 | 1.5 | 2.1 |
| $t\bar{t}H$ ($M_H = 170GeV$) | 2.8 | 2.0 | 3.6 | 1.4 | 1.4 | 2.0 |
| $t\bar{t}H$ ($M_H = 180GeV$) | 2.3 | 1.7 | 3.0 | 1.2 | 1.2 | 1.7 |
| $t\bar{t}H$ ($M_H = 190GeV$) | 1.9 | 1.3 | 2.5 | 1.0 | 0.9 | 1.4 |
| $t\bar{t}H$ ($M_H = 200GeV$) | 1.5 | 1.0 | 1.9 | 0.8 | 0.7 | 1.1 |

$$\frac{\delta(\sigma \times BR_{H\to WW})}{\sigma \times BR_{H\to WW}} = \frac{\sqrt{S + B + (a \cdot B)^2}}{S} \quad . \tag{3.4}$$

of which a is the relative uncertainties of total background, 10% assumed. The dependence on the Higgs boson mass of the relative accuracy of $\sigma_{t\bar{t}H} \times BR_{H\to WW}$ is shown in Figure 3.19 for an integrated luminosity of 30 fb$^{-1}$. The best accuracy is found in the case $M_H = 160$ GeV, where 68.7% is possible in the 2L and 65.5% in the 3L final state, including 10% systematic background uncertainty. The combination of both measurements allows for an accuracy of 47.4%. Figure 3.19 up plots show the accuracy of $\sigma_{t\bar{t}H} \times BR_{H\to WW}$ as a function of Higgs mass between 120 GeV and 200 GeV.

### 3.10.3 Precision of $g_t$ measurement at 30 fb$^{-1}$

For a Higgs boson in the intermediate mass range, measurements of these cross-sections can be valuable inputs to tests of the Standard Model. The process $t\bar{t}H, H \to WW$ is of special interest as a probe of the top Yukawa coupling constant $g_t$. Under the assumption of Standard Model, the top quark Yukawa coupling can be written as following:

$$g_t^2 = \frac{S^{n\mathrm{L}}}{\mathcal{L} \cdot \epsilon_{n\mathrm{L}} \cdot I(m_H) \cdot BR_{H\to WW} \cdot C_{n\mathrm{L}}} \quad . \tag{3.5}$$

the factor $I(M_H)$ is the integral over the parton's momenta in initial states, propagator (width) of gluon or quark (Higgs/W) in middle states and leptons/jets phase space in the final states. Except for the Higgs mass, its dependence are well known on parton

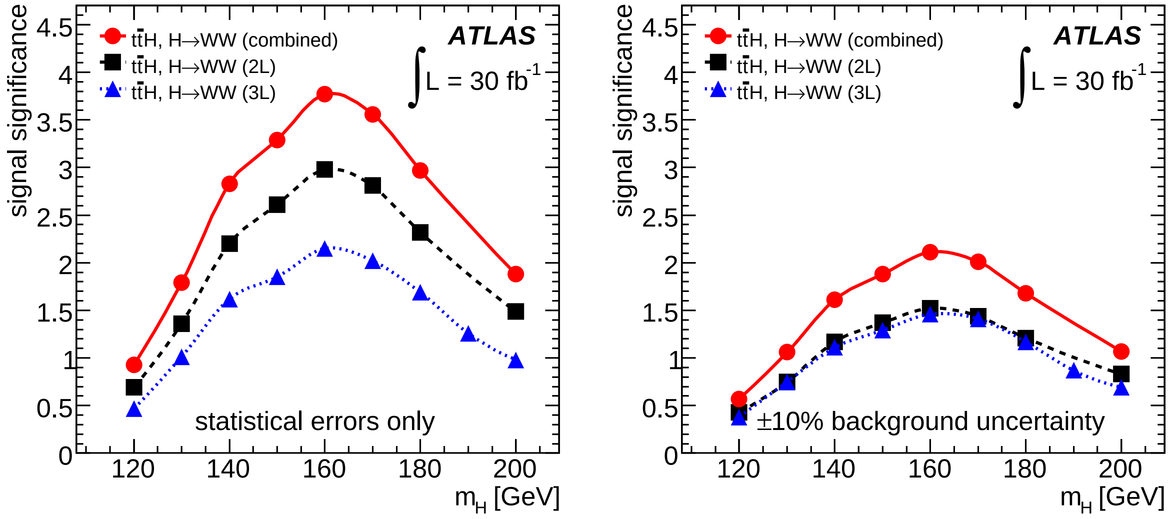

FIGURE 3.18: Signal significances in the $t\bar{t}H, H \to WW$ final states as a function of $M_H$ for 30 $fb^{-1}$ integrated luminosity.

distribution functions, strong interaction $\alpha_s$, top mass, hadronization/fragmentation. For this compact expression we had assumed a scalar type for the Lorentz structure between Higgs boson and top quark, and a near pole production for Higgs/W boson, however this factor $I(M_H)$ is still caculatable/known for more complex situations at certain accuracy. The accuracy of $g_t$ can be given as:

$$\frac{\delta g_t}{g_t} = \frac{\sqrt{S + B + (a \cdot B)^2}}{2S} \oplus \frac{\delta BR_{H\to WW}}{BR_{H\to WW}} \oplus \frac{\delta I(m_H)}{I(m_H)} \quad . \tag{3.6}$$

Assume $\frac{\delta BR_{H\to WW}}{BR_{H\to WW}} = \frac{\delta I(m_H)}{BR_{H\to WW}} = 0.1$ and neglect the correlation of these uncertainties, around Higgs mass of 160 GeV for an integrated luminosity of 30 fb$^{-1}$, The accuracy of $g_t$is found to be 34.3% in the 2L and 32.7% in the 3L final state, including 10% systematic background uncertainty. The combination of both measurements allows for an accuracy of 23.7%. Figure 3.19 down plots show the accuracy of $g_t$ as a function of Higgs mass between 120 GeV and 200 GeV.

## 3.11 Conclusion and discussion

- Based on ATLAS full simulation Monte Carlo, $ttH, H \to WW$ two leptons final state and three leptons final state analysis are performed. For a 160 GeV Higgs boson mass, at $30 fb^{-1}$, the signal are expected to be 56 for two lepton final state and 25 for three lepton final state, while the statistical significance are 3.0 and 2.1 separately.

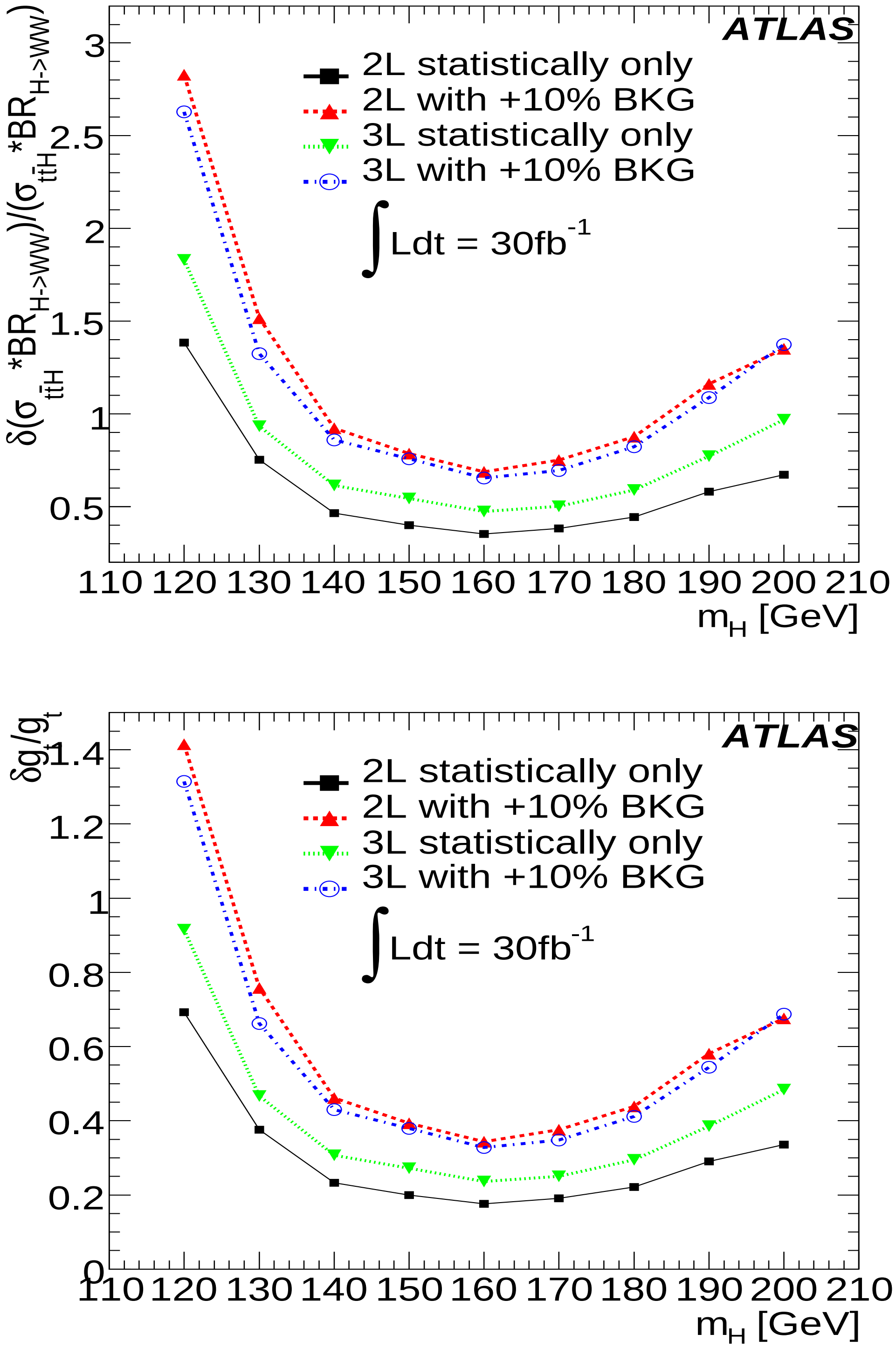

FIGURE 3.19: Accuracy of a measurement of $\sigma_{t\bar{t}H} \times BR(H \rightarrow WW)$(up) and accuracy of $g_T$(down) as a function of $M_H$ for 30 $fb^{-1}$ integrated luminosity.

- A set of detailed analysis performed on trigger, isolation, and pileup effects. The trigger have a impact less than 1% on the significance when a high pT isolated lepton is required. Pileup decrease the lepton identification efficiency, isolation selection performance and increase jets multiplicity, all these have a total decrease of $\sim 20\%$ of the significance, mostly blamed for the $t\bar{t}$ because of the decrease of isolation performance on non-isolated lepton rejection and increase of jet multiplicity.

- A complete study of the systematics uncertainty studies on luminosity and detector performance has been performed, the total uncertainties is 4%(5%) for 2L(3L) signal and 7%(12%) for backgrounds. While the theoretical uncertainties are 8%.

- After three years of low luminosity run of ATLAS and a $30fb^{-1}$ integrated luminosity, combining all the two lepton and three lepton channels, the combined branching ratio of $\sigma_{ttH} \times BR_{H\to WW(*)}$ could reach an accuracy of 47.4%, while the top quark Yukawa Coupling could reach 23.7%.

- $t\bar{t}H, H \to WW^{(*)}$ is a number counting experiment, the systematics uncertainties analysis showed that the precision of Yukawa coupling constant measurement is dominated by the level and uncertainty of backgrounds. Therefore, it is mandatory to develop real data control samples to estimate the backgrounds and uncertainties. This will be the next important direction for the $t\bar{t}H, H \to WW^{(*)}$ analysis

- The use of fitting with the constrains of W and top mass to reconstruction $t\bar{t}H, H \to WW^{(*)}$ events(so called mass constraint fit), and the use of multivariate analysis to distinguish the signal and backgrounds, are also directions to improve the performance of this analysis.

# Chapter 4

# Combined Test Beam description

Contents

## 4.1 Introduction

It is important to know the detector performances before and for physics analysis, especially for the systematic uncertainties studies. Test beam is one of the key methods to know the performance of detector before data taking. It can be used to study the identification and reconstruction of certain particles. Every module of the detector was tested during the building phase and with test beams as standardalone detector with minimal mater in front. Therefore, it is important to know the performance by putting all components of the detector as close as possible to the real detector geometry and material distributions. In detector combined mode, it is possible to identify particles using combined detector information. For example, the energy of low $p_T$ electrons, should be measured by combining the calorimeter and inner detector information, since the energy resolution of the calorimeter is worsen at low energy while inner detector has better performance of momentum measurement at low $p_T$ region. Moreover, it is important to have similar mater distribution as much as possible since mater distribution can affects the performances, especially for very lower energy(VLE) particles.

During summer and autumn of 2004, ATLAS combined test beam (CTB) was performed at beam line H8 of Super Proton Synchrotron at CERN [54]. This was the first time to put all ATLAS sub-detector together and tested in combined model. The goal of this CTB was to demonstrate that all the ATLAS sub-detectors (barrel slice) can take combined data using ATLAS (prototypes and/or series production) read-out electronics and software. The goals of these tests are:

- Integrate the DAQ system, level 1 trigger, the detectors. Test level 1 trigger at LHC collision frequency. This can be seen as a pre-commissioning of the TDAQ system.

- Combined Reconstruction of muons, electrons and pions using the information from the Inner Detector, the combined Calorimetry and the Muon Spectrometer.

- Test of the reconstruction and simulation software, tuning of the Monte Carlo to the test beam data.

- Energy and position resolutions, efficiencies and noise.

- ID: Global system performance and data handling, pixel spatial resolution, and efficiency vs beam intensity.

- Calorimeters: energy calibration and sharing, electronic vs hadronic energy measurements, linearity and uniformity versus energy and eta, shower containment and profiles, studies of energy losses in passive material(cryostat walls), and jet reconstruction. In CTB2004, special runs were taken at very low energy(VLE) of $p_T < 10GeV$. These are first dedicated runs for calorimeter very low energy response study.

- Muon Spectrometer: General stability and uniformity studies of MDT chambers. Test of the barrel and end-cap trigger and alignment systems. Muon momentum measurements in the end-cap stand.

## 4.2 ATLAS Test Beam detector setup

The test beam table setup use final production modules of the various sub detectors, and mimic to ATLAS final configuration as much as possible. The set-up of the combined test beam is shown in figure 4.1.

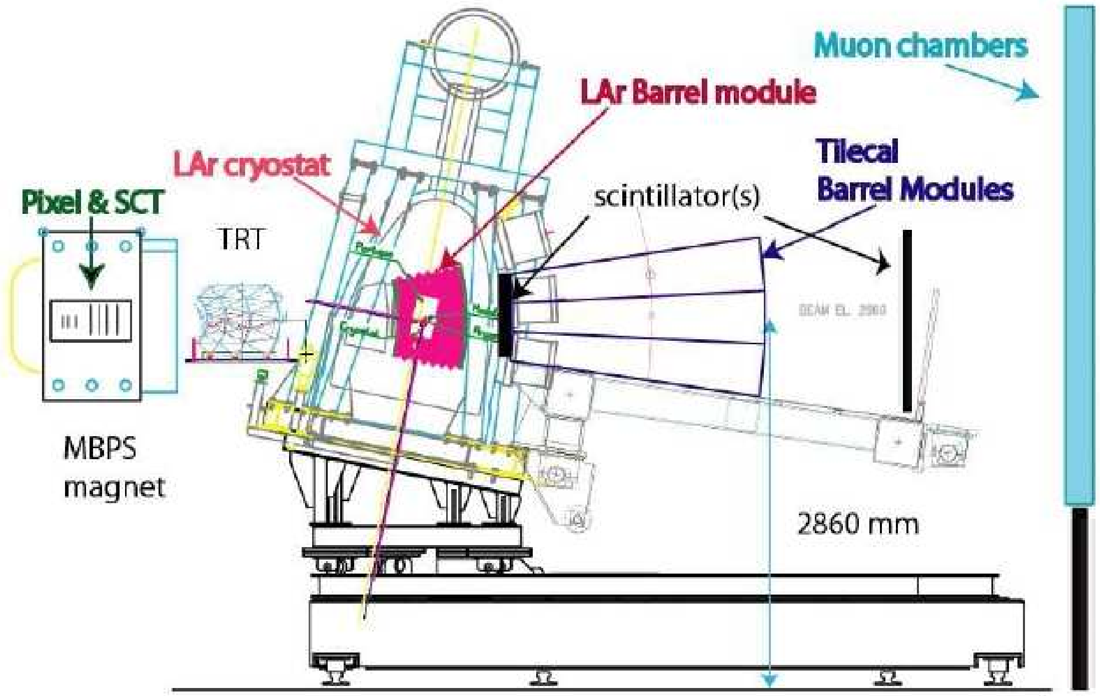

FIGURE 4.1: Schematic of test beam table setup. The beam particles first hit the pixel and SCT modules, and then continue towards the TRT, Calorimeters,and Muon modules. In the coordinate system used, the beam travels in the positive x direction, y points upwards, and z points out of the paper, which also is the positive eta direction. The table containing the calorimeters could be translated and totated to simulate that the particles come from the interaction point at different $\eta$.

The first part of the detector system in the beam line is the Inner Detector, represented by 6 modules of pixel, 2 in the pixel B layer and 2 for pixel layer 1 and 2 each, with an active size of $x \times y = 60.8 \times 16.4mm^2$; 4 SCT layers with 2modules per layer covering an area of $x \times y = 120 \times 120mm^2$; two TRT barrel wedges, each is equivalent to 1/16 of the circumference of a cylinder, with inner radius of 558 mm and outer radius of 1080 mm and overall length(along the x axis) of 1425.5mm. Both Pixel and SCT were installed inside a 2 T magnetic field created by the MBPS dipole magnet. However the TRT was always kept outside for technical reason, which is different from the ATLAS detector configuration. Then followed, the prototype of EM calorimeter, housed in a cryostat filled with liquid argon. For the hadronic Tile calorimeter, three barrel and three extended barrel modules were used. A couple of meters behind the table, there are a fraction of the barrel Muon Spectrometer, a Monitored Drift Tube(MDT) BOS(Barrel Outer Small) chamber, and four more barrel MDT stations(seven chambers) were placed further downstream. One end-cap Cathode Strip Chamber, six end-cap MDT chambers at three stations, one end-cap Thin Gap Chamber(TGC) triplet, and two TGC doublets placed in sequence. There was also a muon trigger consisting of two $10 \times 10cm^2$ scintillators, two trigger stations of barrel Resistive Plate Counters and magnets installed.

## 4.3 The test beam line

The beam in the H8 beam line is produced by protons extracted for the SPS at energies up to 400GeV. The typical intensity of the primary beam is about $10^{12}$ protons per burst. The proton beam from the SPS is guided to the North Area, direct onto T4 target of up to 300 mm thick Beryllium plate, where a shower of secondary particles is produced. In the North Area, there are 4 beamlines, two from the T4 taget(H6,H8), and two from the T2 target(H2,H4). In standard conditions, the secondary beam energy in the H8 beam line can be adjusted between 10 GeV and 350 GeV. A secondary filter target can be used to achieve a higher electron or pion fraction in the beam. As secondary target, one can choose either 8 or 16 mm lead, or 1000 mm of Polyethylene plus an absorber, air or lead, to obtain pure electrons or pions.

The beamline consists of a number of magnets, quadrapole and dipoles, for focusing and bending the particles and selecting the right momentum by controlling the magnet currents of a vertical magnetic spectrometer.

In addition, the H8 beamline offers the possibility of very low energy beams. To achieve this, the beam is directed on an additional target further downstream (T48), close to the experiment, and a dedicated magnetic spectrometer, to provide energies from 1 to 9 GeV particles.

## 4.4 Beamline instrumentation

In addition to the detector modules, various beam instruments have been placed in the H8 beam line [54]. The data from this elements have been recorded together with the event data to allow off line data quality control. Some of the scintillators were also used to trigger the readout. The layout of the beam instruments is shown in 4.2, including the configuration of scintillators, beam chambers and Čerenkov detector. The detailed position of each beamline instrumentation is shown in table 4.1.

### 4.4.1 Čerenkov counters

There are three one meter long Čerenkov counters along the H8 beam line: CHRV1(HE,Helium) is furthest upstream, CHRV2(HE/VLE) are names of two Čerenkov counters, one is on the High Energy beam line path and the other is on the Very Low Energy beam line path. They are used to identify muon/pion/electrons. These Čerenkov counters operate as threshold counter, only the velocity of particles above a certain threshold will produce a signal. For a given momentum of beam, the pressure of the gas can be set so that only certain particle bellow a mass threshold will reach the velocity threshold. The sperate possibility for Helium and Nitrogen are show in figure 4.3.

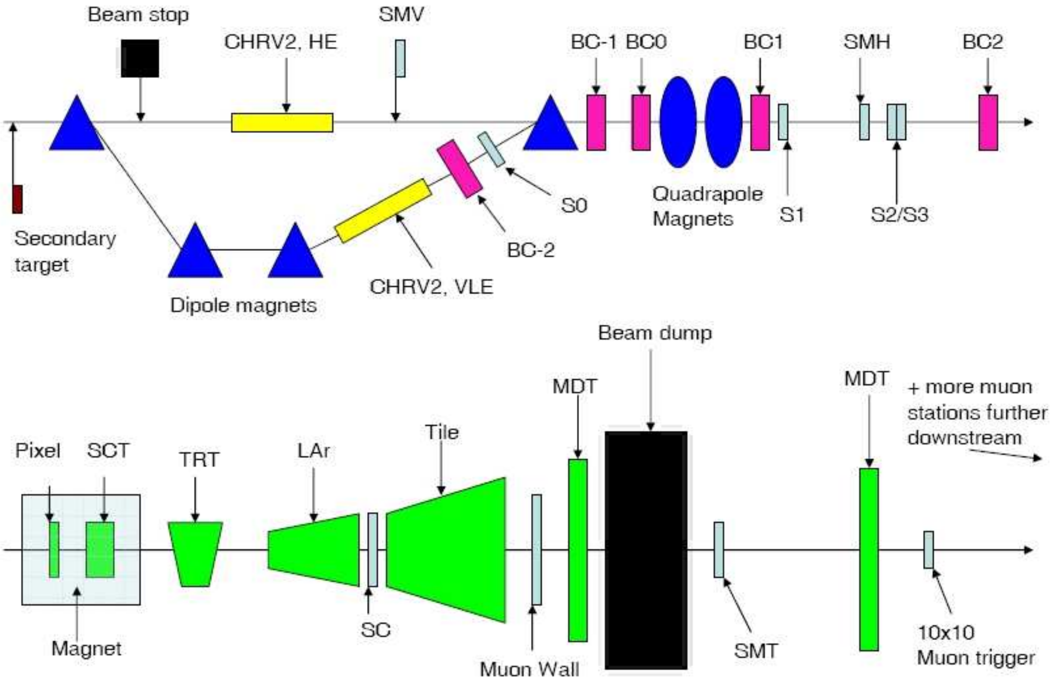

Figure 4.2: Schematic outline of the beamline instrumentation, and also of the ATLAS sub-detector elements.

| Beam element | z position | Beam element | z position |
|---|---|---|---|
| VLE target | -45219 | S2 | -7558,-7558,NA |
| CHRV1 | -114294 | S3 | -7523,-7523,NA |
| CHRV2,HE | -18677 | BC2 | -4813,-7590,NA |
| CHRV2,VLE | -20877 | Pixel box | 146 |
| SMV | -17677 | SCT | 512 |
| BC-2 | -19862($x \sim 511$) | TRT1 | 1152 |
| BC-1 | -13685 | LAr | 3768($\eta = 0$) |
| BC0 | -12540 | SC | 4568 |
| BC1 | -9190 | TileCal | 4598($\eta = 0$) |
| S1 | -8843 | Muon Wall | 7394 |
| SMH | 8083,NA,NA | SMT | 20669 |

Table 4.1: The distances are given in mm, z(=y=x)=0, is at the front surface of the ID magnet, the position is given at the start of the Čerenkov's. For the detectors it is as follows: front wall of Pixel box, geometrical center of the SCT box, center of the cylindrical arc of the TRT, start of LAr module, and start of the TileCal modules. Some of the Beam line instruments was in different position and is divided into three periods; Period1 from 2 August until 22 September, Period2 from 22 September until 3 November, and Period3 from 3 November until 15 of November. NA = Not Available in that run period. SMV is only used during VLE runs [55].

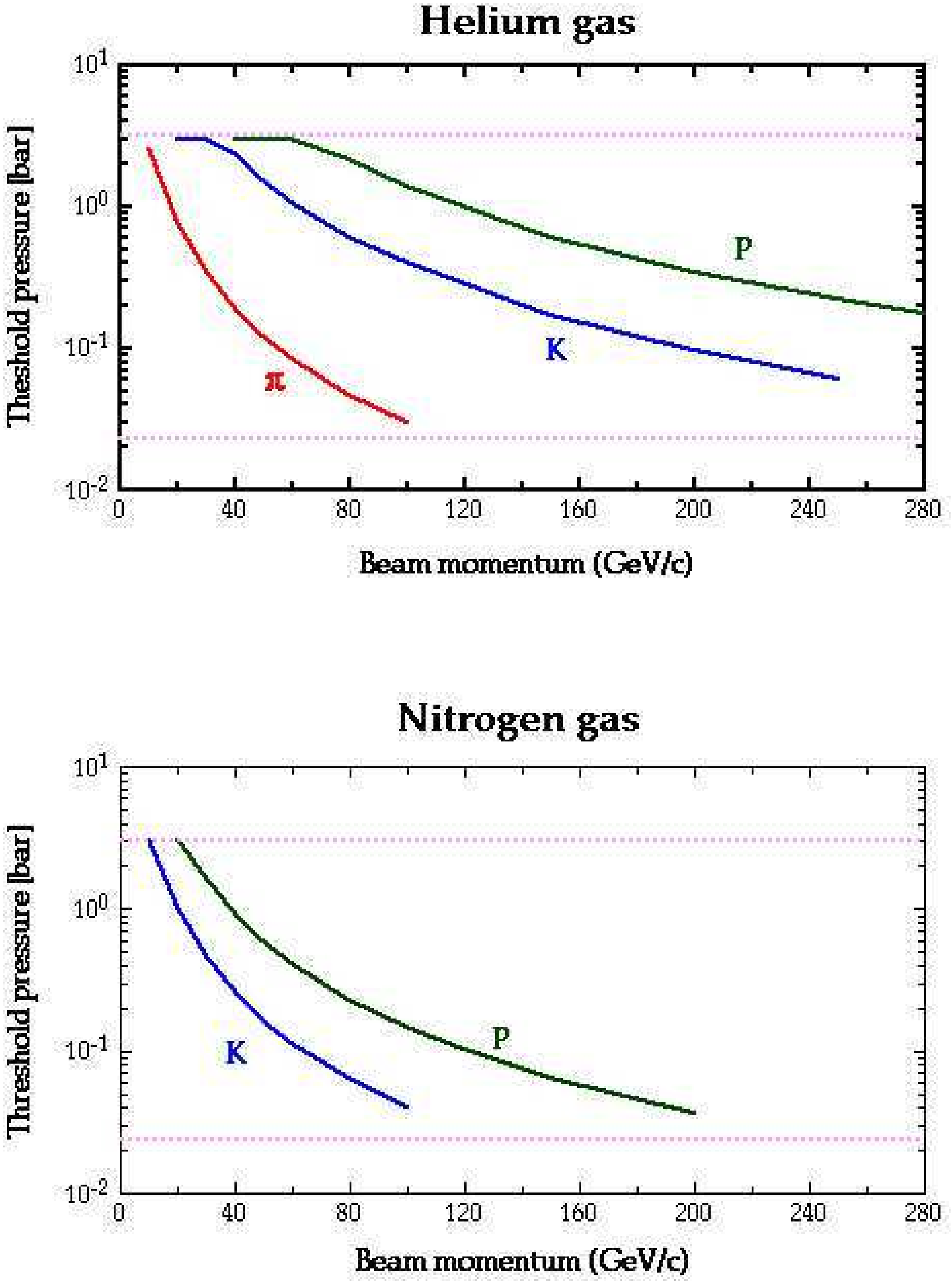

FIGURE 4.3: The threshold pressure as a function of the beam momentum for different particles in Helium(up) and Nitrogen(bottom) gas. The dotted line indicates the minimum(29 mbar) and maximum(3 bar) pressure possible in the Čerenkov counters.

### 4.4.2 Beam Chambers

There are in total five beam line chambers, which are used to detect the profile of beam. Beam Chamber BC-2 is the beam chamber which is only located in the VLE beam line, while BC-1, BC0, BC1, BC2 are common to both beam line. BC-2, BC-1, BC0, together with a magnet B8(which is local between BC-2 and BC-1), formed a spectrometer to determine the energy of the VLE beam.

There are four readouts concerning to the x, y position determination, The Beam Profile Chamber reconstruction algorithm calculates the x and the y position on the chamber from the four TDC(Time to Digital Converter) measurements with the calibration constants of a factor and an offset that converts the time-difference between the two TDC values into a position. These calibration constants are obtained by calibration procedure. And the calculation is reliable only when all these four TDC read out exist. The spacial resolution of x and y directions both are about 200 $\mu m$.

### 4.4.3 Scintillators

There are several kinds of scintillators in the beamline, Some of them were used for trigger purposes, others used for beam qualities selections. The signal amplitudes of the scintillators were digitized and written out together with the detector data. For some of the scintillators the signal phase with respect to the readout clock was measured as well.

- **S0:** In VLE beam line path and only functional in VLE mode, just after BC-2 and CHRV2(VLE). It has a big size of $10 \times 10 cm^2$ and it is used for checking the beam intensity and quality, and also for the Time-Of-Flight(TOF) measurement.

- **S1:** This is a big ($10 \times 10 cm^2$) scintillator located after the last quadrupole magnet. The amplitude as well as the phase of the signal of this scintillator is measured.

- **S2 and S3:** These are two small scintillators ($3 \times 3 cm^2$) used in the trigger. They are read out by two photomultipliers. The signal phase was measured for both photomultipliers, the amplitude only for one.

- **Muon Veto:** This scintillator is located in the high energy beam line and used to veto muon passing through the high energy beam stop during low energy runs.

- **Muon Halo:** This is also a big scintillator with a small hole in the center. It was used to veto muon outside of the beam axis.

- **Muon Tag:** This scintillator was placed behind the beam dump in order to identify muons.

- **Muon Wall:** This was a set of 12 scintillators behind the Tile Calorimeter.

- **Cryostat Scintillators:** Two large scintillators located between the liquid argon cryostat and the Tile Calorimeter.

### 4.4.4 Trigger and readout

At the test beam, the main beam trigger consists of scintillators S1, S2 and S3. While other scintillators such as SMH, SMV and SMT were also used as additional sources. A beam particle which gives a signal in all the triggers will give rise to a Master trigger, and a Level 1 Accept. The Master trigger will start the common crate TDC, and open up a gate for reading out ADC. A dedicated computer is used to monitor the data at different stage. Figure 4.4 shows the schematic overview of trigger logic.

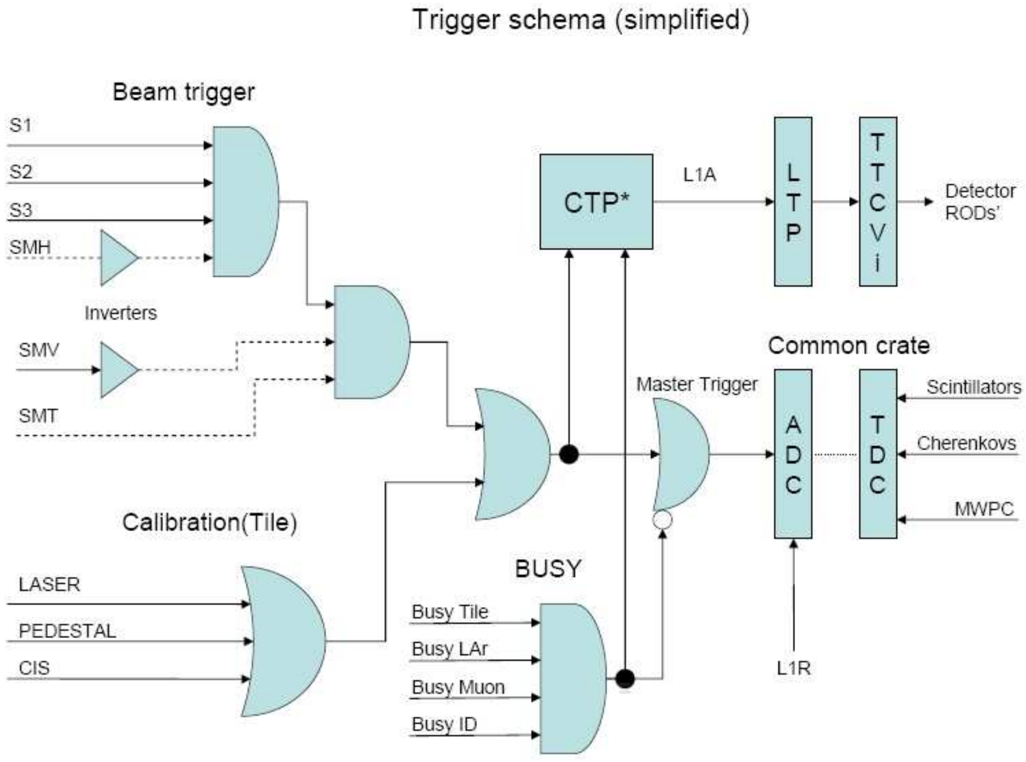

FIGURE 4.4: Simplified schema of CTB trigger logic. The Cental Trigger Processor(CTP) is emulated, except for the 25 ns run periods

## 4.5 Energy Reconstruction in Liquid Argon

Different particles can be identified and reconstructed using ID, Calorimeter or Muon spectrometer information, and almost all physics objects we are interested in will leave energy signal in the calorimeter system. Here I only concentrate on electron reconstruction performance studies in EM calorimeter. Energy measurement is the most important function of a calorimeter, and in the following will present energy reconstruction in the EM calorimeter.

### 4.5.1 Energy reconstruction of single cell

The Signal is collected by Front End Boards, where it pass through a pre-amplifier, a shaper and then sampled by a 12 bit ADC, which has a pedestal about 1000 ADC counts of the undershoot of the shaper. Figure 4.5 shows the triangular shape as well as the shaped signal. The samples are sent to Read-Out-Driver in the counting room via an optical link. The single cell energy is computed off-line using the formula:

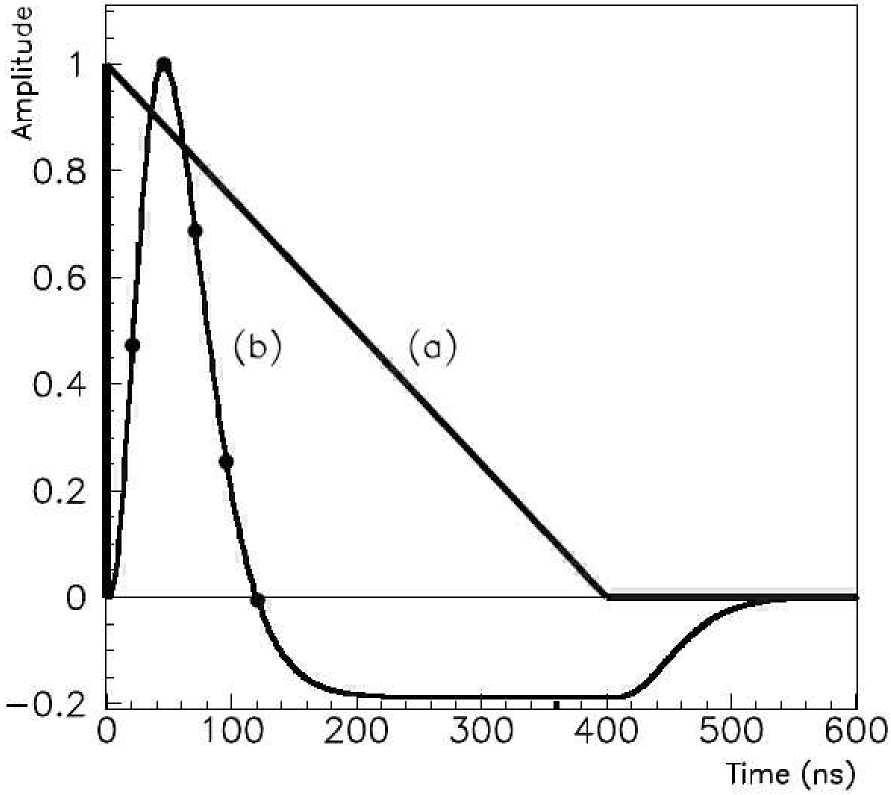

FIGURE 4.5: Form of the ionization signal(a) and the shaped ionization signal(b)

$$E = F_{DAC\to\mu A} \cdot F_{\mu A\to MeV} \cdot \frac{M_{phys}}{M_{cali}} \sum_{j=0,2} R_j [ADC_{peak}]^j, \tag{4.1}$$

While the electronic calibration constants used are the following [56]:

#### 4.5.1.1 $\mathbf{ADC_{peak}}$

This factor is the peak of the shaped ionization signal computed by optimal filtering or by some alternative methods.

- Optimal Filtering method: The method of Optimal Filtering (OF) is an elegant way to compute the peak of a shaped ionization signal and at the same time minimizing the noise contribution. The amplitude A and the time offset $\tau$ of such a signal can be computed by the formulas:

  $$A = \sum a_i s_i, \tag{4.2}$$

  $$A_\tau = \sum b_i s_i, \tag{4.3}$$

  where $a_i$ and $b_i$ respectively are the energy and time Optimal Filtering Coefficients (OFC) and $s_i$ are the pedestal-subtracted ADC samples. Note that the time information is only meaningful if the ionization signal is sufficiently above noise.

  The OFC are computed for each cell and gain using the following formula for the signal:

  $$S(t) = A \cdot (g(t) - \tau g'(t) + n(t)), \tag{4.4}$$

  where g(t) is the normalized shape of the ionization signal, $g'(t)$ is its first derivative and n(t) is the noise component given by the noise autocorrelation matrix.

- Highest Sample: Use the highest ADC sample. This leads to a positive bias since the noise does not cancel out.

- Fixed sample: Use a sample which index is fixed in certain period.

- Cubic or Parabolic Interpolation: Interpolate a 2nd or 3rd order polynomial on 3 or 4 samples respectively (if the maximum is above a given threshold). Since the signal shape is not parabolic neither cubic around the maximum, these interpolations lead to biased results. One can derive corrections to these biases using calibration run. For historical reasons, this has been done for the parabolic case, but not the cubic one. Therefore, one mainly use the parabolic bias-corrected method as an alternative reconstruction method when OFC are not available.

#### 4.5.1.2 Ramp factors $\mathbf{R_j}$

These factors are the second order electronics ramps factors converting the ADC to DAC. The relation of ADC counts to DAC is measured on a regular basis by the electronic calibration system. Figure 4.6 shows a simple graphical representation on the way detector

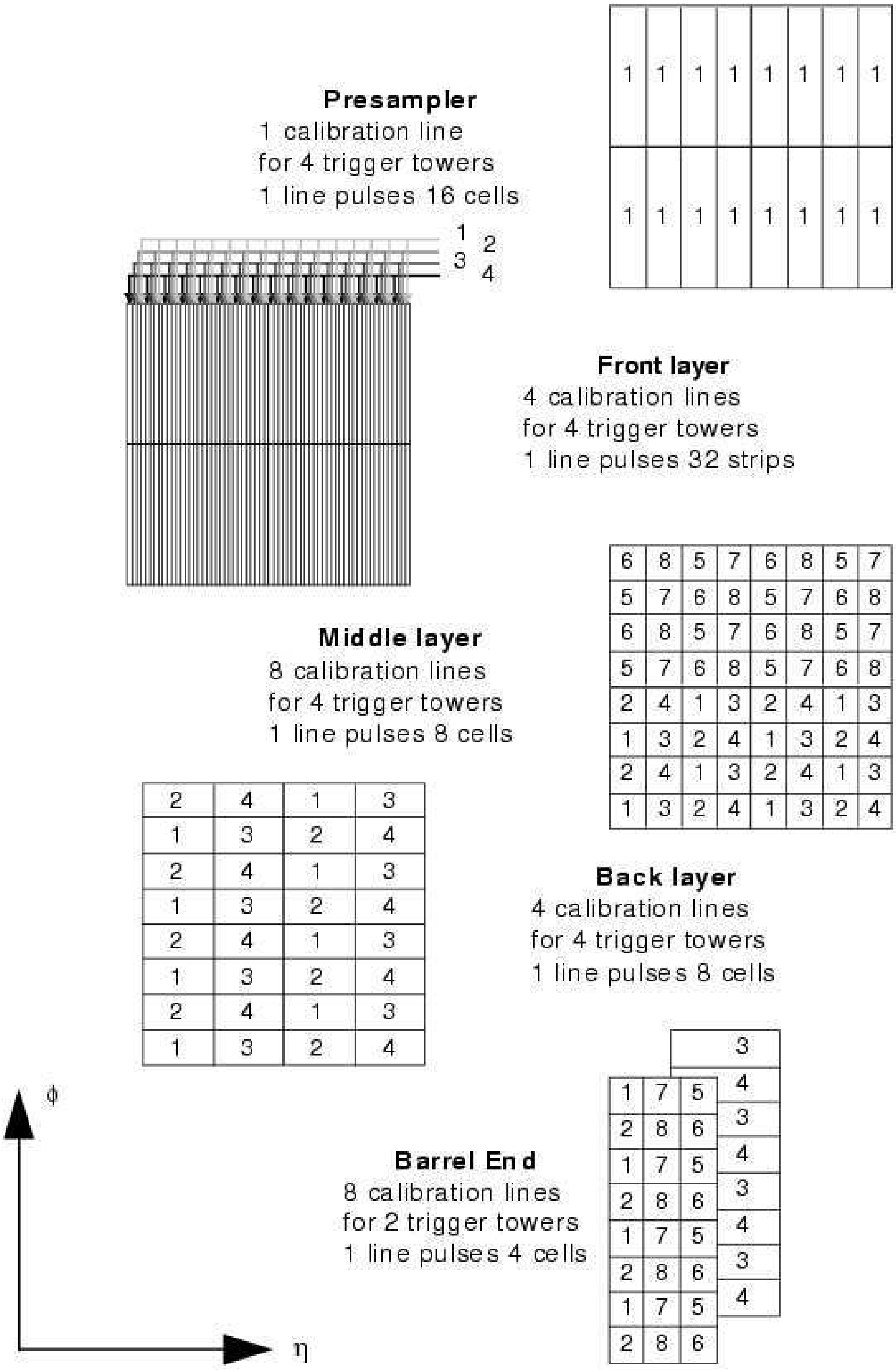

FIGURE 4.6: Description of the pattern pulsed by each calibration line [57]

cells are pulsed by calibration board. The polynomial ramp is used to take possible non-linearities of the electronic chain into account.

To extract $R_j$, one need to obtain the $ADC_{peak}$ versus DAC curves. Typically, input 100 times of 16 values of DAC currents, and get an averaged calibration wave for each DAC. subtract the wave corresponding to DAC=0 of all other waves. Then, reconstruct $ADC_{peak}$. The relation of DAC and $ADC_{peak}$ for each component of calorimeter are shown in figure 4.7:

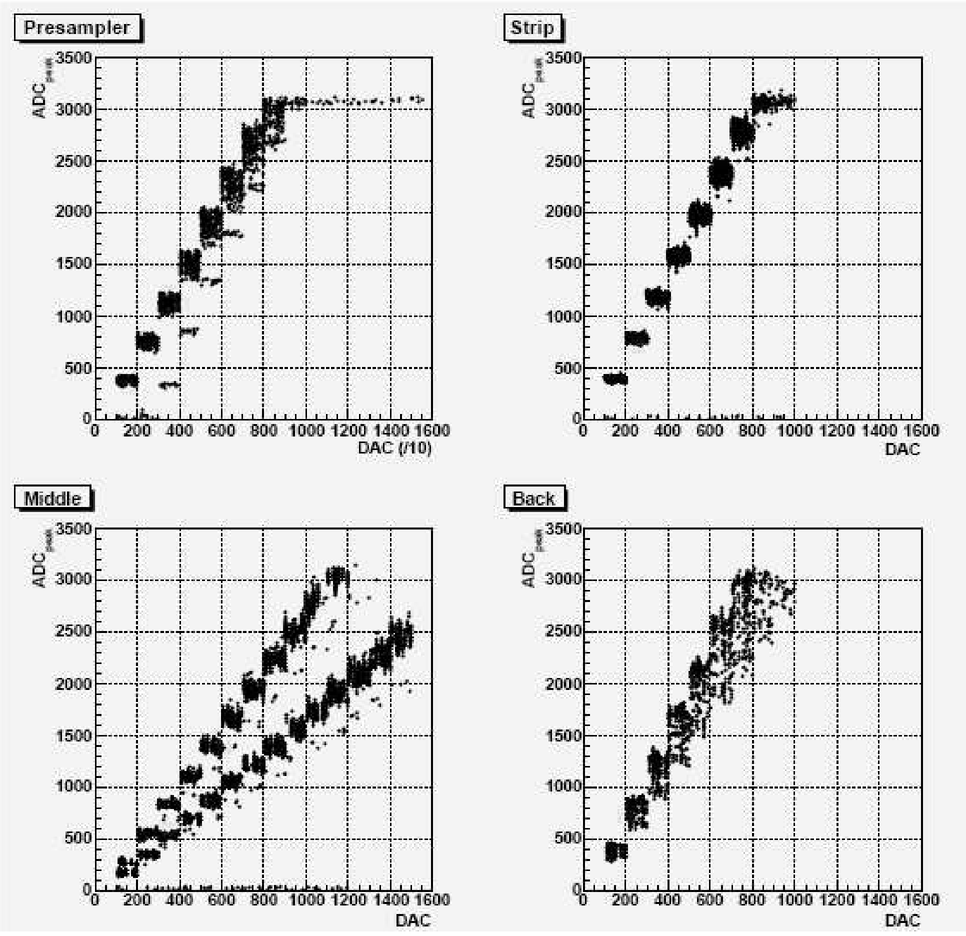

FIGURE 4.7: $ADC_{peak}$ versus DAC curves obtained in a high gain ramp run for the 4 layers of the module (low $\eta$ cabling). Because of the shortage of FEBs, MID2 and MID3 FEBs were used for MID0 and MID1 cells; this explains the two slopes observed in the distribution for the Middle layer as the preamplifiers have different gains.

A parabolic interpolation on the non-saturating points is then used to extract the $ADC_{peak}$ to DAC relation:

$$DAC = R_0 + R_1 \cdot ADC_{peak} + R_2 \cdot ADC^2_{peak}, \tag{4.5}$$

where $R_0$,$R_1$and$R_2$ are ramp coefficients.

#### 4.5.1.3 $\mathbf{F_{DAC\rightarrow\mu A}}$ and $\mathbf{F_{\mu A\rightarrow MeV}}$

These two factors are converting the DAC into MEV.

The $F_{DAC\rightarrow\mu A}$ factor is determined by the calibration board specificities and the injection resistor on the mother board. The amplitude of the signal is controlled by a 16 bit DAC, providing a voltage between 0 and 1 V, with

$$F_{DAC\rightarrow\mu A}(\mu A/DAC) = \frac{76.295\mu V}{R_{inj}}, \tag{4.6}$$

where $R_{inj}$ is the injection resistor.

The factor $F_{\mu A\rightarrow MeV}$ converts the current ($\mu A$) into energy(MeV). It is different for the accordion and presampler parts of the calorimeter and could determined through several means. In the straight sections of the accordion folds, where the electric field is simple and homogeneous the conversion factor from energy deposit to the induced current can be easily calculated from the drift time and the average energy needed to create a single electron/ion pair. For argon, this corresponds to W=23.6 eV per $e^-$/ion-pair. An energy deposit of one eV frees electrons with a total charge of e/W and the same amount of ions (e is the elementary charge). The ions drift very slowly inducing a small current that is neglected in the following calculation. The electrons drift quickly and induce a current at the signal electrode. As the electrons get absorbed at the anode, the current decreases. This leads to the triangular shape of the signal. The peak current is induced by the charge of all the electrons drifting with the velocity v over the distance d. The peak current per deposited charge q is given by:

$$I = \frac{q \cdot v}{d} \tag{4.7}$$

Since the drift time is determined by the gap width and the velocity $t_d = d/v$ and the charge per deposited eV is given by q/E = e/W, then:

$$I/E = \frac{e}{W \cdot t_d} \tag{4.8}$$

The drift velocity v depends on the electric field and the temperature of the argon. The Geant4 simulation of the Liquid Argon Calorimeter includes a detailed description of the electrical field and charge-collection in the folds of the accordion, yields a results of I/E = 14.2 nA/MeV. The I/E factor can be derived by comparing the energy deposit predicted by the simulation with the current measured in the beam test, assuming that all other effects are properly described in the simulation. This gives I/E = 16 nA/MeV, from 2002 Test Beam data. There is still some uncertainty about the I/E factor(such as the temperature of Liquid Argon. In CTB2004, a factor 1.03 is applied to correct this current to energy factor derived from 2002 test beam) and thus the absolute calibration of the accordion calorimeter. The final verification of this value will be based on physics data, mainly by exploiting the precise knowledge of the mass and shape of the Z boson, using the so-called in-situ calibration.

#### 4.5.1.4 $\frac{\mathbf{M_{phys}}}{\mathbf{M_{cali}}}$

This factor corrects the ramp factors for the difference between the calibration and physics signal heights. It is mainly because of the presence of the inductance L between the injection points of the two currents. Figure 4.8 shows the $\frac{M_{phys}}{M_{cali}}$ in CTB2004.

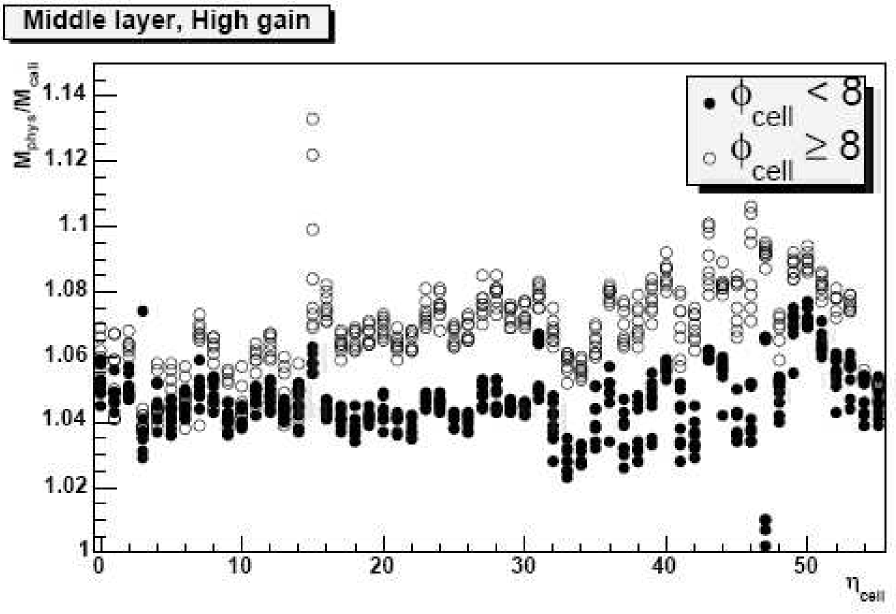

FIGURE 4.8: $\frac{M_{phys}}{M_{cali}}$ factor as obtained from the RTM parameters for Middle layer cells, High gain, Barrel.

#### 4.5.1.5 Pedestal and noise

Pedestal is the output of each channel without beamline or calibration signal, It depends on the electronic of FEB and temperature of FEB. Pedestals stored in the databases were measured every 8 hours with dedicated runs. In addition and when available, pedestals from random triggers taken during physics runs were added to cope with the FEB temperature instability. The pedestal is computed for each cell and shaper gain by an average over a given number of periodic triggers (typically about 1000 ADC counts during the 2004 CTB) and over the number of samples (typically 7) leading to an uncertainty of $\sigma$=84 ADC counts. The RMS of pedestal is noise.

#### 4.5.1.6 Cross-Talk

The readout signal of the calorimeter cells is affected by mostly capacitive cross-talk. Detailed measurements have been performed during previous beam tests [58, 59] and a cross-talk map has been produced. The biggest cross-talk (about 7%) can be observed between neighboring strip cells.

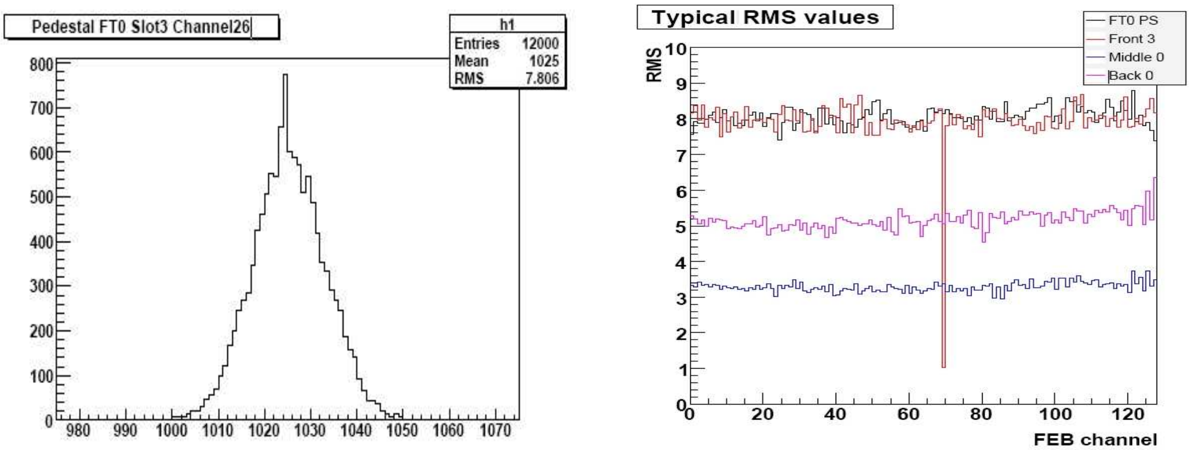

(a) Pedestal distribution for one channel over 6 samples and 2000 event

(b) Typical pedestal RMS distributions for low $\eta$ FEBs

FIGURE 4.9: Typical Pedestal and its RMS(noise) in CTB2004

The cross-talk has two major effects on the readout signal: first, a fraction of the energy of a cell is spread out to its neighbors and second, the pulse shape is distorted. Since neighboring cells will be contained in the same cluster the loss of signal to the neighbors does not change the cluster energy significantly. But the situation for calibration runs is different: every cell is pulsed individually and independently from its neighbors, so signal gets lost to the neighbors and the reconstructed calibration pulse peak is lower. The reconstructed ramp coefficients are therefore higher by this fraction (they compensate the cross talk induced loss of signal). This effect is relevant in the strips and has to be corrected.

### 4.5.2 Performance of electron energy reconstruction in EM calorimeter

Electron always deposit energy in EM calorimeter, the number of particles in its shower fluctuates statistically, and the total ionization signal is proportional to the number of charged particles, so, the reconstruction energy fluctuates in the same way, with a gaussian approximation. This is the so called sampling(stochastic) term of the calorimeter. Further more, a constant term is needed to account for instrumentation effects independent from the shower development like non-uniform absorber thickness. So, the resolution of electron energy can be expressed as following:

$$\frac{\sigma(E)}{E} = \frac{a}{\sqrt{E(GeV)}} \oplus b \tag{4.9}$$

However, the electron resolution results should base on well calibrated energy. Figure 4.11 shows the linearity and resolution achieved with Test Beam 2002 electrons. It shows that from $p_T \geq 15\ GeV$, the non-linearity is under 0.1%, while the resolution stochastic term is $10\%/\sqrt{E}$ and the constant term is 0.17%. This test beam had less

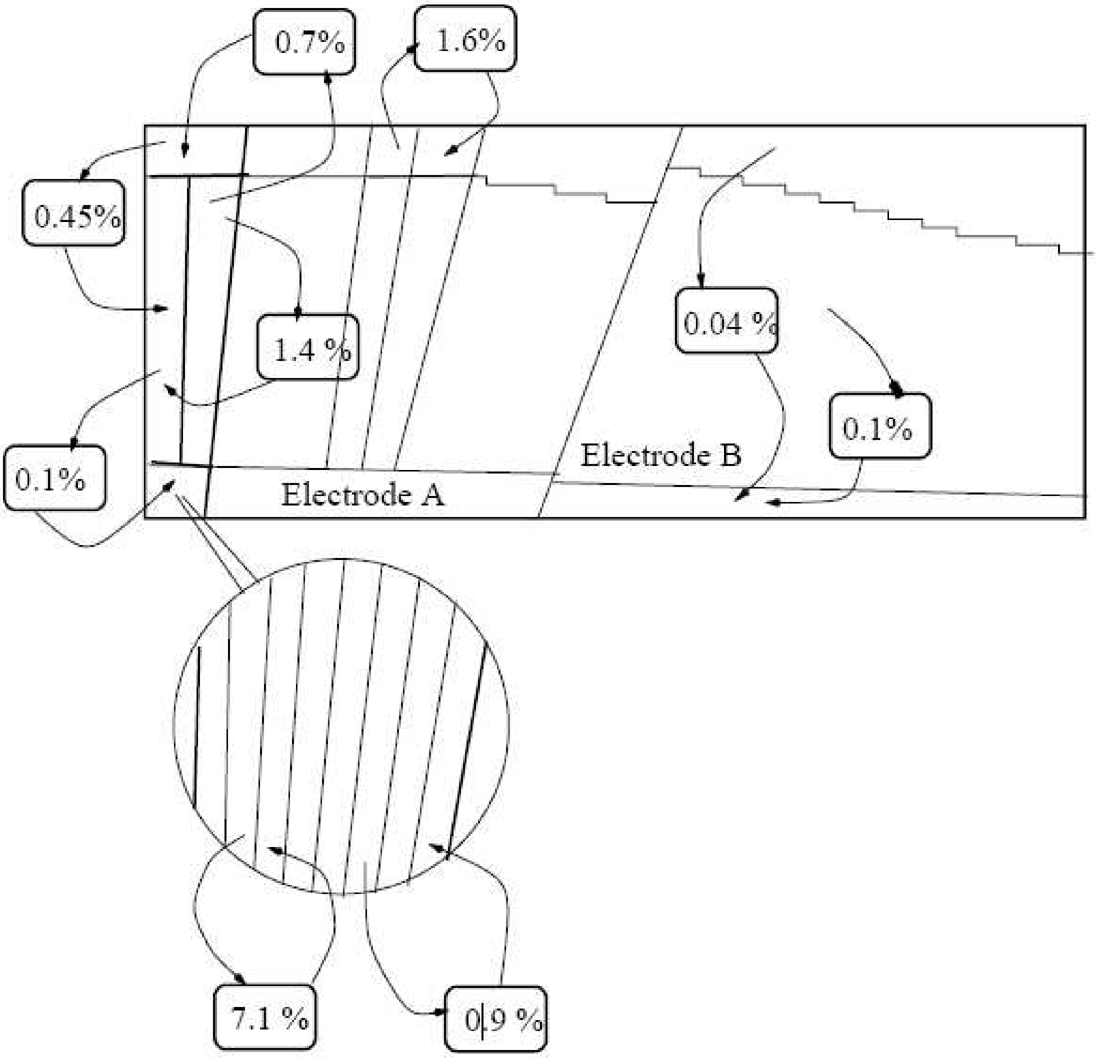

FIGURE 4.10: Cross-talk measured in module M13

material in front of calorimeter compared to ATLAS real detector configuration, which makes the linearity and resolution optimistic. So, the combined test beam 2004 is necessary for us to understand the expected performance of ATLAS calorimeter. From these two plots, we can see clearly that at the VLE region point of 10 GeV, both the linearity and resolution are degraded. Energy point lower than 10 GeV was not probed then. One reason of this degradation is that calorimeter VLE electron performance is more sensitive to the material distribution in front of calorimeter, this VLE electron performance needs further studies, especially when the calorimeter with the real detector configuration, having more material in front than Test Beam 2002. However, in ATLAS real detector, the linearity and resolution of VLE electrons can be improved by using Inner Detector information, which is more accurate for electron momentum measurement at low energy region. Meanwhile, an independent linearity study of calorimeter VLE particles is also very important. In the Combined Test Beam 2004, the slice of ATLAS detector has almost the final material distribution, and dedicates runs were taken for VLE particles studies. This is the motivation of the combined test beam 2004 VLE electron studies introduced in the following chapter.

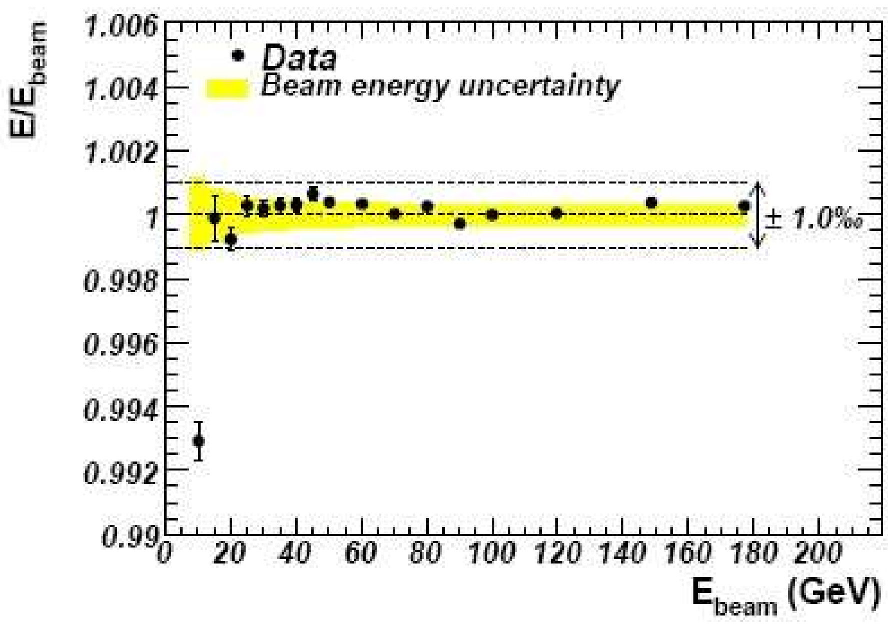

(a) electron linearity,All points are normalized to the value measured at Ebeam = 100 GeV.

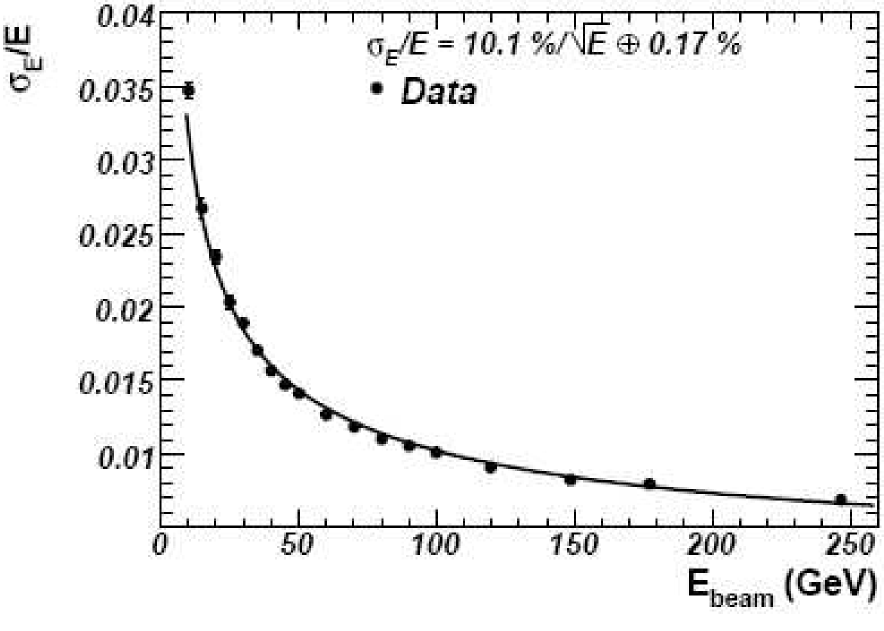

(b) electron resolution,Electronic noise was subtracted from the data before plotting the results. The curve represents the results of a fit to the data using 4.9

FIGURE 4.11: Linearity and fractional resolution of response as a function of the electron beam energy, Ebeam, for a barrel LAr electromagnetic module at $|\eta| = 0.687$, energy from 10 to 245 GeV, note this results is from test beam 2002, the calorimeter is a standalone detector and with minimal mater in front [60]

# Chapter 5

# Combined Test Beam data analysis

## Contents

The linearity of electron energy measurement is essential in the in-situ calibration of electron using $Z \rightarrow ee$ events. The in-situ calibration constrains the di-electron invariant mass distribution to the well-known Z boson line shape, and obtain the absolute energy scale. In ATLAS, electron energy resolution are expected to be better in electromagnetic calorimeter than in Inner Detector in a big $p_T$ range. The electron energy is obtained from calorimeter information reconstruction, possible combining Inner Detector information at low energy region. In order to achieve the global constant term $< 0.7\%$, the calorimeter inter-calibrate $|\eta| < 2.4$ region constant term must within 0.5%, which is satisfied by construction uniformity of LAr and confirmed in Test Beam2002(shown in figure 4.11). However, these results are from standalone detector with minimal mater distribution in front, and only probe energy $>= 10GeV$(the linearity of 10 GeV point is $\sim 1\%$). It is interesting to know the performance of physics objects reconstruction if all sub detectors are implemented, mater distribution highly similar to real ATLAS detector, and explore $E_T < 10\ GeV$ region. Combined Test Beam 2004 provide an unique condition of combined detectors, real mater distribution, and dedicated VLE runs for VLE electron studies. The following will show the studies on Linearity of Very Low Energy electrons, both with real test beam data and possible improvement calibration schema based on MC studies.

## 5.1 CTB VLE electron energy linearity studies

The energy of test beam electrons $E_{beam}$ can be determined by other means than calorimeter detector, such as magnet spectrometer, to a very high precision. This $E_{beam}$ could be used as the truth energy of the electron to determine the linearity and resolution. For the VLE beam line, the trajectory of each particle can be determined using beam chambers and magnet, which can be used to calculate the single particle truth energy with high precision. For the reconstruction in the calorimeter $E_{reco}$, the default parametrization of $E_{reco} = offset + w_0 \cdot E_0 + w_{01} \cdot \sqrt{E_0 \times E_1} \frac{1}{f_{sampling}}(E_1 + E_2 + E_3) + w_3 \cdot E_3$ is used, with $w_{01} \cdot \sqrt{E_0 \times E_1}$ term represent the energy deposit between presample and accordion. Here, $E_0, E_1, E_2, E_3$ are the energy deposited in presample, strips, middle and back part of EM calorimeter, offset, $w_0, w_{01}, w_3, f_{sampling}$ are the corresponding electron calibration constant. In this part, the linearity of VLE electron is presented and compared to HE configuration electron using beam energy. The run numbers used in this analysis are listed as following.

| Energy point [GeV] | Run Number | $\eta$ | $\phi$ | beam energy [GeV] |
|---|---|---|---|---|
| **1** | 2102101 | 0.442 | 0 | $0.988 \pm 0.025$ |
| **2** | 2102099 | 0.442 | 0 | $1.990 \pm 0.013$ |
| **3** | 2102098 | 0.442 | 0 | $2.985 \pm 0.008$ |
| **5** | 2102097 | 0.442 | 0 | $5.016 \pm 0.005$ |
| **9** | 2102096 | 0.442 | 0 | $9.011 \pm 0.003$ |
| **9(HE)** | 1004161 | 0.442 | 0 | $9.198 \pm 0.003$ |

TABLE 5.1: electron Run and its nominal energy, $\eta$ position used in this study

### 5.1.1 VLE electron selection criteria

All the selection criteria of electrons are described as following:

- **Good Event Selection:**
  Events mush have good trigger signatures(Trigger==1), and have reconstructed only one energy cluster in electromagnetic calorimeter($cl\_nc\_tb\_em == 1$).

- **Scintillator Identification:**
  Events must have less hits in $muTag$ scintillator($sADC\_muTag < 460$, not a muon event), and have more hits in CHRV2($sADC\_C2 > 650$, electron candidate) as shown in fig 5.1.

- **Calorimeter electron ID:**
  The shower shape of the particles is electron like, which has less fraction of energy

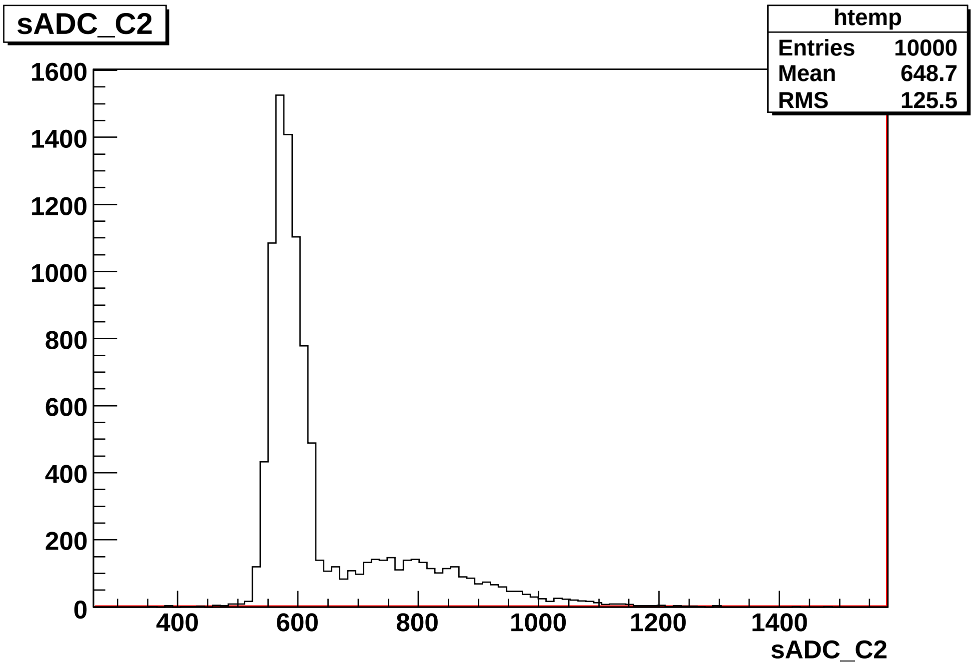

FIGURE 5.1: The distribution of scintillator CHRC2 ADC counts, the peak events at lower region are electron candidates

leakage in the hadronic calorimeter first sampling($Eh\_Tile < 700MeV$) compared to muon events as shown in fig 5.2; and have more fraction of energy deposit in the electromagnetic calorimeter first sampling($cl\_eemb1\_tb\_em/cl\_ecluster\_tb\_em > 0.2$) compared to $\pi$ events, these two criteria mainly reject muon and $\pi$ events to ensure a pure electron sample is selected

- **Good Beam Chamber information:**
  Since the beam chamber information is used to determinate the trajectory of each electron, it is important to make sure that these beam chamber(BC-2, BC-1, BC0) information are in good value region. That is, every beam chamber read out is correct and the combined information is reliable(fig 5.3,5.4):
  - The read out of X direction have a meaning for every beam chamber, It is not zero.
  - The X position read out of each beam chamber is in the physics region.

After the selection described above, the energy spectra of 9GeV VLE and HE configurations are shown in fig 5.5 and very consistent with each other. The energy deposit in each EM compartments are shown in fig 5.6. Since there is more material in HE than in VLE configuration, HE shower is earlier and more likely to have more energy deposited in presampler than electron from the VLE beam line. However, despite the material difference, VLE and HE beam line electron reconstructed energy have very similar behavior.

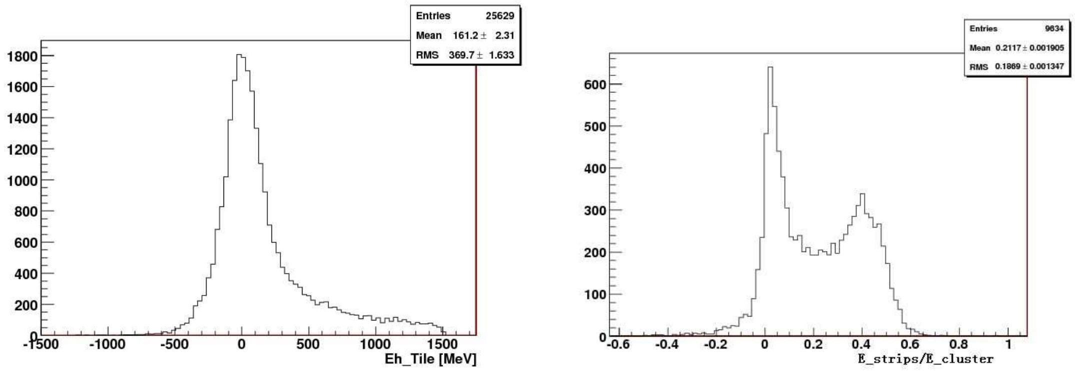

(a) Hadronic calorimeter first sampling energy distribution

(b) The energy fraction distribution of strips to the reconstructed energy, the peak events around zero are muon candidates while higher region are electron candidates

FIGURE 5.2: Hadronic calorimeter first sampling energy distribution and the energy fraction distribution of strips to the reconstructed energy

### 5.1.2 Reconstruction of single VLE electron true energy

Instead of using the nominal energy $E_{beam}$ as the truth energy, we prefer to measure the true energy of each particle to calculate the linearity, which will give more precise results. Here, a method of measuring single electron energy by magnet and beam chamber is presented for precision electron linearity studies at event level.

- **Deflection angle of each VLE electron at B8 magnet:**
  Since VLE electrons are deflected at B8 magnet and pass three beam chambers(BC-2,BC-1,BC0,as figure 5.7) before they enter the detector, it is possible to determine their trajectories with these beam chambers and magnet up to a high precision. The deflection angle of electron at B8 can be expressed in equation 5.1 or a approximate form in equation 5.2.

$$\alpha = cos^{-1}\frac{L_1(L_4-L_3)+(\frac{x_3L_4-x_4L_4}{L_4-L_3}-x_1-L_1tan\theta_0)(x_4-x_3)}{\sqrt{L_1^2+(\frac{x_3L_4-x_4L_4}{L_4-L_3}-x_1-L_1tan\theta_0)^2}\sqrt{(L_4-L_3)^2+(x_4-x_3)^2}} \quad , \qquad (5.1)$$

$$\alpha = \frac{x_1-\frac{x_3L_4-x_4L_4}{L_4-L_3}cos(\theta_0)}{L_1/cos(\theta_0)}+\frac{x_4-x_3}{L_4-L_3}+\theta_0 \quad , \qquad (5.2)$$

  of which, $L_1 = 4258mm$ is the distance of BC-2 to the center of B8 magnet; $L_3 = 1919mm$ is the distance of BC-1 to the center of B8 magnet; $L_4 = 3064mm$ is the distance of BC0 to the center of B8 magnet; $\theta_0 = 0.120rad$ is the nominal deflection angle of VLE configuration at B8; $x_1, x_3, x_4$ corresponding to the X position measured by BC-2,BC-1,BC0 separately(in mm). The HE particles and VLE particles beam line are in the same trajectory between BC0 and BC-1. The measured

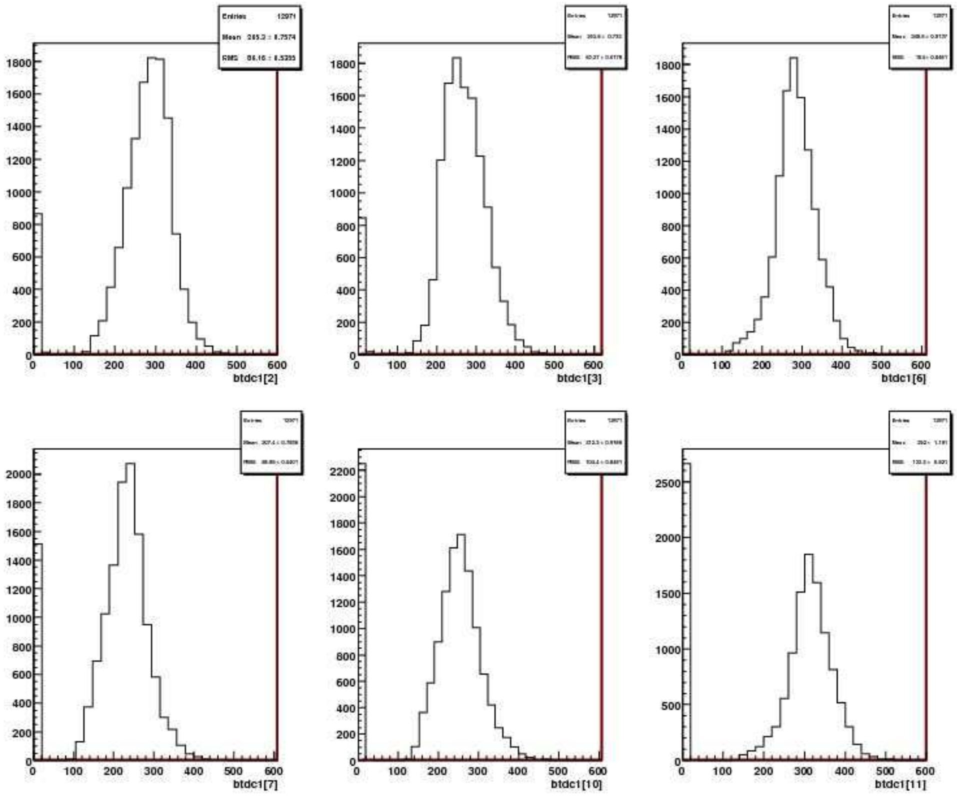

FIGURE 5.3: The ADC counts of beam chamber X direction output, the zero bin indicates that this beam chamber measurement is not reliable

XBC0 and XBCm1 differences of HE electron and VLE electron are all off zero and similarly around -3.6 mm as shown in figure 5.8. Beam line along z axis is assumed in this part of beam, which means that the differences of XBC0 and XBCm1 should be around zero. In order to recover this alignment correction, a shift of +3.6 mm is added on XBC0(similar results obtained either subtract 3.6 mm of XBCm1 or add 1.8 mm to XBC0 and subtract 1.8 mm of XBCm1). Figure 5.9 shows the distribution of single electron deflection angle after the assumption of beam along z axis correction. We can get that:

- The distribution of electron deflection angle is not a Gaussian. and slightly asymmetric of the mean value.
- The mean value of the deflection angle is very close to the nominal deflection angle of electron, for all the VLE electron 9,5,3,2,1GeV runs.

- **Single Electron Energy:**
  Once get the deflection angle of electron at B8, one can calculate the energy mea-

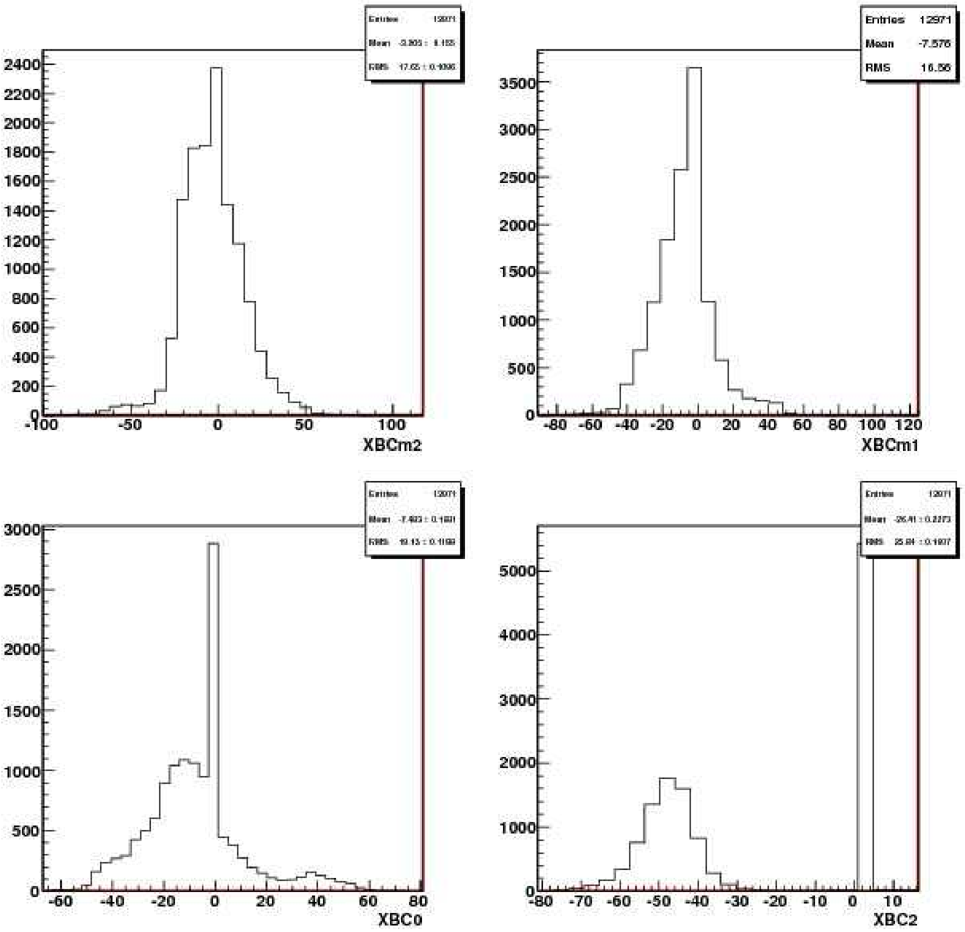

FIGURE 5.4: The beam chamber measured X position [mm] of Beam Chamber -2, -1, 0 and 2, the zero bin means that the beam chamber measurement is not reliable

sured by beam chamber according to:

$$\int Bdl = \sum_{i=0}^{6} a_i \cdot I^i \quad , \tag{5.3}$$

$$E_{BCmeasured}[GeV] = \frac{299.79}{\alpha[mrad]} \int Bdl[Tm] \quad . \tag{5.4}$$

of which I is the current of B8 magnet, $a_0 - a_6$ are the coefficients concerning the magnet itself, and given by table 5.2. $\alpha$ is the electron deflection angle, given in mard. $E_{BCmeasured}$ is the electron energy, given in GeV.

Figure 5.10 shows the Beam Chamber measured energy for VLE electrons. The mean value is very close to the nominal beam energy for each point. And an asymmetric behavior is found for the distributions. These electron energy measurement, so called $E_{BCmeasured}$, could improve the accuracy of linearity and resolution compared to the method using only nominal beam energy as shown in the next section.

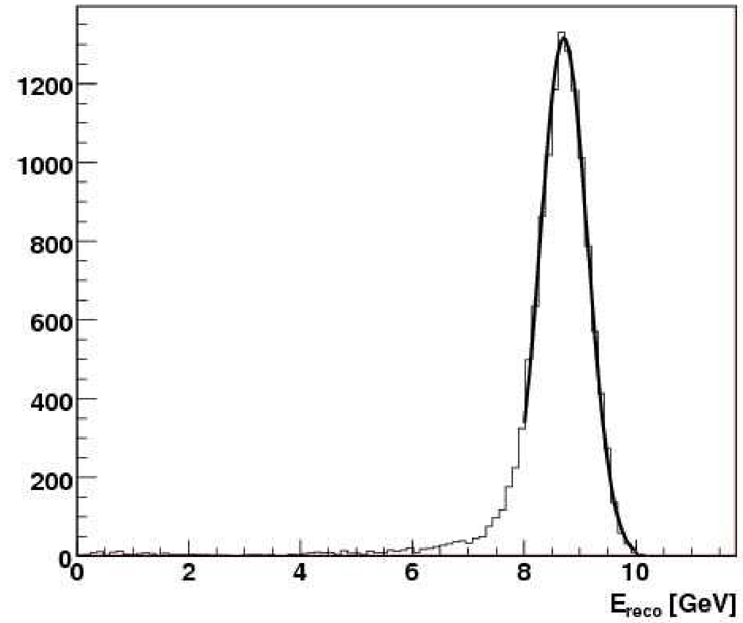

(a) Reconstructed LAr energy of VLE 9 GeV run 2102096, unit in GeV. The gaussian fitted mean value is 8.973 GeV

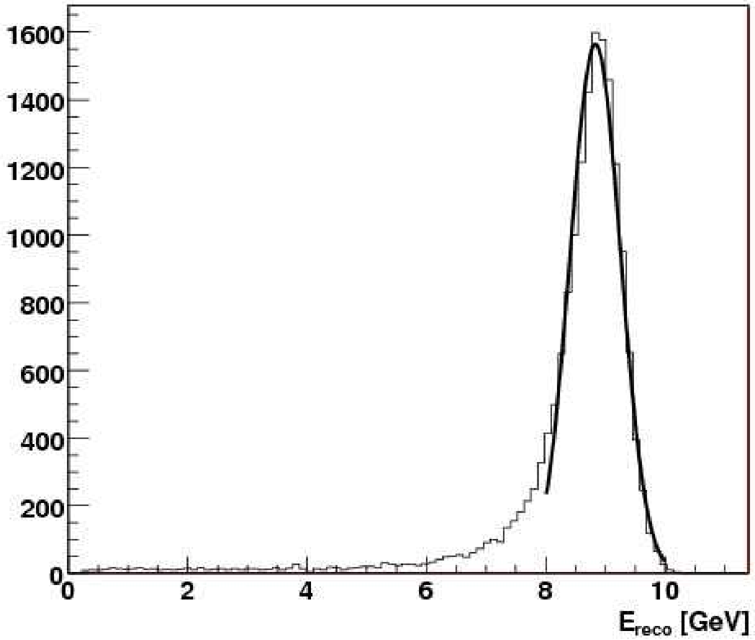

(b) Reconstructed LAr energy of HE 9 GeV run 1004161, unit in GeV. The gaussian fitted mean value is 9.097 GeV

FIGURE 5.5: Energy reconstructed in LAr for VLE and HE electrons, they consistent with each other. The small differences are due to the beam energy differences of VLE and HE electrons

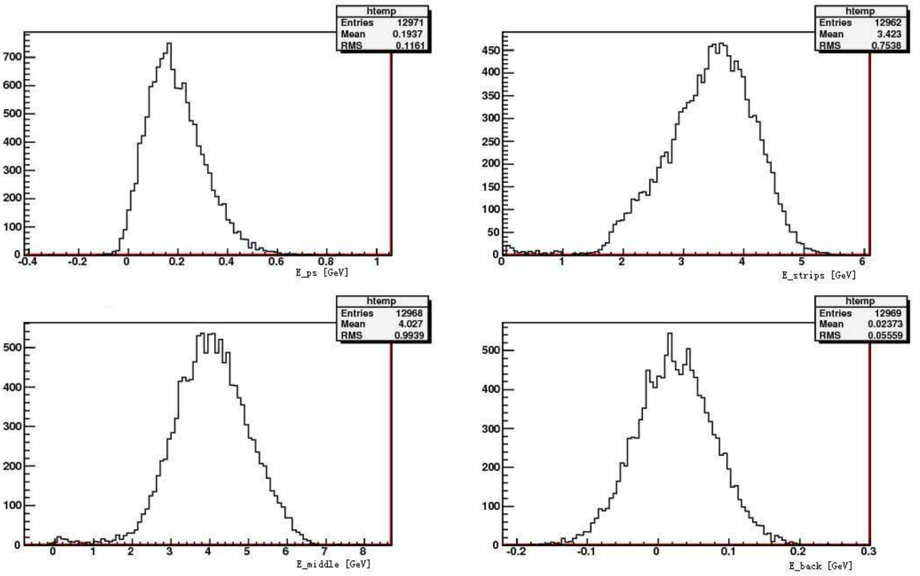

(a) Reconstructed LAr energy in presampler(up-left), strips(up-right), middle(down-left), back(down-right) of VLE 9 GeV run 2102096, unit in GeV

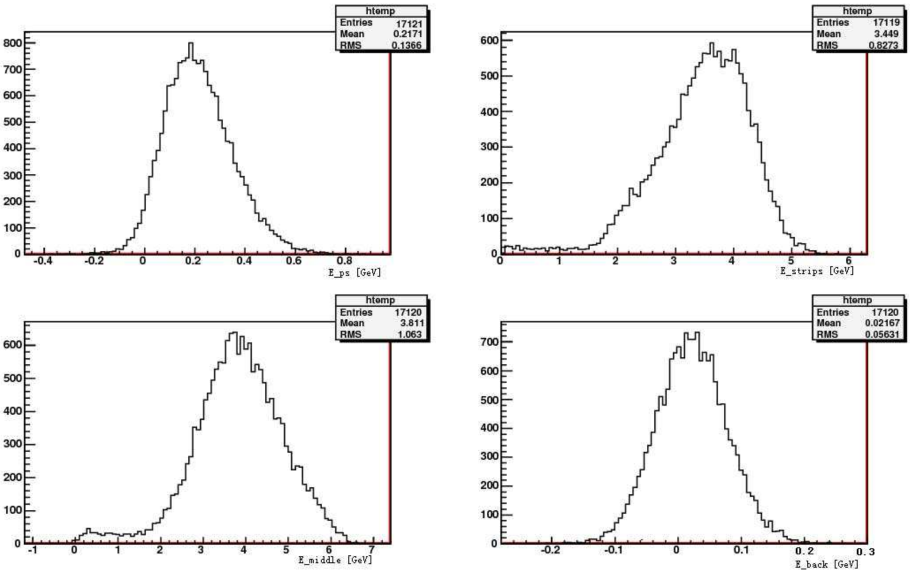

(b) Reconstructed LAr energy presampler(up-left), strips(up-right), middle(down-left), back(down-right) of HE 9 GeV run 1004161, unit in GeV

FIGURE 5.6: Energy reconstructed in LAr compartments for VLE and HE electrons

| $a_0$ | $a_1$ | $a_2$ | $a_3$ |
|---|---|---|---|
| $-0.2417 \times 10^{-3}$ | $0.5727 \times 10^{-2}$ | $0.3993 \times 10^{-6}$ | $0.2999 \times 10^{-8}$ |
| $a_4$ | $a_5$ | $a_6$ | |
| $-0.1256 \times 10^{-10}$ | $0.6386 \times 10^{-14}$ | $0.1034 \times 10^{-17}$ | |

TABLE 5.2: B8 magnet coefficients for charged particle momentum calculation

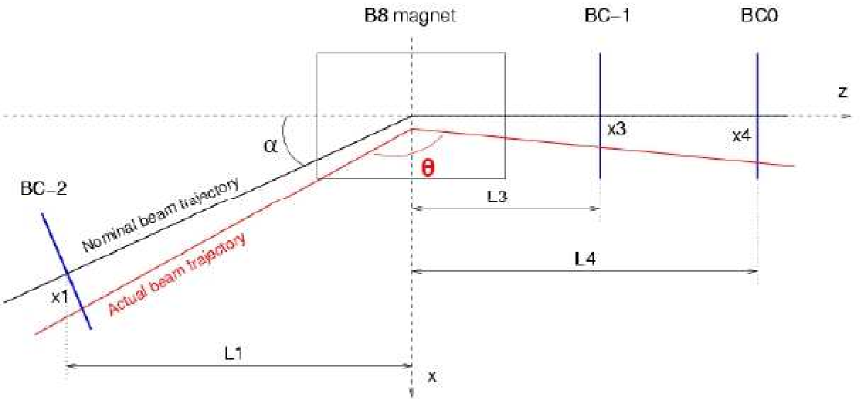

FIGURE 5.7: configuration of beam chamber and B8 magnet for VLE beam

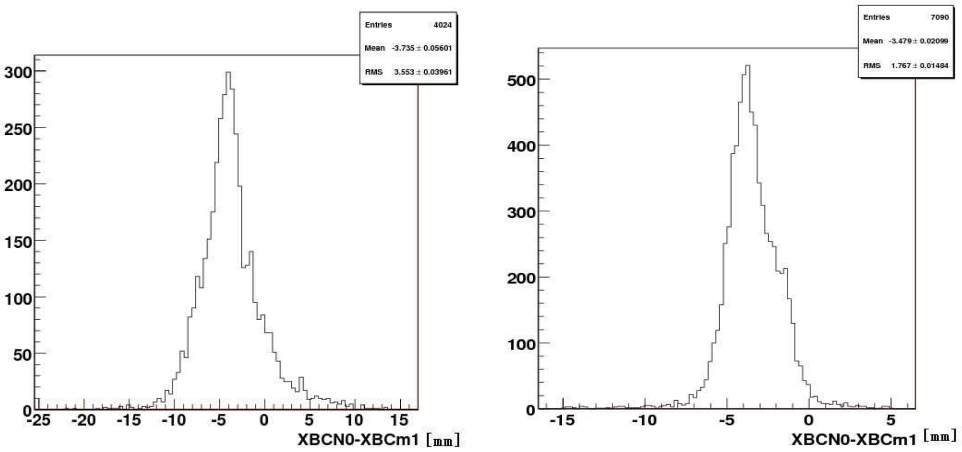

(a) Beam Chamber 0 and Beam Chamber -1 measured X position differences of VLE electron 9 GeV run

(b) Beam Chamber 0 and Beam Chamber -1 measured X position differences of HE electron 9 GeV run

FIGURE 5.8: Beam Chamber 0 and Beam Chamber -1 measured X position differences of VLE and HE electron 9 GeV runs, they all have a shift around -3.6 mm. since the beam along z axis assumption, this -3.6 shift is recovered by adding 3.6 mm to XBC0

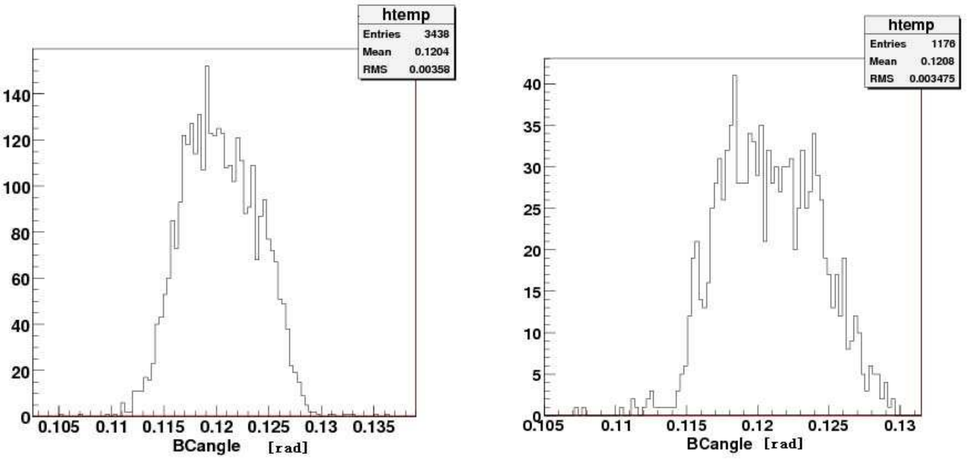

(a) 9GeV electron deflection angle (b) 5GeV electron deflection angle

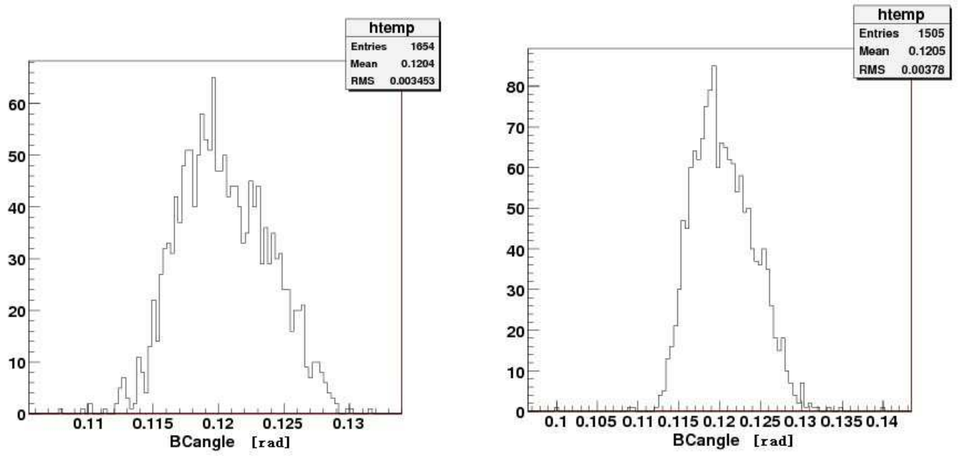

(c) 3GeV electron deflection angle (d) 2GeV electron deflection angle

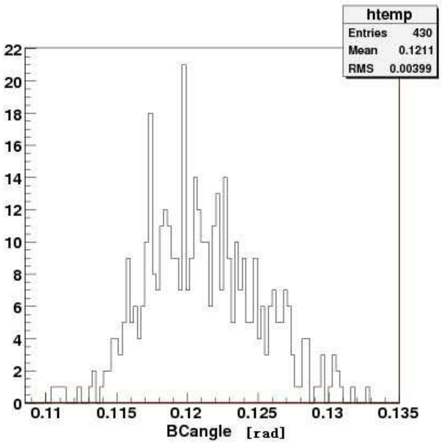

(e) 1GeV electron deflection angle

Figure 5.9: Beam Chamber measured deflection angle of VLE electrons

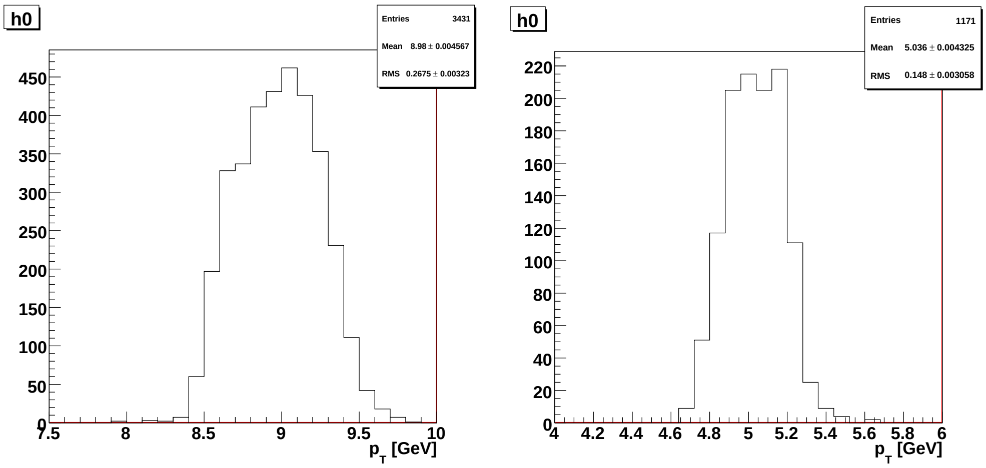

(a) 9GeV electron beam chamber measured energy distribution

(b) 5GeV electron beam chamber measured energy distribution

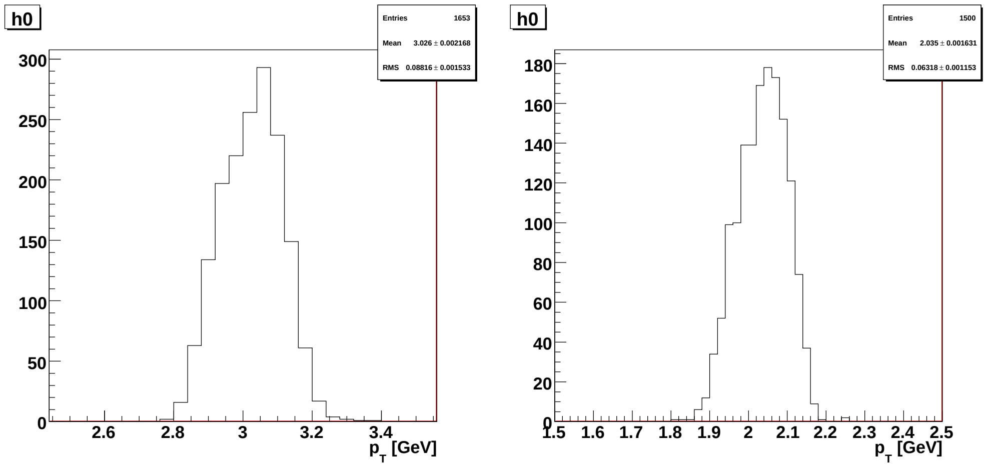

(c) 3GeV electron beam chamber measured energy distribution

(d) 2GeV electron beam chamber measured energy distribution

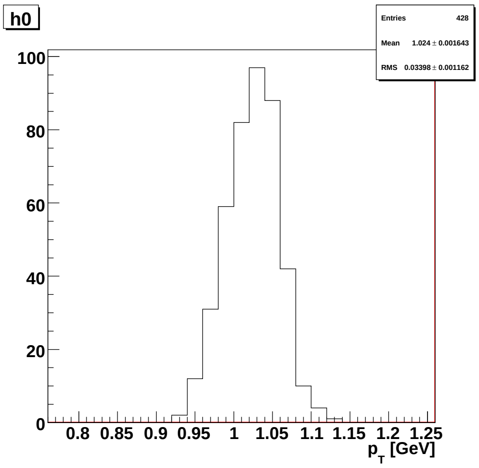

(e) 1GeV electron beam chamber measured energy distribution

FIGURE 5.10: Beam Chamber measured energy of VLE electrons

### 5.1.3 Calculation of VLE electron $E_{BCmeasured}/E_{reco}$

In order to check the possible improvement of using such Beam Chamber measured energy,$E_{BCmeasured}$, in the electron energy linearity study, we check its correlation with $E_{reco}$ in VLE runs. Good correlations between VLE electron Beam Chamber measured energy obtained as described in last section and Liquid Argon Calorimeter reconstructed energy are obtained for VLE electrons, and 9GeV run's correlation is shown in figure 5.11. Which is a prof that using $E_{BCmeasured}$ is better than a fixed Ebeam in linearity calculation.

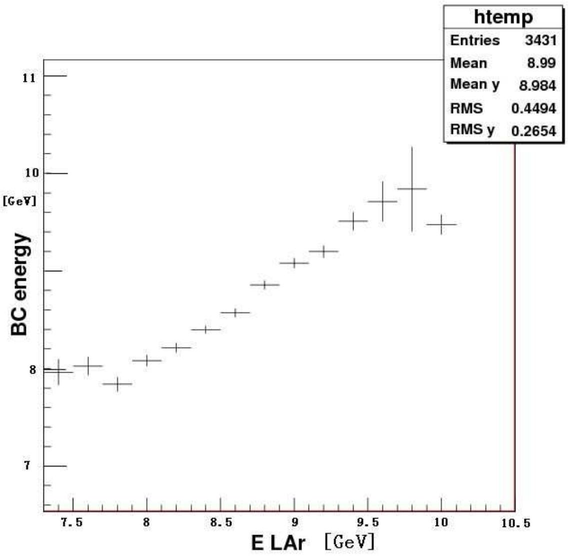

FIGURE 5.11: Beam Chamber measured vs LAr Calorimeter measured energy for VLE 9 GeV electrons

The profile plot of $E_{BCmeasured}/E_{reco}$ as a function of $E_{BCmeasured}$ shows good linearity between these two. And the factor of $E_{BCmeasured}/E_{reco}$ is almost flat for different $E_{BCmeasured}$. In order to obtain this factor, a line of constant is used to fit the profile of $E_{BCmeasured}/E_{reco}$ as function of $E_{BCmeasured}$(Left plot of 5.12). A factor of $1.007 \pm 0.001$ is obtained for 9GeV VLE electron $E_{BCmeasured}/E_{reco}$.

### 5.1.4 Linearity of VLE electron LAr measured energy

To Check the consistence of VLE electrons linearity and HE electrons, we compare the factor $E_{BCmeasured}/E_{reco}$ of VLE 9GeV electrons and $E_{beam}/E_{reco}$ of HE 9GeV electrons, these are the only energy points that HE and VLE configuration electrons that have the same injection energy. Although there are material distribution differences and different beam instrumentation, after electron selection and gaussian fit on the energy peak of HE electron, a factor of 1.009 is obtained for HE 9GeV electron $E_{beam}/E_{reco}$, which is in good agreement with the VLE electron.

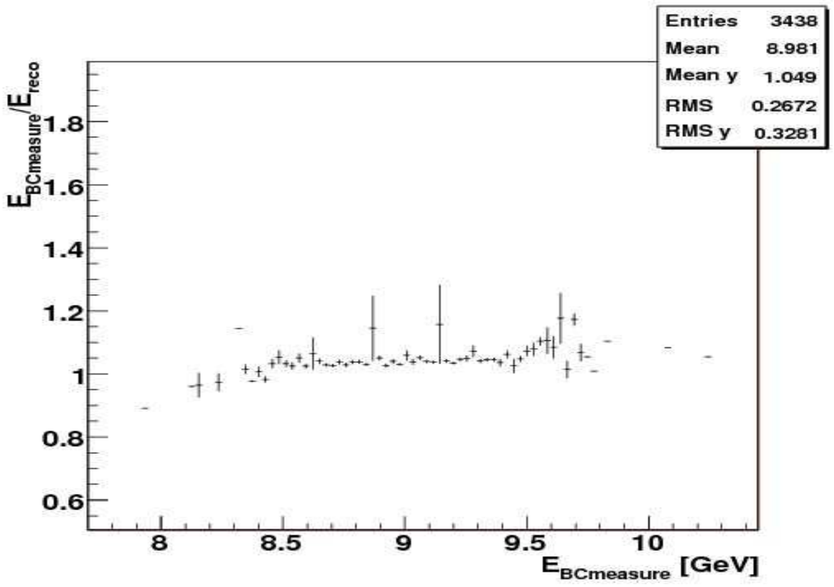

FIGURE 5.12: the factor $E_{BCmeasured}/E_{reco}$ as a function of $E_{BCmeasured}$ for VLE 9 GeV electrons, similar plots are obtained for different VLE electron runs

To obtain the VLE electron energy linearity, the same procedure for other VLE electron runs up to 1GeV are performed to obtain the factor of $E_{BCmeasured}/E_{reco}$ as for 9 GeV VLE electrons. The figure 5.13 shows the VLE configuration electron linearity from 1 GeV to 9 GeV. The linearity of VLE is roughly within 1% from 9 GeV to 5 GeV electrons, while it degrades at lower energy. Therefore, this LAr energy reconstruction scheme could used for the low energy linearity. Anyhow, further research are needed for detail studies to improve the calorimeter linearity for the energy in the 1 GeV to 5 GeV range.

## 5.2 Calibration of electron energies in EM calorimeter

In order to explore the possible improvements on the linearity of VLE electrons, different sets of VLE electron energy calibration procedures are tried. Since there are dead material in the front and within the calorimeter, the energy deposited in active material is not the only energy deposit of the electron. In addition, there are also possible leakage and out of the electron cone energy losses. So, the sum of these active energy cells is not the correct representation of this electron's true energy. In order to obtain correct energy, with good linearity and resolution, a calibration procedure is performed at the cell energy level. At the region of 15 $GeV \leq p_T \leq 245$ $GeV$, the current default calibration is good enough for a good non-linearity less than 0.1% and decrease to about 1% at 10GeV as shown in figure 4.11 in Test Beam 2002 studies, upon good knowledge of the material distribution and modeling, as well as proper calibration formula and constants. But for energy less

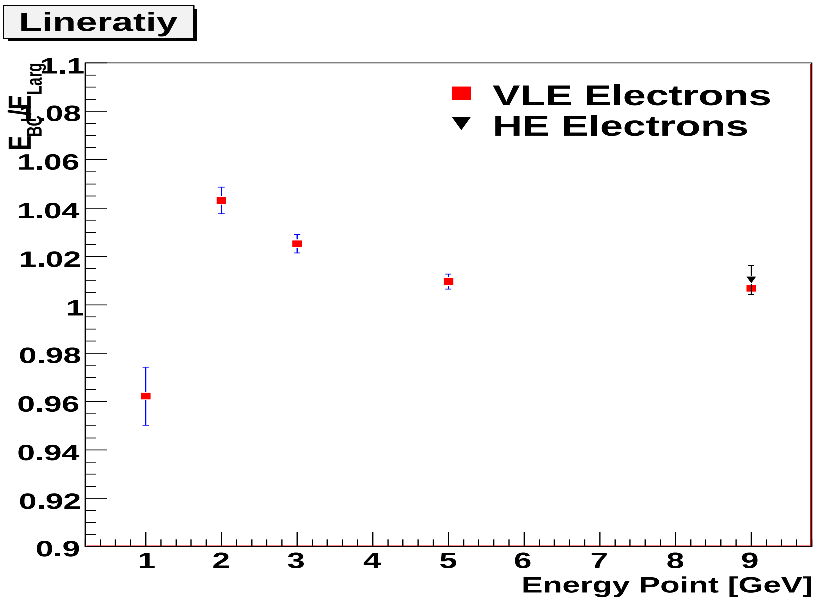

FIGURE 5.13: Linearity of LAr Calorimeter measured energy for electrons, they agrees well at 9GeV of HE and VLE configuration

than 10 *GeV* VLE electrons, with the real detector matter distribution, the calibration procedure need to be optimized by comparing MC and data since the energy measurement is sensitive to material in front of the calorimeter, especially for VLE particles.

### 5.2.1 Combined Test Beam electron simulation

VLE electron MC simulation start from a particle gun which generate single electron at a given energy, and point at a fix $\eta, \phi$ direction. Then, these electrons pass the simulation of CTB2004 geometry configuration as described in figure 5.14.

Geant4 [61] has been chosen as the main simulation tool in the ATLAS simulation, including CTB2004. It was shown that it describes electromagnetic interactions with a good accuracy, for both QGSP_EMV and QGSP_BERT at high energy region, while better performance but with a factor 2 slower of QGSP_BERT for VLE electron at low energy. Geant4 is incorporated in the ATLAS software framework. It is configured by python-based job options. The generation of CTB electrons by particle gun and simulation with Geant4 are done in one step.

The output of the detector simulation are so-called hits, an energy deposit in a certain active volume of the detector. In case of the calorimeter, this volume corresponds to a cell. At this point, the effect of the varying electric field in the accordion folds is simulated as well. The hits can be stored in POOL files for further processing or written to a ntuple for visualization with ROOT. During the digitization step the simulated hits are converted to a raw-data like format. This involves introducing effects of the readout chain like electronic noise and cross-talk. This is in general done by applying correction factors and not by a detailed simulation of the detector readout.

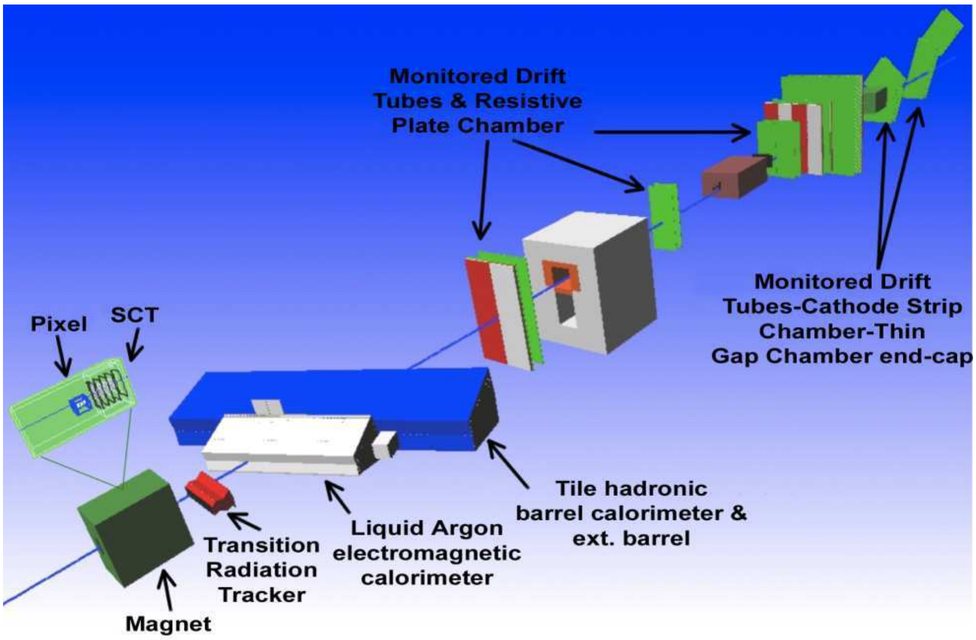

FIGURE 5.14: The geometry of the CTB beamline used in Geant4 simulation. The beam instrumentation is included in details

The file obtained at the digitization can be fed into a reconstruction job that is almost identical to the reconstruction of real data and produces the same combined ntuple that contain all needed reconstructed variables for the analysis. This is the reconstruction step of CTB Monte Carlo.

An important feature of the ATLAS simulation software are the so-called Calibration Hits. This allows to access the energy deposited in all regions of the detector, including inactive regions like the absorbers of the calorimeter or "dead" regions like the cryostat subdivided into electromagnetic and hadronic interactions as well as invisible energy and escaped energy. Calibration hits labeled as "active" give the true energy deposited in the active part of a cell. The normal hits in contrast give the energy deposit corrected by the electric field effects in the accordion folds. These energies are used to calculate the calibration constants for real data.

Here, a calibration method based on $5 \times 5$ [1] clustering algorithm is presented, using a set of VLE electron Monte Carlo runs. Energy point of 9, 5, 3, 2, 1 GeV are used to compute the calibration constants and High Energy runs of 20, 50, 100 GeV electrons are used as a reference for calibration. Table 5.3 lists the main aspects of the used runs, including energy, and the injection position in the detector.

---

[1] It is 5 elemental $\eta$ cells $\times$ 5 $\phi$ elemental cells, since most elemental cell of calorimeter of the dimension of $\Delta\eta \times \Delta\phi = 0.025 \times 0.025$, so, the $5 \times 5$ is within the range of $\Delta\eta \times \Delta\phi = 0.125 \times 0.125$

| Energy[GeV] | Run Number | $\eta$ | $\phi$ |
|---|---|---|---|
| **1** | 2102101 | 0.442 | 0 |
| **2** | 2102099 | 0.442 | 0 |
| **3** | 2102098 | 0.442 | 0 |
| **5** | 2102097 | 0.442 | 0 |
| **9** | 2102096 | 0.442 | 0 |
| 20 | 2102397 | 0.438 | 0 |
| 50 | 2102404 | 0.440 | 0 |
| 100 | 2102398 | 0.438 | 0 |

Table 5.3: Monte Carlo Run and its nominal energy, $\eta$ position used in this study

### 5.2.2 Standard $5 \times 5$ Clustering

For VLE Test Beam, the beam particles are injected in the detector slice at a fixed position. This feature makes the calorimeter clustering simpler than that for ATLAS detector. There are several kinds of clustering in CTB2004 data: the default clustering size is $3 \times 3$ cells of EM calorimeter $\eta \times \phi$, which is widely used and proved to be robust at least in electron energy greater than 15 GeV; also there are $5 \times 5$ and $3 \times 7$ clustering algorithms, which are expected to be more robust with respect to the out of cone energy losses. The typical $5 \times 5$ clustering schema is as following:

- **Seeding:** Start from middle compartment of EM calorimeter, search over all the cells, and take the most energetic cell and take its $\eta, \phi$ as a seed.

- **energy and direction of cluster:** Take the seed as center, calculate the total $5 \times 5$ cells energy as the energy of this cluster, and use the energy weighted $\eta, \phi$ from all the cluster cells as the $\eta, \phi$ of the cluster. Then, use the same seed and same procedure to get the energy of the presample, strip, middle and back layer of the calorimeter.

### 5.2.3 $5 \times 5$ Multiple seeds clustering

The normal $5 \times 5$ clustering works well for electron candidates with energy greater than 15 GeV. Since high energy electron have a big fraction of energy deposited in the middle layer, the proper seed can always be found. However, for the very low energy electrons, especially for energy less than 3 GeV, there is a good fraction of energy deposited before the middle layer. Therefore, if only use the middle compartment, the uncertainties of the seed became an important reason of miscalculation of cluster energy. In order to improve seeding performance, a so called Multiple Seeds Clustering(MSC) procedure is used [62]:

- $\eta$,$\phi$ **of Seeds:**
  - **Seed from strips:** Since the strips are much finer in $\eta$ than for the middle compartment, a new cell energy is defined as:
    $E_{\eta,\phi} = \frac{1}{3}[E_{\eta,\phi} + E_{\eta-4*\Delta\eta,\phi} + E_{\eta+4*\Delta\eta,\phi}]$,

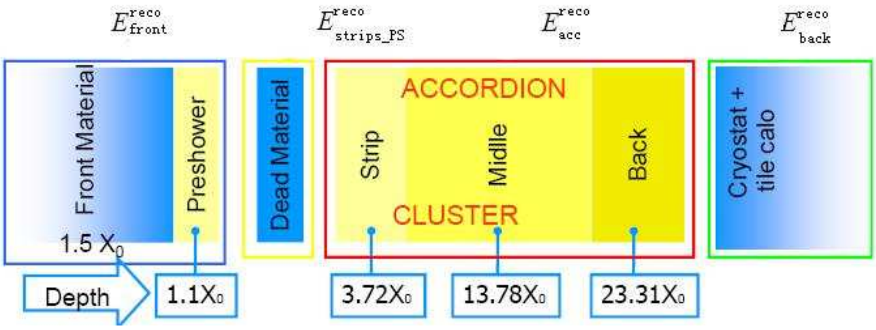

FIGURE 5.15: demonstration of electron EM barrel calorimeter energy reconstruction at $\eta = 0.3$

where $\Delta\eta$ is the width of a strip cell. The $\eta_1, \phi_1$ of the cell which can maximize this variable is taken as seed1.

  - **Seed from middle:** Same as normal seeding, find the most energetic cell and its $\eta_2, \phi_2$ as seed2.

- **Energy of each EM layer:** Energies deposited in each compartment of EM calorimeter are seeded either with seed1 or seed2 or the combination.
  - **Energy of strips:** Take $\eta_1, \phi_1$ as seed, sum up $5 \times 5$ cells around seed of strips layer.
  - **Energy of middle, back:** Middle and back energy calculation seeded using $\eta_2, \phi_2$.
  - **Energy of presampler:** Presample energy calculation seeded using $\eta_1, \phi_2$.
- $\eta, \phi$ **of each layer:** Presampler,strips,middle and back use the energy weighted $\eta, \phi$ from the corresponding MSC $5 \times 5$ EM calorimeter cluster as defined above.

### 5.2.4 Electron energy calibration

Since there are material distributed in front of calorimeter, and also dead mater between presampler, strips, middle and back layers. These material absorb certain amount of particle's energy. The sum of the measured energy deposited in the active material is different from the total energy of the injected EM energy. Moreover, due to the clustering procedure, the injected EM energy may spread out of the limited size of the cluster. In order to recover all these effects for different EM injected particles, a calibration is performed based on the calibrated hits(Figure 5.15). There are several parameterizations for electron. The default one used in the CTB2004 reconstruction is not perfect since the linearity of $\sqrt{E_0 \cdot E_1}$ and the energy deposited between presampler-strips are proven not to be good, especially at very lower energy region. Therefore, in this VLE electron study, this term is removed in the following formula which is now used:

| | $a_0/b_0$ | $a_1/b_1$ | $a_2/b_2$ |
|---|---|---|---|
| $w_0$ | $0.2733143 \pm 0.0061573$ | $0.0552639 \pm 0.0106134$ | $0.0132300 \pm 0.0012546$ |
| offset | $0.6610342 \pm 0.0151541$ | $0.7112527 \pm 0.0343073$ | $0.0321833 \pm 0.0020202$ |

TABLE 5.4: global fitted parameters of $w_0$ and offset

$$E = offset + w_0 \cdot E_0 + \frac{1}{f_{sampling}}(E_1 + E_2 + E_3) + w_3 \tag{5.5}$$

Of which, $E_0, E_1, E_2, E_3$ are the energy deposited in the presampler, strips, middle and back separately, they are calculated using the $5 \times 5$ MSC clustering procedure. A linearity relationship is assumed for the energy deposited in presampler and before presampler and between presampler-strips with respect to the energy measured in presampler, which is represented as $offset + w_0 \cdot E_0$. $\frac{1}{f_{sampling}}(E_1 + E_2 + E_3)$ represents the energy correction of accordion parts of EM calorimeter, taking into account the inactive material. $w_3$ is the energy leakage correction. Here, all there calibration constant are using a energy dependence parameterizations. And they are dependent on $\eta$. Since these constants are related to the configuration of the detector, they are obtained from MC studies.

#### 5.2.4.1 Calculation of offset and $w_0$

Offset and $w_0$ are determined by the energy deposit in the material before presampler $E_{DM}^{upstream}$, the energy that deposit in presampler active material $E_{PS}^{active}$ and in the passive material $E_{PS}^{passive}$, the energy deposit in the passive material between presampler and strips $E_{DM}^{PS-strips}$. A linearity of these energy to the presampler measured energy is given by: $offset + w_0 * E_{PS}^{active} = E_{DM}^{upstream} + E_{DM}^{PS-strips} + E_{PS}^{active} + E_{PS}^{passive}$. A fit is performed to give the offset and $w_0$ for each MC energy point. Figure 5.16 shows the fit for the energy point of 100, 50, 20, 9, 5, 3, 2, 1 GeV electron.

To obtain offset and $w_0$ for all energies other than these points, a fit of offset and $w_0$ is performed, with the formula:

$$w_0 = b_0 + b_1 \cdot log(E_{beam}) + b_2 \cdot \sqrt{E_{beam}} \quad , \tag{5.6}$$

$$offset = a_0 + a_1 \cdot E_{beam} + a_2 \cdot E_{beam}^2 \quad , \tag{5.7}$$

Figure 5.17 shows $w_0$ and offset as a function of beam energy, table 5.4 gives the parameter of these two formulas.

#### 5.2.4.2 Calculation of $f_{sampling}$

The Energy deposited in the passive material in accordion EM calorimeter is recovered by a $1/f_{sampling}$ factor applied on the measured energy in the accordion:

$$f_{sampling} = \frac{E}{E + E_{acc}^{passive}} \tag{5.8}$$

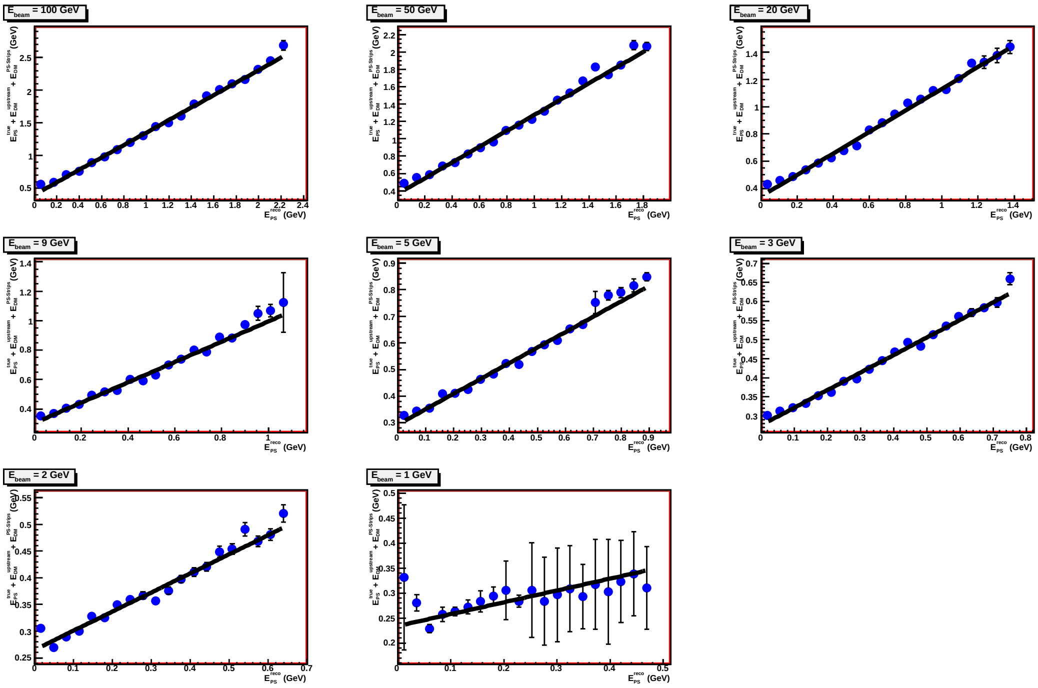

FIGURE 5.16: $(E_{PS}^{true}+E_{DM}^{upstream}+E_{DM}^{PS-strips})$ vs $E_{PS}^{reco}$,for Energy point of 100GeV, 50GeV, 20GeV, 9GeV, 5GeV, 3GeV, 2GeV, 1GeV.

Here, acc denotes the energy deposit in accordion EM calorimeter(strips, middle and back calorimeter), and passive indicate the passive material in EM calorimeter. After obtaining $f_{sampling}$ for each energy point from simulation, a fit of function shown in equation 5.9 is applied.

$$f_{sampling} = c_0 + c_1 \cdot E_{beam}^{c_2} \quad , \tag{5.9}$$

And $c_0 = 1.0006456, c_1 = 0.1432732, c2 = -0.8084607$ for the $f_{sampling}$.

Figure 5.18 shows the fit of $(E + E_{acc}^{passive})/E$ as a function of energy measured in accordion.

#### 5.2.4.3 Energy leakage calculation

The leaked energy $w_3$ can be calculated from:

$$w_3 = E_{active}^{Tile} + E_{passive}^{Tile} + E_{DMTileLeak} \tag{5.10}$$

with $E_{active}^{Tile} + E_{passive}^{Tile} + E_{DMTileLeak}$ is the total energy leakage in tile calorimeter, including the deposited energy of active, passive material of Tile, dead material between LAr and Tile and Tile leakage. Figure 5.19 shows the distribution of $w_3$(left) and the fit results. The fitting formula is:

$$w_3 = d_0 \times E + d_1 \times E^2 \tag{5.11}$$

with a assumption that the energy leakage is zero if the particle energy extrapolated to zero. The fitted parameters are $d_0 = 1.7564358e-03, d_1 = 1.5190291e-05$.

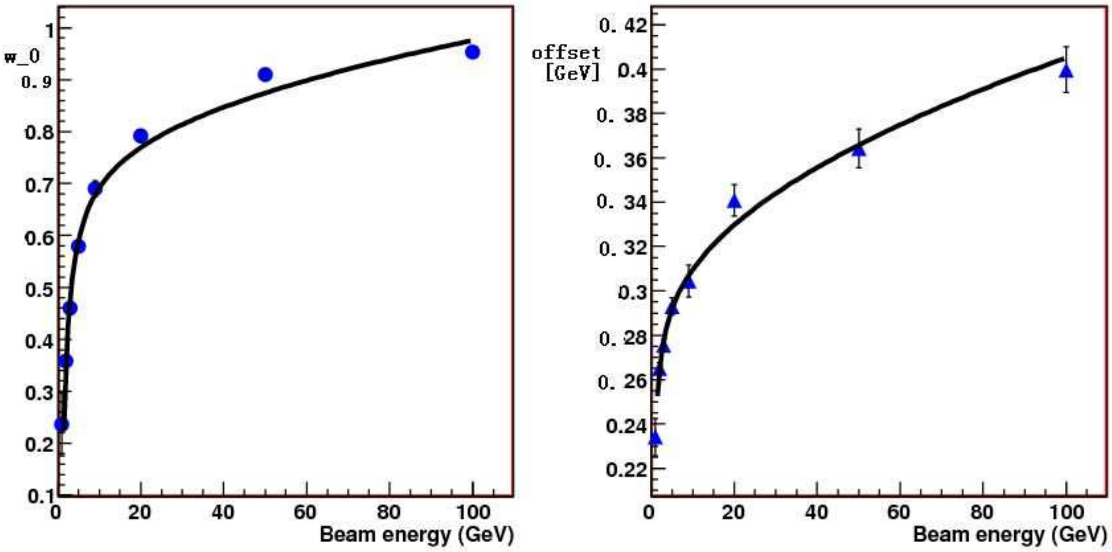

FIGURE 5.17: parametrization of $w_0$(left plot) and offset(right plot) as function of beam energy

#### 5.2.4.4 Calculation of total energy $E_{reco}$

After having obtained the fitted parameters of these constants, one can calculate the reconstructed energy using formula 5.5 with:

- $E^0_{beam} = \sum_{i=0}^{3} E_i^{reco}$.
- $E^j_{beam} = offset(E^{j-1}_{beam}) + w_0(E^{j-1}_{beam}) \times E^{reco}_{PS} + \frac{1}{f_{sampling}(E^{j-1}_{beam})}(E^{reco}_{strips} + E^{reco}_{middle} + E^{reco}_{back})) + w_3(E^{j-1}_{beam})$.
- Stop when $|(E^j_{beam} - E^{j-1}_{beam})/(E^j_{beam} - E^{j-1}_{beam})| < 10^{-6}$.
- computation stops at roughly three iterations to get the right energy.

Figure 5.20 shows the reconstructed energy of each MC sample. They show a good gaussian distributions of the energy shape at high energy part of the energy spectra, and a small tail at low energy region due to bremsstrahlung, which are expected in the simulation. The gaussian fitted mean values are taken as the reconstructed energy $E_{reco}$. Figure 5.21 up plots shows the ratio of MC reconstructed energy over input beam energy as function of beam energy, the non linearity is roughly within 1% from 1 GeV to 9 GeV. The bottom plot shows MC resolution as function of beam energy.

The calorimeter energy linearity of CTB 2004 MC electrons can achieve 1% level by using 5 × 5 MSC clustering and deposited energy parametrization. This calibration formula and constants can be used in future CTB real data reconstruction, with all other corrections, to study the linearity and resolution of VLE electrons under the real detector configuration.

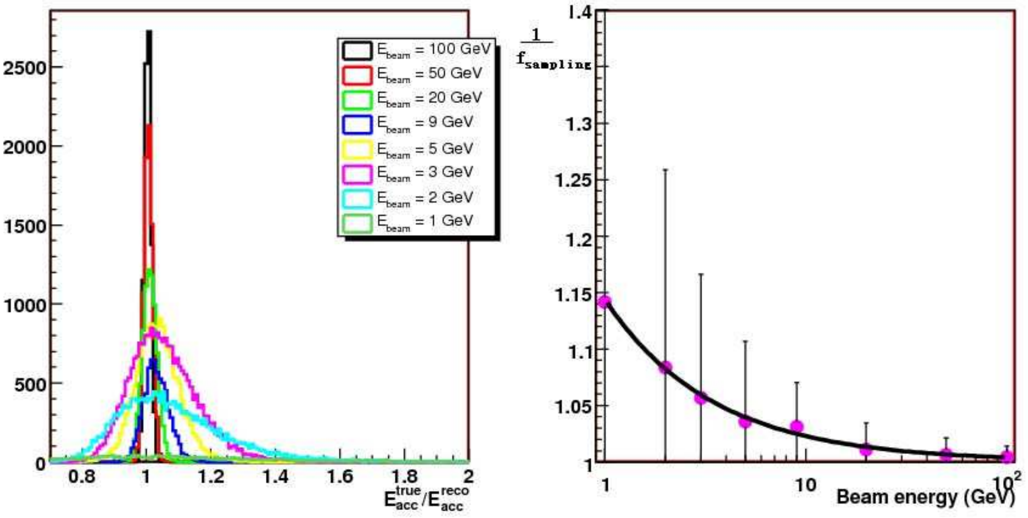

FIGURE 5.18: distribution of $(E + E_{acc}^{passive})/E$ for different energy points(left) and parametrization of $f_{sampling}$ as a function of beam energy(right)

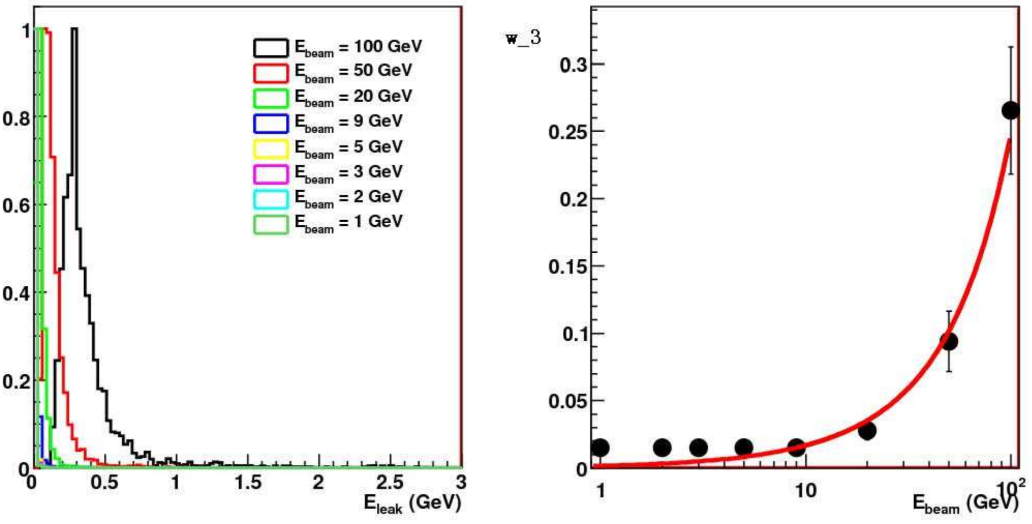

FIGURE 5.19: Eleakage distribution(left) and its fitted correction curve(right)

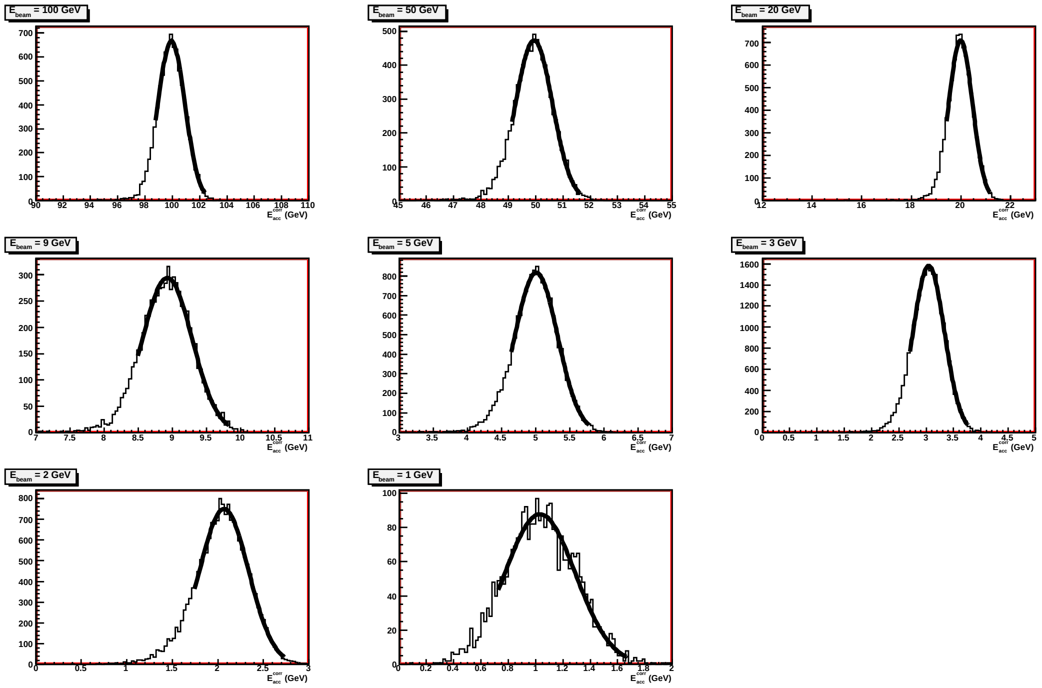

FIGURE 5.20: MC $E_{reco}$ distribution of different energy point, a gaussian is fitted on the peak

## 5.3 Conclusion and discussion

For electron energy less than 10 GeV, the calibration is not as accurate as for HE electrons, partly due to seeding efficiency not as good as in high energy cases, partly due to the calibration procedure that can not describe electrons at very lower energy especially to recover energy between Presample(PS) and Strips. A method based on the beam chamber information, was introduced in the first part to measure single electron injected energy of test beam VLE data, and to check the linearity at event-by-event level, using current CTB default calibration configuration. The non-linearity is within 1% from 9GeV to 5GeV, and degraded to 5% for 1 GeV to 5 GeV. This is the first time the VLE electron linearity is studied. Meanwhile, VLE electron linearity matches very well with HE electrons at 9 GeV. The second part of this chapter introduces a multiple seed $5 \times 5$ clustering procedure, and an energy parameterizations to calibrate VLE electrons. This calibration schema do not use the square root term of PS and Strips which is used to estimate the energy deposited in PS and Strips, instead, it implement this term into weighting factor of PS energy. This solve the problem of wrong seeding and energy deposited in dead mater between PS and Strips non linearity at very low energy problem, and reach 1% non linearity from 1 GeV to 9 GeV. It shows a possible improvement to the VLE electron energy linearity. This method allow to measure with a good precision the energy of VLE electron without the use of the inner detector which provide a very interesting and independent method.

However, electron linearity can be improved by combining the information of Inner Detector, which is more accurate at low energy region than high energy region. This is

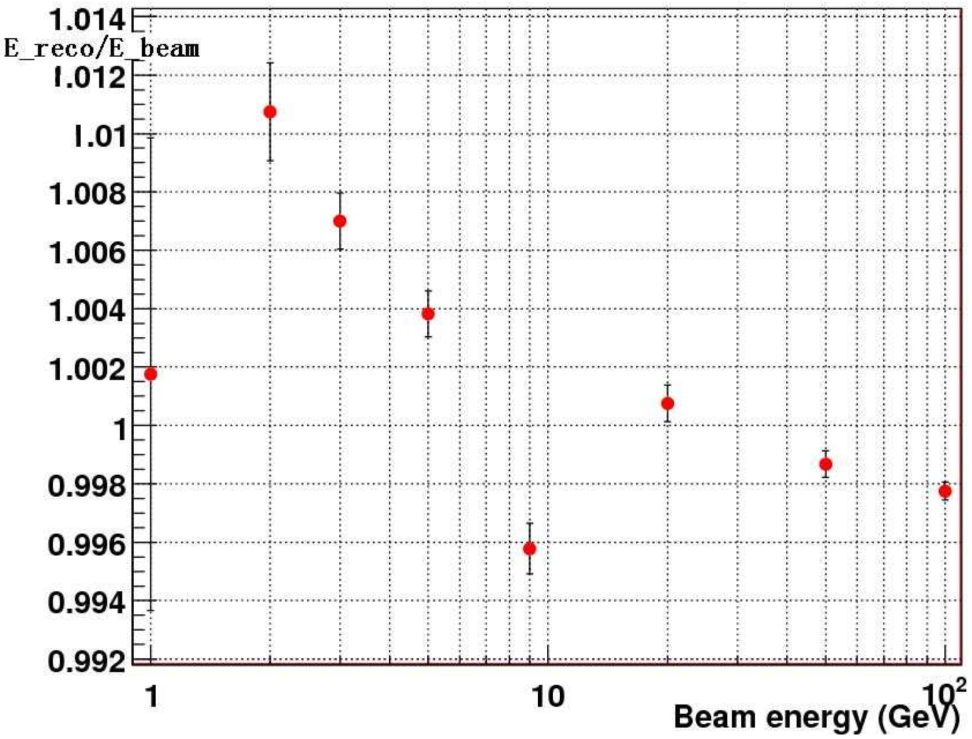

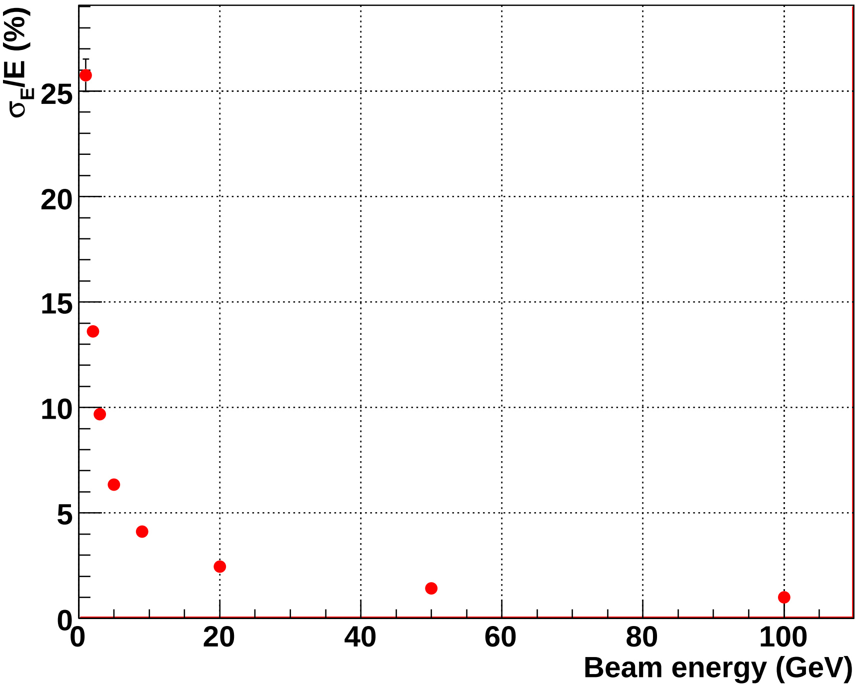

FIGURE 5.21: MC linearity of $E_{reco}$ and resolution as a function of $E_{beam}$

what will be done to reconstruct the electron energy in ATLAS at low energy region. The study of electron combined sub-detector measurements can also be done in the Combined Test Beam 2004, which has the inner detector in front of the calorimeter and with or without magnet filed. However, this is beyond the scope of this thesis.

# Chapter 6

# Summary and prospects

Using ATLAS Computing System Commissioning Monte Carlo full simulation data, this thesis studies the measurement of the top-quark Yukawa Coupling at $30fb^{-1}$ integrated luminosity for low luminosity run by studying $t\bar{t}H, H \rightarrow WW^{(*)}$ channel within the intermediate Higgs mass range from 120 to 200 GeV. This thesis is the first to present a detailed analysis of trigger and pileup effects as well as all possible systematic uncertainties. For a Higgs mass of 160 GeV, and including all the systematics, the signal significance has been exceed $2\sigma$ by combining two leptons and three leptons final states results. The combined branching ratio of $\sigma_{t\bar{t}H} \times BR_{H \rightarrow WW^{(*)}}$ can reach an accuracy of 47%, and gives important information on the top quark Yukawa Coupling. This work is the first complete study of the $t\bar{t}H, H \rightarrow WW^{(*)}$ channel using full simulation data, including a detailed estimate of the systematic uncertainties.

The most difficult part of the $t\bar{t}H, H \rightarrow WW^{(*)}$ analysis is to extract the signal from the abundant background since the total cross section of signal is only 0.1% of the typical $t\bar{t}$ background. Moreover, signal have a complex final state of at least four jets, two leptons, two neutrinos. It is very difficult to reconstruct the Higgs mass spectra. Lepton isolation is one of the most important method to suppress reducible backgrounds. This thesis develops a dedicated Cone Isolation procedure, which suppress the main background of $t\bar{t}$ by a factor 5.

The next challenge of this analysis is to have a more precise estimation of the backgrounds. Since $t\bar{t}H, H \rightarrow WW^{(*)}$ is a number counting experiment, the systematic uncertainty analysis showed that the precision on the Yukawa coupling constant measurement is dominated by the level and uncertainty of backgrounds. Therefore, it needs to develop a real data control sample to estimate the backgrounds and related uncertainties. This will be the next important direction of $t\bar{t}H, H \rightarrow WW^{(*)}$ analysis.

In addition, the use of fitting with the constrains of W and top mass to reconstruction $t\bar{t}H, H \rightarrow WW^{(*)}$ events(so called mass constraint fit), and the use of multivariate analysis to distinguish the signal and backgrounds, are also the directions to improve the performance of this analysis.

The measurement of Higgs and top quark Yukawa Coupling constant need accurate information on the $H \rightarrow WW^{(*)}$ branching ratio, or accurate measurement of the Higgs width. The resolution of Higgs boson mass at LHC is of the order of a GeV [7], More accurate measurement of the Higgs width will need the ILC.

However, in addition to measuring the LHC $\sigma_{t\bar{t}H} \times BR_{H\to WW^{(*)}}$ combined branching ratio, one can also, through a combination of other Higgs decay model studies such as the $H \to bb$, give the partial-width ratio, and thus access the relationship between the coupling constants of Higgs to different fermions and bosons, and give the information on the origin of the mass [10].

Lepton energy scale uncertainty is one of the important systematics uncertainty sources for the $t\bar{t}H, H \to WW^{(*)}$ analysis, and a good linearity of Very Low Energy(VLE) electron can improve the performance of estimating the electron energy scale. This thesis also presents my work on the VLE electron calibration of Combined Test Beam(CTB) data. The linearity of the CTB real data VLE electron is extracted, on an event by event basis, with a new method based on beam chamber information and is shown to reach a non linearity better than 1% from 5 to 9 GeV and 5% from 1 to 5 GeV. Using Monte Carlo calibration constant, from a $5 \times 5$ Multiple Seeding Clustering method, and only applied for the time being on simulated data, a 1% non linearity from 1 to 9 GeV is achieved, indicating a very promising technic to be used on real data.

# Bibliography

[1] H. Liu, X. Cai. *The principle of Quark and Lepton dynmatics.* Hua Zhong Normal University Publisher, Dec. 1999.

[2] C.B. Yang, X. Cai. *Preface of Quark and Lepton dynmatics.* Hua Zhong Normal University Publisher, Mar. 2000.

[3] Abdelhak Djouadi. The anatomy of electro-weak symmetry breaking. i: The higgs boson in the standard model. 2005.

[4] The ATLAS Collaboration. Lhc design report volume i. http://ab-div.web.cern.ch/ab-div/publications/LHC-DesignReport.html.

[5] Roberto Bonciani, Stefano Catani, Michelangelo L. Mangano, and Paolo Nason. NLL resummation of the heavy-quark hadroproduction cross- section. *Nucl. Phys.*, B529:424–450, 1998.

[6] Abdelhak Djouadi. The anatomy of electro-weak symmetry breaking. ii: The higgs bosons in the minimal supersymmetric model. 2005.

[7] The ATLAS collaboration. Atlas detector and physics performance. technical design report. vol. 2. CERN-LHCC-99-15.

[8] The LEP Collaborations. A combination of preliminary electroweak measurements and constraints on the standard model,. 2005. hep-ex/0412015.

[9] The LEP Electroweak Working Group. The lep electroweak working group plots. http://lepewwg.web.cern.ch/LEPEWWG/.

[10] D. Zeppenfeld et al. The higgs working group summary report,. 2000. hep-ph/0002258.

[11] W. Beenakker et al. Higgs radiation off top quarks at the tevatron and the lhc. *Phys. Rev. Lett.*, 87:201805, 2001.

[12] M. Duehrssen. Prospects for the measurement of higgs boson coupling parameters in the mass range from 110 - 190 gev/$c^2$, 2003. ATL-PHYS-2003-030 (2003).

[13] M. Duhrssen et al. Extracting Higgs boson couplings from LHC data. *Phys. Rev.*, D70:113009, 2004.

[14] Klaus Desch and Markus Schumacher. Model independent determination of the top Yukawa coupling from LHC and LC. *Eur. Phys. J.*, C46:527–531, 2006.

[15] F. Maltoni, David L. Rainwater, and S. Willenbrock. Measuring the top-quark yukawa coupling at hadron colliders via t anti-t h, h to w+ w-. *Phys. Rev.*, D66:034022, 2002.

[16] J. Levêque, J. B. de Vivie, V. Kostioukhine, and A. Rozanov. Search for the standard model higgs boson in the $t\bar{t}h$, $h \to ww^{(*)}$ channel, 2002. ATL-PHYS-2002-019 (2002).

[17] B. Mellado et al. Higgs production cross-sections and branching ratios for the atlas higgs working group, 2007. com-phy-2007-024.

[18] Cern grey book. http://greybook.cern.ch/.

[19] J. M. Campbell, J. W. Huston, and W. J. Stirling. Hard interactions of quarks and gluons: A primer for LHC physics. *Rept. Prog. Phys.*, 70:89, 2007.

[20] The ATLAS Collaboration. The atlas experiment at the cern large hadron collider, com-phys-2007-102.

[21] ATLAS Collaboration. Inner detector: Technical design report, 1997. CERN/LHCC/97-016/017.

[22] ATLAS Collaboration. Atlas pixel detector: Technical design report, 1998. CERN/LHCC/98-013.

[23] ATLAS Collaboration. *Liquid Argon Calorimeter: Technical Design Report.* CERN/LHCC/96-041, 1996.

[24] ATLAS Collaboration. *Tile Calorimeter: Technical Design Report.* CERN/LHCC/96-042, 1996.

[25] B. Aubert et al. Construction, assembly and tests of the atlas electromagnetic barrel calorimeter. *Nucl. Instrum. Methods*, A558:388–418, 2006.

[26] D.M. Gingrich et al. Construction, assembly and testing of the atlas hadronic end-cap calorimeter. *JINST*, 2:p05005, 2007.

[27] Atlas internal note, 1993. MUON-NO-24.

[28] Precision Chamber Group. Atlas internal note, 1997. MUON-NO-181.

[29] M. Deile et al. Performance of the atlas precision muon chambers under lhc operating conditions. *Nucl. Instrum. Methods*, A518:65–68, 2004.

[30] M. Deile et al. Resolution and efficiency of the atlas muon drift-tube chambers at high background rates,. *Nucl. Instrum. Methods*, A535:212–215, 2004.

[31] G. Avolio et al. Test of the first bil tracking chamber for the atlas muon spectrometer,. *Nucl. Instrum. Methods*, A523:309–322, 2004.

[32] G. Bencze et al. Position and timing resolution of interpolating cathode strip chambers in a test beam. *Nucl. Instrum. Methods*, A 357:40, 1995.

[33] R. Santonico. R. Cardarelli, V. Makeev. Avalanche and streamer mode operation of resistive plate chambers. *Nucl. Instrum. Methods*, A 382:470, 1996.

[34] R. Cardarelli et al. Performance of a resistive plate chamber operating with pure cf3br. *Nucl. Instrum. Methods*, A 333:399, 1993.

[35] M. Atac et al. Self-quenching streamers. *Nucl. Instrum. Methods*, A 200:345, 1982.

[36] ATLAS Computing Group. Atlas computing technical design report, 2005. lhcc-2005-022.

[37] Torbjorn Sjostrand, Stephen Mrenna, and Peter Skands. Pythia 6.4 physics and manual. *JHEP*, 05:026, 2006.

[38] ATLAS Collaboration. Monte carlo generators for the atlas computing system commissioning, To be published in CSC book.

[39] The ATLAS Collaboration. Higgs boson searches at the large hadron collider, To be published in CSC book.

[40] Stefano Frixione and Bryan R. Webber. The mc@nlo 3.2 event generator, 2006. hep-ph/0601192.

[41] Michelangelo L. Mangano, Mauro Moretti, Fulvio Piccinini, Roberto Pittau, and Antonio D. Polosa. Alpgen, a generator for hard multiparton processes in hadronic collisions. *JHEP*, 07:001, 2003.

[42] Borut Paul Kersevan and Elzbieta Richter-Was. The Monte Carlo event generator AcerMC version 2.0 with interfaces to PYTHIA 6.2 and HERWIG 6.5, 2004. hep-ph/0405247.

[43] The ATLAS Collaboration. Overall trigger strategy for the electron and photon selection. To be published in CSC book.

[44] The ATLAS Collaboration. Performance of the atlas muon trigger slice with simulated data. To be published in CSC book.

[45] The ATLAS Collaboration. Identification of electrons with the atlas detector. To be published in CSC book.

[46] The ATLAS Collaboration. Muon reconstruction and identification performance in atlas: Studies with simulated monte carlo samples. To be published in CSC book.

[47] ATLAS Collaboration. Csc-jet5. To be published in CSC book.

[48] G. Alexander et al. A Comparison of b and (u d s) quark jets to gluon jets. *Z. Phys.*, C69:543–560, 1996.

[49] G. Abbiendi et al. Inclusive analysis of the b quark fragmentation function in Z decays at LEP. ((B)). *Eur. Phys. J.*, C29:463–478, 2003.

[50] D. Cavalli et al. Performance of the atlas fast simulation atlfast, 2007. ATL-PHYS-INT-2007-005 (2007).

[51] K. Cranmer. “lepstats4lhc”, software available at *phystat.org* repository. [packages/0703002].

[52] K. Cranmer. “profile likelihood number counting combination”, software available at *phystat.org* repository. [packages/0803001].

[53] Particle Data Group. Review of particle physics. *J. Phys.*, G33:1–1232, 2006.

[54] V. Giangiobbe P. Johansson L. Pribyl M. Volpi B. Di Girolamo, A. Dotti. Beamline instrumentation in the 2004 combined atlas testbeam, 2005. com-tech-2005-001.

[55] Thomas Koffas Beniamino Di Girolamo, Manuel Gallas. Atlas barrel combined run in 2004 test beam setup and its evolutions, 2005. ATC-TT-IN-0001, EDMS ID 406980.

[56] M.Aleksa et al. 2004 atlas combined testbeam computation and validation of the electronic calibration constants for the electronmagnetic calorimeter, 2004. ATL-LARG-PUB-2006-003.

[57] B. Cleland et al. Cabling of the atlas liquid argon calorimeters., 2003. ATL-AL-ES-0004.

[58] D. Lacour F. Orsini F. Hubaut, B. Laforge. Test beam measurement of the crosstalk in the em barrel module 0, 2000. ATL-LARG-2000-007.

[59] F. Hubaut. Crosstalk measurements in the em barrel module 0 from 99’, may 00’ and july 00’ beam tests, 2000. ATL-LARG-2000-009.

[60] M. Aharrouche et al. Energy linearity and resolution of the ATLAS electromagnetic barrel calorimeter in an electron test- beam. *Nucl. Instrum. Meth.*, A568:601–623, 2006.

[61] John Allison et al. Geant4 developments and applications. *IEEE Trans. Nucl. Sci.*, 53:270, 2006.

[62] Marco Delmastro. Calibration of vle electrons using the ”calibration hits” method at the ctb: status and perspectives, 2007.

[63] ATLAS Collaboration. Detector level jet corrections. To be published in CSC book.

[64] The ATLAS collaboration. Atlas detector and physics performance technical design report. volume 1. CERN-LHCC-99-14.

[65] G. Corcella et al. Herwig 6.5 release note, 2002. hep-ph/0210213.

# Acknowledgements

As time elapsed swiftly, in the blink of an eye, my five years of life for Doctor's Degree coming to an end. On the occasion of the completion of this thesis, I would like to express my sincere thanks to my teachers, classmates, friends and family who ever gave me consideration and help over the years!

First of all, I thank my Doctoral Supervisor Researcher Jin Shan in China. Every step of my growth in research can not be separated from Professor Jin's hard cultivation. Professor Jin's sharp thinking, rigorous academic style and meticulous research make a deep influence on me. In scientific research work, Professor Jin's ideas about science are from a strategic height, he often treats specific issues sharply, and with a real sense of commitment to the job and his ideas, even closing to addicted, all of these deeply affect my future study and work.

I thank my Doctoral Supervisor Dr Emmanuel Monnier in France. From the first day I encountered Dr Emmanuel, his zealous style and exuberant energy gave me a deep impression. Both in research work or daily life, Emmanuel can always find a solution of the difficulty from the unexpected perspective. During the discussion, Emmanuel can easily seize the differences between the two sides to find the key to the problem and give solutions. Emmanuel's spirit of scientific research and personal charm touched me so deep; he will ever be an example in my life.

I thank Associate Researcher Lv Feng for his help on my scientific research and my life in the ATLAS Group, especially for him examining and improving the results of my thesis. I thank Associate Researcher Shan Lianyou, whether in my start work of the BES in the first year or later physical analysis of the ATLAS process, he gave me a lot of details of the guidance and useful discussions on the research. I extend my thank to Associate Researcher Ji Xiaobin and Dr Fang Shuangshi for their help on my work of BES.Thank Researcher Tong Guoliang, Shen Xiaoyan, Ouyang Qun and Associate Researcher Xu Guofa for their help on me. Thank Dr Liao Hongbo, Dr Zhuang Xuai, Dr Li Xiaoling, Ge Junyan, Bai Yu, Zhu Xingwang, Diao Liying, Huang Yanping, Yuan Li, Liu Hongbang for their weekly exciting discussions in B424 and of their consideration on my daily life.Thank Dr Yuan Jianming, Dr Zhou Nengfeng, Zhang Zhenxia, Li Jiang, Tian Junping, Mohanmod, Liu Beijiang, Zhan Zhichao, Zhu Zhili, Yang Ming, Xiao Tao, Qin Hu, Jiang Xingyu, Li Yuanliu and other students in my office to create a good research environment in B410.Thank my roommates Cai Quan, Zhu Jihao and Tao Junquan for those happy days that we spent together. Thank Jean-Baptiste de Vivie, Laurent Vacavant, Pascal Pralavorio, Fabrice Hubaut, Bernardo Resende, Lorenzo Feligioni, Karim Bernardet of the Particle Physics Centre of Marseille(CPPM) for their discussions and

help, special thanks to Fanny Lessous for her consideration and help on my life, to Ms. Charling Tao and ZuXuan Qian for their consideration on me.

Thank Professor Lou Yuqing, Associate Researchers Qin Bo and Deng Jingsong, Associate Professor Zhu Chengguang, Classmates Liu Minghui and Sun Lei for working together in CPPM, two years of life in Marseille gave me sweet memories in my life.

Thanks long but paper short, it is inevitable to drop someone, together to express my deep gratitude to all my teachers and students for their consideration.

Thank my wife Rao Hongmei for her understanding and support on my work; thank my father, my mother and my sister for their care and attention, your solicitude is my work force.

# Abstract

The Higgs boson is one of the elementary particles which is predicted by the Standard Model, and which is the only one unobserved experimentally. Searching for the Higgs particles is the primary goal of many high energy experiments in the last decades. According to the Standard Model, $W^{\pm}, Z^0$ bosons obtain masses from vacuum spontaneous symmetry breaking via the Higgs Mechanism, while fermions obtain masses via Yukawa Couplings with Higgs boson. Yukawa Coupling, as one of the most important properties of Higgs boson, can distinguish whether the Higgs is Standard Model like or not.

The Large Hadron Collider(LHC) at CERN is a proton-proton collider with a designed center of mass energy of 14TeV. ATLAS is a general purpose particle detector located at one of the colliding point of the LHC. Data taking is expected to start this summer. The primary physics goals of the ATLAS experiment are Higgs searches, SUSY particles searches and Electro-Weak precision measurements...

Using ATLAS Computing System Commissioning(CSC) Monte Carlo full simulation data of the $t\bar{t}H, H \rightarrow WW^{(*)}$ channel, this thesis studies the feasibility of measuring top-quark Yukawa Coupling up to $30fb^{-1}$ integrated luminosity, within the intermediate Higgs mass range from 120 to 200 GeV. For the first time, trigger, pileup effects as well as all possible systematic uncertainties are extensively studied. For a Higgs mass of 160 GeV, with the detailed systematics uncertainties studied, the signal significance is shown to exceed $2\sigma$ by combining two leptons and three leptons final states together. The combined branching ratio of $\sigma_{t\bar{t}H} \times BR_{H\rightarrow WW^{(*)}}$ can reach an accuracy of 47%, and gives important information on the top quark Yukawa Coupling. This is the first study of the $t\bar{t}H, H \rightarrow WW^{(*)}$ channel based on full simulation data, including a complete and detailed study of the systematic uncertainties.

The most difficult part of the $t\bar{t}H, H \rightarrow WW^{(*)}$ analysis is to extract signal from an abundant background since the total cross section of signal is only 0.1% of the main background. Moreover, signals have a complex final state of at least four jets, two leptons, two neutrinos, making the Higgs mass reconstruction very difficult. Lepton isolation is one of the most powerful method to suppress reducible backgrounds. This thesis develops a special Cone Isolation procedure, which suppress by a factor 5 the main $t\bar{t}$ background.

Lepton energy scale uncertainty is one of the important systematics for the $t\bar{t}H, H \rightarrow WW^{(*)}$ analysis. A good linearity of Very Low Energy(VLE) electrons can improve the performance of estimating electron energy scale. The second part of this thesis presents a study of the linearity of VLE electron from 2004 ATLAS Combined Test Beam(CTB) data. First, a method based on beam chamber information is used to extract the linearity on a event by event basis. Then, a method based on calibration constants from $5 \times 5$ Multiple Seeding Clustering is presented, and tested on MC data only, showing a possible method to further improve the linearity of VLE electron energy on real data.

**keywords:** Higgs, Yukawa Coupling, ATLAS, Test Beam

# Abstract

Le boson de Higgs est l'une des particules élémentaires prédites par le modèle standard, et la seule pas encore observée expérimentalement. La recherche de la particule de Higgs est l'objectif premier de nombreuses expériences à haute énergie au cours des dix dernières années. Selon le modèle standard, les bosons $W^{\pm}, Z^0$ bosons obtiennent leurs masses de la brisure spontanée de la symétrie du vide par le mécanisme de Higgs, tandis que les fermions obtiennent leurs masses par couplage de Yukawa avec le boson Higgs. Ce couplage est une des plus importantes propriétés du Higgs et permet de distinguer si il est de type modèle standard ou non.

Le Grand Collisioneur de Hadron (Large Hadron Collider ou LHC) au CERN est un collisionneur proton-proton avec une énergie dans le centre de masse de 14 TeV. ATLAS est un détecteur de particules de type généraliste situé auprès d'un des points de collision du LHC. Le début de la prise des données est prévue pour cet été. Les principaux objectifs de physique de l'expérience ATLAS sont les recherches du boson de Higgs, de particules SUSY et les mesures de précision électro-faibles.

Utilisant des données Monte-Carlo ATLAS CSC (Computing System Commissioning) en simulation complète du canal $t\bar{t}H, H \rightarrow WW^{(*)}$, cette thèse présente une étude de la mesure du couplage de Yukawa du quark top pour une lumisosité intégrée de $30fb^{-1}$ dans la gamme de masses du boson de Higgs allant de 120 à $200GeV/c^2$. Pour la première fois, les effets du système de déclenchement, de l'empilement des événements, ainsi que de toutes les erreures systématiques possibles ont été extensivement étudiés. Pour une masses du Higgs de $160GeV/c^2$, en incluant toutes les erreures systématiques, la significance obtenue du signal est supérieure à $2\sigma$ en combinant les états finaux à deux et trois leptons. Le rapport d'embranchement combiné $\sigma_{t\bar{t}H} \times Br_{H \rightarrow WW^{(*)}}$ peut atteindre une précision de 47 % et donner des informations importantes sur le couplage de Yukawa du quark top. C'est la première étude du canal $t\bar{t}H, H \rightarrow WW^{(*)}$ en simulation détaillée du détecteur ATLAS, incluant une étude complète et détaillée des erreures systématiques.

La partie la plus difficile de l'analyse de $t\bar{t}H, H \rightarrow WW^{(*)}$ est d'extraire le signal du bruit de fond abondant car la section efficace du signal est seulement 0.1% de celle du bruit de fond $t\bar{t}$. En outre, le signal présente un état final complexe d'au moins quatre jets, deux leptons et deux neutrinos qui rendent très difficile la reconstruction du spectre de masse du Higgs. L'isolation leptonique est un des moyens les plus importants pour supprimer le bruit de fond réductible. Cette thèse développe une procédure dédiée d'isolation en cone permettant de supprimer le bruit principal $t\bar{t}$ par un facteur 5.

L'incertitude sur l'échelle d'énergie leptonique est l'une des principales sources d'incertitude systématique pour cette analyse $t\bar{t}H, H \rightarrow WW^{(*)}$. Une bonne linéarité de réponse pour des électrons de très basses énergies(VLE) permettrait d'améliorer la performance de l'estimation de l'échelle d'énergie des électrons. Cette thèse comprend également une étude de la linéarité de la réponse à des électrons VLE avec des données de tests en faisceau combiné (CTB) d'un secteur du détecteur ATLAS. Une première méthode basée sur l'utilisation, événement par événement,de chambre à fils proche du faisceau est présentée. Puis une autre méthode est étudiée par simulation Monte-Carlo. Elle est basée sur l'utilisation d'un étalonnage s'appuyant sur une constante de calibration obtenue par une aggrégation des énergies par graine multiple de 5 par 5. Les résultats de simulation de cette méthode permettent d'envisager une amélioration future de la linéarité de réponse à des électrons VLE.

**mots-clés:** Higgs, Yukawa Coupling, ATLAS, Test Beam